CHARACTERISTICS OF AZIMUTHAL THERMOACOUSTIC INSTABILITIES IN MULTI-NOZZLE CAN COMBUSTORS

A Dissertation
Presented to
The Academic Faculty

By

Jeongwon Kim

In Partial Fulfillment
of the Requirements for the Degree
Doctor of Philosophy in the
College of Engineering
George W. Woodruff School of Mechanical Engineering

Georgia Institute of Technology

December 2021

CHARACTERISTICS OF AZIMUTHAL THERMOACOUSTIC INSTABILITIES IN MULTI-NOZZLE CAN COMBUSTORS

Thesis committee:

Dr. Timothy Lieuwen
Aerospace/Mechanical Engineering
Georgia Institute of Technology

Dr. Adam Steinberg
Aerospace Engineering
Georgia Institute of Technology

Dr. Devesh Ranjan
Mechanical Engineering
Georgia Institute of Technology

Dr. Alan Hale
Arnold Engineering Development Complex
Arnold Air Force Base

Dr. Michael Leamy
Mechanical Engineering
Georgia Institute of Technology

Date approved: November 8, 2021

This thesis is dedicated to my love, Dohee Kim, and my little boy, Rohan Kim

ACKNOWLEDGMENTS

It would not have been possible for me to complete my PhD without supports and encouragement from many individuals.

First and foremost, I would like to express my deepest appreciation to my advisor, Dr. Timothy Lieuwen. I feel very lucky for joining this research group led by Dr. Lieuwen. Whenever I had discussions with you, every time I was amazed by your insights and innovative thoughts. I have learned so much from him during my PhD life; not just in research and scientific side but also as a human being. His support and advice always encourage me not to give up the race in the middle. I would also like to thank Dr. Leamy. The ME 6444, nonlinear system course, taught by him was significantly helpful to me to complete the chapter 7 in this thesis. Before taking this course, I was not even thinking about the modeling in my thesis, but this course inspired me to work on the modeling, and provided beautiful results. I would also like to thank Dr. Devesh Ranjan, Dr. Adam Steinberg, and Dr. Alan Hale who agreed to be a part of my defense committee.

Next, I would like to thank research engineers, David Wu, Ben Emerson, and Vishal Acharya. Wu, I have learned so many things from you in terms of the experimental setup and running the facility, but I want to especially thank you for helping me adapt quickly to the new environment. Whenever I had a question about something related to American culture, health insurance, housing, etc, you were the first person who came up in my mind. Specifically, I won't forget the day when I consulted with you about career negotiation. That conversation significantly affected my career. Ben, thank you for your support for my research, especially the AEDC project. Whenever I had a hard time with the project, you always encouraged me, provided nice feedback, and supported my results during the meeting. Without your help, I would not be able to finish the project this well. Vishal, I learned so much knowledge from discussions with you. Whenever I asked you questions, you gave me other questions and tasks related to my questions, which was a little bit stressful to

me. Looking back, however, I realized that those methods really strengthen my basics and broaden my knowledge. For both Vishal and Ben, I would like to express my thankfulness for giving me the advice about my future career as well.

I would also like to thank my lab folks, Athanasios Moshos, Timothy Cook, Henderson Johnson, Subodh Adhikari, Raghul Manosh, Wesley Gillman, Kotaro Koike, Thomas Pritchard, Christopher Douglas, Vedanth Nair, Hanna Ek, Aravind Chandh, Tony John, Sukruth Somappa, Austin Matthews, Angie Zhang, and Sai Kaza, who started or shared the graduate life with me. Although taking graduate level courses was not fun, I really enjoyed struggling with homework and projects and studying for exams over the night with them. Athanasios, thank you for organizing fun activities with our lab folks. In addition, I would not forget the day we worked overnight to run the MHI experiments. I would like to express my special thanks to Subodh because without his assistance (especially Labview), I would not be able to collect data and complete my thesis. Raghul, I and Dohee really enjoyed talking to you, especially when we made fun of you, but remember that this is because we love you. Chris and Tony, thank you for actively having discussions with me for my research. You guys are one of the smartest people I have ever known. Wes, I really enjoyed working with you on the MHI project, especially tightening/loosening the giant bolts and nuts...Just kidding:) If it were not for you, I would not finish the MHI project this well. Kotaro, thanks for translating from English to Japanese during our MHI telecon meeting. Sai, the party boy in the combustion lab. My graduate life would be less fun without you. And thanks to others as well.

Lastly, I deeply appreciate all the support from my wife, Dohee Kim. You are the most driving force for anything in my life. Whenever I was struggling with my research and future career, you were the one who infinitely encouraged me to never give up. Without your love, support, and patience, it would not have been possible to complete my PhD. I could not imagine how difficult it is to support the graduate student husband, and you did it! I promise that from now on, I won't make your life that hard again ever, and I will

compensate you for your hardship with the full of happiness. Rohan, my little boy, you won't probably remember this moment, but ever since you were born, you have been my second driving force in my life. Thank you for being born in this world, and motivating me to work harder. I can't wait for living the rest of my life with my family.

Finally, I gratefully acknowledge the support of Mitsubishi Heavy Industry and Arnold Engineering Development Complex for their financial support to make this work possible.

TABLE OF CONTENTS

LIST OF TABLES

LIST OF FIGURES

LIST OF ACRONYMS

CCW Counter Clock Wise

CW Clock Wise

EI Effective Independence

FEM Finite Element Method

FP Fixed Point

ISAAC Independence Sector Assumption in Annular Combustor

LES Large Eddy Simulation

LHS left hand side

LOS line-of-sight

LW Left-Ward

NSE Navier Stokes Equation

OR Outer Ratio

PDF Probability Density Function

PR Pilot Ratio

RH Routh Hurwitz

RHS right hand side

RW Right-Ward

SR Spin Ratio

TR Travel Ratio

SUMMARY

This study investigates azimuthal thermoacoustic instabilities in a multi-nozzle can combustor. Azimuthal modes can be modeled as a superposition of two counter rotating eigenmodes where they can either compete and potentially suppress one of them (spinning wave) or coexist (standing wave), depending on the operating conditions. In order to identify the dominance of each eigenmode, multiple sensors must be mounted at different azimuthal locations. This study first introduces a methodology to determine the optimal sensor locations for identifying the azimuthal mode. The optimal locations are determined in such a way that they minimize the variance of the estimated amplitude of two counter rotating waves for a given number of sensors and acoustic modes. This leads to simultaneous nonlinear equations, the solution of which provides the optimal sensor locations for identifying a single mode. Although the solutions can be obtained computationally, the paper suggests a physically intuitive approach for identifying these sensor locations. Lastly, the paper shows illustrative examples for optimally identifying multiple modes, which relies on computational effort.

Based on the measurements obtained from optimally located sensors, the paper describes dynamical behaviors of two counter rotating waves. The experimental data were taken at different mass flow rates as well as different azimuthal/radial fuel staging in a multi-nozzle can combustor. It is shown that at low flow rates with uniform fuel distribution, the two waves had similar amplitudes, giving rise to a standing wave. However, the two amplitudes were slowly oscillating out of phase to each other, referred to as a quasi-periodic standing wave, and the phase difference between the two waves also shows oscillatory behavior. For intermediate flow rates, the dynamics showed intermittency between standing and counter-clockwise (CCW) mixed waves, indicating that the system is bistable. It is found that the spin ratio, which quantifies the dominance between standing and CCW mixed waves, and phase difference, which is directly related to the orientation of

the anti-nodal line, transition simultaneously, implying a physical coupling between these two quantities. For high flow rates, the system stabilized at a CCW mixed wave most of the time. These experimental observations demonstrate that not only the amplitudes of two waves but also the phase difference plays an important role in the dynamics of azimuthal mode. For non-uniform azimuthal fuel staging, the modal dynamics exhibited only an oscillatory standing wave behavior regardless of the mass flow rates. Compared to the uniform fuel staging, however, the pressure magnitude considerably decreased, which provides a potential strategy to mitigate and/or suppress the instabilities.

Based on the experimental observations, the paper develops the low order modeling that governs the nonlinear azimuthal thermoacoustic oscillations. Utilizing the Galerkin projection of wave equations yields two set of second order differential equations, which are coupled through the nonlinear source terms. The governing equations are further simplified to the first order differential equations by using the method of averaging, allowing us to access to amplitudes and phases dynamics. The fixed point and stability analyses show that the system's non-uniformity has a significant impact on the onset of the instability and the modal nature as well as the preference in spinning direction. When the system first reaches the limit cycle, the azimuthal mode starts from a standing wave. Further increase in the linear growth rate may change the system from a standing to a mixed wave depending on the nonlinear coefficients. The numerical simulation shows that the frequency spacing between two eigenmodes and the background noise are responsible for quasi-periodic oscillation in modal dynamics during the standing wave, which are observed in the experimental data as well. To reproduce the intermittency between standing and a mixed wave observed from the experiments, the flame linear growth rate is modeled with a parametric noise. The dynamics of the amplitudes and phases are simulated to reproduce the phase average portraits. These are qualitatively compared with the phase portraits obtained from the experiments, and the model proved to be in good agreement with the experimental results.

CHAPTER 1

INTRODUCTION

1.1 Motivation

As the regulation of NOx emissions has become stringent, many combustion systems in modern gas turbines now rely on lean, premixed operating conditions, which introduce a new challenge called "combustion instabilities". These instabilities are serious problems in that they can cause flash back, blow off, limit the turbine's operating conditions, reduce hardware lifetimes, and finally destroy the combustor hardware [1]. For example, Figure 1.1 is a picture of a can combustor both before and after having been exposed to the combustion instabilities. The left picture shows a clean perforated dump plane around the multiple nozzles, whereas the right picture shows the dump plane being destroyed by the combustion instabilities. The parts of the hardware can propagate downstream and damage the turbine blades, resulting in a significant financial loss.

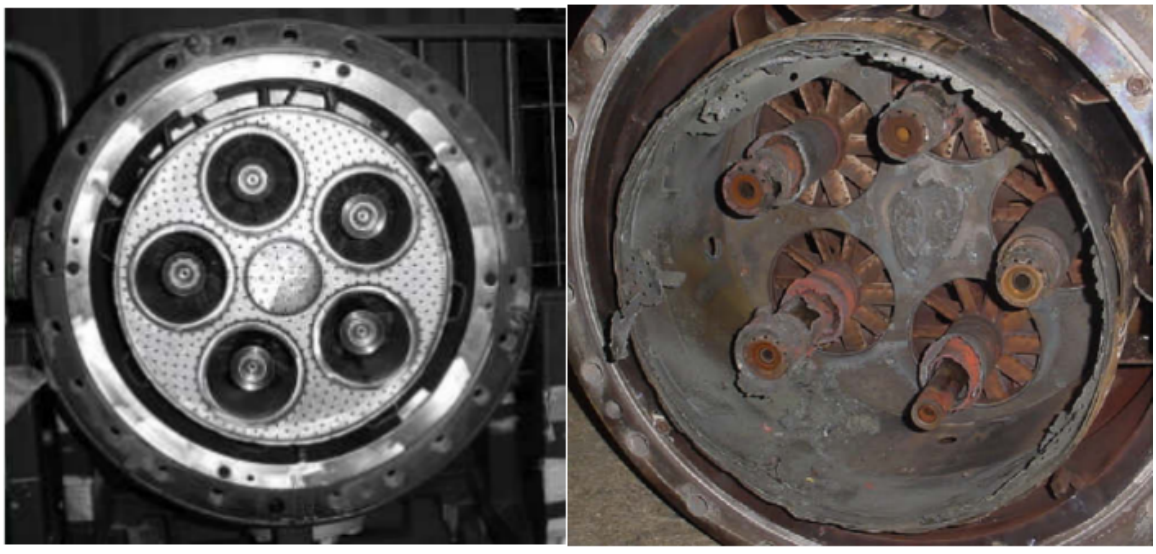

Figure 1.1: (a) New burner nozzle assembly before exposed to combustion instability. (b) Failed burner assembly after combustion instability [2].

These instabilities can excite different acoustic modes, depending upon geometry or operating conditions. In annular combustors, for example, the instabilities appear as low frequency longitudinal [3, 4, 5, 6] or azimuthal [7, 8, 9] modes. Can type combustors [10] and jet engine augmentors [11, 12, 13, 14, 15, 16] also exhibit high-frequency azimuthal modes. The major focus of this study is high-frequency thermoacoustic azimuthal mode.

Prior studies of these azimuthal wave dynamics have largely focused on annular combustors. Comparable studies of modal dynamics of azimuthal modes in can combustors are relatively scarce. A key difference between the annular and can combustors is the number of degrees of freedom of acoustic wave motions. Wave motions are nearly one-dimensional in annular combustion chambers where the annulus width is small relative to the overall diameter. Moreover, the "thin gap" assumption is remarkably accurate even when this ratio is not small in annular combustors [17]. In contrast, azimuthal modes are inherently two- or three-dimensional in can combustion chambers. Thus, one question arises as to how this additional degree of freedom manifests itself in azimuthal modal dynamics.

This study aims to reveal the modal dynamics of azimuthal mode in a multi-nozzle can combustor. The dynamics are investigated experimentally, and then a low order model has been developed to capture the experimental observations. This study will improve the understanding of the mechanism of the azimuthal thermoacoustic instabilities so that the future combustors will have less experience with the instabilities, and thus, expand the operating window.

1.2 Background

Combustion instability is an oscillation driven by a heat release fluctuation coupled with one or more natural acoustic modes of the combustor. This phenomenon was first observed in 1859 by Professor Rijke [18]. He observed that when heat source was placed inside a glass tube, the sound was produced whose frequency was nearly the fundamental natural mode of the tube. Later in 1878, Rayleigh theorized the necessary condition for the

combustion instability, called "Rayleigh criterion" [19]. It states that the phase difference between acoustic pressure and heat release fluctuation must be within $\pm 90^{\circ}$ to add energy to the system. This criterion can be formulated in a mathematical way as follow.

$$\int_V \int_t p'(\vec{x},t) q'(\vec{x},t) dt dV > 0 \tag{1.1}$$

The physical interpretation of the Rayleigh criterion is that when the heat release fluctuation, which results in oscillations in local gas expansion/compression, is in phase with pressure oscillations, the acoustic energy is periodically added by pdV work. Note that this criterion is a necessary condition for combustion instability. In order for any system to be self-excited, the value of the integral in Equation 1.1 must exceed the volume-integral of the system damping, i.e., the net energy must be added to the oscillating mode. The sources of the damping include losses of acoustic energy through inlet and outlet boundaries and energy transformation from acoustics to vorticity. When the net energy is positive, the oscillation amplitude exponentially grows in time. As the amplitude grows, however, the flame experiences nonlinear effects such as saturation in flame area fluctuation [20] or flame extinction [21, 22, 23]. These nonlinear effects typically increase system damping until the net energy becomes zero, causing the amplitude to saturate into a limit cycle.

To add energy to the acoustic field periodically, the heat release must be consistently perturbed by some mechanisms to close the feedback loop. This feedback cycle between heat release fluctuation and acoustics consists of three processes as shown in Figure 1.2. The heat release oscillations induce acoustic oscillations, which propagate upstream and downstream with a speed of sound. The upstream wave excites the vorticity and equivalence ratio fluctuations, which advects to the flame region with a bulk velocity. These oscillations lead to heat release fluctuations that close the feedback loop.

The detailed mechanisms of how acoustic oscillations excite the oscillations in heat release rate have been studied by several researchers [17, 24, 25]. In general, these mechanisms involve one or multiple pathways, but here we will briefly discuss three representa-

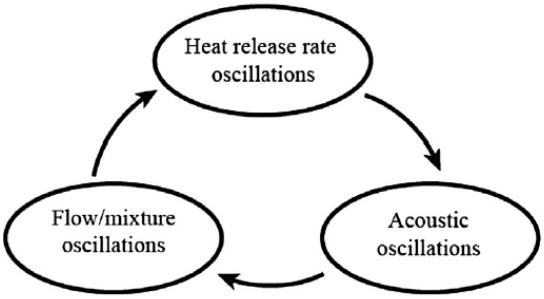

Figure 1.2: Thermoacoustic feedback cycle

tive coupling mechanisms. The first one is the "velocity-coupled mechanism", in which the heat release is sensitive to the velocity disturbances originated from acoustic and/or vortical disturbances [26, 27, 28, 29, 30, 31, 32], where the vortical disturbances are excited by the interaction between acoustic and mean flow fields [33, 34, 35]. The velocity disturbances perturb the flame speed, wrinkling the flame surface area, which, in turn, oscillates the heat release rate. The characteristic delay times between velocity and heat release oscillations are associated with a convective time from the vortex's point of origin to the midpoint of the flame.

We next consider the "equivalence ratio (fuel/air ratio) oscillation mechanism" [36, 37, 38, 39, 40, 41, 42, 43, 44, 45, 46, 47, 48]. When the local equivalence ratio is perturbed by acoustic wave at the injection point, the disturbance in equivalence ratio propagates to the flame region, leading to heat release oscillation through multiple pathways, including fluctuations in flame speed and mixture heat of reaction. The characteristic delay times between equivalence ratio and heat release oscillations are also associated with a convective time from the fuel injection point to the midpoint of the flame.

Lastly, consider the coupling between acoustic pressure and heat release rate. Note that the acoustic pressure is isentropically related to fluctuations in temperature, velocity, and density. Acoustic pressure generated from the flame can travel, reflect at the boundaries, and travel back to the flame region. This reflected wave perturbs the flame through disturbances in the reaction rate, flame speed, and reactant density. Compared to the velocity

and equivalence ratio couplings, the effect of pressure coupling at very low frequencies is of $O(M)$, and thus, is often neglected in low Mach number flows [17, 49, 50, 51, 52, 53]. However, there are some instances where the pressure coupling mechanism is dominant relative to other mechanisms, e.g., high frequency or flat flames propagating through homogeneous mixtures [54, 55, 56, 57, 49].

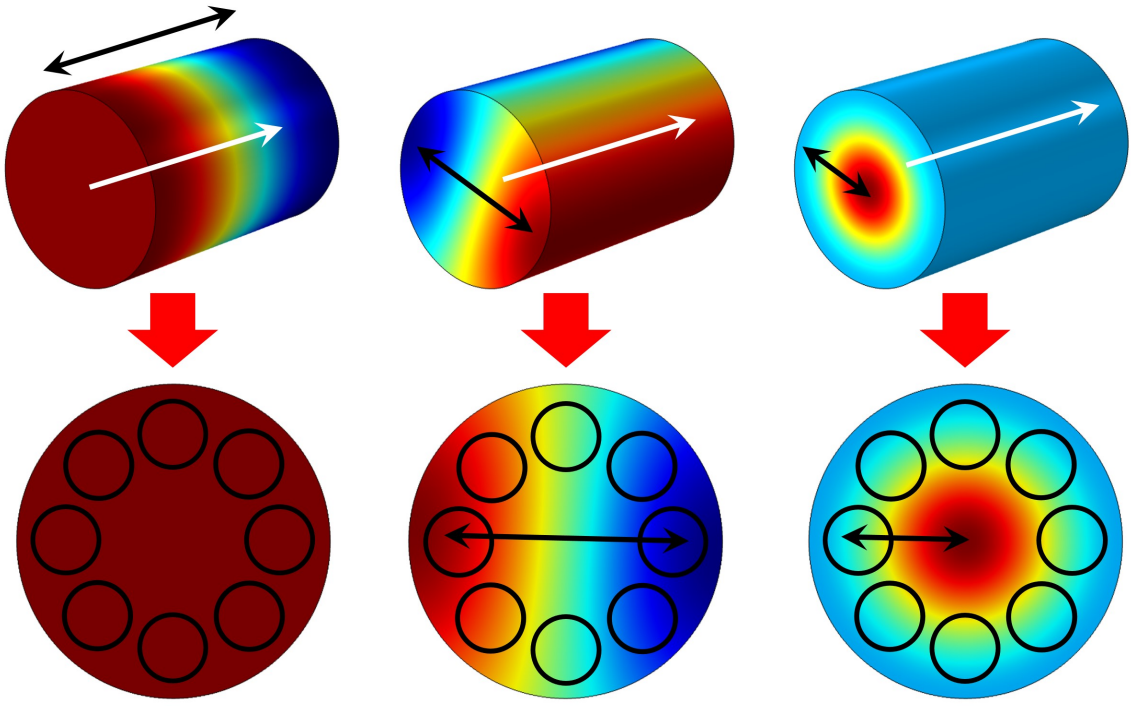

(a) Longitudinal mode (b) Azimuthal mode (c) Radial mode

Figure 1.3: Natural modes in a can combustor with multiple burners. Black and white arrows denote the oscillation and flow directions, respectively. Black circles represent the burners.

Combustion instabilities can occur over a wide range of frequencies, so operators in air-breathing systems often classify the instabilities based on their frequencies. For instance, "low frequency" instabilities are often called "humming" or "rumble", and "high frequency" ones are referred to as "screech". However, it is more natural to categorize them based on natural modes because the instabilities are associated with one of the natural frequencies of the combustors. Given that the combustors are typically cylindrical (or annu-

lar), the natural modes are classified as longitudinal, azimuthal, and radial modes as shown in Figure 1.3. The direction of the pressure oscillation for longitudinal mode is parallel to the flow direction, whereas the direction for azimuthal and radial modes are perpendicular to the flow. For this reason, the azimuthal and radial modes together are often referred to as "transverse mode". Note that the natural frequency of the radial mode is higher than that of the azimuthal mode. This can be explained by using a time of travel analogy. Given that the frequency is inversely proportional to a wave travel time, the acoustic wave for the radial mode travels from the center to the outer radius, whereas the wave for the azimuthal mode propagates from the outer radius to the opposite side. Since the travel time for the radial mode is shorter, its natural frequency is higher. However, the relative frequencies between transverse and longitudinal modes are strongly dependent on the geometry. For example, if the axial length is much shorter than the radial length, the natural frequency of the longitudinal mode would be higher than that of the transverse mode, or vice versa. Therefore, low frequency instabilities do not necessarily mean that it is the longitudinal mode. For example, annular combustors with shorter axial dimension experience low frequency azimuthal mode.

This study focuses on high frequency azimuthal mode instabilities. Before we get into the detail of the high frequency instabilities, it is worthwhile to compare them with the low frequency, longitudinal modes [58]. Typical longitudinal acoustic modes in real combustors have a longer wavelength than the flame length in the direction of the mean flow, which can be quantified by the Helmholtz number, He,

$$He_L = \frac{\delta_x}{\lambda_L} << 1, \qquad He_T = \frac{\delta_r}{\lambda_A} > 0.1 \tag{1.2}$$

where δ is the flame length and λ is the acoustic wavelength. The subscripts, L, A, x, r, denote longitudinal, azimuthal, axial, and radial. For small Helmholtz number, $He_L \ll 1$, the flame can be regarded as "compactness". The assumption is very powerful in that the flame describing function can be assumed as a global quantity, i.e., the pressure magnitude and

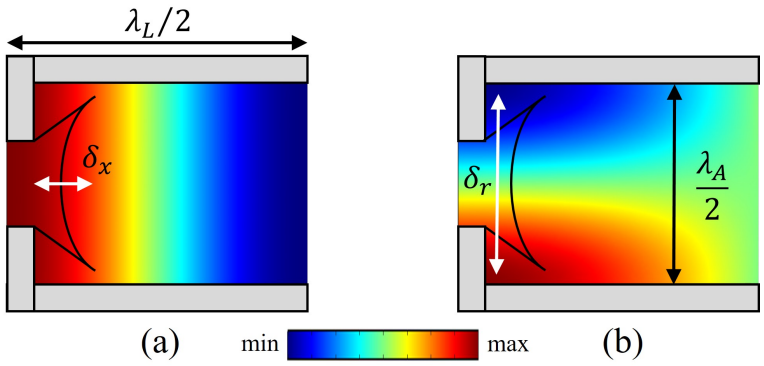

Figure 1.4: Schematic of (a) longitudinal and (b) azimuthal acoustic mode with respective flame heat release region.

phase are less dependent on space in a flame region. This is well illustrated in Figure 1.4 (a). For longitudinal modes with long wavelength, pressure variation across the flame is negligible, and thus, the flame can be regarded as a global quantity.

However, this assumption is not valid for high frequency azimuthal modes where the acoustic wavelength is comparable to the flame length in the azimuthal direction, $He_T > 0.1$. In other words, the acoustic field exhibits multi-dimensionality where the magnitude and phase of acoustic pressure vary in the azimuthal and radial direction. See Figure 1.4 (b). This multi-dimensional acoustic field introduces three-dimensional hydrodynamics instabilities or helical flow disturbances that subsequently perturb the flame differently. In other words, depending on the flame location with respect to the acoustic structure, different flame/flow dynamics appear. For example, O'Connor et al. [59, 60, 61, 62] showed that when the flame is located at the location of the maximum pressure magnitude, referred to as pressure anti-node, the flame fluctuates axisymmetrically, which leads to axisymmetric hydrodynamic flow instabilities, see Figure 1.5 (a) and (c). In addition, the flame experiences large pressure oscillation, which could propagate upstream through the injector, and perturb the air/fuel ratio, referred to as "injector coupling" [63, 64, 65, 66, 67]. In contrast, for a flame located at the minimum pressure magnitude, or pressure node, the pressure field is out of phase across the burner centerline, exciting helical flow disturbances. This is illustrated in Figure 1.5 (b) and (d). As the acoustic wavelength in the azimuthal direction

is comparable to the nozzle/injector, each flame exhibits different behavior. Therefore, one needs to describe the flame dynamics locally, which makes the analysis much complicated.

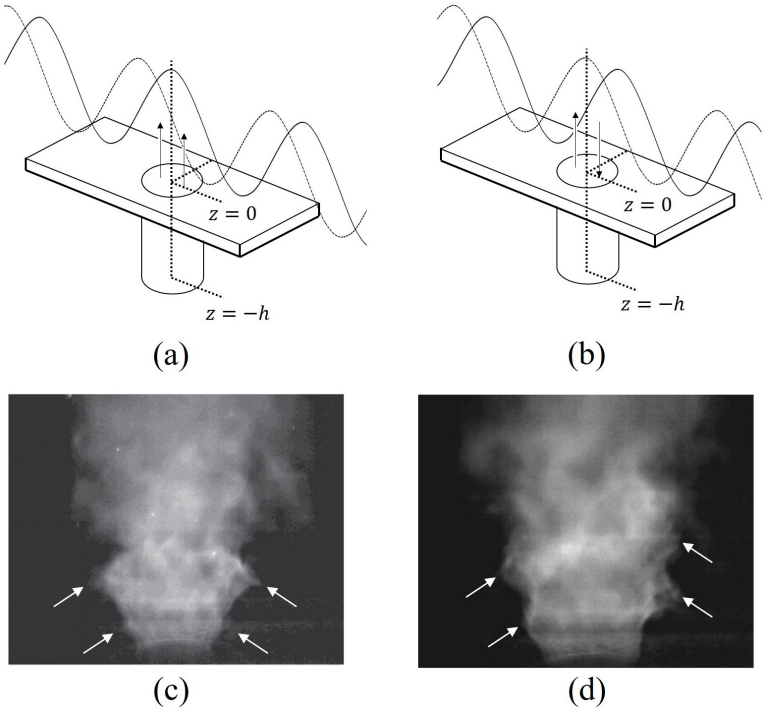

Figure 1.5: Schematic of burner located at (a) pressure anti-node and (b) pressure node. The solid and dotted lines denote acoustic pressure and velocity, respectively. Instantaneous flame image where flame is located at (c) pressure anti-node and (d) pressure node. Reproduced from O'Connor et al. [62]

One interesting thing about the azimuthal mode is that the pressure (anti-) nodal line can locate anywhere around the circumference because of its geometrical axisymmetry. This means that the (anti-) nodal line can rotate or randomly fluctuate in time, allowing each burner to experience pressure anti-node and node at different time instants. The dynamics of the (anti-) nodal line will be addressed later.

The other interesting phenomenon about the azimuthal mode is its acoustic structure. Given that the azimuthal mode is a superposition of two CW/CCW waves, the acoustic mode can be a standing, spinning, or a mixed mode depending on the relative strength between two spinning waves. For example, if CW/CCW waves have equal amplitude, then the resultant mode is a purely standing wave as shown in Figure 1.6 (a). In this case, the

pressure magnitude is spatial dependent, whereas the phase is constant except at pressure node, i.e., the phase abruptly shifts by 180° at the pressure node. If CW/CCW waves have different, but finite amplitudes, the final mode is a mixed wave where both pressure magnitude and phase are spatial dependent (Figure 1.6 (b)). Lastly, when either of CW or CCW wave has zero amplitude, the final mode is a purely spinning wave. In this case, the magnitude is constant, but the phase variation is linear (Figure 1.6 (c)).

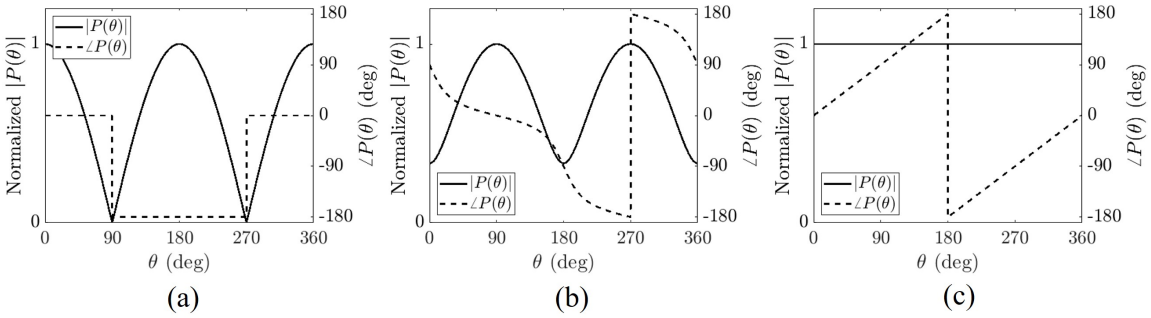

Figure 1.6: (a) Standing wave with pressure anti-node at 0°, 180° and node at 90°, 270°. (b) CW dominant mixed wave with pressure anti-node at 90°, 270° and node at 0°, 180°. (c) CCW spinning wave.

Unlike the longitudinal and radial modes where the possible acoustic structures are discrete, the structures for azimuthal mode are continuous, i.e., the relative amplitudes between CW/CCW waves can be arbitrary and the (anti-) nodal line can locate anywhere around the circumference. This characteristic is originated from the periodicity in the azimuthal direction. The following question is then how acoustic structures manifest themselves in real applications. The answer to this question is addressed in the next section.

1.3 Literature Review

This section introduces the previous studies regarding the dynamics of azimuthal mode, i.e., acoustic structure as well as its orientation. The studies are classified as computational, experimental, and analytical approaches.

We first consider computational studies. The advantage of computational analysis is its

cost-effectiveness. Compared to the experimental approach, which could be significantly expensive, simulations can be performed as long as computational power is affordable. This benefit especially stands out for the azimuthal mode analysis. For example, most experimental works explore combustion instability using simplified configuration because of the cost. Instead of the full annular or annular-can combustors, only one sector is replicated to reproduce the thermoacoustic instability as shown in Figure 1.7. This simplification is legitimate for a longitudinal mode because, as mentioned in the previous section, the dynamics of each burner are almost identical, i.e., acoustically compact. Thus, one sector can be a representative of the full annular combustor. However, the physics of azimuthal mode in a single sector and in a full annular combustor differ significantly. For example, the acoustic boundary conditions in a single sector are different from those in the full annular combustor. For this reason, one may reproduce the standing wave in a single sector using loud speakers on both ends, but not the spinning wave. Thus, the dynamics of standing and spinning waves cannot be captured from a simplified configuration. In order to capture the dynamics, one needs a full annular combustor facility, which would be costly, or one may rely on the computational analysis.

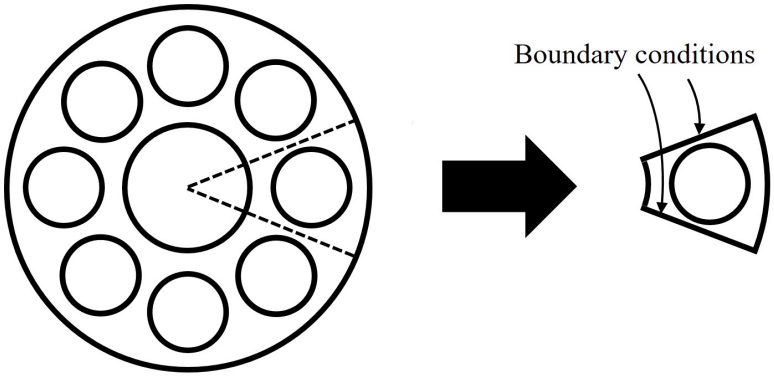

Figure 1.7: Illustration of simplified geometry from a full annular to a single sector burner.

Large Eddy Simulation (LES) has received considerable attention for analyzing the azimuthal instabilities in full annular combustors because of its low price. Selle et al. [68]

used a compressible LES to analyze an industrial gas turbine burner mounted on a square laboratory combustion chamber. They found that the hydrodynamic instability, or processing vortex core, occurs for a non-reacting flow, but the first azimuthal mode driven by thermoacoustic instability shows up for a reacting flow. The azimuthal mode rotates in one direction, i.e., spinning wave. Staffelbach et al. [65] and Wolf et al. [69] presented a massively parallel LES of a full helicopter combustion chamber, and showed that the spinning wave is dominant during the limit cycle. They also found that the injector coupling may be a mechanism driving the azimuthal mode. Later, Sensiau et al. [70] applied the Independence Sector Assumption in Annular Combustor (ISAAC) to LES simulations. The ISAAC basically states that the injector coupling is the only driving mechanism of heat release fluctuation. They adopted an n-tau model to each flame, and found that a standing wave is present for azimuthal symmetry, i.e, the case where all flames have identical gain and time delay. When the symmetry is broken, a spinning wave shows up. Later, Wolf et al. [71, 72] found that the dominant mode is a standing wave with a slowly rotating anti-nodal line at a mean swirl velocity, but the mode intermittently switches to a spinning wave. Similarly, Ghani et al. [73] used the LES to study a swirled single burner inside a rectangular chamber, and found that the self-excited azimuthal mode intermittently switches between standing and spinning waves. Schmitt et al. [74] also computationally studied a cylindrical combustor equipped with multiple coaxial injectors, and observed a standing dominant wave.

We next consider the experimental studies of the azimuthal mode. The appearance of standing and spinning waves was first reported by Kreb et al. [75, 76]. They installed multiple pressure transducers along the circumference in the full scale gas turbine, and observed standing as well as spinning waves. Moeck et al. [77] explored the azimuthal instabilities in a Rijke tube with 12 injectors, and observed the standing as well as mixed waves.

Using an academic annular combustor, Worth et al and Dawson et al, [78, 79, 9, 80]

investigated the dynamics of azimuthal modes at different burner geometries. Particularly, they found that the system transitions from switching between standing and spinning waves to a standing dominant wave with increasing the burner spacing or the number of baffles. When using the alternating swirl direction along the circumference, the mode remains the standing wave. The other study by Worth and Dawson [81] investigated the effects of equivalence ratio on the azimuthal modal dynamics. They observed that the mode transitions from the CCW spinning to the standing wave with increasing the equivalence ratio. Specifically, during the standing wave, the oscillation of the (anti-) nodal line was observed. They first proposed a phase averaged technique to illustrate the modal dynamics, which will be addressed later. Later, Faure-Beaulieu et al. [82] conducted the same experiments with a reduced number of burners, and observed the standing wave at a low equivalence ratio, but spinning wave at a high equivalence ratio.

Bourgouin et al. [83] carried out the azimuthal mode analysis with MICCA facility, and observed intermittency between the standing and spinning waves. They first introduced the concept of spin ratio, which quantifies the dominant mode between standing and spinning waves. The same group [84] explored the azimuthal mode with the same facility without the swirler, and found the standing wave with a nodal line located at a fixed azimuthal position. However, they reported that the nodal line sometimes rotates abruptly by 90°, or randomly changes. They also reported a new pattern of thermoacoustic instability, called the slanted mode [85], which is a combination of purely longitudinal and azimuthal modes where the azimuthal mode exhibited the standing wave. Later, the same group [86] used a matrix arrangement of small orifices in the injection system to eliminate the turbulent nature of swirling flames. From that facility, they observed the CW/CCW dominant waves, and reported that the direction of the spinning wave depends on the initial conditions, and once the direction is determined, it can persist as long as the operating conditions are not altered. Specifically, during the spinning wave, they observed that the nodal line sometimes rotates at a speed of acoustic frequency, but other times it stays at preferred azimuthal

locations. Laera et al. [87] and Prieur et al. [88, 89] investigated the azimuthal mode with the same MICCA combustor, and observed both standing, spinning, and switching modes. In addition, the nodal line of the standing wave was located at a fixed azimuthal position.

Using a sub-scale annular combustor without bulk swirl, Mazur et al. [90] ran experiments at various flow rates and equivalence ratios, and observed a standing wave at low amplitudes, but a spinning wave at high amplitudes. Specifically, the spinning wave showed bistability between CW and CCW, but a preference in CW direction. They speculated that despite the absence of bulk swirl, the higher probability of exciting CW is due to geometrical asymmetry or flow non-uniformity [70]. Cohen et al. [4] observed the spinning azimuthal mode from a can combustor equipped with symmetric fuel lines. They reduced the instability amplitude by introducing asymmetric fuel staging, but did not report the modal dynamics for this case.

The behavior of azimuthal mode in a single burner swirl stabilized combustor was also investigated by Schwing et al. [91]. They observed a CCW spinning wave whose direction coincides with the swirl direction. Later, the same group [92, 93, 58] reported the standing wave at low amplitude with low swirl intensity, but spinning wave at high amplitude with high swirl intensity.

To summarize the experimental observations, the azimuthal mode can manifest itself as the standing, spinning, or switching modes depending on the operating conditions and geometries. When the mode is stabilized to either standing or spinning wave, the nodal line predominantly stays at a fixed azimuthal position even though it sometimes drifts and rotates in a stochastic manner.

Based on these observations, numerous studies have proposed models to capture the physics controlling which type of mode is present. These are generally nonlinear, as linear models can generally allow for any arbitrary superposition of these disturbances. This problem appears to first have been treated by Schuermans et al. [94]. They examined the nonlinear interaction of the two orthogonal standing eigenmodes of an azimuthal mode and

showed that, when the system is linearly stable, only one standing mode persists under steady state conditions; the other standing mode is driven to zero. However, when the system is linearly unstable, both standing modes coexist, resulting in a spinning wave in one direction, either CW or CCW. Which mode dominates is solely a function of initial conditions. Similarly, Stow and Dowling [95] developed a time domain network model using two orthogonal standing eigenmodes, and found that the spinning wave is always preferred to the standing wave during the limit cycle. Hummel et al. [96, 92] investigated similar nonlinear interaction, but using two counter-rotating eigenmodes. They found similar results with Schuermans's work, but showed that loss of degeneracy in terms of frequencies and growth rates causes one spinning wave to be more realizable than the other spinning wave. However, the above works cannot capture the experimental observations where the standing wave persists during the limit cycle.

To reproduce this experimental result, several studies have included the presence of asymmetries in their models. Such non-asymmetries can exist in geometry, flow, or flame, such as due to azimuthal variations in fuel-air ratio, swirl directions of individual nozzles, or a discrete number of nozzles distributed azimuthally. Using two orthogonal standing eigenmodes, Noiray et al. [97] incorporated flame asymmetries into a nonlinear model, showing that it could lead to standing wave during the limit cycle. Similarly, Bauerheim et al. [98] used two counter-rotating eigenmodes, and theoretically showed that non-identical flame transfer functions between the burners induce the standing wave during the limit cycle, but the azimuthal bulk mean flow causes non-degenerate growth rate, resulting in spinning wave. However, their work is limited to a linear regime. Ghirardo et al. [99] demonstrated that despite the identical burners with no swirling flow, the instability mode could be either standing or spinning wave depending on the nozzle spacing. However, these studies cannot explain "switching mode" between standing and CCW/CW spinning waves during the limit cycle, which was observed from the experiments.

To account for this switching mode, Noiray and Schuermans [100] first introduced

background noise effects by including the stochastic additive forcing into their model. They showed that the stochastic forcing may be responsible for the switching mode, but their model cannot capture the bimodal probability distribution observed in the experiments. Later, Faure-Beaulieu et al. [82] developed a low order model with non-uniform flame describing function as well as the noise intensity, and found that the bimodal probability distribution between CCW/CW modes is achieved with a sufficient level of turbulent noise intensity. However, this model cannot explain the switching mode between standing and spinning waves observed from the experiments [9, 81]. Ghirardo et al. [101] showed that the background noise pushes the azimuthal mode towards the standing wave, but the experimental studies by Worth and Dawson [81] showed that the transition from standing to spinning wave is rather abrupt, showing intermittency. This intermittency cannot be reproduced from Ghirardo's model unless the noise intensity itself is intermittent. To reflect this intermittency, Bothein et al. [102] showed that the even very small fluctuation of flame temperature non-uniformity driven by the stochastic effect can induce the switching mode between standing and spinning waves. On the other hand, Ghirardo and Juniper [103] accounted for the sensitivity of heat release to transverse velocity oscillations, and showed that the standing and spinning waves could be bistable at the intermediate sensitivity, and thus, the mode could intermittently switch between them. This, however, is only one possible explanation. In terms of nodal line dynamics, low order models predicted that introducing non-axisymmetries makes the nodal line stay at a certain azimuthal location [82, 104].

1.4 Scope of Work

As seen from the previous section, computational or theoretical studies miss at least one of the experimental observations, e.g., standing wave limit cycle or oscillatory nodal line dynamics. The ultimate goal of the study is to reduce these gaps between experimental observations and analytical approaches.

This thesis consists of three parts. The first part addresses the question of how to optimally identify the azimuthal mode with a given number of pressure sensors. Assuming the noise is additive Gaussian, the uncertainty of the estimated pressure can be quantified by a mean of statistical properties. Then, the optimal probe location can be determined such that it minimizes the uncertainty. This will allow us to extract the physical quantities, such as spin ratio and nodal line position, with minimum uncertainty, and thus identify the modal dynamic accurately.

Next, this work will demonstrate the modal dynamics of azimuthal mode obtained from a multi-nozzle can combustor. Specifically, the experimental tests were conducted over a range of flow rates/thermal power settings and azimuthal/radial symmetry of nozzle fueling, in order to better elucidate the functional relationship between modal dynamics, operating conditions, and azimuthal/radial asymmetry. These experimental data will provide an insight into key parameters that control the system's dynamics. Additionally, the modal dynamics will be described in phase portrait to filter out the contribution of high dimensional dynamics, such as turbulent components. This phase portrait is significantly useful to describe the complicated modal dynamics in a simple way.

As a final step, this proposed work will develop a low order modeling that captures the experimental observations. The existing low order models cannot capture the following observations simultaneously: (i) the standing wave during the limit cycle, (ii) a periodic oscillation of the standing wave nodal line, (iii) the intermittency between standing and spinning waves, and (iv) preference in spinning direction during spinning wave limit cycle. The low order model developed in this study will capture all of these by introducing three key parameters, i.e., flame non-uniformity, frequency spacing, and stochastic forcing.

The rest of the thesis is organized as follows. Chapter 2 briefly introduces the basic equations and derives important governing equations that will be used throughout this paper. Chapter 3 introduces the experimental facility and diagnostics as well as the post-processing. Chapter 4 presents the optimal sensor placements for single and multiple az-

imuthal modes. Chapter 5 first introduces the acoustic mode shape analysis, and chapter 6 presents the experimental results such as pressure time series, dynamics of two spinning waves, and phase portrait. Chapter 7 introduces the low order model of azimuthal mode. The last chapter 8 presents conclusions and future works for this topic.

CHAPTER 2

RELEVANT THEORY

In this chapter, we introduce important basic equations with several assumptions. The derivation of these equations can be found in any classical acoustic textbooks or [17].

2.1 Linearized Euler Equations

The conservation variables (ϕ), density, velocity, and pressure, are governed by the well-known Navier Stokes Equation (NSE). In acoustics, these conservation variables perturb from their time averaged values, and thus, can be modeled as a sum of the time averaged values and a first order perturbation, i.e

$$\phi(\boldsymbol{x}, t) = \bar{\phi}(\boldsymbol{x}) + \epsilon\phi'(\boldsymbol{x}, t) \tag{2.1}$$

where bar ($^-$) donotes the time averaged value, prime (') the time-dependent acoustic quantities, and ϵ the smallness. Substituting Equation 2.1 into the NSE, neglecting viscous, thermal diffusion, source/sink term, and second order $O(\epsilon^2)$ terms leads to the following conservation equations:

$$\frac{\partial \rho'}{\partial t} + \boldsymbol{\nabla} \cdot (\bar{\rho}\boldsymbol{u'} + \rho'\bar{\boldsymbol{u}}) = 0 \tag{2.2}$$

$$\bar{\rho}\Big(\frac{\partial \boldsymbol{u'}}{\partial t} + \bar{\boldsymbol{u}} \cdot \boldsymbol{\nabla}\boldsymbol{u'} + \boldsymbol{u'} \cdot \boldsymbol{\nabla}\bar{\boldsymbol{u}}\Big) + \rho'(\bar{\boldsymbol{u}} \cdot \boldsymbol{\nabla}\bar{\boldsymbol{u}}) + \boldsymbol{\nabla}p' = 0 \tag{2.3}$$

$$\frac{\partial p'}{\partial t} + \bar{\boldsymbol{u}} \cdot \boldsymbol{\nabla}p' + \boldsymbol{u'} \cdot \boldsymbol{\nabla}\bar{p} + \gamma(\bar{p}\boldsymbol{\nabla} \cdot \boldsymbol{u'} + p'\boldsymbol{\nabla} \cdot \bar{\boldsymbol{u}}) = 0 \tag{2.4}$$

Equation 2.2 – Equation 2.4 are called linearized continuity, momentum, and energy equa-

tions, respectively, and they altogether are called ***Linearized Euler Equations*** (LEEs).

2.2 Wave & Helmholtz Equation

This section introduces the wave equation. Here, we assume homogeneous mean quantities (i.e., not a function of space), no mean flow, and an isentropic process. The isentropic assumption provides an additional relationship between pressure and density fluctuation, i.e., $p' = c^2\rho'$, making the linearized continuity equation redundant. With these assumptions, combining the linearized momentum and energy equations yields the ***Wave Equation***.

$$\frac{\partial^2 p'}{\partial t^2} - c^2\nabla^2 p' = 0 \tag{2.5}$$

Assuming the perturbation terms oscillate harmonically in time allows to express them in terms of a complex Fourier series, i.e.

$$\boldsymbol{p}'(\boldsymbol{x}, t) = \text{Real}\Big(\sum_{n=1}^{N} \hat{\boldsymbol{p}}_n(\boldsymbol{x}) \exp(-i\omega_n t)\Big) \tag{2.6}$$

The hat symbol ($\hat{}$) represents the mode shape of the solution variables at a distinct angular frequency, ω_n. Applying Equation 2.6 to Equation 2.5 allows expressing the wave equation in the frequency domain.

$$k^2\hat{p} + \nabla^2\hat{p} = 0. \tag{2.7}$$

Here $k = \omega/c$ is the wavenumber. Note that the summation can be dropped by making use of the orthogonality between each mode shape. Equation 2.7 is called the ***Helmholtz Equation***.

2.3 General Solution of Helmholtz Equation

This section derives the general solution of the wave and Helmholtz equation. The general solution can be obtained by the method of separation of variables. Since typical combustors have circular or annular geometries, we perform the analysis in a cylindrical coordinate system. The Helmholtz equation in a cylindrical system is given by:

$$\frac{1}{r}\frac{\partial}{\partial r}\left(r\frac{\partial \hat{p}}{\partial r}\right) + \frac{1}{r^2}\frac{\partial^2 \hat{p}}{\partial \theta^2} + \frac{\partial^2 \hat{p}}{\partial z^2} + k^2\hat{p} = 0 \tag{2.8}$$

Assume the form of the solution, $\hat{p}$, as follows:

$$\hat{p}(r, \theta, z) = R(r)\Theta(\theta)Z(z) \tag{2.9}$$

Substituting Equation 2.9 into Equation 2.8, and dividing both side by $R\Theta Z$ yields

$$\frac{1}{R}\frac{d^2R}{dr^2} + \frac{1}{rR}\frac{dR}{dr} + \frac{1}{r^2\Theta}\frac{d^2\Theta}{d\theta^2} + \frac{1}{Z}\frac{d^2Z}{dz^2} + k^2 = 0 \tag{2.10}$$

Equation 2.10 can be rewritten as:

$$\frac{1}{Z}\frac{d^2Z}{dz^2} = -\frac{1}{R}\frac{d^2R}{dr^2} - \frac{1}{rR}\frac{dR}{dr} - \frac{1}{r^2\Theta}\frac{d^2\Theta}{d\theta^2} - k^2 \equiv -k_z^2 \tag{2.11}$$

Note that the left hand side (LHS) of Equation 2.11 is only a function of z, but the right hand side (RHS) is not. Therefore, the RHS must be a constant, which is defined as $-k_z^2$, to satisfy Equation 2.11. Here, the minus sign follows conventions.

$$\frac{1}{Z}\frac{d^2Z}{dz^2} = -k_z^2 \rightarrow \frac{d^2Z}{dz^2} + k_z^2 Z = 0 \tag{2.12}$$

The solution of Equation 2.12 is given by:

$$Z(z) = A_1 e^{ik_z z} + A_2 e^{-ik_z z} \tag{2.13}$$

where $A_{1,2}$ are the amplitudes of $\pm z$ traveling waves, which are determined by the axial boundary conditions, and k_z is the axial wavenumber. Similarly, rearranging Equation 2.10 as follows.

$$\frac{1}{\Theta}\frac{d^2\Theta}{d\theta^2} = -\frac{r^2}{R}\frac{d^2R}{dr^2} - \frac{r}{R}\frac{dR}{dr} - \frac{r^2}{Z}\frac{d^2Z}{dz^2} - r^2k^2 \equiv -m^2 \tag{2.14}$$

The RHS is defined as $-m^2$ as it is not a function of θ. Equation 2.14 can be rewritten as:

$$\frac{d^2\Theta}{d\theta^2} + m^2\Theta = 0 \tag{2.15}$$

The solution of Equation 2.15 is

$$\Theta(\theta) = fe^{im\theta} + ge^{-im\theta} \tag{2.16}$$

Here, f and g are the amplitudes of CCW/CW spinning waves, and the constant, m is the azimuthal wavenumber, which must be an integer to ensure the fact that Θ is single valued in θ.

Lastly, equation for R can be expressed as:

$$r^2\frac{d^2R}{dr^2} + r\frac{dR}{dr} + (r^2k_r^2 - m^2)R = 0 \tag{2.17}$$

where $k_r^2 = k^2 - k_z^2$. Introducing a new variable, $\tilde{r} = rk_r$, Equation 2.17 can be written as:

$$\tilde{r}^2\frac{d^2R}{d\tilde{r}^2} + \tilde{r}\frac{dR}{d\tilde{r}} + (\tilde{r}^2 - m^2)R = 0 \tag{2.18}$$

This equation is known as the Bessel function. The solution of Equation 2.18 is given by

$$R(\tilde{r}) = B_1J_m(\tilde{r}) + B_2Y_m(\tilde{r}) \tag{2.19}$$

or equivalently,

$$R(r) = B_1 J_m(rk_r) + B_2 Y_m(rk_r) \tag{2.20}$$

where $B_{1,2}$ are constants determined by the radial boundary conditions, and J_m and Y_m are the Bessel functions of the first and second kind, respectively. Substituting Equation 2.13, Equation 2.16, and Equation 2.20 into Equation 2.9 gives the general solution of the Helmholtz equation in a cylindrical system.

$$\hat{p}(r,\theta,z) = \left(A_1 e^{ik_z z} + A_2 e^{-ik_z z}\right)\left(f e^{im\theta} + g e^{-im\theta}\right)\left(B_1 J_m(rk_r) + B_2 Y_m(rk_r)\right) \tag{2.21}$$

From Equation 2.6, the general solution of the wave equation is as follows:

$$\begin{aligned} p'(r,\theta,z,t) = \text{Real}\Big\{ &\left(A_1 e^{ik_z z} + A_2 e^{-ik_z z}\right)\left(f e^{im\theta} + g e^{-im\theta}\right) \\ &\left(B_1 J_m(rk_r) + B_2 Y_m(rk_r)\right) e^{-i\omega t} \Big\} \end{aligned} \tag{2.22}$$

where

$$k^2 = \left(\frac{\omega}{c}\right)^2 = k_r^2 + k_z^2 \tag{2.23}$$

Equation 2.23 is called a ***dispersion relation***. It relates the wavenumber of a wave to its frequency. For purely longitudinal modes, for example, $k_r = 0$, giving rise to $k_z = k = \omega/c$. Thus, the axial wavenumber is simply the angular frequency divided by a speed of sound. For transverse modes ($k_r \neq 0$), however, an interesting thing can happen. Rearranging Equation 2.23 in terms of k_z,

$$k_z = \sqrt{\left(\frac{\omega}{c}\right)^2 - k_r^2} \tag{2.24}$$

If the term inside the square root is positive, k_z would be a real number. If the term is

negative, k_z would be an imaginary number. Define $k_z = i\hat{k}_z$ where $\hat{k}_z$ is a real number, and substitute this into the axial component in Equation 2.21.

$$\hat{p}(z) \sim \left(A_1 e^{-\hat{k}_z z} + A_2 e^{\hat{k}_z z}\right) \tag{2.25}$$

Equation 2.25 shows that the axial wave is no longer traveling, but rather the amplitude exponentially decays/grows. For example, the first (A_1) and second terms (A_2) on the right hand side in Equation 2.25 indicate that the amplitude exponentially decays(A_1)/grows(A_2) as the wave travels in positive z direction. However, exponential growth to infinity does not physically make sense, and thus, A_2 must be zero for the wave traveling in a positive z direction. Therefore, only the first term remains. This wave is called an ***evanescent wave***, and it can only happen in transverse modes, which will be shown in chapter 5 later.

CHAPTER 3
EXPERIMENT OVERVIEW

This section first introduces the experimental facility used in this study. The facility is an industrial scale that can operate at approximately 2.5 MW thermal power with a high Reynolds number. Acoustic pressure was measured with high frequency pressure transducers. In addition, line-of-sight (LOS) CH* chemiluminescence was recorded by high speed camera. Lastly, this section explains the post-processing of the recorded data.

3.1 Experimental Combustor Facility

Figure 3.1 shows the experimental facility. Air from four inlets passes a critical orifice, making the upstream boundary condition as a pressure rigid, and enters near the axial midpoint of the rig and flows through an annular section in the upstream direction, cooling the chamber wall. At the front of the test article, the preheated air passes through one of eight outer ('O') and center pilot ('P') nozzles (Figure 3.1 (b)). Each nozzle consists of a swirler and fuel injector, and natural gas is used as fuel. The swirl directions of the pilot and outer nozzles are CW and CCW, respectively. Fuel flow through the outer and pilot is controlled separately, quantified by a pilot ratio (PR),

$$PR = \frac{\dot{m}_P}{\dot{m}_P + \dot{m}_O} \tag{3.1}$$

where $\dot{m}_P$ and $\dot{m}_O$ are the fuel flow rate through the pilot and outer nozzles, respectively. In addition, the outer nozzles are connected to two separate fuel lines, $O1$ and $O2$ (Figure 3.1 (c)), where fuel flow rate through each line is quantified by an outer ratio (OR),

$$OR = \frac{\dot{m}_{O2}}{\dot{m}_{O1} + \dot{m}_{O2}} \tag{3.2}$$

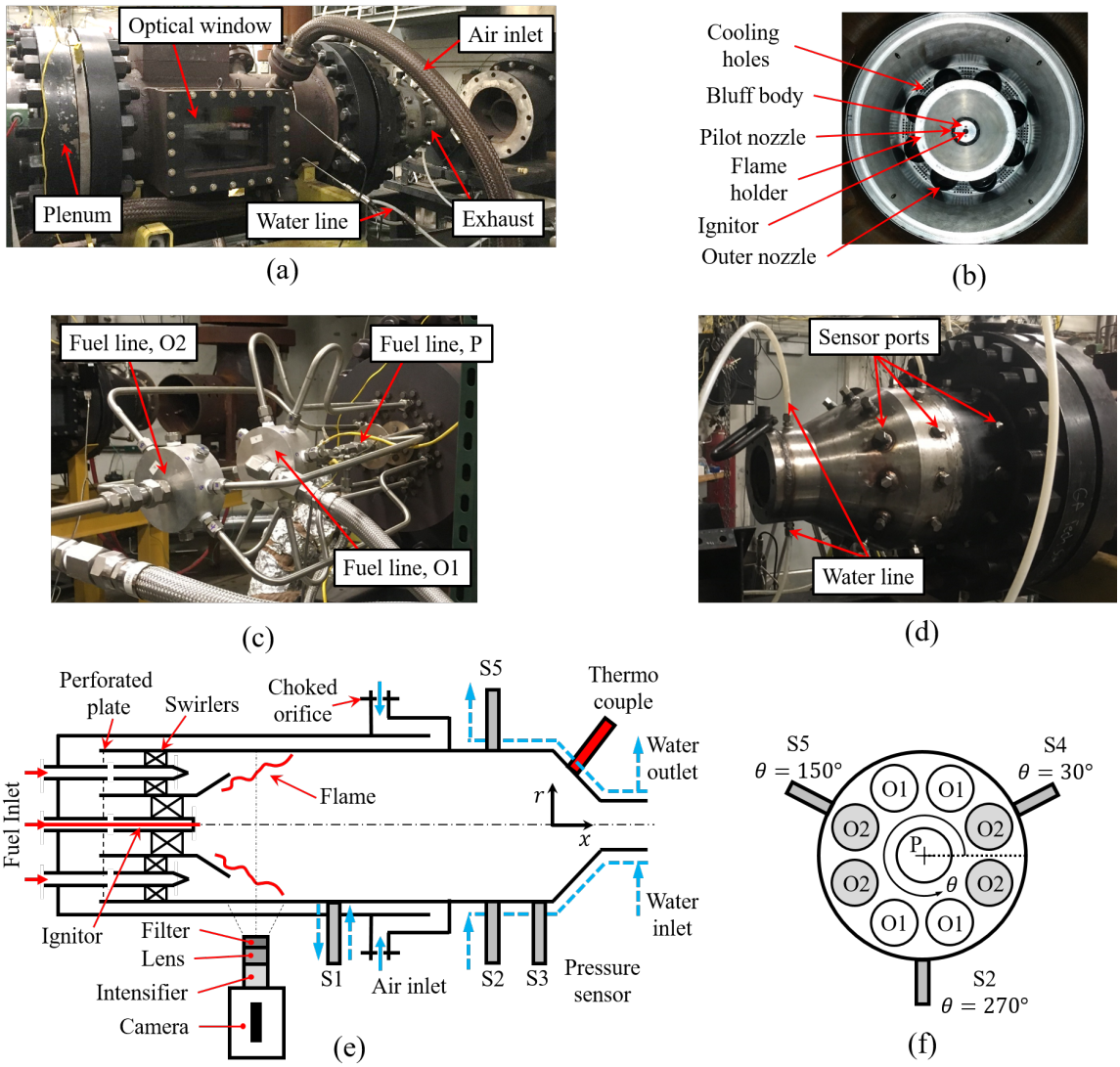

Figure 3.1: Experimental facility: (a) image of combustor, (b) image of multi-nozzle, (c) fuel line configuration, (d) sensor ports, (e) side-schematic of combustor, (f) sensor and fuel configurations.

Thus, $OR = 0.5$ means uniform fuel staging in the azimuthal direction, and the non-uniformity gets severer with increasing (decreasing) OR from 0.5. Notice that the fuel configuration of $O1$ and $O2$ described in Figure 3.1 (f) is one example of arbitrary configurations. The combustor consists of a liner whose diameter is 0.29 m and length is 1.2 m. Two types of materials were used for the liner; steel and quartz (Figure 3.2 (a) and (b)). The steel liner was used for exploring the operating conditions, and the quartz tube was used for optical diagnostics at a certain condition. The combustor product accelerates near the downstream contraction area and exits the system through the water-cooled exhaust. The simulation shows that the flow is chocked at the outlet, and thus, the outlet boundary condition can be assumed as a pressure rigid for low Mach number flow [17].

3.2 Flow System

The supply of the air and natural gas to the combustor is accomplished through 1 and 3 circuits, respectively, regulated independently upstream of the combustor. For example, Figure 3.3 shows fuel lines installation. Although not shown here, air line configu-

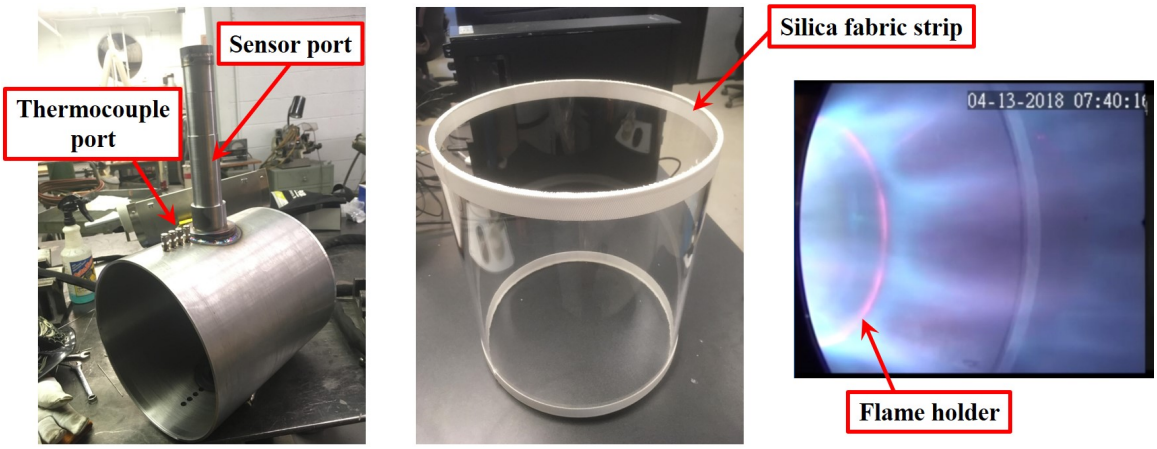

Figure 3.2: (a) Metal (steel) liner with sensor and thermocouple ports. The sensor port is designed to be water-cooled, and thermocouples are used to monitor the temperature near the sensor. (b) Quartz tube with silica fabric strip. The strip is used to minimize air leakage. (c) Camcorder image. Flames are attached to the outer edge of the flame holder.

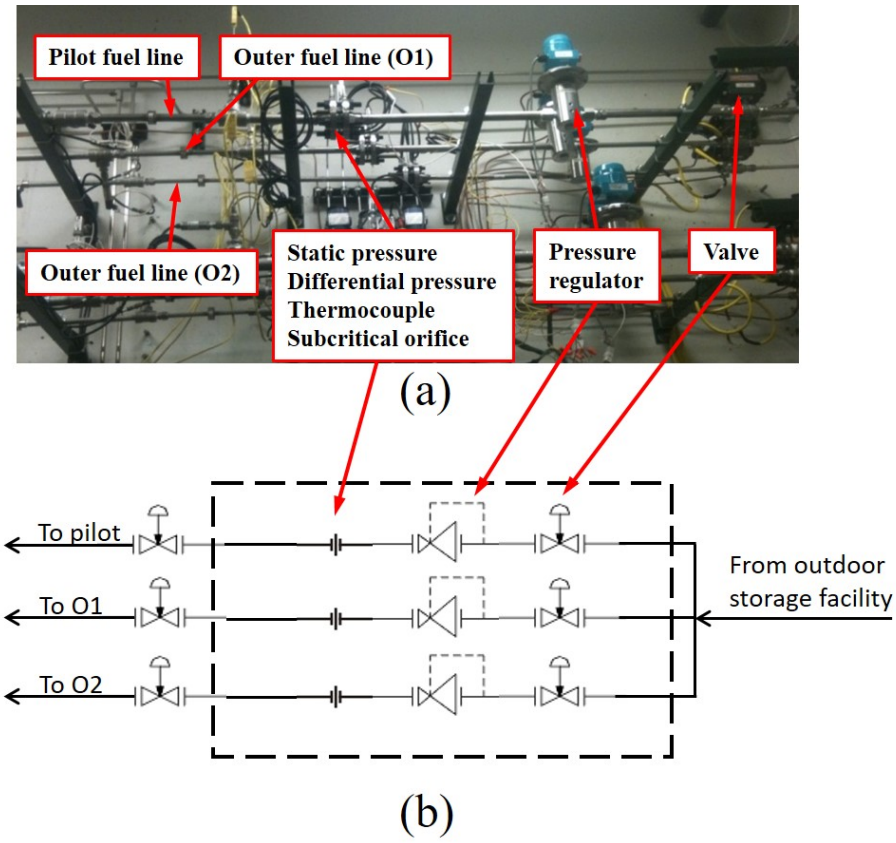

Figure 3.3: Experimental facility: (a) Photograph of flow metering and control segment of fuel lines. (b) Schematic of fuel lines

ration is similar to the fuel lines. As shown in Figure 3.3, each circuit is equipped with a pressure regulator, subcritical orifice, static pressure sensor, differential pressure sensor, and thermocouple. The pressure regulator controls the upstream pressure specified by the user. The static pressure and differential pressure sensors are used to measure the upstream/downstream pressure across the subcritical orifice, and the thermocouple measures the downstream fluid temperature. With these measurements, a mass flow rate through each circuit is calculated in real time by using the Reader-Harris/Gallagher equation [105].

3.3 Acoustic Measurement

In order to reconstruct the acoustic mode shape, we need multiple sensors at distinct locations. Total five 6021A Kistler pressure sensors (sensitivity: 62 pC/bar, range: 10 MPa, accuracy: $\pm 1\%$) were used to measure the dynamic pressure signals in the post-flame region. The facility has total of 36 ports at the exhaust (3 rows $\times$ 12 ports per row), and two ports at the upstream chamber (Figure 3.1 (d)). Thus, we can choose five among 38 ports to measure the acoustic pressure, providing flexibility of the sensor locations. Note that the sensor locations illustrated in Figure 3.1 (e) is just one example of arbitrary locations. All sensors are water-cooled to prevent from being damaged by combustion heat. They are connected to a Kistler 5181A differential charge amplifier (sensitivity: 10mV/pC, range: $\pm$10V, accuracy: $\pm 0.5\%$). The accuracy of the measurement is determined by a combination of the sensor and charge amplifier:

$$\underbrace{10\ \mathrm{V}}_{\text{charge amp. range}} \times \underbrace{\frac{1\ \mathrm{pC}}{0.01\ \mathrm{V}}}_{\text{charge amp. sensitivity}} \times \underbrace{\frac{1\ \mathrm{bar}}{62\ \mathrm{pC}}}_{\text{sensor sensitivity}} \times \underbrace{\pm 1\ \%}_{\text{sensor range}} = \pm 0.16\ \mathrm{bar} = \pm 16\ \mathrm{kPa}. \quad (3.3)$$

This value denotes the maximum deviation from a best fit line through the calibration curve, i.e., ± 16 kPa is the worst error you could get. This uncertainty can be considerably reduced by implementing a least squares fit from multiple sensors, which will be explained in chap-

ter 4. The pressure signal was recorded at the sampling frequency of 20 kHz, and then digitized by a National Instrument (NI 9215).

3.4 CH* Chemiluminescence Measurement

CH* chemiluminescence imaging is performed at various test conditions, with the camera positioned level, and perpendicular to the centerline of the combustion chamber. (Figure 3.1 (e)) A Photron Fastcam SA-X2 is used to capture video data at a sampling rate of 12.5 kHz, with a resolution of 1024x1024 pixels. At this resolution, the camera's on-board hard drive is capable of storing 5452 images. Two partitions are used, so each partition is 2726 images spanning a time 0.218 sec, each. Image decks are downloaded from the camera hard drive to an external hard drive through a gigabit Ethernet cable. A Nikon Nikkor 35 mm diameter lens with focal length of 50 mm is used. Incident light is first optically filtered using a lens with peak wavelength transmission at 434 nm, and then intensified using a LaVision High Speed IRO, with the gate set to the full width of the open camera shutter. The optical filter, lens, IRO, and camera are all attached end to end in this order. In each take, the optical inlet to the filter is placed approximately 0.3 m from the centerline of the test section.

3.5 Post Processing

3.5.1 Acoustic measurement

After stabilizing the operating condition, only a certain portion of the signals during the instabilities are extracted for post-processing. A time-series pressure signal, given by $p(\theta, t)$, is band-pass filtered around each peak frequency, f_p, with a rectangular bandwidth $df = 60$ Hz to not only isolate each acoustic mode from the other modes, but also improve

the signal to noise ratio [93]:

$$p'(\theta,t) = \mathcal{F}^{-1}\Big[\mathcal{F}\{p(\theta,t)\}\cdot \mathrm{H}\Big(f-\Big(f_p-\frac{df}{2}\Big)\Big)\cdot \mathrm{H}\Big(-f+\Big(f_p+\frac{df}{2}\Big)\Big)\Big] \tag{3.4}$$

Here, $p'(\theta,t)$ is a filtered pressure signal, $\mathcal{F}$ is the Fourier transform, and H is the Heaviside function. The bandwidth is determined such that it is wide enough, but includes only a single peak frequency such that $p'(\theta,t)$ contains only one acoustic mode. The filtered signal is then transformed into an analytic signal, $\hat{p}(\theta,t)$, by applying the Hilbert transform, $\mathcal{H}$ [93]:

$$\hat{p}(\theta,t) = p'(\theta,t) + \mathcal{H}[p'(\theta,t)] \tag{3.5}$$

This analytic signal is a complex number whose absolute value and angle correspond to its magnitude and phase, respectively. The signal is then fitted to the solution of the wave equation described later.

3.5.2 CH* chemiluminescence imaging

The objective of CH* images is to compare the heat release fluctuation data with the pressure signal. It is assumed that the intensity of the images is proportional to the heat release rate [93]. However, since the camera records the LOS integrated heat release, the pressure must be reconstructed and integrated equivalently to compare between them. Therefore, the following quantities are evaluated from the CH* images and the pressure signal:

$$\begin{aligned} Q(t) &= \int_{x_1}^{x_2}\int_0^R \underbrace{\int_{-R}^{R} q(x,y,z,y)dz}_{=Q_{img}(x,y,t)}\, dydx \\ P(t) &= \int_0^{\pi}\int_0^R p_{r\theta}(r,\theta,t) r dr d\theta \end{aligned} \tag{3.6}$$

Here, Q_{img} is the heat release data of each image, which is already integrated into z-direction because of the LOS effect, $x_{1,2}$ are the axial coordinate of the left and right edges of the image, and Q is the "top half" integrated heat release. In short, Q is the sum of the intensity of the top half image. $p_{r\theta}$ is the reconstructed pressure distribution (reconstruction method is introduced in chapter 5 in the azimuthal and radial space, and P is the top half integrated pressure fluctuation. Q and P are then band-pass filtered at around their peak frequencies in a similar way described in Equation 3.4,

$$\begin{aligned} Q'(t) &= \mathcal{F}^{-1}\Big[\mathcal{F}\{Q(t)\}\cdot \mathrm{H}\Big(f-\Big(f_p-\frac{df}{2}\Big)\Big)\cdot \mathrm{H}\Big(-f+\Big(f_p+\frac{df}{2}\Big)\Big)\Big] \\ P'(t) &= \mathcal{F}^{-1}\Big[\mathcal{F}\{P(t)\}\cdot \mathrm{H}\Big(f-\Big(f_p-\frac{df}{2}\Big)\Big)\cdot \mathrm{H}\Big(-f+\Big(f_p+\frac{df}{2}\Big)\Big)\Big] \end{aligned} \tag{3.7}$$

Lastly, the filtered signals are transformed into analytic signals by taking the Hilbert transform.

$$\begin{aligned} \hat{Q}(t) &= Q'(t)+\mathcal{H}[Q'(t)] \\ \hat{P}(t) &= P'(t)+\mathcal{H}[P'(t)] \end{aligned} \tag{3.8}$$

The procedures is described in Figure 3.4. To compare the magnitude and phase between heat release and acoustic pressure, the pressure data is downsampled from 20 kHz to 12.5 kHz.

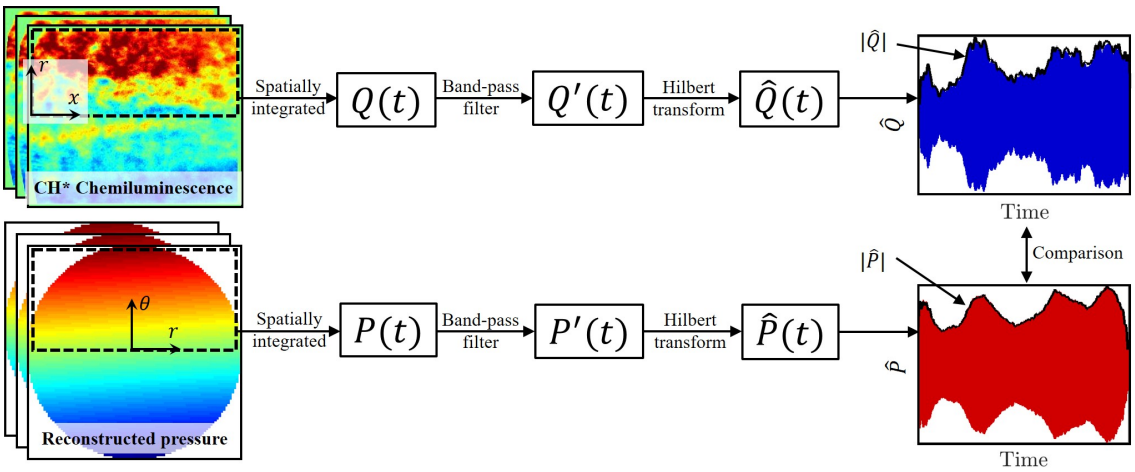

Figure 3.4: Post-processing procedure of the CH* image and reconstructed pressure time series.

CHAPTER 4
OPTIMAL SENSOR PLACEMENT

4.1 Introduction

Because there are many potential modes that can occur inside the combustor, it is not straightforward to determine which particular acoustic mode is being excited, particularly at higher frequencies where many different modes are present close to each other. For example, the first azimuthal (1A) mode of a duct may be very similar in frequency to the fifth longitudinal (5L) mode. Mitigation measures differ depending upon the spatial characteristics of the excited acoustic mode. Similar considerations apply to the fatigue loading of hardware and modeling the relationship between instability amplitude and hardware life. Finally, even the issue of determining maximum pressure oscillation amplitudes is non-trivial, as the same pressure magnitude measurement at a given spatial location, could correspond to major differences in maximum amplitudes, depending upon the sensor location relative to nodes and anti-nodes.

For practical systems, however, one cannot monitor the pressure everywhere inside the chamber as the pressure transducers are placed at discrete locations. To estimate the maximum pressure magnitude, the measured pressure signals from multiple locations must be interpolated/extrapolated, which requires the mode shape information [106]. Identifying mode shape is important in that it provides the optimal placement for acoustic dampers [106, 107, 108]. To identify the acoustic mode shape, analytical, computational, and experimental approaches have been developed. For example, Lee and Santavicca [109] suggested using at least three pressure transducers along the length of the combustor to identify a longitudinal mode, and explained that modes can be identified by estimating a frequency based on combustor geometry. Hale et al. [110] developed a screech wave analysis methodology

to differentiate between transverse, longitudinal, and complex modes. Krebs et al. [75], Singla et al. [111], and Bourgouin et al. [83] combined experimental measurements with numerical results to confirm the observed acoustic modes. However, these studies did not address the issue of optimal sensor placement for modal identification.

This optimal placement question has been studied in vibration monitoring [112, 113, 114, 115, 116]. For example, Kammer [114] proposed a method called Effective Independence (EI), which has been used for many applications [117, 118, 119]. Based on the candidate target modes preselected from the FEM, EI method finds a given number of sensor locations that maximize the determinant of the Fisher information matrix, which is defined as the product of the mode shape matrix and its transpose. Another approach utilizes energy matrix rank optimization [120]. This method basically finds the sensor configuration such that it maximizes the strain energy of the structure. A similar method can be done based on the kinetic energy rather than strain energy [121].

We are aware of one study that considered this question for the acoustic problem. Schuermans [122] calculated variance of the least squares method for pressure estimates derived from discrete sensor locations, and suggested that the error is minimized when the distances between the sensors are equally spaced with $\Delta x = c/n\omega$ where $c, n,$ and ω are speed of sound, the number of sensors, and angular frequency. However, it turns out that although the uniformly spaced sensors provide good results for one frequency, it may yield infinite error at different frequencies.

This chapter proposes a methodology to determine the optimal sensor locations in the azimuthal direction. It follows Schuermans' work [122], who quantified how sensor location influences propagation of noise and uncertainty in modal identification, but the paper extends it by determining optimal sensor locations using similar to the Fisher information matrix, introduced by Kammer [114]. As noted earlier, EI method starts from a large set of candidate sensor locations obtained from FEM, and iteratively removes them based on the Fisher information matrix, leaving the optimal sensor locations. However, explicit expres-

sion of this Fisher information matrix can be obtained for azimuthal modes, enabling us to analytically determine the optimal sensor locations. In addition, the method is applied to the case where multiple modes are simultaneously considered.

4.2 Theoretical Formulation

4.2.1 Modelling of azimuthal acoustic mode

As shown in chapter 2, the acoustic mode shape in a cylindrical coordinate is given by Equation 2.21.

$$\hat{p}(r,\theta,z,t) = \underbrace{\left(A_1 e^{ik_z z} + A_2 e^{-ik_z z}\right)}_{\text{Axial}} \underbrace{\left(f e^{im\theta} + g e^{-im\theta}\right)}_{\text{Azimuthal}} \underbrace{\left(B_1 J_m(rk_r + B_2 Y_m(rk_r)\right)}_{\text{Radial}} e^{-i\omega t} \tag{4.1}$$

To estimate azimuthal modes, multiple pressure sensors must be installed at the same axial and radial, but different azimuthal locations. Then, the difference in pressure signal between the sensors is attributed to only the azimuthal component, i.e., the axial and radial components are the same across the sensors. Thus, we can omit the axial and radial components.

$$\hat{p}(\theta,t) = f(\tau)e^{i(m\theta-\omega t)} + g(\tau)e^{-i(m\theta+\omega t)} \tag{4.2}$$

Here, $f(\tau)$ and $g(\tau)$ are slowly time varying amplitudes of CCW and CW azimuthal waves, respectively (also called as Riemann invariants), m is azimuthal mode number, which must be integer because of the azimuthal periodicity, ω is the angular frequency, and τ is a "slow" time scale, i.e., $\tau = \epsilon t$ where $\epsilon \ll 1$. $\hat{p}(\theta,t)$ is the analytic function representation for pressure obtained using the Hilbert transform of the time series signal. See. Equation 3.5. We will work through this analysis for the case where the pressure sensors are mounted at the same axial and radial locations, but this approach can be readily generalized to different

axial locations. Notice that Equation 4.2 assumes a single azimuthal mode, but in real applications, multiple azimuthal modes could appear simultaneously. In this case, one can bandpass filter the signal around each peak in the spectrum.

Equation 4.2 is the pressure expression for one sensor at θ. Given multiple signals from each sensor, $\hat{p}(\theta, t)$ in Equation 4.2 can be rewritten as:

$$P = MX \;\text{ where }\; P = \begin{bmatrix} \hat{p}(\theta_1, t) \\ \hat{p}(\theta_2, t) \\ \vdots \\ \hat{p}(\theta_n, t) \end{bmatrix},\; M = \begin{bmatrix} e^{im\theta_1} & e^{-im\theta_1} \\ e^{im\theta_2} & e^{-im\theta_2} \\ \vdots & \vdots \\ e^{im\theta_n} & e^{-im\theta_n} \end{bmatrix},\; X = \begin{bmatrix} f(\tau)e^{-i\omega t} \\ g(\tau)e^{-i\omega t} \end{bmatrix}. \quad (4.3)$$

Here, n is the number of sensors, θ_j is the sensor j^{th} location, P is analytic pressure matrix from each sensor, M is a spatial matrix, and X is time dependent matrix that needs to be evaluated. Our goal is to estimate the matrix X, as it provides the information of the mode shape or the pressure distribution along the circumference. To illustrate this point, we can further decompose $f(\tau)$ and $g(\tau)$ (or Riemann invariants) into their magnitudes and phases, i.e., $f(\tau) = F(\tau)e^{i\varphi_F(\tau)}, g(\tau) = G(\tau)e^{i\varphi_G(\tau)}$,

$$\hat{p}(\theta, t) = F(\tau)e^{i(m\theta + \varphi_F(\tau) - \omega t)} + G(\tau)e^{-i(m\theta - \varphi_G(\tau) + \omega t)} \quad (4.4)$$

The magnitude of pressure along the circumference can be obtained by taking an absolute value of Equation 4.4.

$$\begin{gathered} |\hat{p}(\theta, \tau)| = \left[F(\tau)^2 + G(\tau)^2 + 2F(\tau)G(\tau)\cos(2m\theta + \varphi_{FG}(\tau))\right]^{1/2} \\ \text{where }\; \varphi_{FG}(\tau) = \varphi_F(\tau) - \varphi_G(\tau). \end{gathered} \quad (4.5)$$

Notice that the pressure magnitude at θ depends only on $F(\tau),\; G(\tau)$ and $\varphi_{FG}(\tau)$, which are all included in the matrix, X. These three are the parameters that determine the mode

shape, e.g., if $F(\tau) = G(\tau)$, it is a purely standing wave where the pressure magnitude depends on θ. If either of $F(\tau)$ or $G(\tau)$ is zero, it is a purely spinning wave where the pressure magnitude is constant along the circumference. Otherwise, it is a combination of standing and spinning waves, i.e., a mixed wave. $\varphi_{FG}(\tau)$ determines the location of the pressure (anti) node, i.e., the location where the pressure magnitude is (maximum) minimum. The pressure anti-node is located at

$$\theta_a(\tau) = \frac{2k\pi - \varphi_{FG}(\tau)}{2m} \quad \text{where} \;\; k = 0, 1, 2, \ldots, \tag{4.6}$$

and its magnitude is given by

$$|\hat{p}\big(\theta_a(\tau), \tau\big)| = F(\tau) + G(\tau) \tag{4.7}$$

4.2.2 Variance of Riemann invariants

In real turbulence systems, certain levels of background noise are inevitable. Assuming additive noise with zero mean and variance of σ_n^2, Equation 4.3 can be rewritten as:

$$P = MX + \epsilon \;\; \text{where} \;\; \epsilon \sim N(0, \sigma_n^2 I) \tag{4.8}$$

where I is a complex identity matrix and P is now a random variable. We also assume that the noises are uncorrelated and have the same variance between the sensors, i.e., the pressure estimates from two sensors at the same location have uncorrelated noise contributions from the measurement system. Then, the expectation and variance of P are given by

$$\begin{aligned} E(P) &= E(MX) + E(\epsilon) = E(MX) = MX \\ \mathrm{Var}(P) &= \mathrm{Var}(MX) + \mathrm{Var}(\epsilon) = \mathrm{Var}(\epsilon) = \sigma_n^2 I. \end{aligned} \tag{4.9}$$

Therefore, the random variable P follows $P \sim N(MX, \sigma_n^2 I)$. The time dependent matrix,

X, can then be estimated by using a least squares method [83],

$$\hat{X} = (M^*M)^{-1}M^*P, \tag{4.10}$$

where $\hat{X}$ is the estimate of X and M^* is a complex transpose of M. The expectation and variance of $\hat{X}$ are given by

$$\begin{aligned}
E(\hat{X}) &= E((M^*M)^{-1}M^*P) = E((M^*M)^{-1}M^*MX) + E((M^*M)^{-1}M^*\epsilon) \\
&= E(X) + (M^*M)^{-1}M^*E(\epsilon) = X \\
\mathrm{Var}(\hat{X}) &= \mathrm{Var}((M^*M)^{-1}M^*P) = \mathrm{Var}((M^*M)^{-1}M^*MX) + \mathrm{Var}((M^*M)^{-1}M^*\epsilon) \\
&= \mathrm{Var}(X) + (M^*M)^{-1}M^*\mathrm{Var}(\epsilon)((M^*M)^{-1}M^*)^* \\
&= (M^*M)^{-1}M^*M((M^*M)^*)^{-1}\sigma_n^2 \\
&= ((M^*M)^*)^{-1}\sigma_n^2 = (M^*M)^{-1}\sigma_n^2.
\end{aligned} \tag{4.11}$$

Notice that M^*M in Equation 4.11 corresponds to the Fisher information matrix, introduced by Kammer [114]. Substituting the matrix M in the variance of $\hat{X}$ yields

$$\begin{aligned}
\mathrm{Var}(\hat{X}) &= \frac{\sigma_n^2}{n^2 - D}\begin{bmatrix} n & -\sum_{j=1}^{n} e^{2im\theta_j} \\ \sum_{j=1}^{n} e^{-2im\theta_j} & n \end{bmatrix} \\
\text{where } D(\theta_1, \ldots, \theta_n; n, m) &= \sum_{j=1}^{n} e^{2im\theta_j}\sum_{k=1}^{n} e^{-2im\theta_k} = \sum_{j=1}^{n}\sum_{k=1}^{n}\cos\phi_{jk}, \\
\phi_j &= 2m\theta_j,\ \phi_{jk} = \phi_j - \phi_k.
\end{aligned} \tag{4.12}$$

The diagonal elements of this matrix are the variance of Riemann invariants, $f(\tau)$ and $g(\tau)$, given by σ_f^2 and σ_g^2.

$$\sigma_f^2 = \sigma_g^2 = \frac{n}{n^2 - D}\sigma_n^2 \rightarrow \frac{\sigma_f^2}{\sigma_n^2} = \frac{\sigma_g^2}{\sigma_n^2} = \frac{n}{n^2 - D} \equiv h(D) \tag{4.13}$$

Equation 4.13 explicitly shows that the variance associated with the local sensors, σ_n^2, propagates to the variance of Riemann invariants, factored by $h(D)$.

4.2.3 Optimizing sensor locations

As our goal is to minimize the variance of Riemann invariants, the optimization problem can be posed by finding sensor locations that minimize $h(D)$. The nature of this minimization problem depends on the values spanned by D. First, $D \leq n^2$ as shown below.

$$D = \sum_{j=1}^{n} \sum_{k=1}^{n} \cos \phi_{jk} \leq \sum_{j=1}^{n} \sum_{k=1}^{n} 1 = n^2 \tag{4.14}$$

Moreover, since $h(D)$ monotonically increases with $D \leq n^2$, the minimum $h(D)$ occurs at the minimum D. Therefore, given the number of sensors, n, and the azimuthal mode number, m, our goal is to find the optimal sensor locations, $\theta_1, \ldots, \theta_n$, that minimize D. In order to find the minimum, we first need to find D at a critical point:

$$\frac{\partial D}{\partial \phi_p} = \sum_{j=1}^{n} \sin \phi_{jp} = 0 \quad \text{for} \quad p = 1, \ldots, n \tag{4.15}$$

Without loss of generality, we can fix $\phi_1 = 2m\theta_1 = 0$. For $p = 1$, Equation 4.15 becomes

$$\sum_{j=1}^{n} \sin \phi_{j1} = \sin(\phi_1 - \phi_1) + \cdots + \sin(\phi_n - \phi_1) = 0 \rightarrow \sum_{j=1}^{n} \sin \phi_j = 0 \tag{4.16}$$

Next, consider Equation 4.15 for a general case.

$$\sum_{j=1}^{n} \sin \phi_{jp} = \sin(\phi_1 - \phi_p) + \cdots + \sin(\phi_n - \phi_p) = 0 \tag{4.17}$$

Using trigonometric identities,

$$\begin{aligned}(\sin\phi_1\cos\phi_p - \cos\phi_1\sin\phi_p) + \cdots + (\sin\phi_n\cos\phi_p - \cos\phi_n\sin\phi_p) = 0 \\ \rightarrow \cos\phi_p(\sin\phi_1 + \cdots + \sin\phi_n) - \sin\phi_p(\cos\phi_1 + \cdots + \cos\phi_n) = 0\end{aligned} \tag{4.18}$$

Since the bracket in the first term is zero by Equation 4.16, the second term must be zero.

$$\sin\phi_p(\cos\phi_1 + \cdots + \cos\phi_n) = 0 \;\text{ for }\; p = 2, \ldots, n \tag{4.19}$$

There are two possible solution families, given below, that satisfy Equation 4.19.

$$\text{(i)}\;\; \sum_{j=1}^{n}\cos\phi_j = 0, \quad \text{or} \quad \text{(ii)}\;\; \sin\phi_j = 0 \;\text{ for }\; j = 2, \ldots, n \tag{4.20}$$

Next, consider $\sum_{j=1}^{n}\cos\phi_{jk}$.

$$\begin{aligned}\sum_{j=1}^{n}\cos\phi_{jk} &= \cos(\phi_j - \phi_k) + \cdots + \cos(\phi_n - \phi_k) \\ &= (\cos\phi_1\cos\phi_k + \sin\phi_1\sin\phi_k) + \cdots + (\cos\phi_n\cos\phi_k + \sin\phi_n\sin\phi_k) \\ &= \cos\phi_k(\cos\phi_1 + \cdots + \cos\phi_n) + \sin\phi_k \underbrace{(\sin\phi_1 + \cdots + \sin\phi_n)}_{=0} \\ &= \cos\phi_k \sum_{j=1}^{n}\cos\phi_j\end{aligned} \tag{4.21}$$

If (i) in Equation 4.20 is the solution, then Equation 4.21 yields

$$\sum_{j=1}^{n}\cos\phi_{jk} = 0. \tag{4.22}$$

This leads to the following at the critical point.

$$D = \sum_{j=1}^{n} \sum_{k=1}^{n} \cos \phi_{jk} = 0 \tag{4.23}$$

If (ii) in Equation 4.20 is the solution, then,

$$D = \sum_{j=1}^{n} \sum_{k=1}^{n} \cos \phi_{jk} = \sum_{k=1}^{n} \cos \phi_k \sum_{j=1}^{n} \cos \phi_j = \left(\sum_{j=1}^{n} \cos \phi_j \right)^2 > 0 \tag{4.24}$$

Therefore, D at the critical point can take either zero (Equation 4.23) or positive (Equation 4.24) values. Now, consider $D = 0$ at a critical point. This point may be a local minimum, local maximum, or a saddle point. If the point is either a local maximum or a saddle point, then there must exist $D < 0$ at the critical point since D is differentiable and periodic. This contradicts Equation 4.23 and Equation 4.24. Thus, $D = 0$ at the critical point must be a local minimum as well as a global minimum.

$$\min D = 0 \tag{4.25}$$

At the minimum D, the following must hold by Equation 4.15 and Equation 4.22.

$$\sum_{j=1}^{n} \sin \phi_{jk} = \sum_{j=1}^{n} \cos \phi_{jk} = 0 \ \text{ for } \ k = 1, \ldots, n. \tag{4.26}$$

Therefore, the optimal sensor locations are such that they satisfy Equation 4.26. Substituting Equation 4.25 into Equation 4.13 yields:

$$h(\min D) = \frac{1}{n} \tag{4.27}$$

Equation 4.27 states that the variance ratio of the Riemann invariants is inversely proportional to the number of sensors when they are optimally located.

Consider next the case of multiple modes being simultaneously present. In general, the optimal location for one mode, m_i, may be different than another one, m_j. As such, an approach is needed to weight the optimum location across the modes of interest. There are a number of different ways to do this and there is no "best" method for this weighting. For example, it may be that one mode is more damaging than another, and so will want to be better identified. We present results later using a "mini-max" strategy, which optimizes the worst case; i.e., sensor locations where the maximum value of D over all m_j is minimized.

$$\{\theta_1, \ldots, \theta_n\} = \underset{\theta}{\operatorname{argmin}} \left[\max_{m_j} D(\theta_1, \ldots, \theta_n; n, m_j), j = 1, \ldots, N \right] \tag{4.28}$$

Another method, referred to as "mini-sum" strategy hereafter, is to find sensor locations that minimize the sum of D over all m_j.

$$\{\theta_1, \ldots, \theta_n\} = \underset{\theta}{\operatorname{argmin}} \left[\sum_{j=1}^{N} D(\theta_1, \ldots, \theta_n; n, m_j) \right] \tag{4.29}$$

In either case, the optimal locations for multiple modes cannot be obtained analytically and must be identified computationally for a given number of sensors, n, and azimuthal modes, m_j.

4.2.4 Optimal locations for a single mode: Exact solutions and physical interpretation

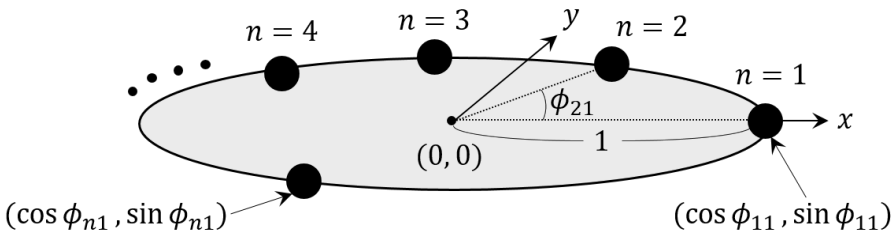

Figure 4.1: n point masses on a round table for k=1

Equation 4.26 consists of n nonlinear simultaneous equations, which actually has an exact solution. Moreover, we can determine a very helpful physical interpretation of this

solution for a single mode, which can also be used to intuit the optimum distributions for a small number of sensors [123]. Suppose the number of n points with mass, M, are distributed around the circumference of a round table in such a way that the moment at the center is zero (Figure 4.1). Then, the following must hold.

$$\begin{aligned}(\bar{x},\bar{y}) &= \left(\frac{1}{nM}\sum_{j=1}^{n} M\cos\phi_{jk}, \frac{1}{nM}\sum_{j=1}^{n} M\sin\phi_{jk}\right) \\ &= \left(\frac{1}{n}\sum_{j=1}^{n}\cos\phi_{jk}, \frac{1}{n}\sum_{j=1}^{n}\sin\phi_{jk}\right) = (0,0) \;\text{ for }\; k=1,\ldots,n \\ &\rightarrow \sum_{j=1}^{n}\sin\phi_{jk} = \sum_{j=1}^{n}\cos\phi_{jk} = 0 \;\text{ for }\; k=1,\ldots,n\end{aligned} \tag{4.30}$$

The last expression in Equation 4.30 is identical to Equation 4.26. Therefore, configuration for minimizing D can be easily found by balancing n point masses on the round table. The actual sensor location is then $\theta_j = \phi_j/2m$.

4.2.5 Variance of estimated pressure

Given the estimated matrix, $\hat{X}$, the estimated complex pressure, $\hat{P}$, at each sensor location can be evaluated as the following.

$$\hat{P} = M\hat{X} \tag{4.31}$$

The mean and the variance of $\hat{P}$ is then given by

$$\begin{aligned}E(\hat{P}) &= E(M\hat{X}) = ME(\hat{X}) = MX = P \\ \mathrm{Var}(\hat{P}) &= \mathrm{Var}(M\hat{X}) = M\mathrm{Var}(\hat{X})M^{*} = M(M^{*}M)^{-1}M^{*}\sigma_n^2 \equiv \sigma_{\hat{p}}^2\end{aligned} \tag{4.32}$$

Substituting the matrix, M, into the variance $\hat{P}$ yields:

$$\sigma_{\hat{p}}^2 = \frac{2\sigma_n^2}{n^2 - D} \begin{bmatrix} n - \sum_{j=1}^{n} \cos\phi_{1j} & \cdots & \ddots \\ \vdots & \ddots & \vdots \\ \ddots & \cdots & n - \sum_{j=1}^{n} \cos\phi_{nj} \end{bmatrix} \tag{4.33}$$

The diagonal elements are the variance of estimated complex pressure for each sensor. The variance ratio between the measured and the estimated pressure for sensor, k, is then given by:

$$\frac{\sigma_{\hat{p},k}^2}{\sigma_n^2} = \frac{2}{n^2 - D}\left[n - \sum_{j=1}^{n} \cos\phi_{kj}\right] \quad \text{for} \quad k = 1, \ldots, n \tag{4.34}$$

For optimal sensor placement, $D = 0$ and $\sum_{j=1}^{n} \cos\phi_{kj} = 0$ from Equation 4.25 and Equation 4.26, and thus,

$$\frac{\sigma_{\hat{p},k}^2}{\sigma_n^2} = \frac{2}{n}. \tag{4.35}$$

Notice that the estimated variance ratio does not depend on sensor location, i.e., it is constant at $2/n$ across the sensors.

4.3 Results

This section illustrates several results to help understand the methodology for determining the optimal sensor locations. In the first example, the optimal sensor locations are calculated when optimizing for a single azimuthal mode. The second example illustrates the "mini-max" and "mini-sum" approaches by looking at the same problem but with considering multiple azimuthal modes. The last example illustrates the effect of optimal sensor placement compared to the non-optimal case.

4.3.1 Optimal sensor locations for a single azimuthal mode

Two sensors ($n = 2$)

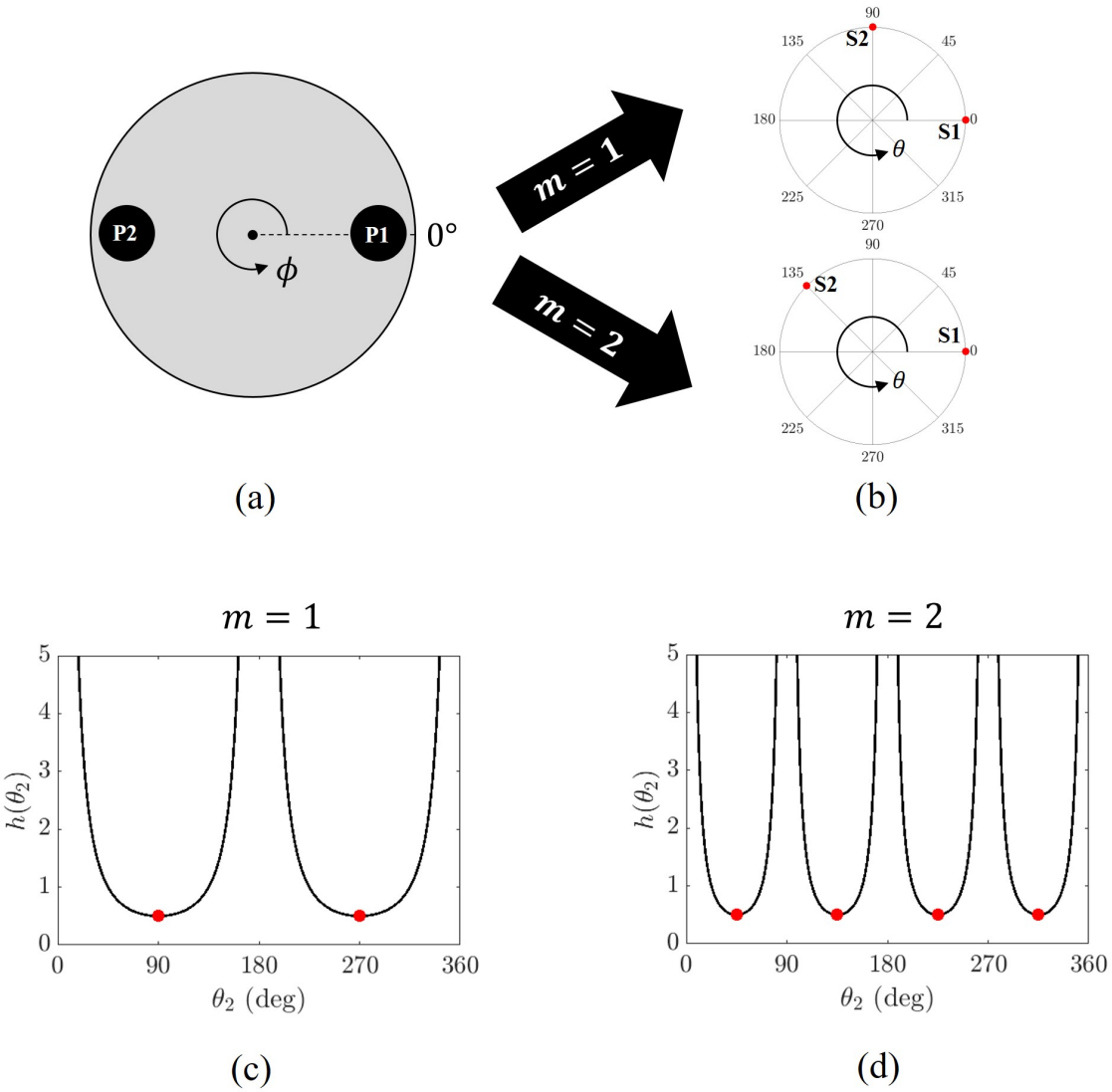

Figure 4.2: (a) Two point masses and a round table. (b) Optimal sensor locations, top: $m = 1, k = 0$ and bottom: $m = 2, k = 1$. $h(\theta_2)$ as a function of S2 location for (c) $m = 1$ and (d) $m = 2$. S1 is located at 0°. The red dots indicate the minimum $h(\theta_2)$.

The first example considers the case where we would like to optimize the location of two sensors (S1 and S2). Recalling the round table approach, two point masses must be located 180° apart to balance the table. Without loss of generality, we can fix the first point

mass (or sensor) at 0. Then, the second point mass must be located at 180°.

$$\begin{aligned} \text{Point } 1 : \phi_1 = 0 \rightarrow \theta_1 = \tfrac{\phi_1}{2m} = 0 \\ \text{Point } 2 : \phi_2 = \pi + 2k\pi \rightarrow \theta_2 = \tfrac{\phi_2}{2m} = \left(\tfrac{1}{2} + k\right)\tfrac{\pi}{m} \end{aligned} \quad \text{where } \; k \in \mathbb{Z} \tag{4.36}$$

For the first azimuthal mode $(m = 1)$, Equation 4.36 indicates optimal sensor locations at (0°, 90° or (0°, 270°). Similarly, the optimum sensor locations for the second azimuthal mode $(m = 2)$ would be (0°, 45°), (0°, 135°), (0°, 225°), and (0°, 315°). Figure 4.2 (a) describes the round table with two point masses and Figure 4.2 (b) shows one of the optimal sensor configurations for $m = 1$ and 2. To visualize the effect of the optimal locations on the uncertainty propagation, a variance ratio of Riemann invariants to noise, $h(\theta_2)$, was numerically calculated as a function of S2, as shown in Figure 4.2 (c) . The figure shows that for $m = 1$ case, $h(\theta_2)$ is minimized to $1/n = 0.5$ when S2 is at 90° or 270°, which is consistent with Equation 4.36 and Equation 4.27. In this case, the variance ratio of estimated to measured pressure is $\sigma^2_{\hat{p}}/\sigma^2_n = 2/n = 1$ for any sensor, i.e., there is no reduction of the estimated complex pressure from the measured pressure. This is because the degree of freedom of a least squares fit is $n-2$, which yields zero in this case. Similarly, for $m = 2$ case, $h(\theta_2)$ is minimized to $1/n = 0.5$ when S2 is at 45°, 135°, 225° or 315°. The plot also quantifies the effect of the sensor not being located optimally.

Three sensors ($n = 3$)

Consider a case where we want to detect one azimuthal mode with three sensors. Three point masses must be uniformly distributed to balance the round table. The optimal placement is then given by:

$$\begin{aligned} \text{Point } 1 : \phi_1 = 0 \rightarrow \theta_1 = \tfrac{\phi_1}{2m} = 0 \\ \text{Point } 2 : \phi_2 = \tfrac{2\pi}{3} + 2k_1\pi \rightarrow \theta_2 = \tfrac{\phi_2}{2m} = \left(\tfrac{1}{3} + k_1\right)\tfrac{\pi}{m} \\ \text{Point } 3 : \phi_3 = \tfrac{4\pi}{3} + 2k_2\pi \rightarrow \theta_3 = \tfrac{\phi_3}{2m} = \left(\tfrac{2}{3} + k_2\right)\tfrac{\pi}{m} \end{aligned} \quad \text{where } \; k_1, k_2 \in \mathbb{Z} \tag{4.37}$$

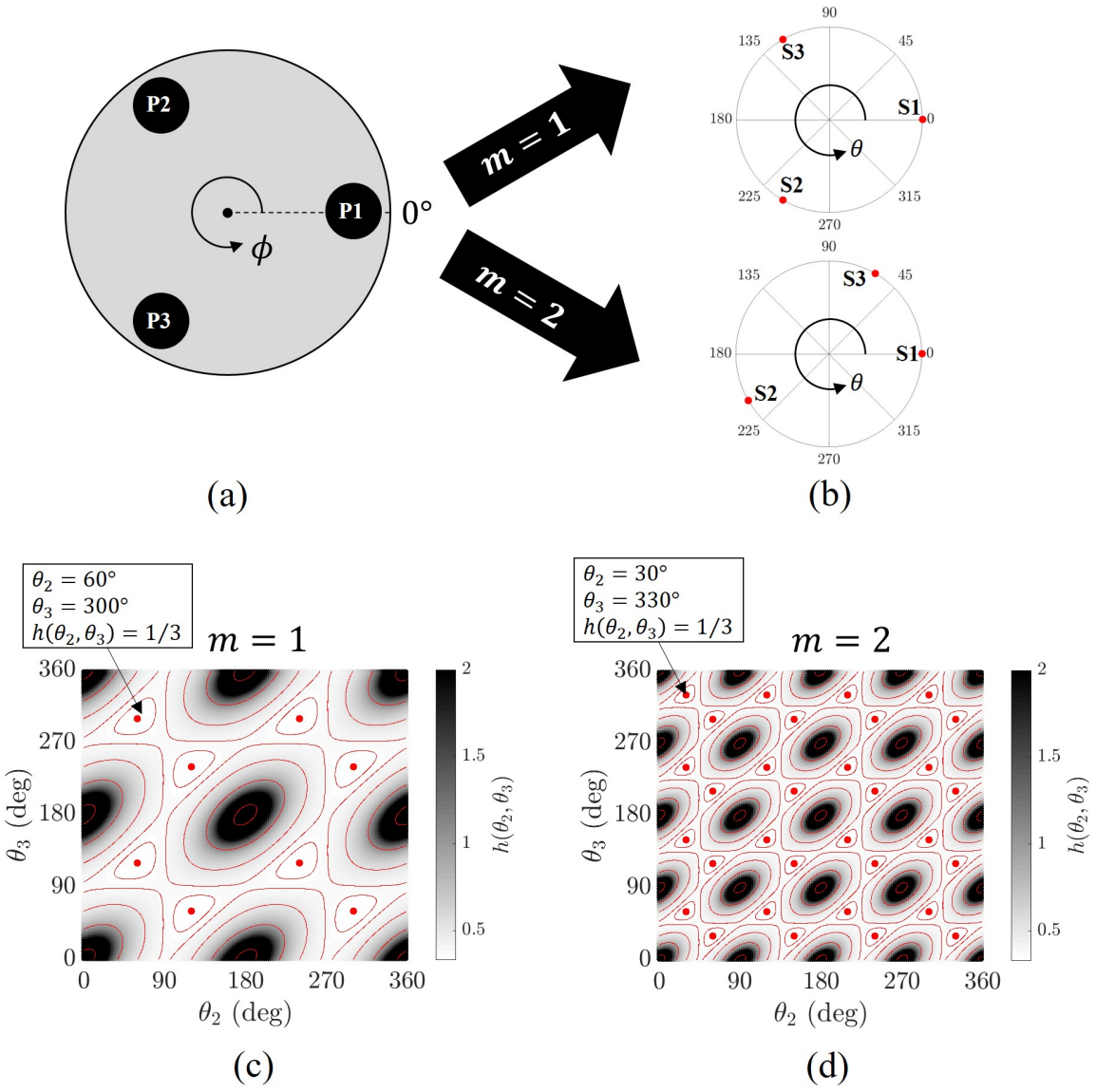

Figure 4.3: (a) Three point masses and a round table. (b) Optimal sensor locations, top: $m = 1, k_1 = 1, k_2 = 0$ and bottom: $m = 2, k_1 = 2, k_2 = 0$. $h(\theta_2, \theta_3)$ as a function of S2 and S3 locations for (c) $m = 1$ and (d) $m = 2$.

Figure 4.3 (a) shows the round table with uniformly distributed point masses and Figure 4.3 (b) is one of the optimal configurations for $m = 1$ and 2. Figure 4.3 (c) and (d) represent the dependence of $h(\theta_2, \theta_3)$ in S2 and S3 space for each m. Here, the grayscale indicates $h(\theta_2, \theta_3)$, the red lines are contour lines, and red dots denote the locations at which $h(\theta_2, \theta_3)$ is minimized. The figure shows that when the sensors are optimally located, the Riemann invariant ratio, $h(\theta_2, \theta_3)$ becomes $1/n = 1/3$ at the minimum. Additionally, the variance

ratio of estimated to measured pressure is calculated as $\sigma_{\hat{p}}^2/\sigma_n^2 = 2/n = 2/3$ for any sensor. This indicates that three sensors that are optimally located reduce the uncertainty by factor of $2/3$.

Four sensors $(n = 4)$

From the solutions for $n = 2$ and $n = 3$, it is possible to construct solutions for all higher values of $n > 3$. We can illustrate this procedure for $n = 4$, noting that the two sensor solution can be superposed to provide a solution for four sensors; for example, write Equation 4.26 as:

$$\begin{aligned} \sum_{j=1}^{4} \sin\phi_{jk} = \sum_{j=1}^{2} \sin\phi_{jk} + \sum_{j=3}^{4} \sin\phi_{jk} = 0 \ \text{ for } \ k \in 1,2,3,4 \\ \rightarrow \begin{array}{l} \sum_{j=1}^{2} \sin\phi_{jk} = 0 \ \text{ for } \ k \in 1,2 \\ \sum_{j=3}^{4} \sin\phi_{jk} = 0 \ \text{ for } \ k \in 3,4 \end{array} \end{aligned} \tag{4.38}$$

The two bottom equations represent one possible solution, which is a superposition of the $n = 2$ solution. However, a question arises as to whether there are additional solutions; i.e., where the sum from $j = 1$ to 4 is zero, even while the sums from $j = 1$ to 2 and 3 to 4 are nonzero. For $n = 4$ and 5, we did numerically verify that they were the only solutions. Note that the relative orientation of the (S1, S2) and (S3, S4) two sensor pairs is arbitrary, so there is an infinite number of possible configurations. Specifically, the point masses are balanced as long as each pair of them are 180° apart. The optimal placement is then given by:

$$\begin{gathered} \text{Point } 1 : \phi_1 = 0 \rightarrow \theta_1 = \tfrac{\phi_1}{2m} = 0 \\ \text{Point } 2 : \phi_2 = \pi + 2k_1\pi \rightarrow \theta_2 = \tfrac{\phi_2}{2m} = \left(\tfrac{1}{2} + k_1\right)\tfrac{\pi}{m} \\ \text{Point } 3 : \phi_3 = k_2 \rightarrow \theta_3 = \tfrac{\phi_3}{2m} = \tfrac{k_2}{2m} \\ \text{Point } 4 : \phi_4 = k_2 + \pi + 2k_3\pi \rightarrow \theta_4 = \tfrac{\phi_4}{2m} = \left(\tfrac{k_2}{2\pi} + \tfrac{1}{2} + k_3\right)\tfrac{\pi}{m} \\ \text{where } \ k_1, k_3 \in \mathbb{Z}, \ 0 \leq k_2 \leq 2\pi \end{gathered} \tag{4.39}$$

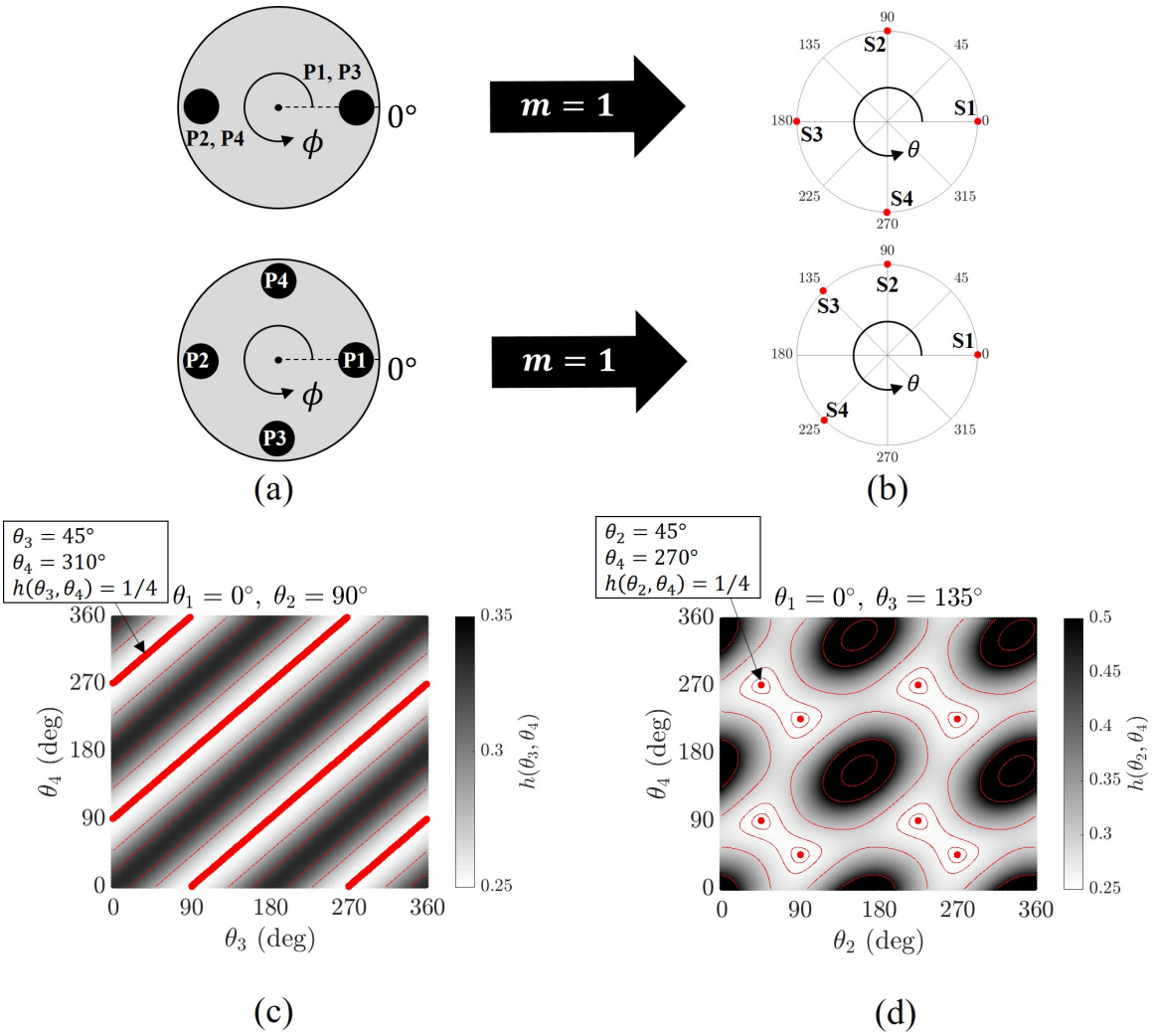

Figure 4.4: (a) Four point masses and a round table. (b) Optimal sensor locations, top: $m = 1, k_1 = k_3 = 0, k_2 = 2\pi$, bottom: $m = 1, k_1 = k_3 = 0, k_2 = 3\pi/2$. $h(\theta_3, \theta_4)$ as a function of two sensors given that the other two are fixed at (c) 0° and 90° or (d) 0° and 135°. The grayscale, red lines, and red dots indicate h, contour of h, and the minimum h, respectively.

For example, the top of Figure 4.4 (a) and (b) is the case where $m = 1, k_1 = k_3 = 0$ and $k_2 = 2\pi$, and the bottom is the case where $m = 1, k_1 = k_3 = 0$ and $k_2 = 3\pi/2$. To visualize the dependence of h with respect to four sensors, we fixed two sensors and plotted h as a function of the other two sensors, as shown in Figure 4.4 (c) and (d). The optimal configurations yields $h = 1/n = 1/4$ and the estimated pressure ratio is $\sigma_{\hat{p}}^2/\sigma_n^2 = 2/n = 1/2$. All solutions have the same variance ratio and, therefore, all provide equivalent

performance. As such, the specific configuration that a user would want to choose would be based upon access to installation.

4.3.2 Optimum sensor locations for multiple azimuthal modes

In this section, we consider how these results evolve when identifying multiple sensors. To illustrate, consider the optimal placement of four sensors (as in the prior section), but for the first three azimuthal modes simultaneously. The mini-max approach requires numerically finding the minimum of $\max_{m_j} D$ for entire combinations of the sensor locations. In other words, D in Equation 4.12 is evaluated for each m_j value and the maximum D at each combination is taken and plotted in Figure 4.5 (a). Here, $\max_{m_j} D$ at each (θ_3, θ_4) combination is denoted as grayscale, and S1 and S2 are fixed at 0° and 90° to visualize $\max_{m_j} D$ in two dimensional space. The combinations at which $\max_{m_j} D$ is minimized are then numerically found and chosen as optimal configurations denoted by red dots. Notice that, unlike Figure 4.4 (c), the number of solutions is discrete due to considering multiple azimuthal modes simultaneously. A total of 2 out of 8 optimal configurations are unique, which are shown in Figure 4.5 (c) and (d). Specifically, the uniformly spaced configuration is no longer optimal because that leads to $h(D)$ being infinity when $m = 2$. In general, when the sensors are equally spaced, there may be an azimuthal mode at which the variance becomes infinitely large. If that azimuthal mode is one of the candidate modes we care about, it is desirable to avoid the equally spaced configuration.

The mini-sum approach finds the optimal locations that minimize the sum of D over each azimuthal mode number, m_j. Figure 4.5 (b) plots the sum of D in (θ_3, θ_4) space, and minimum (optimal) locations are denoted as red dots. Notice that the optimal locations are identical to those in Figure 4.5 (a).

For either configurations in Figure 4.5 (c) and (d), $\max_{m_j} D$ or sum of D is minimized to zero, and thus, the variance ratio, $h(D)$ and $\sigma_{\hat{p}}^2/\sigma_n^2$, are calculated as 0.25 and 0.5, respectively, for all azimuthal mode numbers considered here. Since the variance is not biased by

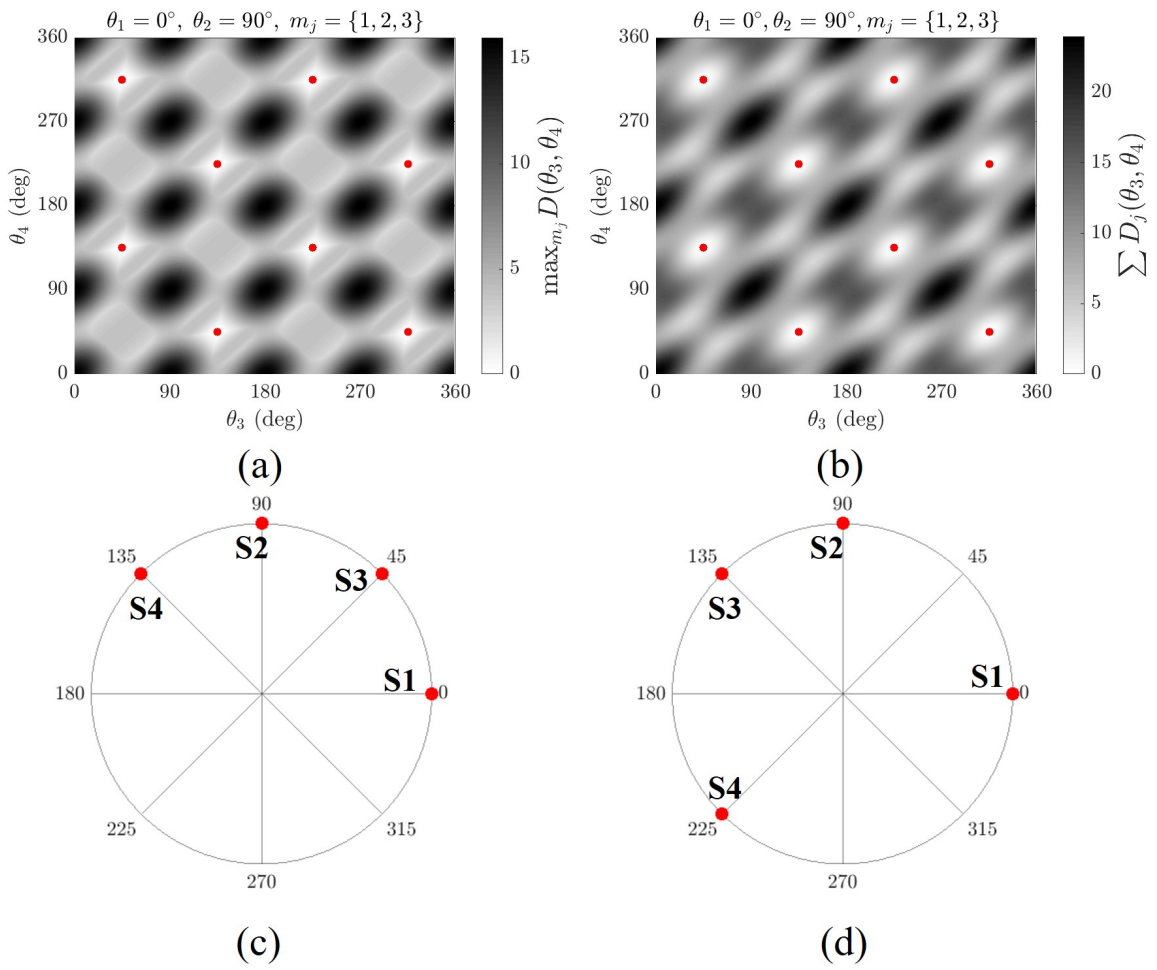

Figure 4.5: (a) $\max_{m_j} D$ as a function S3 and S4 locations. The red dots indicate the minimum value of $\max_{m_j} D$. (b) $\sum D$ as a function S3 and S4 locations. The red dots indicate the minimum value of $\sum D$. (c), (d) Two optimal sensor locations.

the azimuthal mode number, one can determine the actual mode number among the candidates by identifying which one provides the smallest variance between the measured and the estimated complex pressure signal.

The full results for $n = 2 - 4$ sensors are summarized in Appendix A. It presents the optimal sensor locations with a different number of sensors and azimuthal mode numbers for up to three modes. For example, it shows that if $n = 2$, then an optimal location (note that there are other optimum locations as well) of the second sensor to identify the $m = 1, 2$, and 3 modes individually is 90°, 45°, and 30°, respectively, with respect to the first sensor. However, an optimum location to identify all three modes simultaneously is at

37°.

4.3.3 Example results: Pressure reconstruction from optimal sensor placements

This section illustrates these results on synthetic time series data. Table 4.1 shows the parameter setting for the synthetic data with additive Gaussian noise. The sensor location for case 1 is arbitrarily selected as a reference, whereas that for case 2 is determined from the optimal locations, Figure 4.5 (c). Given this parameter set, the pressure anti-node is located at $\theta_a = -60^\circ$ (or 300°) and its magnitude is $|p(\theta_a)| = F + G = 1.8$.

Figure 4.6 (a) shows a detailed and long time series version of the simulated signals from each probe. The dots indicate the true signal without the noise, and the lines are the fitted signals obtained by using a least-squares method. The fitted line and the true signal are in good agreement, indicating that the least-squares method is successfully applied. Figure 4.6 (c) illustrates the same plots for case 2.

Figure 4.6 (b) and (d) represent a PDF of the difference between true and measured signal (blue) and the difference between true and fitted signal (orange) for each sensor. The variance of the noise is set to 0.1 for all cases. Compared to the variance of the measured signal, the variance of the fitted signal is lower for both cases 1 and 2, implying that the least-squares fit reduces the uncertainty. For case 1, the variance of the fitted signal depends on each probe location, e.g., sensors 2 and 4 have the same variance (0.047) whereas sensor 1 has a maximum variance (0.066) and sensor 3 has a minimum variance (0.039). On the other hand, the variances of the fitted signals are similar to each other for case 2, i.e., in this case, they are all 0.05, which is half of the noise variance. This is consistent with the result

Table 4.1: Parameter setting for synthetic data

Case	m	f_{sample} (Hz)	f_{acoustic} (Hz)	F	G	φ_{FG} (deg)	σ_n^2	Sensor location (deg)			
								S1	S2	S3	S4
1	1	20,000	1,600	1.0	0.8	120	0.1	0	60	220	240
2								0	90	135	225

from Equation 4.35, i.e., the variance ratio, $\sigma_{\hat{p}}^2/\sigma_n^2$, for optimal configuration is 0.5 for all sensors.

Figure 4.7 (a) shows the pressure magnitude distribution along the circumference obtained from Equation 4.5. The red solid line indicates the true pressure magnitude and the gray and black lines are for cases 1 and 2, respectively. The solid lines are the mean pressure magnitude, the dashed lines are 95% confidence interval, and the vertical dotted lines are the sensor locations. Strictly speaking, the distribution of the pressure magnitude is not normal (Equation 4.5), especially around the pressure node (Figure 4.7 (c)). Based on the normality test (not shown here), however, one can reasonably assume the normal distribution around the pressure anti-node, as shown in Figure 4.7 (b).

Around the pressure node in Figure 4.7 (a), the mean pressure magnitudes for case 1 are closer to the true value than that for case 2. This is because the sensors for case 1 are more concentrated around the pressure node, e.g., sensors 3 and 4 (gray). In contrast, the mean pressure magnitude for case 2 is more accurate than that for case 1 around the pressure anti-node for the same reason. Specifically, the confidence interval for case 2 is much narrower than that for case 1 around the pressure anti-node. This observation shows that case 2 configuration is better to minimize the overall uncertainty of the magnitude around the pressure anti-node. One may argue that the sensor configuration for case 1 would be more useful when the pressure anti-node is located around the sensors. The problem is that the pressure anti-node can locate anywhere or even rotate in the circular geometry for the azimuthal mode. Therefore, the sensor configuration for case 2 is likely to capture the magnitude of the pressure anti-node more accurately.

4.4 Conclusion

This chapter has introduced a methodology to determine the optimal sensor placements for detecting azimuthal acoustic modes. Given the number of sensors and the modes of interest, the optimal locations are selected in such a way that it minimizes the variance of

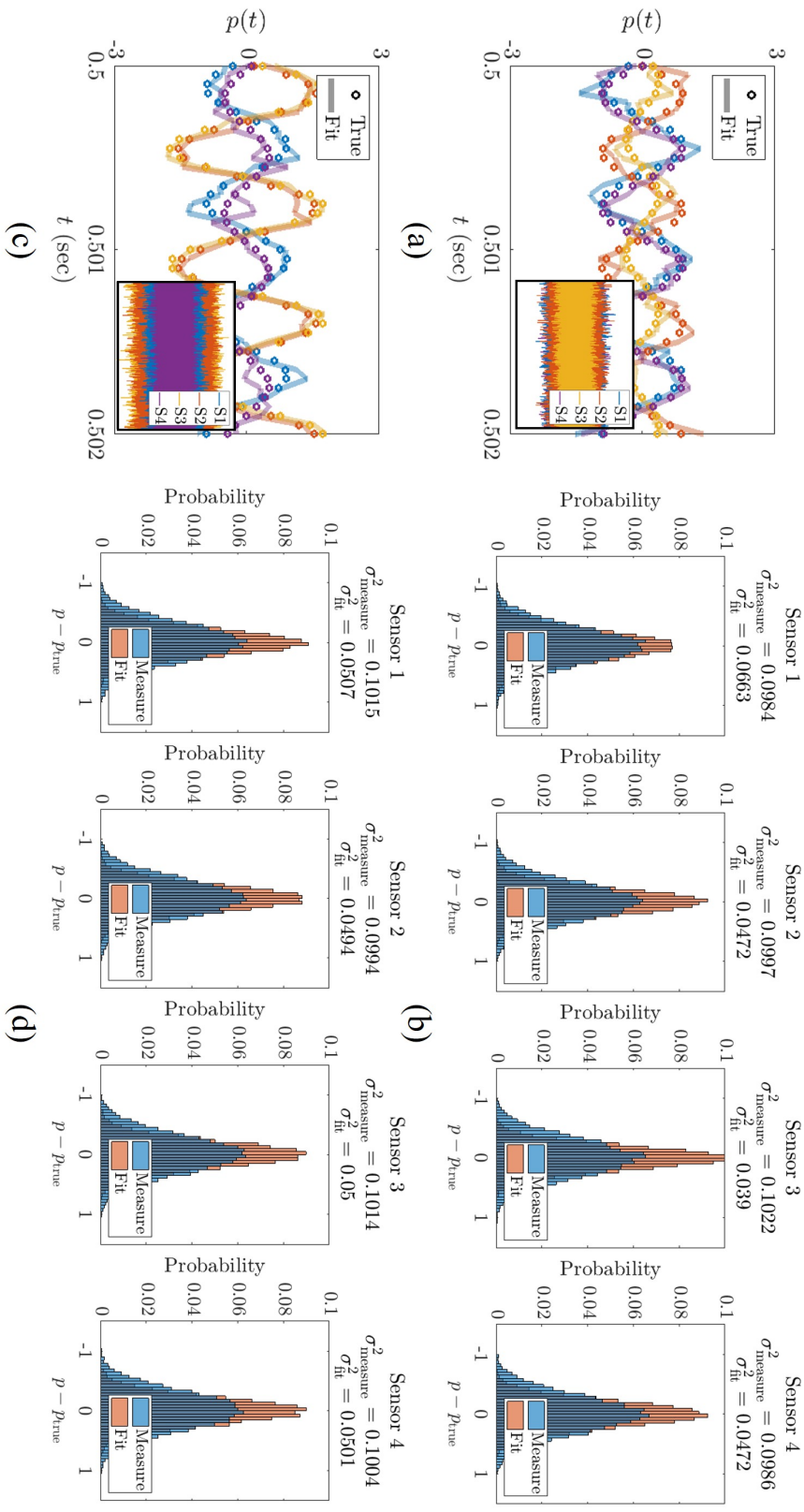

Figure 4.6: (a) Pressure signal in time series for (a) case 1 and (c) 2. Dots: true signals, lines: fitted signals using a least squares method. Subfigures show the zoom out version. PDF of difference between true and measured/fitting signals for (b) case 1 and (d) 2.

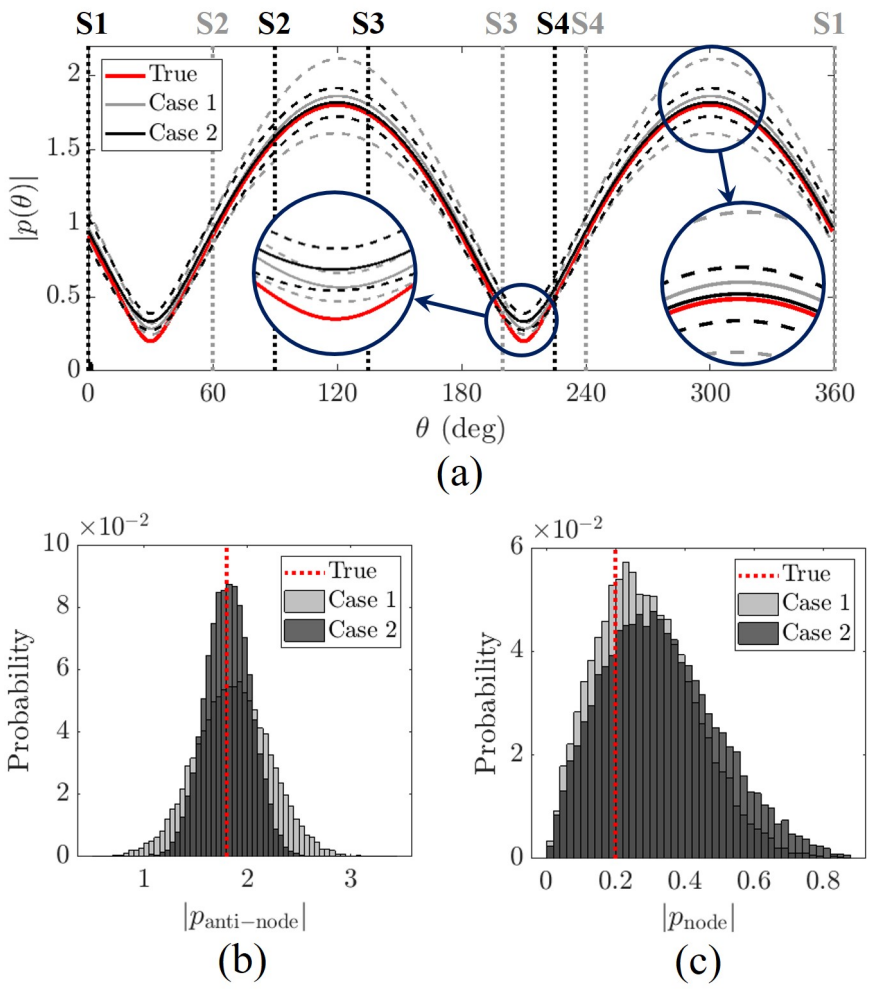

Figure 4.7: (a) Pressure magnitude distribution along the circumference. Red, gray, and black lines represent the true, case 1, and case 2, respectively. The solid lines are mean value, dashed lines are 95% confidence interval, and vertical dotted lines are sensor locations. PDF of pressure magnitude at (b) anti-node and (c) node.

the estimated amplitudes of CW and CCW waves (or Riemann invariants). The explicit expression for such locations requires solving simultaneous nonlinear equations, the physical interpretation of which allows us to obtain the solutions intuitively. For $n \geq 4$, the optimal locations can be obtained from the combination of a lower number of sensors. It is found that the optimal placements decrease the uncertainty of Riemann invariants by $1/n$ and that of estimated pressure by $2/n$. When the number of modes of interest is more than one, mini-max and mini-sum approaches have been used to weight the different modes. Lastly,

the paper has introduced a model problem to illustrate the effectiveness of the optimal sensor locations. It is shown that the optimal placement provides a better estimate of pressure magnitude at the anti-node.

CHAPTER 5
ACOUSTIC MODE SHAPE ANALYSIS

5.1 Introduction

Thermoacoustic instabilities can occur over a wide range of frequencies and different types of combustors. The particular focus of this thesis is on azimuthal modes. Annular combustors are prone to exhibit low frequency azimuthal modes [7, 8]. On the other hand, can combustors exhibit high frequency azimuthal modes referred to as "screech" [12, 13, 14, 11]. This screech tone is particularly problematic in combustion industries because its high frequency and high amplitude pressure oscillations can damage hardware very rapidly by fatigue failure [10, 124].

Several approaches have been developed to suppress high frequency thermoacoustic instabilities. For example, baffles have been used to modify the acoustic resonance properties and thus dampen the instability in a combustion chamber [125]. In addition, the distribution of propellant injection, porous injector faceplate, and injection geometry have been used to reduce the screech amplitudes [126]. Specifically, acoustic dampers, such as Helmholtz or quarter-wave resonators, are commonly used to suppress high frequency or azimuthal instabilities as they require physically smaller dampers [106, 108, 127]. The performance of these acoustic dampers strongly depends on their location relative to the acoustic mode shapes of the azimuthal instabilities [128, 129, 130, 131]. To efficiently mitigate these azimuthal instabilities by using acoustic dampers, it is significantly important to identify which acoustic mode is excited.

Different approaches have been used for identifying acoustic mode shapes. For example, Krebs et al. [75], Singla et al. [111] and Bourgouin et al. [83] combined experimental measurements with numerical results to validate a modal analysis. Hale et al. [110] devel-

oped a screech wave analysis methodology to differentiate between transverse, longitudinal, and complex modes. Poinsot et al. [65, 132], Wolf et al. [69, 72], and Nicoud et al. [133] used a finite element method (FEM) to determine thermoacoustic modes, including unsteady flame effects.

However, most of the approaches previously mentioned have focused on multi-nozzle annular combustors, where the thin gap assumption is applicable, i.e., the length scale of the annular gap is much shorter than that of the combustor's radius. This assumption is not valid for can combustors, where the geometry is not annular, but cylindrical. In addition, can combustors with a large ratio of axial to radial dimension possess multiple transverse and longitudinal modes with natural frequencies that are very close to one another. Because the frequency spacing is very close, it is difficult to distinguish between each mode solely based upon frequency calculations due to the inherent uncertainty in boundary conditions and temperature profiles. The goal of this chapter is to propose a method for reconstructing the mode shape of high frequency instability. Using multiple sensors in axial and azimuthal directions, the method reconstructs the pressure distribution in each direction. The sensor configuration used in this chapter is shown in Figure 3.1.

5.2 Pressure Reconstruction Method

5.2.1 Azimuthal direction

It has been shown from chapter 4 that the time varying complex amplitudes, $f(\tau)$ and $g(\tau)$, can be estimated by a least squares fit described in Equation 4.10. The error of the least squares fit can be quantified by an R squares value, R^2 [111], i.e.

$$\mathrm{R}_{\theta}^2 = 1 - \frac{||P - M \cdot \hat{X}||^2}{||P||^2} \tag{5.1}$$

where $\|P\|$ denotes the Frobenius norm of P. Here, $\mathrm{R}_{\theta}^2 = 1$ indicates zero error between the fitting and the experimental data.

Once the matrix, X, is estimated, a spin ratio (SR), which quantifies the dominant mode between CW and CCW waves, can be defined as [83]:

$$SR = \frac{F - G}{F + G} \tag{5.2}$$

Here, F and G are the magnitudes of CCW/CW waves. See Equation 4.4. Note that SR ranges from -1 to 1. $SR = 0$ indicates a purely standing wave, $SR = \pm 1$ a purely spinning wave in CW $(-)$ or CCW $(+)$ direction. Otherwise, the mode is a combination of standing and spinning waves, i.e., a mixed wave. The presence of noise in these modal amplitudes introduces bias errors in the SR estimate, whose magnitude was estimated from Monte Carlo simulations. The detailed approach is described in Appendix B.

The pressure distribution in the entire azimuthal direction can be reconstructed as follows:

$$\underbrace{\begin{bmatrix} \hat{p}(\theta'_1, t) \\ \hat{p}(\theta'_2, t) \\ \vdots \\ \hat{p}(\theta'_N, t) \end{bmatrix}}_{P'} = \underbrace{\begin{bmatrix} e^{im\theta'_1} & e^{-im\theta'_1} \\ e^{im\theta'_2} & e^{-im\theta'_2} \\ \vdots & \vdots \\ e^{im\theta'_N} & e^{-im\theta'_N} \end{bmatrix}}_{M'} \times \hat{X} \tag{5.3}$$

where θ'_j $(j = 1, 2, .., N)$ is the azimuthal position ranging from 0 to 2π, and N is the number of grid points. Given the complex spatio-temporal pressure matrix, P', one can plot the magnitude and phase distributions along the azimuthal direction at each realization. However, the actual distributions slowly vary in time because of the unsteadiness, which hinders identification of the mode shape. Thus, to minimize the variation of the distributions,

1. The magnitude distribution at each realization is normalized by its spatial average.

2. The phase distribution at each realization is plotted with respect to one of the sensors.

3. Then, the temporal averages of both distributions with the error bar are plotted to

visualize the mode shape.

5.2.2 Axial direction

The pressure distribution in the axial direction can be reconstructed in a similar way. Considering sensors at the same radial and azimuthal, but different axial locations, the radial and azimuthal components in Equation 2.21 do not contribute to the difference in pressure signals between the sensors. Thus, the acoustic wave in the axial direction can be modeled as a combination of Right-Ward (RW) and Left-Ward (LW) waves with time dependent magnitudes and phases, i.e.

$$\hat{p}(z,t) = (A_1 e^{ik_z z} + A_2 e^{-ik_z z}) e^{-i\omega t} \tag{5.4}$$

where the first and second terms on the RHS denote the traveling wave in RW $(+)$ and LW $(-)$ direction, respectively. Given multiple sensor measurements at the same radial and azimuthal, but different axial locations, Equation 5.4 can be rewritten as a matrix form, i.e.

$$\underbrace{\begin{bmatrix} \hat{p}(z_1,t) \\ \hat{p}(z_2,t) \\ \vdots \\ \hat{p}(z_n,t) \end{bmatrix}}_{P_z} = \underbrace{\begin{bmatrix} e^{ik_z z_1} & e^{-ik_z z_1} \\ e^{ik_z z_2} & e^{-ik_z z_2} \\ \vdots & \vdots \\ e^{ik_z z_n} & e^{-ik_z z_n} \end{bmatrix}}_{L} \times \underbrace{\begin{bmatrix} A_1 e^{-i\omega t} \\ A_2 e^{-i\omega t} \end{bmatrix}}_{Z} \tag{5.5}$$

where x_j $(j = 1, 2, .., n)$ denotes the axial location of j^{th} sensor. The matrix, Z, can be estimated by a least squares fit.

$$\hat{Z} = (L^* L)^{-1} L^* P_z \tag{5.6}$$

It should be noted that, unlike the azimuthal mode number, the axial wavenumber is not necessarily an integer. Therefore, it must be evaluated in advance. Otherwise, the matrix, L, is unknown, preventing us from utilizing the least squares fit, Equation 5.6. This chapter

estimates the axial wavenumber that minimizes a least squares error, using a procedure detailed in Appendix C. The error of the least squares fit is given by

$$\mathrm{R}_z^2 = 1 - \frac{||P_z - L \cdot \hat{Z}||^2}{||P_z||^2}. \tag{5.7}$$

Similar to the SR, a travel ratio, TR, can be defined as follows.

$$TR = \frac{|A_1| - |A_2|}{|A_1| + |A_2|} \tag{5.8}$$

Here, $TR = 0$ indicates a purely standing wave, and $TR = \pm 1$ means purely RW (+) and LW (–) traveling waves. Otherwise, it is a combination of standing and traveling waves. The axial pressure distribution can then be reproduced as follows:

$$\underbrace{\begin{bmatrix} \hat{p}(z'_1, t) \\ \hat{p}(z'_2, t) \\ \vdots \\ \hat{p}(z'_N, t) \end{bmatrix}}_{P'_z} = \underbrace{\begin{bmatrix} e^{ik_z z'_1} & e^{-ik_z z'_1} \\ e^{ik_z z'_2} & e^{-ik_z z'_2} \\ \vdots & \vdots \\ e^{ik_z z'_N} & e^{-ik_z z'_N} \end{bmatrix}}_{L'} \times \hat{Z} \tag{5.9}$$

where $x'_j (j = 1, 2, .., N)$ is an axial coordinate. By plotting the pressure in the axial direction, one can visualize the axial mode shape. Notice that this reconstruction method is not applicable across the flame or the contraction area due to the constant temperature assumption.

5.3 Computational Analysis

The FEM solver COMSOL Multiphysics is used to calculate the acoustic mode shapes at the experimental conditions. Figure 5.1 shows a two-dimensional slice of the entire computational domain. The acoustic boundary condition for the inlet is set to rigid because of the choked orifices, and the outlet to pressure release. All other solid surfaces including

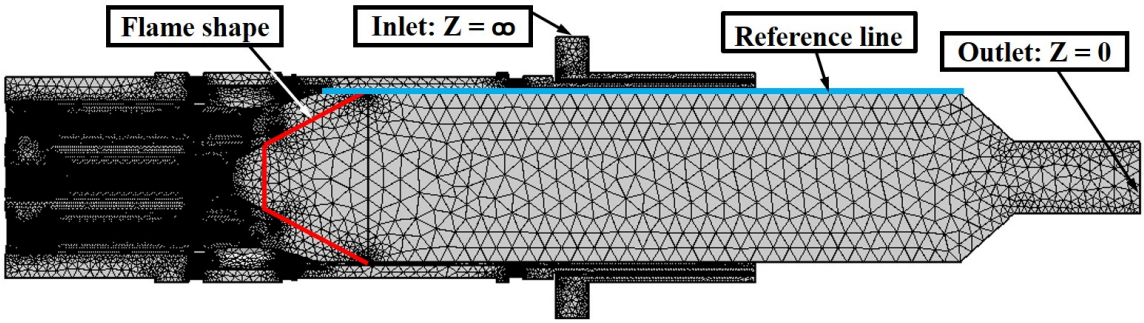

Figure 5.1: Mesh, boundary conditions, and flame shape.

walls are regarded as rigid boundaries with infinite impedance. The flame is regarded as a cone shape, and the temperature of the domains before and after the flame is set to uniform with preheat and combustion temperature, respectively. The detailed description of estimation of combustion temperature is illustrated in Appendix C. The computational domain is meshed with 2,495,747 tetrahedral elements, which gives 3,811,121 degrees of freedom to be resolved. The FEM is then carried out to solve the Helmholtz equation to predict eigenfrequencies and the corresponding mode shapes. Note that the flame transfer function is not considered in the FEM, as it has little impact on the eigenfrequencies and the associated mode shapes. Based upon the frequencies observed from the experiments, this study considers only the first four azimuthal/longitudinal modes, which are shown in Figure 5.2. It was found that the boundary conditions at the outlet have a negligible effect on the eigenfrequencies and the associated mode shapes. This is because the cutoff frequency drops at the area contraction, thus, the wave magnitude exponentially decays in the axial direction, preventing it from interacting with the outlet boundary.

5.4 Results

5.4.1 Frequency spectrum

Figure 5.3 shows the frequency spectrum measured from sensors 1 and 3 for 1 second during the instabilities. The peak frequency of the instability was around 1600 Hz. The rough calculation from the FEM provides that the frequencies of the second azimuthal

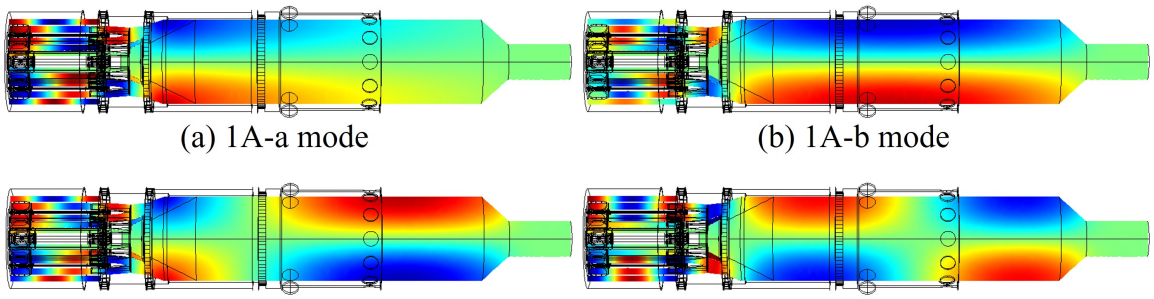

(a) 1A-a mode (b) 1A-b mode

(c) 1A1L-a mode (d) 1A1L-b mode

Figure 5.2: Azimuthal acoustic mode shapes obtained from FEM. 'A' and 'L' stand for azimuthal and longitudinal, respectively.

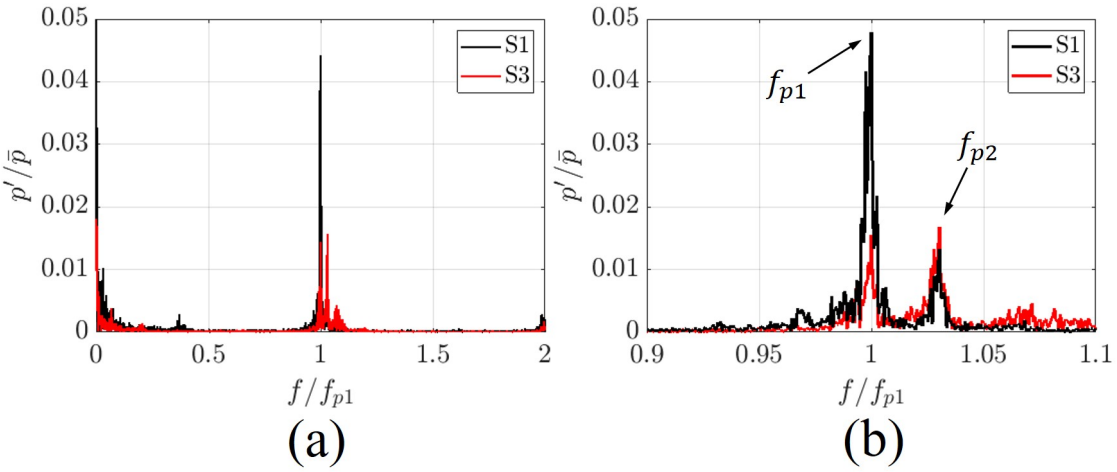

Figure 5.3: Measured frequency spectrum from sensor 1 and 3, (a) zoom out and (b) zoom in version. frequency and pressure amplitude are normalized by its peak frequency and static pressure, respectively.

($m = 2$) and the first radial ($l = 1$) modes occur at approximately 2700 and 3500 Hz, respectively, which are much greater than the observed frequencies. This confirms that the instabilities are either a pure longitudinal ($m = 0, l = 0$) or azimuthal mode ($m = 1, l = 0$).

Notice that two distinct peaks appeared in the spectrum, the first peak at $f_{p1}/f_{p1} = 1$ and the second at $f_{p2}/f_{p1} = 1.03$, illustrating these closely spaced natural frequencies. The acoustic mode identification is carried out for each peak.

5.4.2 Acoustic mode identification

This section describes the pressure dynamics and the acoustic mode shapes during the instabilities. We will investigate the azimuthal and axial dependency separately.

Azimuthal dependency

Figure 5.4 (a) shows the time series signals from each sensor filtered at $f_{p1} \pm df/2$. Notice that the magnitudes (or envelopes) of each signal are similar to each other, but the phases are different. This observation clearly indicates that the instability is not only the first azimuthal mode ($m = 1$), but also close to a spinning wave. CCW and CW waves are extracted by using a least squares fit given by Equation 4.10. Then, the SR and the anti-nodal line are evaluated and plotted in the second and third rows in Figure 5.4. The SR is close to unity indicating that the wave is predominantly spinning in CCW direction.

In Figure 5.4, the anti-nodal line hovers at around 80° and it jumps in CCW direction at $t = 0.4$ s to around 260°. A similar behavior is observed at $t = 0.05$ s, but in this case, the anti-nodal line jumps in the other direction. This behavior seems to occur at the SR near unity. The possible explanation for this phenomenon is that when the mode becomes an instantaneously pure spinning wave, the anti-nodal line disappears, and when the mode comes back to a mixed wave, the anti-nodal line reappears. This re-established anti-nodal line may now be located at completely different locations from the initial location, which appears to be an anti-nodal line jumping. A similar explanation is described in [9]. In

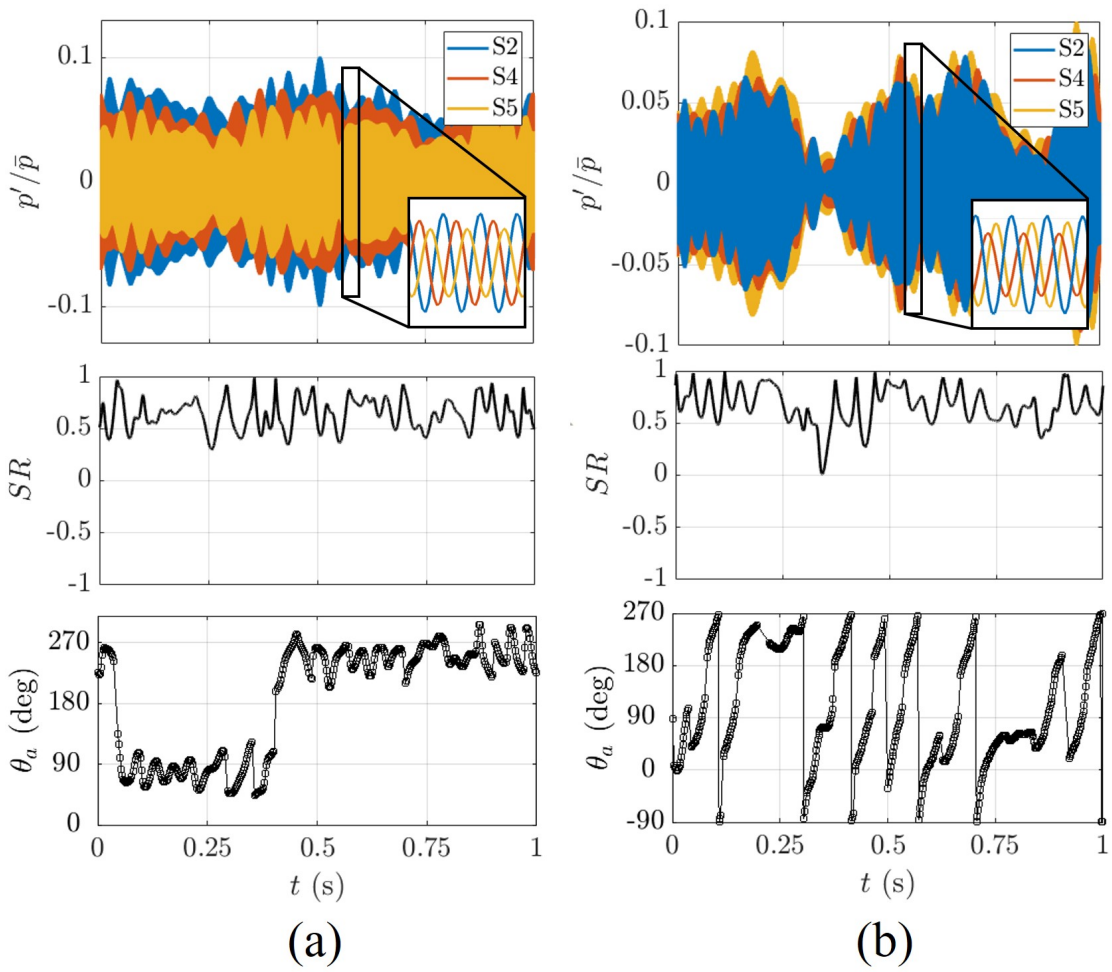

Figure 5.4: First row: measured pressure signals in time series filtered at (a) $f_{p1} \pm df/2$ and (b) $f_{p2} \pm df/2$. The pressure is normalized by static pressure. SR (second row) and anti-nodal line (third row) in time series.

addition, bearing in mind that the anti-nodal line is straight for the first azimuthal mode, the line at 80° is the same at 260°, which implies that the anti-nodal line seems to hover at a fixed location. This may be attributed to the non-uniformity of the temperature or flow field in the azimuthal direction. Lastly, the anti-nodal line is furthest from sensor 5 and closest to sensor 2, yielding the minimum magnitude at sensor 5 and maximum magnitude at sensor 2 in Figure 5.4 (a). As mentioned before, however, the magnitude differences between the sensors are small because of the nearly spinning wave.

Figure 5.4 (b) shows the pressure signals filtered at $f_{p2} \pm df/2$. Notice that the pressure

magnitudes are also similar to each other, implying that the mode is close to the spinning wave. This is obvious in the SR plot in the second row in Figure 5.4 (b) where the SR is close to unity. However, unlike f_{p1}, the anti-nodal line is predominantly rotating in CCW direction.

The pressure magnitude and phase distributions along the azimuthal direction are reconstructed by Equation 5.3 and plotted in Figure 5.5. Here, the black solid line is the temporal averaged pressure distribution and the dashed lines denote the standard error. The red cross represents the temporally averaged magnitude or the phase from each sensor. The blue dash line denotes the distribution for 1A-a (Figure 5.5 (a)) and 1A1L-a (Figure 5.5 (b)) modes from the FEM results in Figure 5.2. The axial location in FEM is selected at the same axial position of sensor 2.

In Figure 5.5 (a), the pressure magnitude of f_{p1} varies in the azimuthal direction, indicating that it is not a pure longitudinal, but an azimuthal mode. In addition, non-zero magnitude at the nodal line implies that the mode is not standing, but rather close to the spinning wave. Last, the phase distribution from the experiments in Figure 5.5 (a) shows an almost linear relationship with θ, which is the characteristic of the spinning wave.

It should be emphasized that the FEM, which solves the Helmholtz equation, provides two orthogonal standing wave solutions. The actual mode is then a linear combination of two solutions. For example, if either of the two solutions is negligible, then the resultant mode is a pure standing wave, whereas if the two solutions are equally dominant, the resultant mode is a pure spinning wave. In real combustors, however, the dominance of each solution depends on the test conditions, providing standing, spinning or a combination of both waves [9, 90, 81, 79]. In Figure 5.5, the two orthogonal solutions are linearly combined in such a way that the resultant mode is similar to those from the experiments.

Figure 5.5 (b) also shows a spinning wave mode shape, but the detail description is omitted here as the general features are similar to those in Figure 5.5 (a).

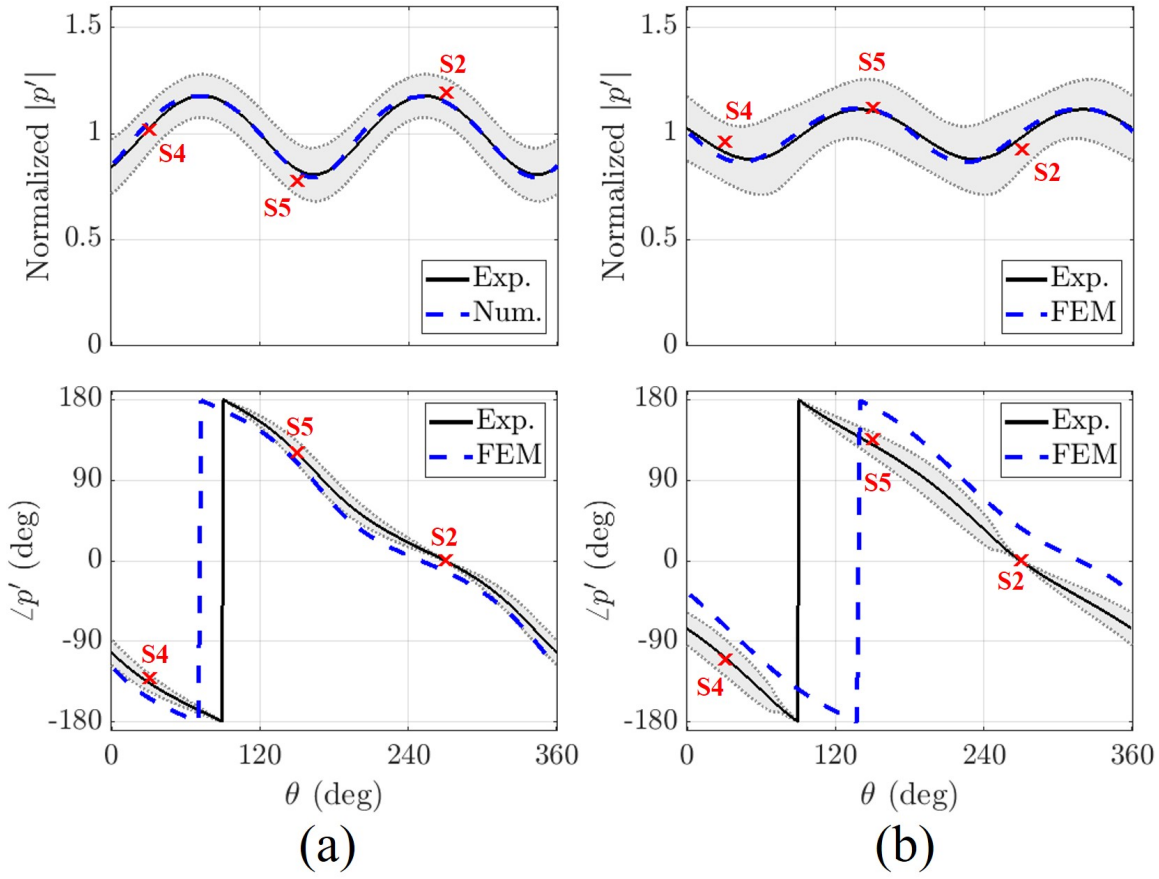

Figure 5.5: Pressure magnitude and phase along the azimuthal direction: (a) f_{p1} (b) f_{p2}. The magnitude is normalized by its spatial averaged value. The phase is plotted with respect to sensor 2.

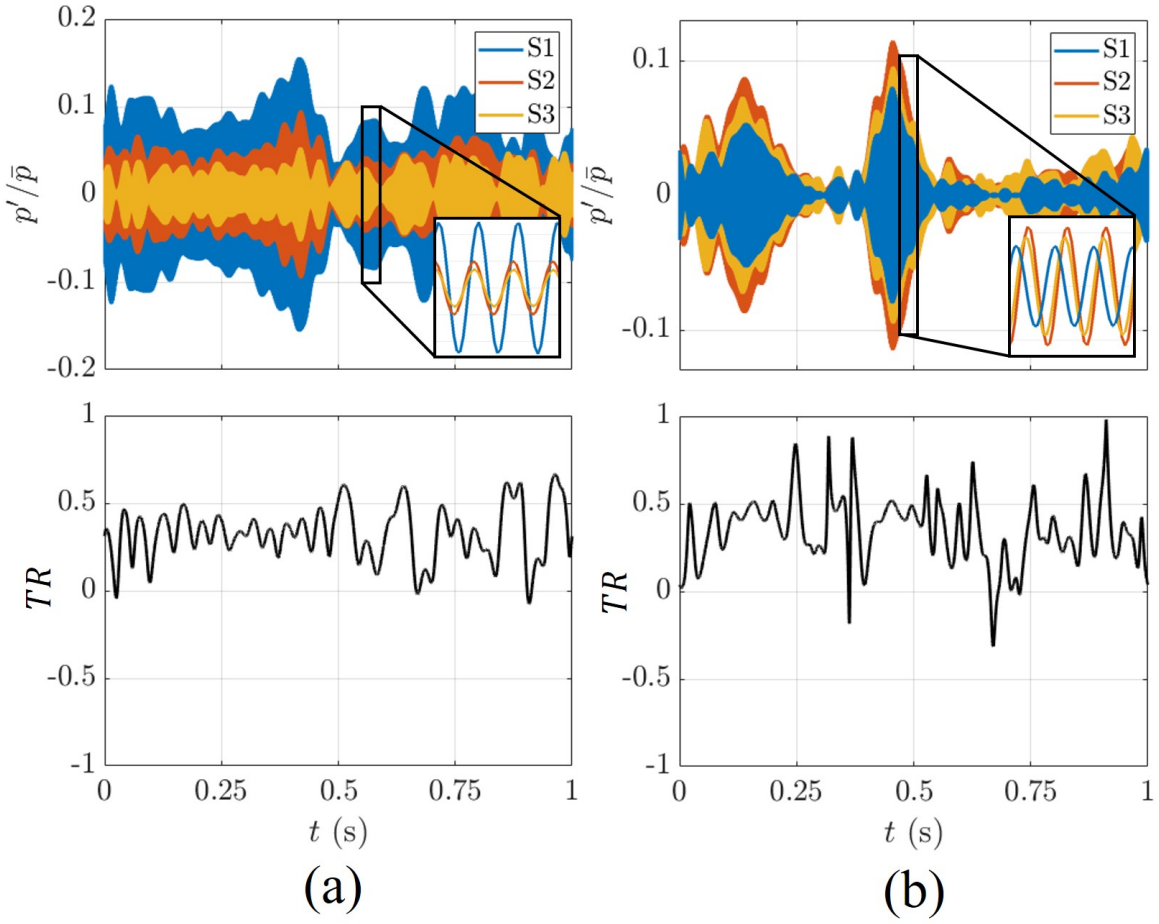

Figure 5.6: First row: measured pressure signals in time series filtered at (a) $f_{p1} \pm df/2$ and (b) $f_{p2} \pm df/2$. The pressure is normalized by static pressure. Second row: TR in time series

Axial dependency

Even though we found the instabilities to be the first azimuthal modes, they may also have an axial dependency. Given the frequency and the estimated sound speed, the axial wavenumber for f_{p1} was found to be purely imaginary, implying that the pressure magnitude exponentially decays in the axial direction as explained in Equation 2.25. This evanescent wave occurs due to a temperature jump across the flame [134]. This feature is evident in the pressure magnitude distribution in Figure 5.7 (a).

Figure 5.6 (a) and (b) describe the pressure signals filtered at $f_{p1} \pm df/2$ and $f_{p2} \pm df/2$, respectively. In Figure 5.6 (a), the pressure magnitude is maximum for sensor 1

and minimum for sensor 3, whereas in Figure 5.6 (b), the magnitude is maximum for sensor 2 and minimum for sensor 1. The second row in Figure 5.6 shows that the TRs for both peaks fluctuate at a positive value, implying that the mode is slightly propagating in the RW direction. For f_{p1}, however, recall that the axial wavenumber is imaginary, yielding the magnitude in RW and LW direction to be $A_{1,2}e^{\mp k_i z}$ where $k_i = k/i$; i.e., the magnitude depends on the axial position as well as $A_{1,2}$. In other words, the acoustic wave generated by the flame propagates in the RW direction, but the magnitude of the RW wave exponentially decays, which then leads to an extremely small magnitude in the LW wave at the reflection boundary. Therefore, the magnitude of the LW wave would be negligible compared to that of the RW wave, leading to a nearly traveling wave in RW direction. The reason for the TR far from the unity in Figure 5.6 (a) is that Equation 5.8 does not account for the axial dependent term, $e^{\mp k_i z}$, when the axial wavenumber is imaginary.

Figure 5.7 presents the pressure magnitude and the phase distributions along the reference line indicated in Figure 5.1. Here, $z = 0$ corresponds to the axial location at the area contraction in the combustor. The FEM is plotted for 1A-a (Figure 5.7 (a)) and 1A1L-a (Figure 5.7 (b)) modes from Figure 5.2. In the first row in Figure 5.7 (a), notice that FEM also predicts the evanescent wave for f_{p1}. However, the discrepancy between the experiments and the FEM appears at the right end of the domain. This difference originates from the fact that for evanescent wave, FEM predicts only the RW wave, resulting in a monotonically decreasing magnitude and constant phase, whereas the reconstruction method takes into account for both RW and LW waves in Equation 5.4. Whether to include the LW wave or not is indeterminate, but without the LW wave, the phase variation between the sensors in Figure 5.7 (a) would not be explained. Except for this deviation, the magnitude and the phase from the experiments are in good agreement with those from the FEM. For f_{p2} in Figure 5.7 (b), the experimental data shows the slightly RW propagating mode, whereas the FEM predicts the perfect standing mode. This may be attributed to the effect of mean flow [17] or the boundary condition at the outlet, i.e., some of the acoustic energy leaves

the domain through the exhaust. However, considering the nodal line location and phase variation in Figure 5.7 (b), the experimental data is close to the FEM results.

To sum up the acoustic mode shapes, we can conclude that f_{p1} and f_{p2} correspond to 1A-a and 1A1L-a modes, respectively, which are described in Figure 5.2 (a) and (c) from the FEM results. The R^2 values of each direction and the frequency comparison between the experimental and the FEM results are summarized in Table 5.1. Here, $\Delta f = |f_{\mathrm{exp}} - f_{\mathrm{FEM}}|$.

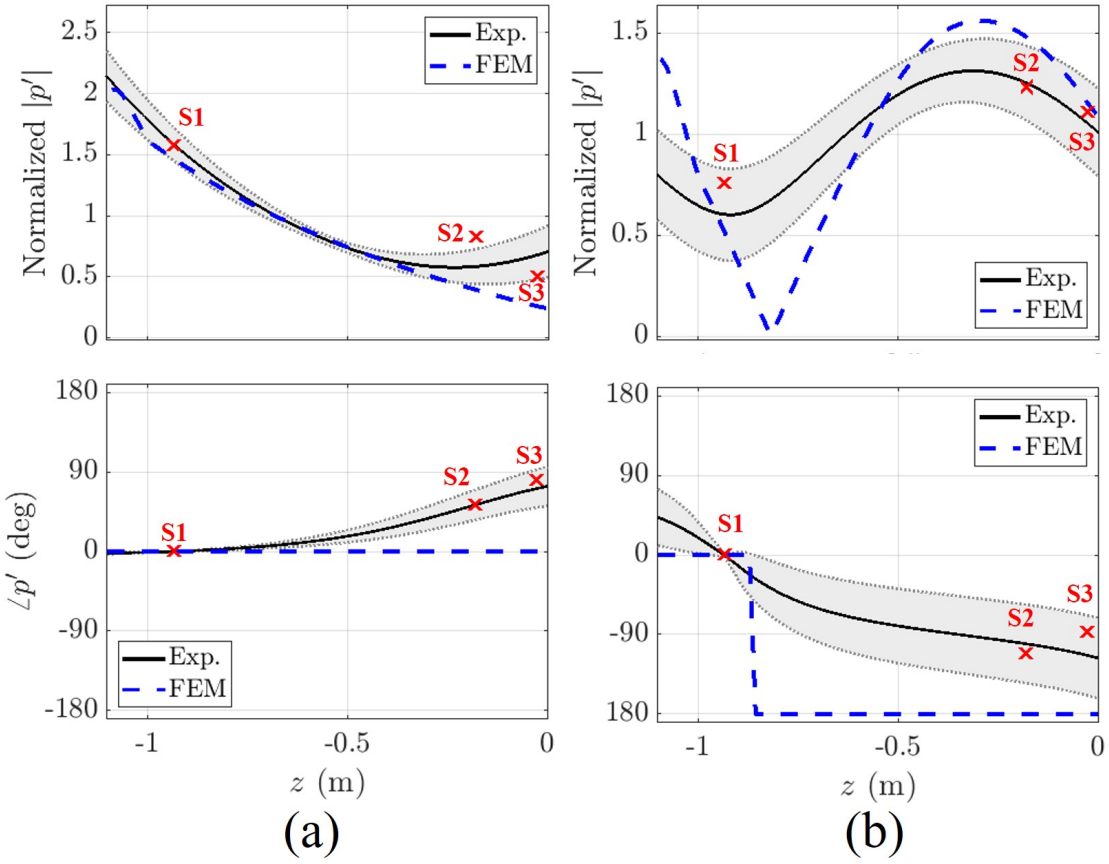

Figure 5.7: Pressure magnitude and phase along the axial direction: (a) f_{p1} (b) f_{p2}. the phase is plotted with respect to sensor 1.

5.5 Conclusion

In this chapter, the acoustic mode shapes of the azimuthal instabilities in a multi-nozzle can combustor have been investigated. During these instabilities, two strong distinct peaks were observed, which is a common observation in a can combustor with a longer axial than radial dimension. The rough calculation from the FEM suggests that the observed frequencies were either a pure longitudinal or azimuthal mode. Next, the different pressure signals between the sensors at distinct azimuthal locations confirm that the instabilities correspond to the first azimuthal modes. However, the axial dependency of each mode is difficult to be identified solely from the FEM as the eigenfrequencies of each mode are too close to each other, which motivates the current study.

This chapter has introduced the methodology to reconstruct the pressure distributions in axial and azimuthal direction by using measured signals from multiple pressure sensors as well as the solution of the wave equation in a cylindrical cavity. The results from the reconstruction method are compared with those from the FEM to validate the method. For the azimuthal distribution, both peaks indicated that the modes are close to a spinning wave. The axial distribution for the first peak showed an evanescent wave, and, for the second peak, it manifested propagating wave. These distributions show a good agreement between the experiments and the FEM results, validating the first and the second peaks as 1A-a and 1A1L-a modes, respectively. In conclusion, the methodology presented in this chapter can be used to identify the high frequency azimuthal acoustic modes even though

Table 5.1: R^2 values and comparison between experimental and fem results.

Frequency	Mode	$\Delta f / f_{\mathrm{FEM}}$ (%)	R^2	
f_{p1}	1A-a	0.139	R^2_θ	0.9961
			R^2_z	0.9543
f_{p2}	1A1L-a	0.422	R^2_θ	0.9940
			R^2_z	0.8912

their frequencies are close to each other.

CHAPTER 6
EXPERIMENTAL INVESTIGATION OF MODAL DYNAMICS OF AZIMUTHAL INSTABILITIES

6.1 Introduction

As explained in section 1.3, most analyses of this azimuthal mode have been performed in annular combustors based on experimental and theoretical approaches. For example, experimental studies have revealed that the azimuthal mode can manifest itself as a spinning wave that propagates in CW or CCW, a standing wave whose nodal line stays at a fixed location or rotates slowly compared to the speed of sound, or a mixed wave, which is a combination of spinning and standing waves. The appearance of spinning, standing, and mixed waves depends on the operating conditions such as equivalence ratio [81] and nozzle geometry [9].

However, comparable studies of modal dynamics of azimuthal modes in can combustors are relatively scarce. A key difference between the annular and can combustors is the number of degrees of freedom of acoustic wave motions. Wave motions are nearly one-dimensional in annular combustion chambers where the annulus width is small relative to the overall diameter. Moreover, the "thin gap" assumption is remarkably accurate even when this ratio is not small in annular combustors [17]. In contrast, azimuthal modes are inherently two- or three-dimensional in can combustion chambers. Thus, one question arises as to how this additional degree of freedom manifests itself in azimuthal modal dynamics.

The experiments in this chapter were conducted over a range of flow rates/thermal power settings and azimuthal symmetry of nozzle fueling, in order to better elucidate the functional relationship between modal dynamics, operating conditions, and azimuthal asymmetry in a can combustor. Although this study focuses on azimuthal asymmetry, the

Table 6.1: Operating conditions

Case	Fuel config.	Preheat temp. (K)	Equiv. ratio (-)	PR (-)	OR (-)	Air mass flow (kg/s)
1	1	600	0.55	0.1	0.5	1.2
2						1.4
3						1.54
4					0.55	1.19
5						1.53

effects of other operating conditions are reported in section 6.7.

6.2 Experimental Setup

Figure 6.1 shows the sensor configuration and two different fuel staging configurations. The sensor configuration shown in Figure 6.1 (b) is the optimal location obtained from chapter 4 for detecting the first azimuthal mode. For fuel configuration 1, the alternating pairs of O1 and O2 are placed around the circumference. For configuration 2, O1 and O2 are placed in alternating order. In this chapter, we swept the total mass flow rate of air and fuel, maintaining other parameters, such as preheat temperature and global equivalence ratio, constants. For example, Figure 6.2 shows the time trace of operating conditions at which the experimental data was obtained. Before the data was analyzed, the operating conditions were stabilized for 30 seconds. The sweep was carried out with uniform ($OR = 0.5$) and non-uniform ($OR > 0.5$) azimuthal fuel staging. We will first examine the uniform fuel staging cases at three different mass flow rates and then briefly explore the non-uniform staging cases, which are summarized in Table 6.1.

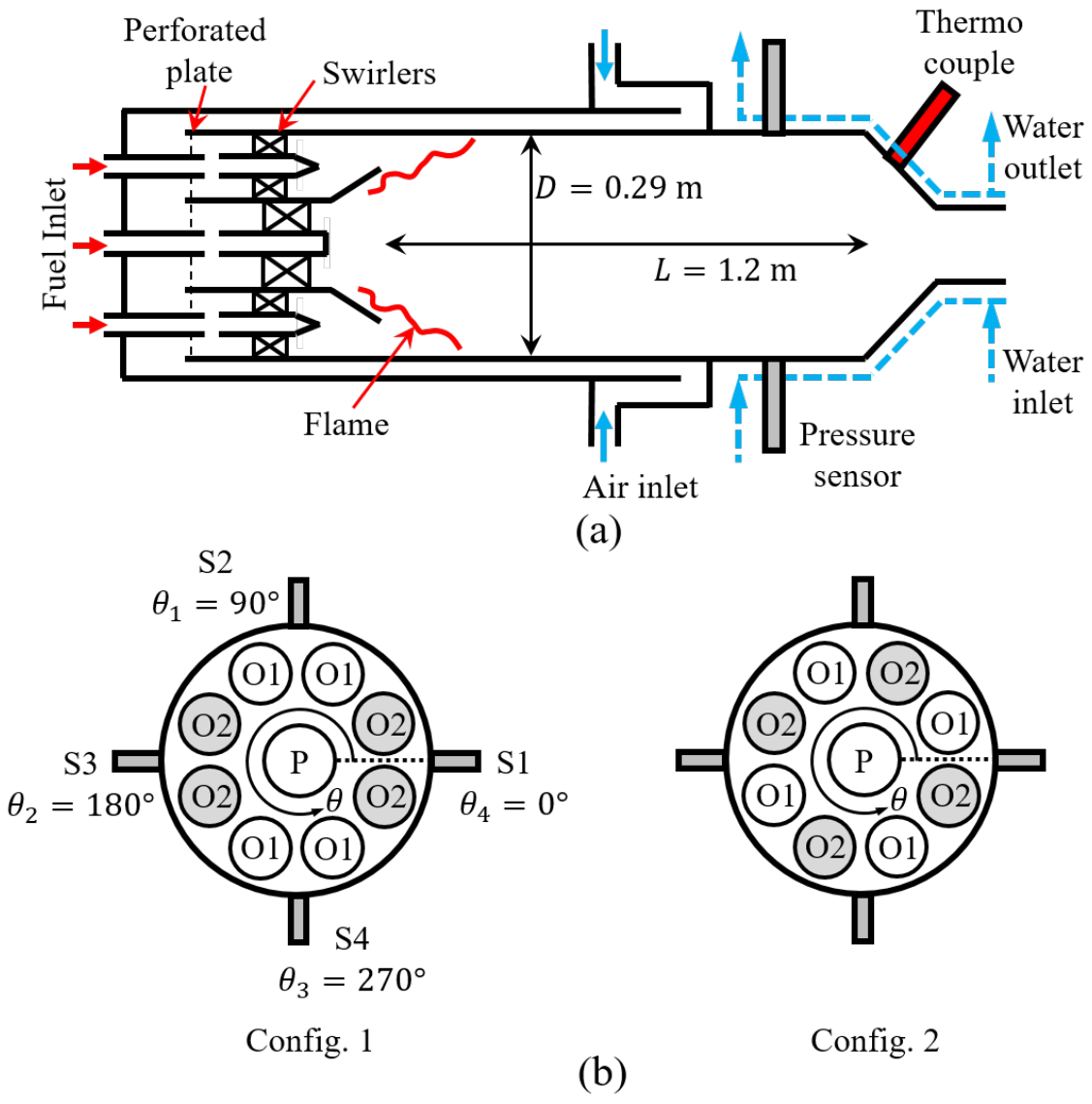

Figure 6.1: (a) Side schematic of combustor. (b) Schematic of multi-nozzle and sensor configuration. 'P' and 'O' denote pilot and outer nozzles, respectively.

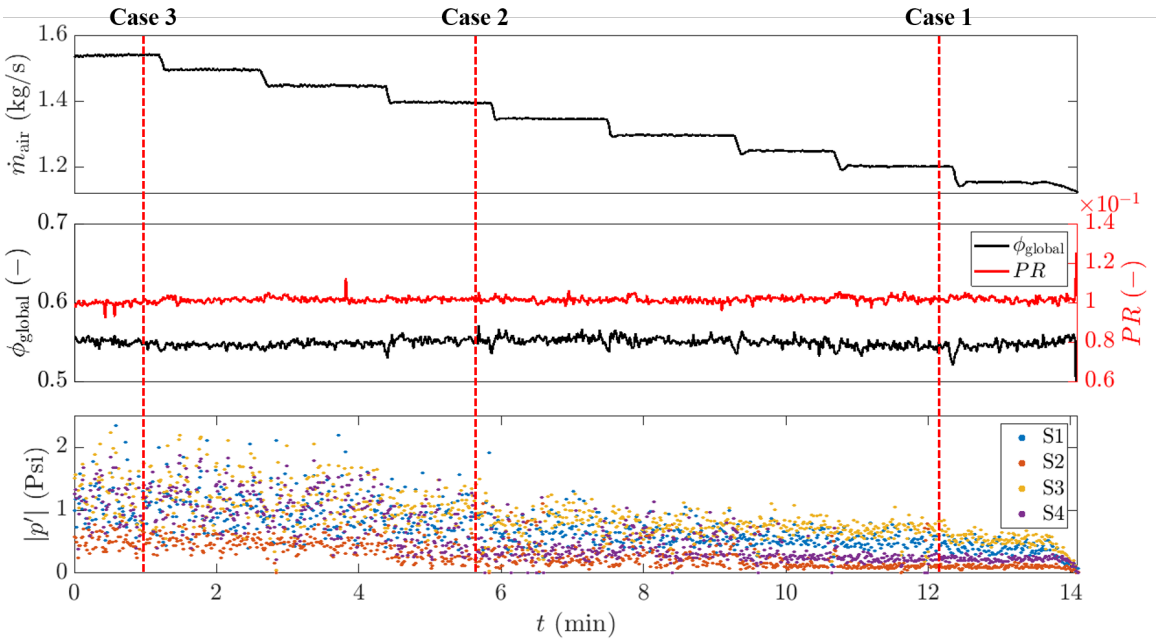

Figure 6.2: Time trace of operating conditions and instability amplitude. Red vertical lines indicate the conditions at which the data is analysed. Top: air mass flow rate, middle: global equivalence ratio and pilot ratio, bottom: instability amplitude from each sensor.

6.3 Mode Characterization

As shown in Equation 4.4, the acoustic pressure in azimuthal direction can be modeled as a superposition of CCW and CW waves.

$$\hat{p}(\theta, t) = Fe^{i(m\theta + \tilde{\varphi}_F - \omega_F t)} + Ge^{-i(m\theta - \tilde{\varphi}_G + \omega_G t)} \tag{6.1}$$

Notice that the oscillation frequencies of CCW/CW waves are set differently to provide a more general expression. However, assuming their difference is small, we can absorb the frequency difference into the phase, and express the oscillation frequencies to be identical by introducing a mean angular frequency, $\bar{\omega}_{FG} = (\omega_F + \omega_G)/2$, and frequency difference, $\Delta\omega = \omega_F - \omega_G$ where $\bar{\omega}_{FG} \gg \Delta\omega$.

$$\hat{p}(\theta, t) = Fe^{i(m\theta + \varphi_F - \bar{\omega}_{FG} t)} + Ge^{-i(m\theta - \varphi_G + \bar{\omega}_{FG} t)} \tag{6.2}$$

Here, $\varphi_F = \tilde{\varphi}_F - \Delta\omega t/2$, and $\varphi_G = \tilde{\varphi}_G + \Delta\omega t/2$. The pressure magnitude as a function of θ is given by Equation 4.5.

$$|\hat{p}(\theta)| = [F^2 + G^2 + 2FG\cos(2m\theta + \varphi_{FG})]^{1/2} \tag{6.3}$$

Here, $\varphi_{FG} = \varphi_F - \varphi_G$.

To remind the readers the important parameters, the spin ratio is defined as Equation 5.2 [83]

$$SR = \frac{F - G}{F + G} \tag{6.4}$$

The anti-nodal line and the corresponding pressure magnitude are given by Equation 4.6 and Equation 4.7.

$$\theta = \frac{n\pi - \varphi_{FG}}{2m} \equiv \theta_a, \quad \text{where} \quad n = 0, 2, 4, \ldots \tag{6.5}$$

$$|\hat{p}(\theta = \theta_a)| = F + G \tag{6.6}$$

For the first azimuthal mode ($m = 1$), $\theta_a = -\varphi_{FG}/2$. Note that φ_{FG} is directly related to the anti-node, which is dependent on the coordinate system.

The quantities, $F,\ G,\ SR,\ \varphi_{FG}$, are extracted from the measurements using a least squares fit (Equation 4.10) and used to describe the modal dynamics of the azimuthal mode.

6.4 Phase Portrait Reconstruction

As shown in the previous section, the azimuthal mode can be modeled as a superposition of two CW/CCW waves, which provides 3 degrees of freedom, i.e., the amplitudes of each wave (F and G) and their phase difference (φ_{FG}). Describing these dynamics in a phase portrait requires three-dimensional space. This portrait with numerous trajectories

may be difficult to interpret because of its complexity. Therefore, the two amplitudes are combined into the spin ratio (SR), and two dimensional phase portrait in SR and φ_{FG} space is visualized.

Furthermore, a phase averaging technique was applied to the time series to eliminate the high dimensional (turbulent) dynamics. The basic idea is to determine the average evolution of SR and φ_{FG} after time, Δt. In other words, given a certain value of SR and φ_{FG} at a time, t, this procedure determines the average behavior of SR and φ_{FG} after time, Δt. Thus, the following procedures were applied to the time series data.

1. Divide phase space (SR, φ_{FG}) into $M \times M$ grid.
2. For each grid, evaluate mean value, $(SR_i, \varphi_{FG,i})$.
3. From time series data, find every points satisfying $|SR - SR_i| < \epsilon_{SR}$ and $|\varphi_{FG} - \varphi_{FG,i}| < \epsilon_{\varphi_{FG}}$ simultaneously, denoted by $(SR(t_i), \varphi_{FG}(t_i))$.
4. Identify every data points, $(SR(t_i + \Delta t), \varphi_{FG}(t_i + \Delta t))$.
5. Compute ensemble average of $(SR(t_i + \Delta t), \varphi_{FG}(t_i + \Delta t))$, denoted by $(\langle SR(t_i + \Delta t)\rangle, \langle \varphi_{FG}(t_i + \Delta t)\rangle)$.
6. Plot vector from $(SR(t_i), \varphi_{FG}(t_i))$ to $(\langle SR(t_i + \Delta t)\rangle, \langle \varphi_{FG}(t_i + \Delta t)\rangle)$ in phase space.
7. Repeat these steps for each SR and φ_{FG} pair. Results are plotted for all pairs with $>$ 10 realizations.

For the results presented here, we used $M = 21, \epsilon_{SR} = 2/M, \epsilon_{\varphi_{FG}} = 2\pi/M$, and $\Delta t = 10$ acoustic cycles. When plotted in this way, limit cycle oscillations appear as fixed points in (SR, φ_{FG}) phase space.

6.5 Results

This section first introduces the uniform fuel staging case in detail such as time series pressure data, frequency spectrum, and phase portrait. The non-uniform staging cases will be shown later.

6.5.1 Uniform fuel staging

Pressure signals in time series

The first row of Figure 6.3 (a) – (c) shows 10 seconds time trace of the raw pressure signals measured from two sensors, S1 and S2, for cases 1 – 3. S3 and S4 are omitted here, as they are similar to S1 and S2, respectively. The bottom of Figure 6.3 (a) – (c) illustrates the ensemble averaged magnitudes of the Fourier transform, which is obtained by estimating the Fourier transform for 1 second of data, averaging the power spectrum, and then taking the square root of the averaged value. The figures show two distinct peaks whose frequency difference is about 53 Hz. The mode shape analysis described in chapter 5 demonstrated that the first and second peaks correspond to the first azimuthal (1A) and the first azimuthal/longitudinal (1A1L) modes, respectively. This chapter focuses on 1A mode only, i.e., the signal is band-pass filtered around 1A with a bandwidth indicated by the shaded region.

As shown in Figure 6.3 (a), when the flow rate is low (case 1), the pressure amplitude for S1 is larger than that for S2, but they are almost out-of-phase, implying that the mode is close to a standing wave. In addition, one can see that the 1A mode in the spectrum consists of two very closely spaced peaks, approximately 6 Hz apart, that will be discussed further later.

For an intermediate flow rate (case 2), the relative amplitude changes in time, i.e., sometimes S1 has a larger amplitude than S2; other times they have similar amplitudes. The spectrum also shows two closely spaced peaks 11 Hz apart, which is higher than case

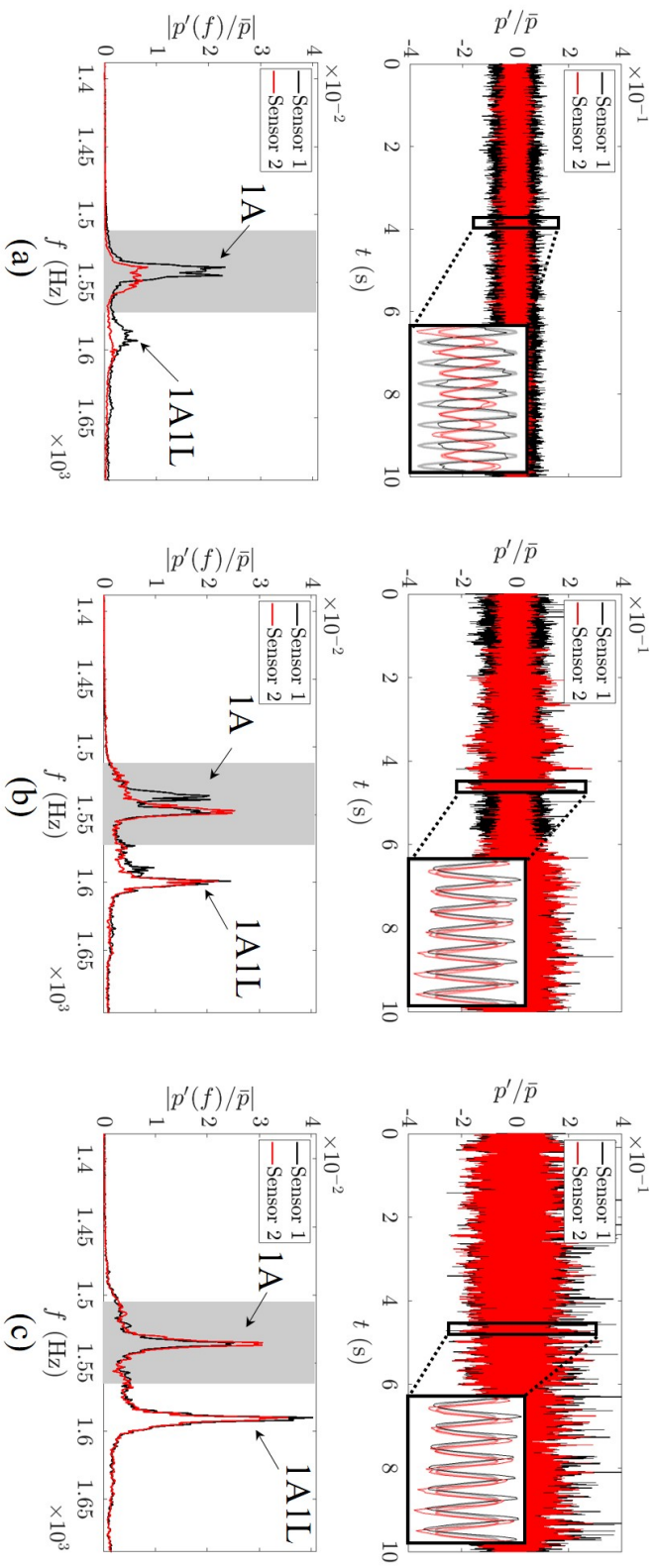

Figure 6.3: Top: raw pressure signals from sensor 1 and 2 for (a) case 1, (b) 2, and (c) 3. In subfigures, thick and thin lines denote the band-pass filtered and raw signals, respectively. Bottom: ensemble-averaged Fourier transform from sensor 1 and 2 for each case.

1.

For a high flow rate (case 3), the amplitudes remain similar to each other all the time, and the spectrum is composed of only a single peak.

Dynamics of CW/CCW wave magnitudes

We next consider the slow time scale characteristics of the extracted parameters. The top of Figure 6.4 (a) – (c) illustrates the time trace of extracted CCW/CW wave magnitudes normalized by static pressure, and the normalized pressure magnitude at the instantaneous anti-node for each case. The bottom of Figure 6.4 (a) – (c) plots the ensemble averaged Fourier transform of CCW/CW waves for each case.

For case 1, F and G are oscillating around a fixed value, but their oscillations are approximately sinusoidal and out-of-phase to each other. The corresponding Fourier transform shows two peaks closely spaced to each other where their difference is about 6 Hz. Bulk azimuthal flow is one potential mechanism for this frequency difference as calculations based upon the computed flow indicate a frequency difference of 10 Hz. If the azimuthal flow were the mechanism for these two peaks, however, the CW and CCW waves would separately peak at one of the two frequencies. However, Figure 6.4 (a) clearly shows that each of the CCW/CW waves has two peaks overlapping each other. These two peaks are a manifestation of a quasi-periodic oscillation, where the instantaneous amplitudes F and G oscillate at their frequency difference. Hereafter, we refer to this as a quasi-periodic standing wave.

For case 2, F and G show intermittency as they sometimes show standing wave behavior observed in case 1; other times F dominates over G. The Fourier transform also exhibits two peaks: the first peak where CCW/CW have a comparable amplitude, the second peak where CCW amplitude is greater than CW amplitude.

For case 3, F dominates over G most of the time, which is also seen in the Fourier transform.

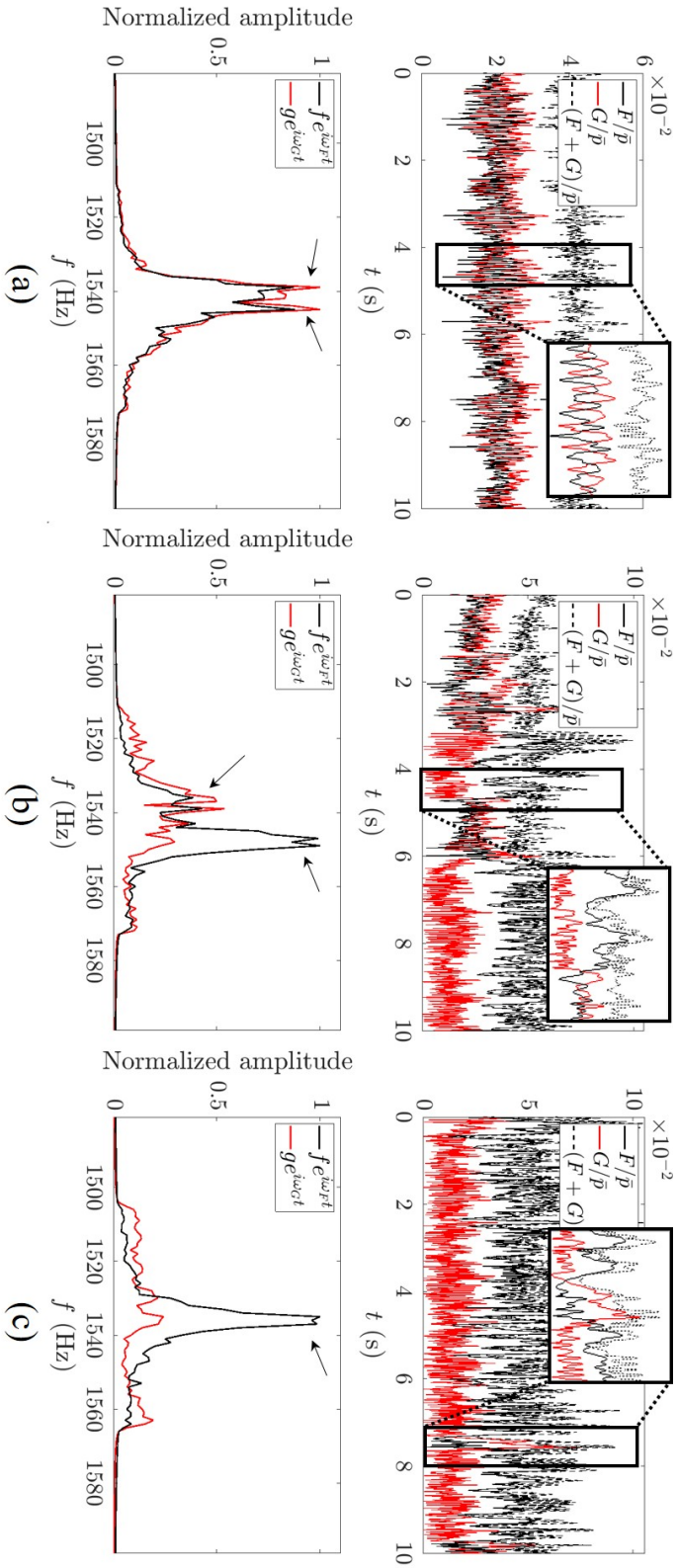

Figure 6.4: Top: time trace of CCW(F)/CW(G) wave magnitudes as well as the pressure anti-node magnitude for (a) case 1, (b) 2, and (c) 3. Bottom: ensemble averaged Fourier transform of CCW/CW waves for each case, normalized by their peak value.

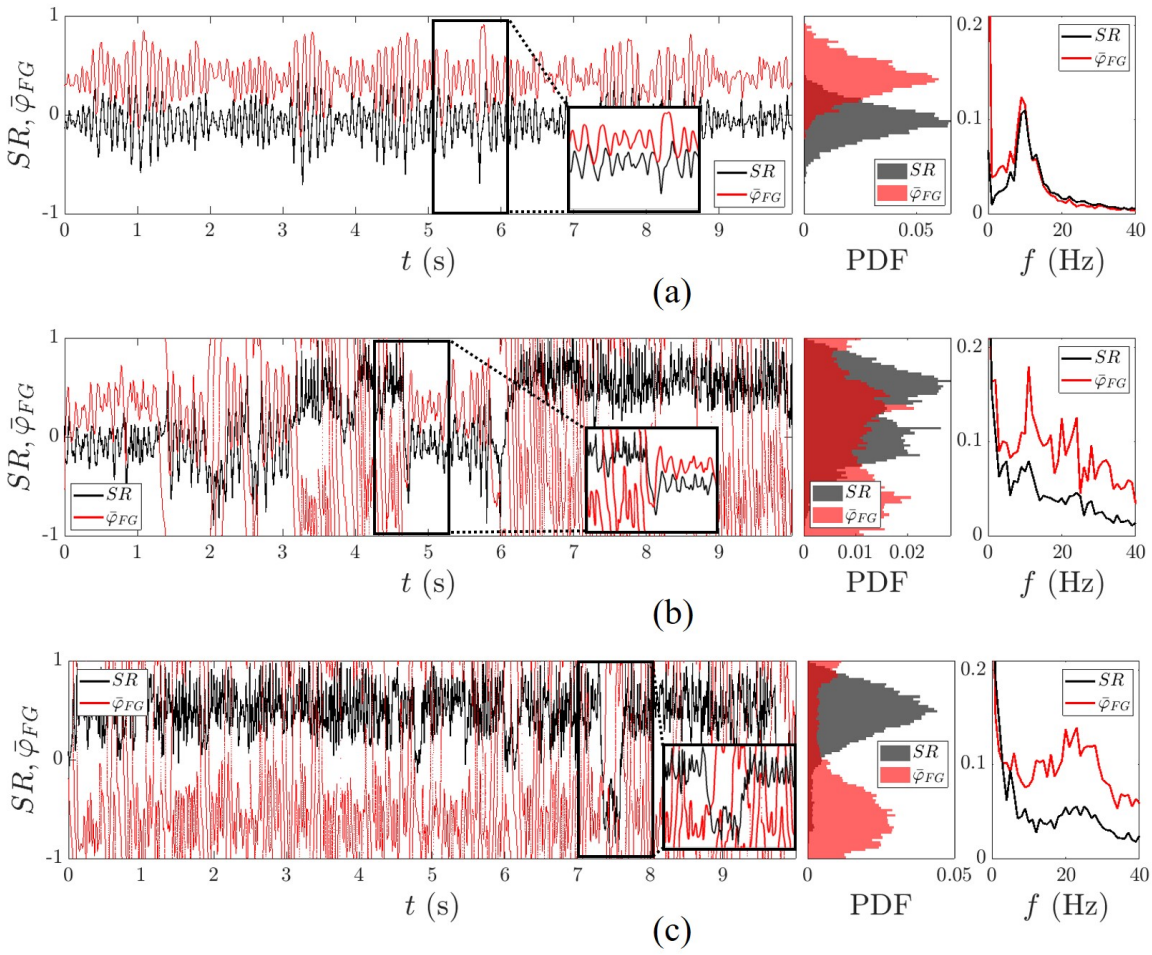

Figure 6.5: SR and $\bar{\varphi}_{FG}$ in time series for (a) case 1, (d) 2, and (g) 3. PDF of SR and $\bar{\varphi}_{FG}$ for (b) case 1, (e) 2, and (h) 3. Ensemble averaged Fourier transform of SR and $\bar{\varphi}_{FG}$ for (c) case 1, (f) 2, and (i) 3.

Dynamics of SR and $\bar{\varphi}_{FG}$

Figure 6.5 plots the time trace of SR and the normalized phase difference, $\bar{\varphi}_{FG} = \varphi_{FG}/\pi$, between CCW/CW waves, their PDFs, and the ensemble averaged Fourier transform for each case. Starting from case 1, SR is oscillating around zero as expected, but $\bar{\varphi}_{FG}$ is also oscillating in a sinusoidal manner. Since $\bar{\varphi}_{FG}$ is directly related to the orientation of the anti-node, the oscillation in $\bar{\varphi}_{FG}$ is equivalent to the oscillation in the anti-nodal line. Also note that the oscillations of SR and $\bar{\varphi}_{FG}$ are not synchronized, but the oscillation in $\bar{\varphi}_{FG}$ leads that in SR by about 90°, e.g., see subfigure in Figure 6.5 (a). This phase lag will

result in a circular orbit in averaged phase portrait, discussed later. The PDFs of SR and $\bar{\varphi}_{FG}$ show a unimodal distribution, implying one stable equilibrium point. The peak of SR PDF is around zero, meaning that the instability mode is close to a standing wave. The peak of $\bar{\varphi}_{FG}$ PDF is around 0.4 or $\varphi_{FG} = 72°$, indicating that the anti-node is located at around $\theta_a = -36°$ from Equation 4.6. This explains the reason for the relative amplitudes and out of phase between S1 and S2 in Figure 6.3 (a), i.e., anti-node is close to S1 than S2, and the node is located between S1 and S2. The FFT in SR and $\bar{\varphi}_{FG}$ shows a dominant peak at around 10 Hz, demonstrating a coherent oscillation. Also, note that the peak frequency in the spectra is close to the frequency spacing observed in Figure 6.4 (a). These observations imply that they are not driven by simply a stochastic forcing, but rather coupled to each other by a lower degree of freedom process.

For case 2, SR and $\bar{\varphi}_{FG}$ intermittently switch between two values. Specifically, SR hops between zero and 0.5, whereas $\bar{\varphi}_{FG}$ hops between 0.4 and -0.7. Note that their transitions occur simultaneously. In subfigure, for example, when SR switches from 0.5 to zero, $\bar{\varphi}_{FG}$ shifts from -0.7 to 0.4, and vice versa. In addition, when $\bar{\varphi}_{FG}$ lingers around -0.7, it sometimes drifts to one/the other directions equivalent to the rotation of the anti-nodal line. The PDFs of SR and $\bar{\varphi}_{FG}$ exhibit a bimodal distribution, implying bistability of the system. Lastly, the peak amplitude around 10 Hz in the FFT is reduced compared to case 1.

For case 3, SR and $\bar{\varphi}_{FG}$ mostly linger around nearly fixed values of 0.55 and -0.7, respectively, indicating that the system has one stable equilibrium point. This is confirmed by a unimodal distribution in the PDF. As discussed in Appendix B, the SR estimate is subject to bias errors, which can influence the interpretation of estimated SR values. Using the approach described there to estimate this bias error leads to an estimated bias of 0.1 ± 0.05. As such, we can confidently say that this $SR = 0.55$ value reflects a mixed wave, not a purely spinning wave with large noise intensity. SR transitions to -0.55 at $t = 7.5$ s, but it immediately returns to 0.55. Also, note that the Fourier transforms for case 3 show no dominant peak compared to case 1.

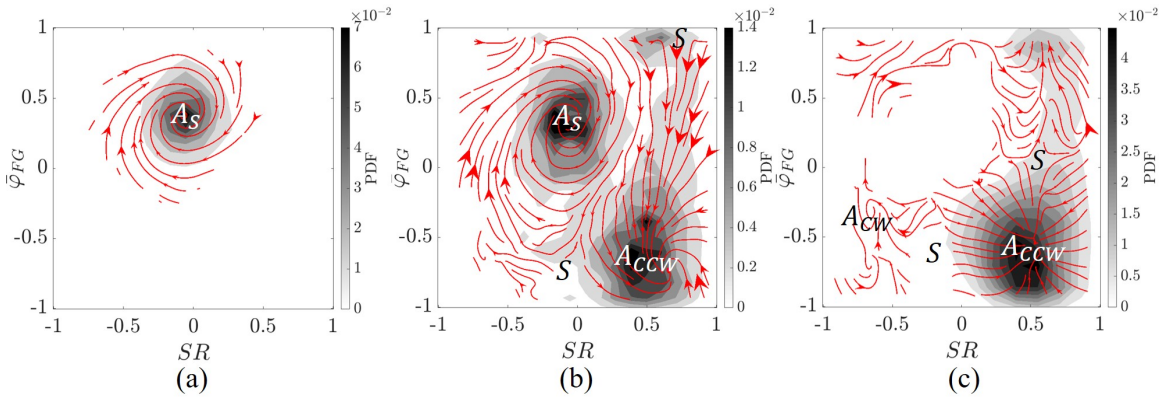

Figure 6.6: Averaged phase portrait in SR and $\bar{\varphi}_{FG}$ space for (a) case 1, (b) 2, and (c) 3. The gray scale denotes the joint PDF of SR and $\bar{\varphi}_{FG}$. The red arrows and their head size indicate the trajectories and velocity magnitude.

Phase averaged portrait

To eliminate the high dimensional (turbulent) dynamics and visualize the low order dynamics, a phase averaging technique, detailed in section 6.4, was applied to each case. When SR and $\bar{\varphi}_{FG}$ are plotted in the phase space, limit cycles and quasi-periodic oscillations appear as Fixed Point (FP)s and closed orbits, respectively (while, theoretically, quasi-periodic orbits are never closed, the averaging procedure necessarily has finite phase space resolution and closes them).

Figure 6.6 shows the SR and $\bar{\varphi}_{FG}$ phase portraits for case 1 - 3. For case 1, the phase portrait shows the trajectories converging to the center, $(SR, \bar{\varphi}_{FG}) = (0, 0.4)$, and the joint PDF shows a unimodal distribution. This implies that the system has one stable attractor at the center, denoted by A_S where subscript 'S' indicates a standing wave. In addition, the trajectories are spiraling in towards the attractor in the CW direction, which is expected from the 90° phase lag between the oscillations in SR and $\bar{\varphi}_{FG}$ described in Figure 6.5 (a). Without the noise contribution, the system would be stabilized at the stable attractor. However, the noise continuously perturbs the system from its attractor, and the system repeatedly converges towards this attractor, forming the CW spiral trajectories.

For case 2, a much larger range of behaviors and attractors are observed and the struc-

ture of the phase portrait is more complex. First, the stable attractor at $(0, 0.4)$ observed from case 1 still exists, but the system shows another stable attractor at $(SR, \bar{\varphi}_{FG}) = (0.55, -0.7)$, denoted by A_{CCW}, which corresponds to the CCW dominant mixed wave. The joint PDF similarly demonstrates discrete peaks associated with these two attractors at $(0, 0.4)$ and $(0.55, -0.7)$. Second, two saddle points, denoted by S, are also observed near the top and bottom boundaries.

For case 3, A_{CCW} still exists at the bottom right corner, but A_S is not visible, demonstrating that it is strongly repelling. Rather, a CW mixed wave attractor, A_{CW}, appears at the bottom left corner although the joint PDF around it is sparse. This implies that A_{CW} may be a stable attractor, but its strength is so weak that the system can be readily expelled from the attractor by the external noise, and it converges to A_{CCW}. The system stays around this attractor most of the time.

Figure 6.6 shows the overall structure of the phase portrait. However, there exist empty regions in the portrait because of either insufficient sampling time or low noise intensity. We have acquired additional phase portraits with longer sampling time at a range of other operating conditions in Appendix D. These portraits show that there is a saddle point in the empty regions in Figure 6.6, but the overall structure remains the same even at different operating conditions.

6.5.2 Non-uniform fuel staging

Dynamics of SR and $\bar{\varphi}_{FG}$

This section presents cases 4 and 5 where the fuel is non-uniformly staged through fuel configuration 1. The fuel staging effect of configuration 2 will be shown in subsection 6.5.4. Here, we present only the dynamics of SR and $\bar{\varphi}_{FG}$ as well as the phase portraits for brevity, i.e., the dynamics of CCW/CW waves and the associated Fourier transform are similar to those in case 1. From Figure 6.7, several observations have been made. First, the quasi-periodic standing wave only appears with non-uniform staging cases. Second, as the

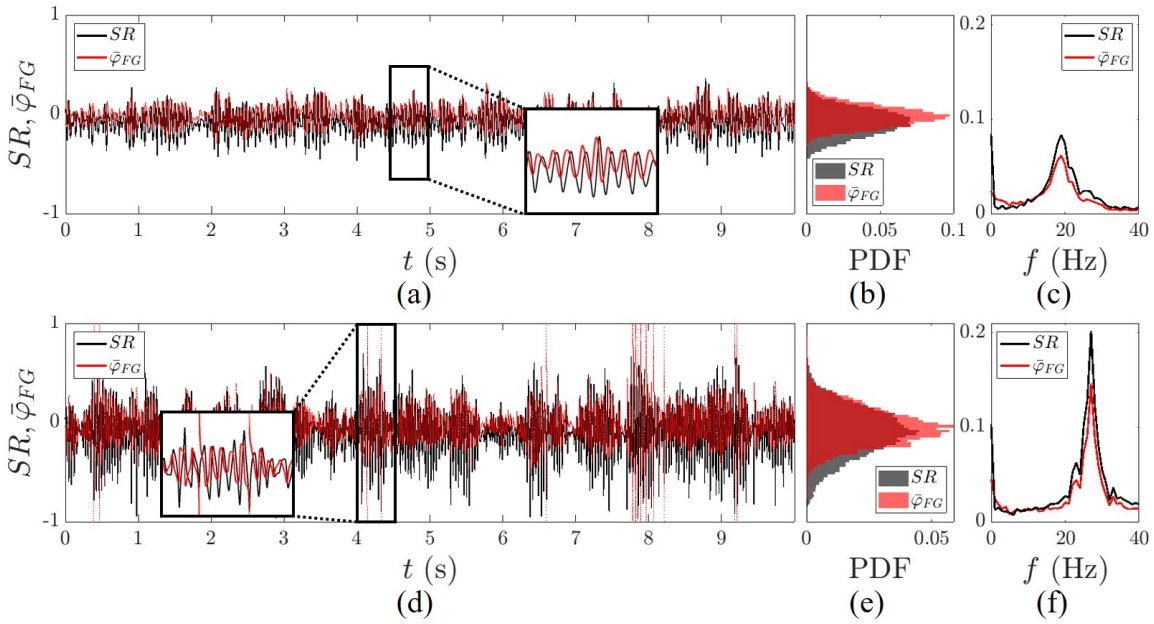

Figure 6.7: SR and $\bar{\varphi}_{FG}$ in time series for (a) case 4, and (d) 5. PDF of SR and $\bar{\varphi}_{FG}$ for (b) case 4, and (e) 5. Ensemble averaged Fourier transform of SR and $\bar{\varphi}_{FG}$ for (c) case 4, and (f) 5.

flow rate increases, the modulation frequency, f_{mod}, increases from 19 Hz to 27 Hz. This increase in frequency was not shown in Figure 6.5 as the mode switches to a mixed wave for a high flow rate. Third, the amplitude of modulation grows with increasing flow rate as shown in the spectra. The dependence of the modulation frequency and amplitude as a function of mass flow rates will be analyzed further in the next subsection.

Phase averaged portrait

Figure 6.8 illustrates the phase portraits for cases 4 and 5. The overall structures are similar to Figure 6.6 (a), i.e., the system possesses a standing wave stable attractor, and the trajectories are spiraling in CW direction. The only difference is that the attractor is now located at $(SR, \bar{\varphi}_{FG}) = (0, 0)$ for both cases as opposed to case 3. This is presumably because the hot flames are oriented in a horizontal direction for fuel configuration 1 with $OR > 0.5$ (Figure 6.1), fixing the anti-nodal line at the horizontal direction. Thus, $\theta_a = \varphi_{FG} = 0$. Comparing cases 4 and 5, the joint PDF in case 5 shows the wider dis-

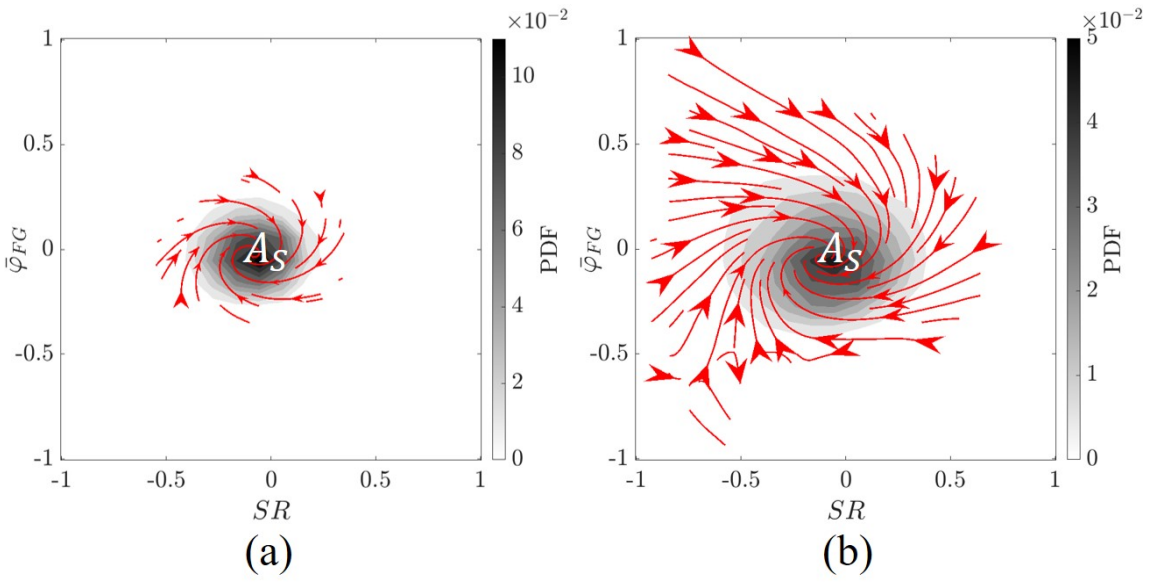

Figure 6.8: Averaged phase portrait in SR and $\bar{\varphi}_{FG}$ space for (a) case 4, and (b) 5.

tribution, demonstrating large amplitude modulations shown in Figure 6.7 (d). In addition, the trajectory velocity is higher for case 5 than case 4 because of the higher modulation frequency shown in Figure 6.7 (f).

6.5.3 Comparison between uniform and non-uniform fuel staging

Figure 6.9 (a) represents the normalized anti-node magnitude, $(F+G)/\bar{p}$, with respect to air mass flow rate with different ORs. The magnitude exhibits a supercritical Hopf bifurcation at a certain mass flow rate, at which it exhibits oscillations at 1A mode. The magnitude increases monotonically with mass flow rates over the range tested here. As shown in the figure, both the location of the Hopf bifurcation and magnitudes are also functions of azimuthal non-uniformity parameter, OR.

Figure 6.9 (b) illustrates SR as a function of anti-node magnitude. The SR in this plot is averaged value over 1 second. At low magnitudes, SR is close to zero, implying a standing wave. For intermediate magnitudes, SR fluctuates between zero and 0.55, demonstrating intermittency. For high amplitudes, SR is stabilized at 0.55. Notice that when $OR > 0.5$, the magnitude is too low to reach the bistable regime, resulting in a standing wave only.

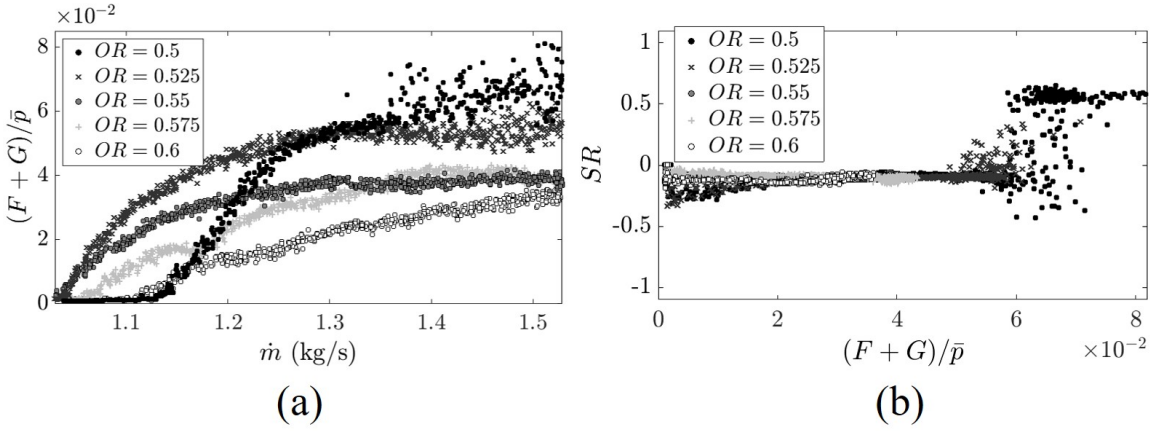

Figure 6.9: (a) Normalized pressure anti-node magnitude as a function of air mass flow rate with different ORs. (b) SR as a function of normalized pressure anti-node magnitude with different ORs.

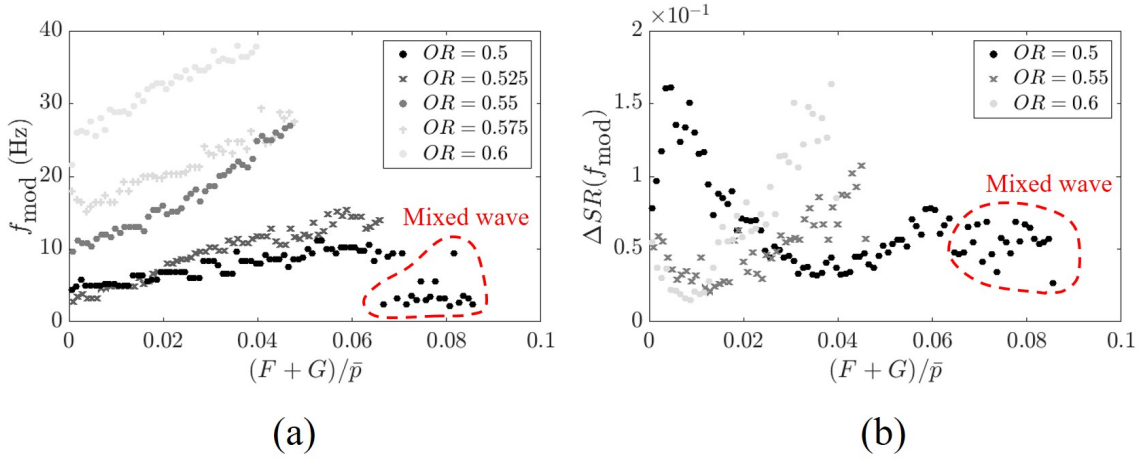

Figure 6.10: (a) SR modulation frequency as a function of normalized anti-node magnitude with different ORs. (b) SR modulation amplitude as a function of normalized anti-node magnitude with different ORs.

We have observed in Figure 6.7 that the SR modulation frequency, f_{mod}, and the associated amplitude, $\Delta SR(f_{\text{mod}})$, vary with mass flow rates. Thus, it is worthwhile to explore their relations in detail. As the instability amplitude is monotonically related to overall combustor power/flow rate for this investigated parameter range (but certainly not in general), these dependencies more probably reflect a sensitivity of this quasi-periodic standing wave to linear amplification/damping parameters (as also suggested by the theory described in chapter 7) that influence combustion instability amplitude. As such, we plot the modulation frequency and the associated amplitude as a function of anti-node magnitude at different ORs in Figure 6.10. Figure 6.10 (a) shows that the modulation frequency increases with the anti-node magnitude as long as the azimuthal mode remains as a standing wave. In addition, the modulation frequency increases with azimuthal non-uniformity. Figure 6.10 (b) shows that as the anti-node magnitude increases, the modulation amplitude first decreases and then increases. This can be understood by examining how small perturbations in wave amplitudes, translate to perturbations in SR:

$$\Delta SR = \frac{2(G\Delta F - F\Delta G)}{(F+G)^2} \tag{6.7}$$

The sinusoidal oscillation in SR, described in Figure 6.5 (a), Figure 6.7 (a) and (d), implies that the derivative of F and G are out-of-phase to each other. Thus, for the case where $\Delta F = -\Delta G$, Equation 6.7 can be rewritten as:

$$\Delta SR|_{\Delta G=-\Delta F} = \frac{2\Delta F}{F+G} = \frac{2\Delta F}{|\hat{p}(\theta_a)|} \tag{6.8}$$

Equation 6.8 explicitly shows that when the anti-node magnitude is small, the small perturbation of F and G induces a large fluctuation in SR. As the anti-node magnitude grows, the SR modulation amplitude decreases. When the increase in ΔF dominates over that in $|\hat{p}(\theta_a)|$, the SR modulation amplitude starts to increase. These are clearly observed in Figure 6.10 (b).

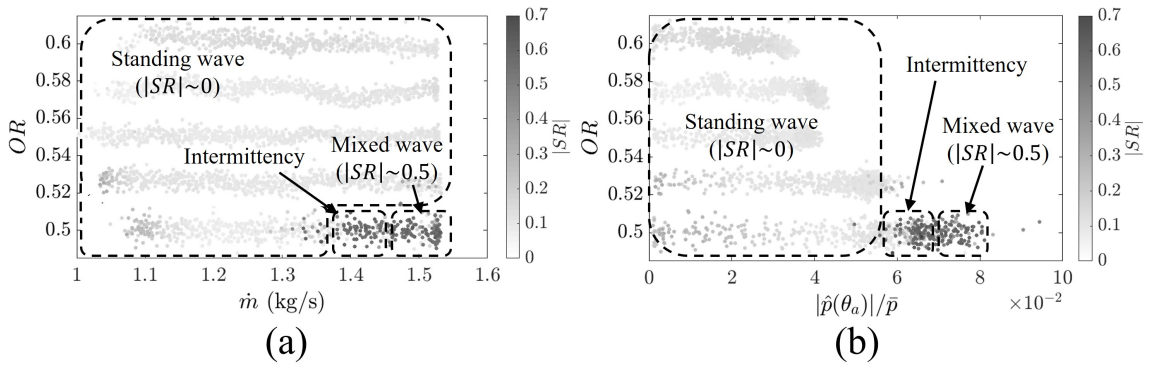

Figure 6.11: (a) Effects of mass flow rate and OR on the mode structure. (b) Effects of anti-node magnitude and OR on the mode structure.

To sum up the overall observations, the system inherently possesses multiple FPs whose stability depends on the operating conditions. For low flow rates with uniform fuel distribution, the attractor consists of a standing wave. For intermediate flow rates, both standing and CCW mixed wave FPs are attractors. In this case, background noise perturbs the system state so that it never lies on one attractor, but is occasionally driven from one attracting domain to another. Lastly, for high flow rate, CW/CCW mixed wave FPs are attractors, but their relative strength considerably differs. When the fuel is staged non-uniformly, the system exhibits only the standing wave FP regardless of mass flow rates. Figure 6.11 summarizes these results, showing them in two different ways. The cloud of points in the images represents the experimental conditions that this plot is based upon.

6.5.4 Effects of fuel staging pattern

Here, we briefly show the effects of fuel staging configuration 2. Figure 6.12 (a) and (b) show the same plots with Figure 6.9 (a) and (b) but with fuel configuration 2. Figure 6.12 (a) demonstrates that the onset of the instability follows similar trends with those for fuel configuration 1, i.e., Hopf bifurcation point advances and delays as the OR increases. As the flow rate increases, however, the pressure magnitudes collapse to each other, implying that the fuel configuration 2 has little effect of mitigating/suppressing the instability. In addition, Figure 6.12 (b) shows that the instability mode exhibits not only a standing wave

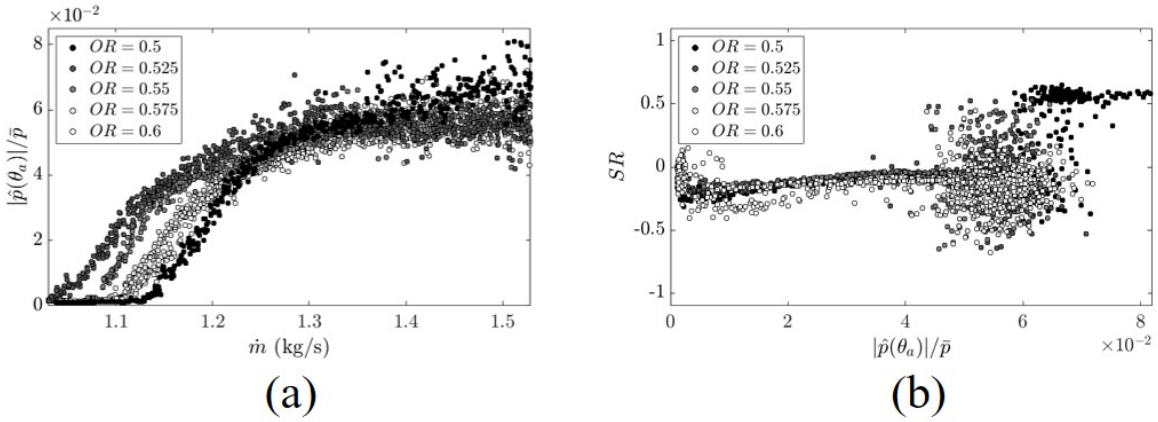

Figure 6.12: (a) Normalized pressure anti-node magnitude as a function air mass flow rate with different ORs. (b) SR as a function of normalized pressure anti-node magnitude with different ORs.

at low magnitudes but also a switching mode at large magnitudes regardless of OR. This suggests that fuel configuration 2 has a negligible impact on modal dynamics.

Figure 6.12 shows a very significant implication. That is, the pattern of the fuel staging plays an important role in controlling the azimuthal instabilities. A natural question is then what pattern has the most impact on the azimuthal mode. This question will be answered in chapter 7.

6.5.5 Relationship between acoustic pressure and heat release fluctuation

Having considered the various modal natures of the azimuthal modes, it is interesting to explore how the heat release fluctuation behaves with respect to acoustic pressure. CH* chemiluminescence image was used to estimate the LOS heat release fluctuation. Unfortunately, when we changed the chamber liner from a metal to a quartz tube, only the standing wave appeared during the instability. It is believed that the static pressure inside the chamber dropped with the quartz tube because of the air leakage, decreasing the overall instability amplitude, and thus, only standing wave showed up.

Before moving on, we would like to introduce the CH* chemiluminescence image. Figure 6.13 illustrates the phase average CH* chemiluminescence image. The average in-

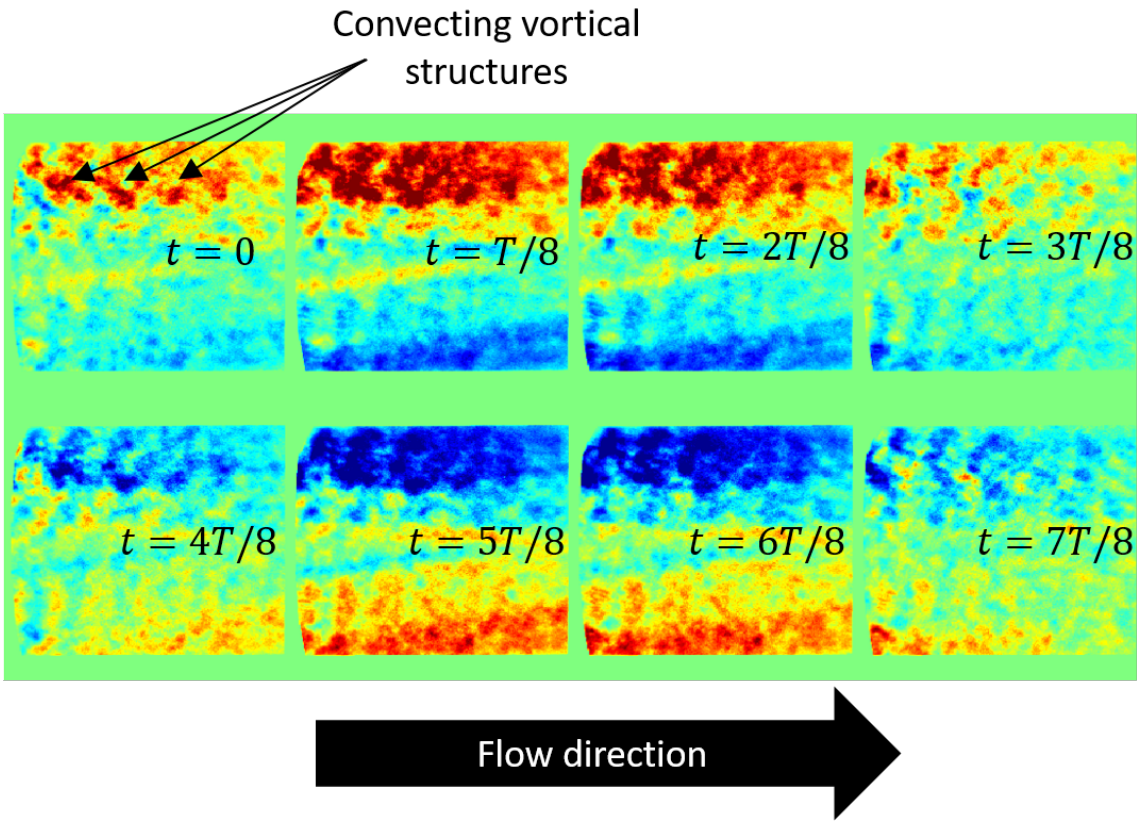

Figure 6.13: Mean subtracted phase average image of CH* chemiluminescence. T denotes one period of acoustic cycle.

tensity over one cycle is subtracted from each frame. Thus, red, blue, and green denote positive, negative, and zero intensity, respectively. As expected, the CH* intensity oscillates in a vertical direction. In other words, the intensities of the top and bottom of the frame are always out of phase to each other. The overall intensity is maximized at $t = T/8$ and $t = 5T/8$. Noting that the intensity is a LOS image, almost zero intensity at the middle implies that the nodal line is located at the middle at this moment. Also, note that the phase average image exhibits somewhat vortical structures convecting downstream. These structures are probably the result of the interaction between acoustics and mean flow gradient [91]. Note that the vortical structures are not clear as those in [91] because Figure 6.13 is the LOS integrated image.

As explained in section 3.4, the top half of the chemiluminescence image was integrated to get a scalar quantity as a function of time. Similarly, the pressure distribution in $r - \theta$

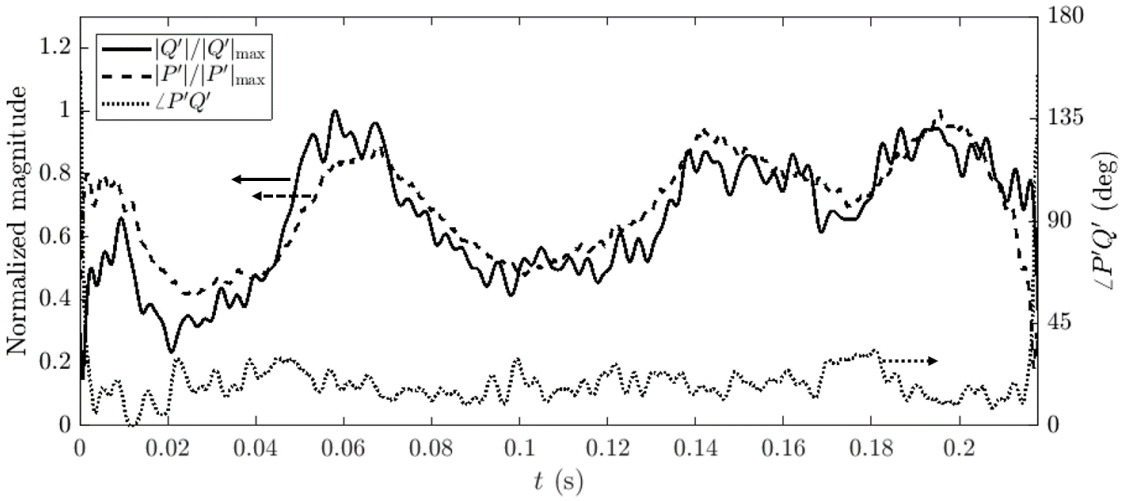

Figure 6.14: The normalized magnitudes and the phase difference between the reconstructed pressure and the heat release fluctuation in time series.

plane was reconstructed using the azimuthal and radial components in Equation 2.21, and then the top half of the pressure was integrated.

The magnitudes and the phase difference between the reconstructed pressure and the heat release fluctuation are described in Figure 6.14. It shows a positive correlation between the magnitudes of these two quantities. In other words, when the pressure magnitude increases/decreases, so does the heat release fluctuation. In addition, the phase difference between two quantities is about $\angle P'Q' \approx 20°$. This satisfies the Rayleigh criterion explained in Equation 1.1 in chapter 1; the phase difference between pressure and heat release fluctuations must be between -90° and 90° to add acoustic energy into the system. Thus, Figure 6.14 implies that the acoustic energy is keep adding into the system, and the same amount of energy is damped out, resulting in finite magnitude oscillations (not exponential growth).

One may ask why the magnitudes of pressure and heat release fluctuations vary in time if the additive acoustic energy is balanced with the damping of the system. This is because the top half of the magnitude depends on the orientation of the nodal line, which varies in time as shown in Figure 6.5 (a) and Figure 6.7. To illustrate this point, Figure 6.15

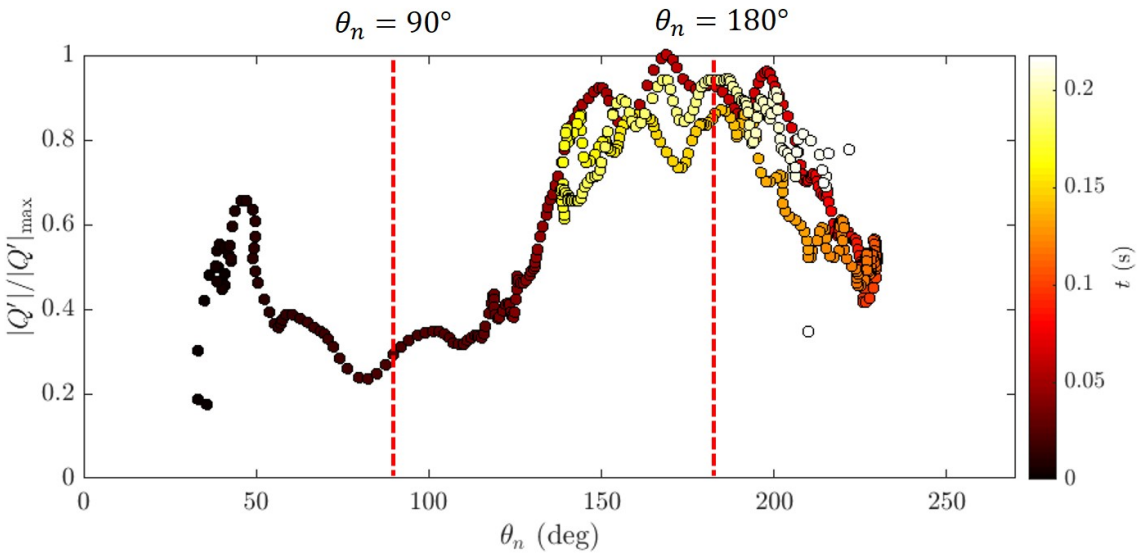

Figure 6.15: The normalized heat release fluctuation magnitude as a function of nodal line orientation. The color denotes sampling time.

represents the normalized heat release fluctuation magnitude as a function of nodal line orientation. First, the nodal line starts from 50°, increases up to 180°, and oscillates around 180°. An interesting point is the relationship between the nodal line orientation and the heat release fluctuation magnitude. It is obvious that when the nodal line is around 90°, the magnitude is minimized, and when the line is around 180°, the magnitude is maximized. Specifically, when the nodal line moves away from 180°, one can clearly see the decrease in the heat release fluctuation magnitude. This is because of the LOS effect.

Figure 6.16 shows the LOS effect when the nodal line is oriented at (a) 90° and (b) 180°. When the nodal line is in a vertical direction (Figure 6.16 (a)), the left and right sides of the heat release are oscillating out of phase to each other. Therefore, when the top half of the chemiluminescence image (the square dash box) is integrated, the left and right sides cancel out, resulting in a minimum magnitude. If it were a purely standing wave ($SR = 0$), then the integrated magnitude would be zero. The fact that the minimum magnitude in Figure 6.15 is not zero implies that the SR is not exactly zero, but close to it. In contrast, when the nodal line is in a horizontal direction (Figure 6.16 (b)), the left and right sides of the heat release are oscillating in phase, enhancing the integrated heat release magnitude.

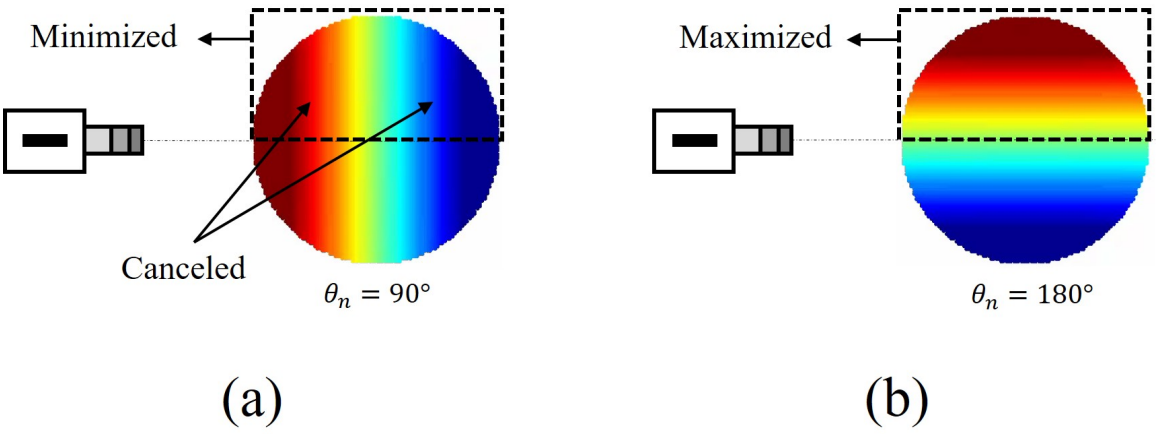

Figure 6.16: Line of sight effect. (a) Nodal line at 90°. (b) Nodal line at 180°.

Thus, the magnitude would be maximized.

A takeaway from these observations is that (i) acoustic pressure and heat release fluctuations are positively correlated, satisfying the Rayleigh criterion and (ii) orientation of (anti-) nodal line has an influence on not only pressure but also the heat release oscillations. Notice that we have observed the (anti-) nodal line oscillation in Figure 6.5 (a) and Figure 6.7. This observation was accomplished from the pressure measurements, which are independent of the chemiluminescence measurement. However, Figure 6.15 shows that chemiluminescence data also supports the oscillation of the (anti-) nodal line.

6.6 Discussion

It is worth emphasizing some common and different findings between this study and the previous works.

First, the dynamics of SR have been reported from several experimental studies. For example, SR exhibits not only standing and spinning waves but also bistable behavior depending on the operating conditions [81, 9, 79]. However, the dynamics of φ_{FG} have received little attention so far. This study experimentally demonstrates that φ_{FG} also has a bistable regime. In addition, when the mode switches from a standing to a spinning wave, φ_{FG} shifts by 180°. These behaviors must be taken into account when developing low

order models.

Second, Figure 6.9 (a) shows that as the mass flow rate increases, the magnitude increases smoothly, implying that the system is transitioning from stable to a limit cycle via a supercritical Hopf bifurcation. These observations can be captured by low order models using a flame describing function with a cubic nonlinearity [97, 100]. However, the transition from a standing to a spinning wave is not smooth, but rather abrupt, as shown in Figure 6.5 (d) and Figure 6.9 (b). This suggests that the transition occurs through a subcritical bifurcation, which requires higher-order nonlinearity. Hence, in order to capture this bistable behavior, one may need to include the terms higher than the cubic order.

Third, the azimuthal fuel staging effect has already been studied by Noiray et al. [97]. The study shows that for m^{th} azimuthal mode, only $2m$ component of the Fourier expansion of the describing function and the temperature field affects the dynamics nature of azimuthal modes. Since the first azimuthal mode appeared in this study, fuel configuration 1 corresponds to $2m$ component. This explains the reason that fuel configuration 1 has a major impact on pressure magnitude, but not configuration 2. However, the dependence of the Hopf bifurcation on the non-uniformity needs further investigation.

Last, Worth et al. [81] reconstructed similar phase portraits in SR and nodal line space. This results in CCW spiral trajectories around a standing wave attractor, which is in the opposite direction from those in this study. This discrepancy originates from the relationship between (anti-) nodal line and φ_{FG}. Note that the relationship in Equation 4.6 involves a minus sign. Therefore, if corresponding to the phase space, one would obtain similar portraits from [81] and this paper.

6.7 Effects of Other Parameters

The prior sections mainly focus on the total flow rates (or thermal power) and azimuthal non-uniformity effects on the instability magnitude and modal nature. This section briefly shows the other parameters effect such as PR or global equivalence ratio. A detailed anal-

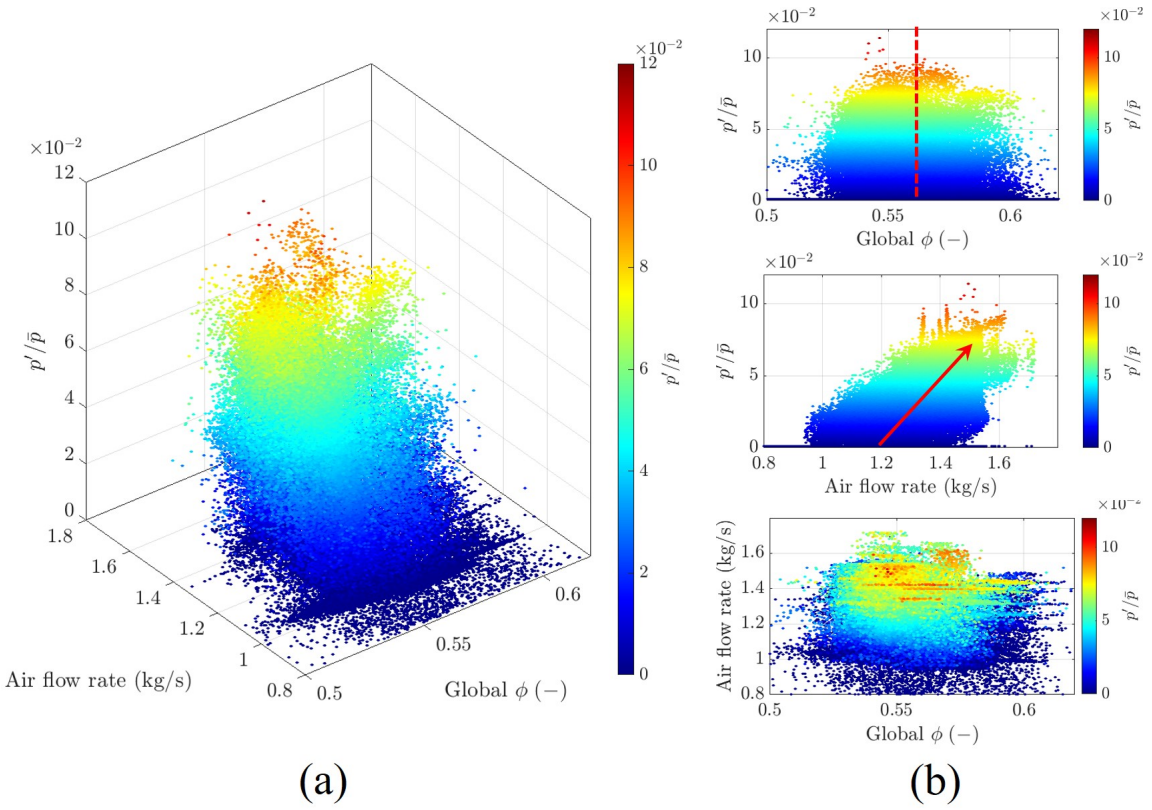

Figure 6.17: (a) Dependence of azimuthal instability magnitude in air flow rate and global equivalence ratio space. (b) Top, middle: side view. Bottom: top view. The color denotes the normalized instability magnitude.

ysis has not been conducted for these parameters, but the results shown in the section will provide a recommendation for future works. The total number of runs and data points we have collected are 64 and 88,752, respectively.

Figure 6.17 illustrates the dependence of azimuthal instability magnitude in air mass flow rate and global equivalence ratio (ϕ). Here, the magnitude is the anti-node magnitude normalized by static pressure. It should be noted that the magnitude is not just a function of air flow rate and global ϕ, but there are other parameters not shown here, i.e., PR and preheat temperature also have an influence on the magnitude. We have chosen the air flow rate and global ϕ to visualize the magnitude plot in three dimensional space.

The top of Figure 6.17 (b) is a side view of Figure 6.17 (a), representing the magnitude as a function of global ϕ. It is shown that the magnitude is maximized around global $\phi =$

0.552, and it decreases as the global ϕ moves away from this value. Although not analyzed in detail, this is presumably due to the variations in flame location, product temperature, and speed of sound. This nonlinear behavior is typical in combustion instabilities. Notice that even though global $\phi = 0.552$ may produce the maximum magnitude, there exist data points with low magnitudes ranging from 0 to 0.1. This implies that the global $\phi = 0.552$ is not a sufficient condition for the maximum magnitude, but there are other parameters that affect the magnitude. For example, the middle of Figure 6.17 (b) shows the instability magnitude as a function of air mass flow rate. it shows that the instability magnitude increases with air mass flow rate, implying that the flow rate is also a key parameter to produce the large instability magnitude. The bottom of Figure 6.17 (b) is the top view of Figure 6.17 (a). It represents that the maximum magnitude occurs at global $\phi = 0.552$ and air flow rate of 1.5 kg/s. Although not explored in this test matrix due to the flow rate limit, it is speculated that the magnitude would increase with a higher mass flow rate.

It is worth noting that even at the operating conditions of global $\phi = 0.552$ and air flow rate of 1.5 kg/s, there still exists data points with relatively low magnitudes. This implies the other hidden parameters affecting the magnitude. To illustrate this point, we have filtered the data point based on different ranges of PR, and plotted the instability magnitude in global ϕ and air flow rate space, similar to the bottom of Figure 6.17 (b), which is illustrated in Figure 6.18. The PR ranges from 0.06 to 0.14 with a step size of 0.01. The white dot indicates the normalized magnitude lower than a threshold, which is 0.01 in this case. The white dot tells us that we have explored those operating conditions, but the magnitude is negligible.

Figure 6.18 explicitly shows that even if the global ϕ and the air flow rate are 0.552 and 1.5 kg/s, respectively, the instability magnitude is still dependent on PR. Specifically, the maximum magnitude occurs at around $0.1 < PR < 0.11$, and when PR deviating from this range, the magnitude decreases, showing nonlinearities. This trend implies a potential strategy to mitigate combustion instability. In fact, utilizing the pilot flame has already

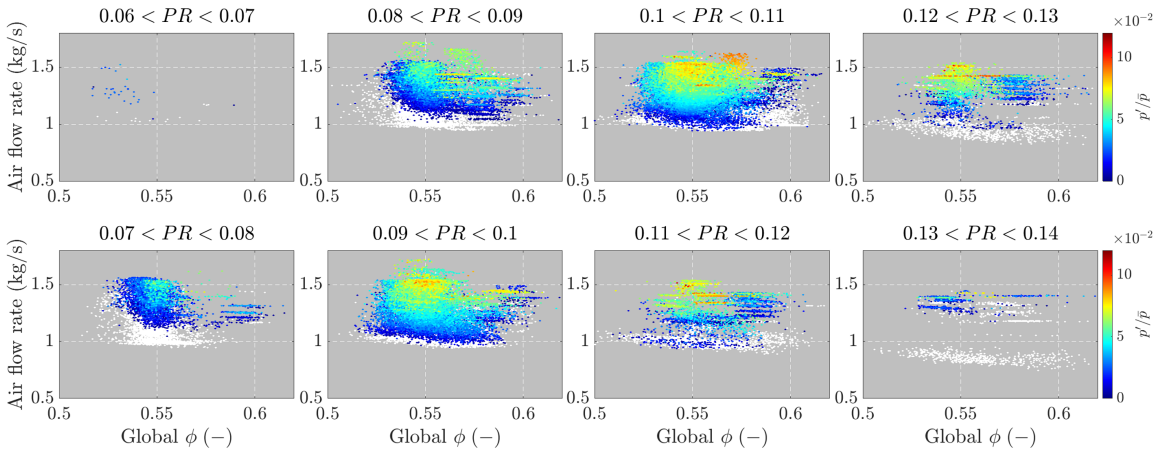

Figure 6.18: Dependence of azimuthal instability magnitude in global ϕ and air mass flow rate space, filtered by PR. The color denotes the normalized magnitude, and white dot represents the normalized magnitudes lower than 0.01.

been used to overcome the combustion instability problem in many applications [5, 3, 135, 136, 137]. However, the prior studies focus on the longitudinal instabilities, not azimuthal ones. To the best of the author's knowledge, Figure 6.18 would be the first report of pilot flame effect on azimuthal instability.

Figure 6.19 (a) represents the dependence of SR in PR and normalized instability magnitude, $p'/\bar{p}$, space. The two parameters, PR and $p'/\bar{p}$, have been selected because they shows a large influence on SR. For example, the top of Figure 6.19 (b) is a side view of Figure 6.19 (a), demonstrating the effect of $p'/\bar{p}$ on SR. It demonstrates that when $p'/\bar{p}$ is small, the SR is clustered around zero, indicating a quasi-periodic standing wave as shown in Figure 6.5 (a) and Figure 6.7 . When $p'/\bar{p}$ gets larger, the SR is distributed between ± 0.5, demonstrating intermittent regime. Further increase in $p'/\bar{p}$ results in SR being either ± 0.5 or zero. These trends are similar to Figure 6.9 (b) except that zero SR at high magnitudes was not observed in Figure 6.9 (b). This is presumably due to the other parameters not explicitly shown here. For example, section 7.3 proved that OR or the azimuthal non-uniformity delays the transition from a standing to a mixed wave. Moreover, although not analyzed here, other parameters such as preheat temperature may have an impact on SR.

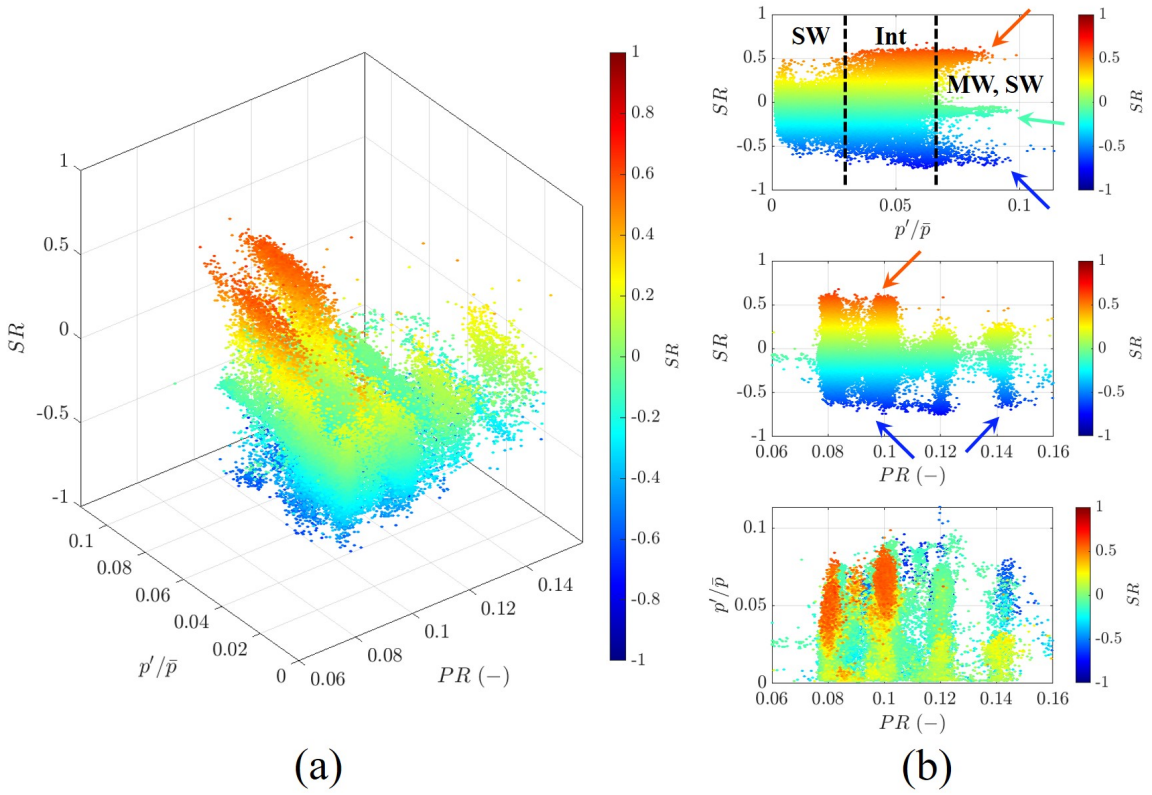

Figure 6.19: (a) Dependence of SR in PR and normalized instability magnitude space. (b) Top, middle: side view. Here, SW = standing wave, Int = intermittency, MW = mixed wave. Bottom: top view. The color denotes the SR.

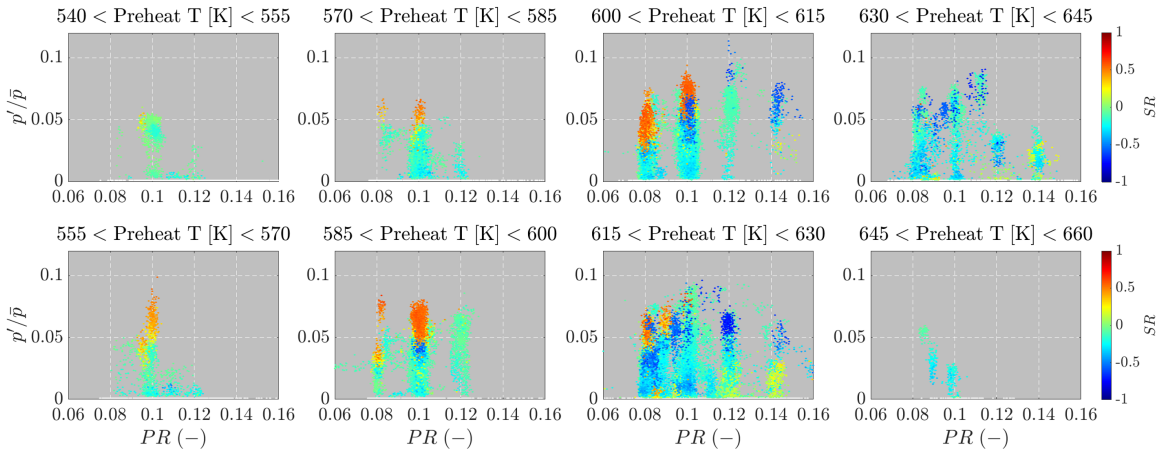

Figure 6.20: Dependence of SR in PR and $p'/\bar{p}$ space, filtered by preheat temperature. The color denotes the SR.

The middle of Figure 6.19 (b) illustrates the dependence of SR on PR. It shows that when the PR is relatively small (0.08 - 0.1), SR ranges between ± 0.5, indicating the azimuthal mode could be a standing or CW/CCW mixed wave depending on the other parameters not shown here. However, when the PR is large (0.12 - 0.14), only the standing and CW mixed wave show up. i.e., CCW mixed wave disappears at high PRs. This observation somewhat agrees with the relationship between the bulk swirl direction and the spinning direction [98]. When PR is high, relative fuel flows through the pilot nozzle increases, and thus, the spinning direction is dominated by the pilot nozzle's swirl direction, which is CW. When PR is low, spinning directions between the outer and pilot nozzles compete with each other, and the system may exhibit the standing or CW/CCW wave. To support this hypothesis, however, measurements of the overall flow field or the detailed CFD analysis need to be provided.

Figure 6.20 is a similar plot with Figure 6.19, but filtered by preheat temperature. The temperature ranges from 540 K to 660 K with a step size of 15 K. The figure shows that the instability magnitude is maximized at preheat temperature between 600 K and 630 K. Notice that the positive (or red) SR only appears around PR between 0.08 and 0.1 at some preheat temperature ranges, which is in agreement with the middle of Figure 6.19 (b). An

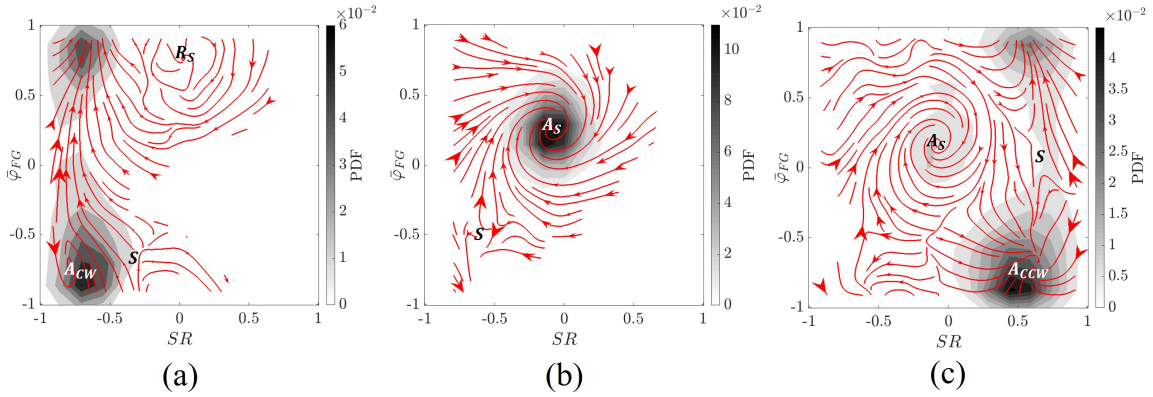

Figure 6.21: Phase portraits for (a) CCW, (b) SW, and (c) CW dominant system.

interesting observation from this figure is the SR change with the increase in temperature. In particular, if focusing on the positive (red) and negative (blue) SR only, one can see that when the preheat temperature is low, the SR is relatively positive (or CCW mixed wave), but it gradually shifts to negative (or CW mixed wave) at higher preheat temperature. This is evident in the preheat temperature ranges of 600 K - 615 K (red dominated) and 615 K - 630 K (blue dominated). This implies the potential impact of preheat temperature on the azimuthal spinning direction. We hypothesize that increasing the preheat temperature alters the dominant bulk swirl direction, but to support this, the flow field measurements or CFD analysis must be provided.

We close this section by introducing representative phase portraits for CW/CCW, and SW dominant system with a large instability magnitude ($p'/\bar{p} \approx 0.08$). Figure 6.21 illustrates each case, and Table 6.2 summarizes each operating condition. Notice that the overall structure of the phase portraits resembles those in Figure 6.6. This similarity demonstrates that even though the operating conditions are different, the overall phase portrait structure remains the same.

6.8 Conclusion

In this chapter, the modal dynamics of azimuthal thermoacoustic instability have been experimentally investigated. Multiple pressure sensors were installed at distinct azimuthal

Table 6.2: Operating conditions for each case in Figure 6.21.

	Figure 6.21 (a)	Figure 6.21 (b)	Figure 6.21 (c)
Δt (s)	30	30	30
Preheat temp. (K)	630	626	606
Global ϕ	0.557	0.576	0.545
PR	0.11	0.11	0.1
OR	0.5	0.487	0.5
Air flow rate (kg/s)	1.343	1.582	1.532
$p'/\hat{p}$	0.088	0.087	0.081
Dominant mode	CW	SW	CCW

locations to extract the CW and CCW wave components from the measurements. The tests were conducted at various mass flow rates with different azimuthal fuel staging, quantified by an outer ratio (OR). No matter what the OR was, the instability amplitude monotonically increased with mass flow rate, but for a uniform fuel staging case, the mode transitioned from standing, intermittent regime, to spinning waves. The phase difference between CW and CCW waves also showed the switching behavior at the bistable regime. The dynamics of spin ratio (SR) and the phase difference (φ_{FG}) were well described in a phase averaged portrait, showing multiple attractors and saddle points. For the non-uniform fuel staging cases, only the standing wave was observed while sweeping the flow rates. In addition, the amplitude was relatively lower than the uniform staging case, and the onset of the instability showed a non-monotonic relationship with the outer ratio. Specifically, a sufficiently high OR delayed the onset of the instability. These observations suggest potential mechanisms to mitigate and/or suppress the instability level in the gas turbines.

CHAPTER 7

LOW ORDER MODELING OF AZIMUTHAL MODE INSTABILITY

7.1 Introduction

As seen in the previous chapter, the azimuthal instabilities in can combustors exhibit a variety of behaviors - including standing, spinning, mixed waves, and intermittent behaviors, as well as periodic limit cycles and quasi-periodic oscillations – depending upon varying power and azimuthal symmetry. Similar behaviors were also observed in annular combustors. For example, experimental studies have reported standing, spinning, and mixed waves depending on the operating conditions such as equivalence ratio [81, 90], wall temperature [89], swirl intensity [93], fuel staging [4], and nozzle geometry [9, 79]. Numerical studies have reported similar behaviors of different azimuthal modes [72, 132, 65, 138, 87].

Based on these observations, numerous studies have proposed models to capture the physics controlling which type of mode is present and its amplitude. These are nonlinear models, as linear models can allow for any arbitrary superposition of disturbances. For example, Equation 7.1 represents general two coupled second order harmonic oscillators.

$$\begin{aligned} \ddot{\eta}_1 + \alpha_1 \dot{\eta}_1 + \omega_1^2 \eta_1 &= f_{NL,1}(\eta_1, \eta_2, \dot{\eta}_1, \dot{\eta}_2) \\ \ddot{\eta}_2 + \alpha_2 \dot{\eta}_2 + \omega_2^2 \eta_2 &= f_{NL,2}(\eta_1, \eta_2, \dot{\eta}_1, \dot{\eta}_2) \end{aligned} \tag{7.1}$$

Here, $\eta_1(t)$ and $\eta_2(t)$ describe the time varying amplitudes of two eigenmodes that are coupled through the nonlinear terms on the RHS. Both eigenmodes are linearly stable when the linear damping terms, $\alpha_{1,2}$, are positive, i.e., any perturbation to the system decays to zero. When either of the linear damping terms is negative, the system is linearly unstable. For a single oscillator, the disturbance amplitudes exponentially grow in time until

they saturate to a limit cycle through the nonlinear terms. Similar behavior can occur for multiple modes, but other behaviors are also possible. For example, even though both eigenmodes are linearly unstable, they do not necessarily coexist at the limit cycle - one eigenmode can completely suppress the other, referred to as "quenching" [139]. This interaction/competition between two eigenmodes is a typical feature of nonlinear systems. For instance, when $\omega_1 = \omega_2$ and $\alpha_1 = \alpha_2 < 0$ in Equation 7.1, a nonlinearity of the form, $f_{NL,1} = -(a\eta_1^2 + \eta_2^2)\dot{\eta}_1$ and $f_{NL,2} = -(a\eta_2^2 + \eta_1^2)\dot{\eta}_2$, allows both modes to co-exist at the limit cycle for $a > 1$, while one mode drives the other to zero if $a < 1$.

Returning to the modeling of azimuthal modes, the azimuthal eigenmodes can be posed in two equivalent ways: (1) as the nonlinear interaction and possibly competition between two standing eigenmodes (e.g., $\cos(m\theta)$ and $\sin(m\theta)$, where m is the azimuthal wavenumber), or, equivalently, (2) as the interaction/competition between two counter-rotating eigenmodes (e.g., $\exp(im\theta)$ and $\exp(-im\theta)$). Depending on the choice of eigenmode pairs as well as the form of nonlinearity, both eigenmodes can coexist or one mode suppresses the other. In addition, the associated eigenvalues could be identical (degenerate) or different (non-degenerate) from each other, depending on the problem setup. For example, two standing waves could be non-degenerate through azimuthal non-uniformities in the system [97], while for two spinning waves, bulk azimuthal flow is a source of non-degeneracy [98].

The nonlinear interactions between these two azimuthal eigenmodes appear to first have been treated by Schuermans et al. [94], who considered a nominally axisymmetric system with degenerate eigenmodes. They examined the nonlinear interaction of two orthogonal standing modes of an azimuthal instability and showed that, when the system is linearly unstable, it evolves to a limit cycle where both standing modes coexist because of their degeneracy. The combination of two standing eigenmodes results in a single spinning wave, which could rotate in either the CW or CCW direction. The direction of the spinning wave is solely a function of initial conditions. Hummel et al. [96, 140] investigated a

similar problem, posing it in the form of two counter-rotating eigenmodes, considering a nominally axisymmetric system, but allowing for non-degeneracy in the forms of different frequencies and/or growth rates of the CW and CCW waves. Similar to Schuermans's work, they showed that only spinning waves are present at limit cycle conditions, but also showed that non-degeneracy causes one spinning mode to be more probable than the other spinning mode. To summarize, these studies point to the fact that the nominally axisymmetric system shows only spinning wave dominant behavior at the limit cycle and, thus, do not capture the fact that standing wave can also be present.

Noting this point, several studies have included the presence of non-uniformities into their models. Such non-uniformities can exist in geometry, flow, or flame, such as due to azimuthal variations in fuel-air ratio, swirl directions of individual nozzles, or a discrete number of nozzles distributed azimuthally. Noiray et al. [97] analyzed a non-degenerate combustor system due to non-uniform flame-acoustic coupling and mean temperature distributions, and showed that two standing modes could coexist for weak non-uniformities, resulting in a spinning or mixed wave. For sufficiently large non-uniformities, only one standing mode survives. Which standing mode appears depends on the shape of non-uniformities. Later, Bauerheim et al. [98] considered a system with non-degeneracy due to non-uniformities as well as azimuthal bulk flow, and showed that non-uniformities promote standing waves, while azimuthal flow promotes spinning waves. A mixed wave could exist when both non-uniformities and azimuthal flow are present. Ghirardo et al. [99] considered a problem with degenerate eigenmodes and identical flames, so that the azimuthal variation was due to the presence of discrete nozzles located azimuthally, and similarly showed co-existing standing/spinning waves, whose relative strengths were a function of nozzle spacing.

As noted earlier, experiments show the presence of erratic switching between standing and spinning waves at a fixed "steady-state" operational point. This switching may occur in three ways. First, consider the case where the deterministic model possesses one stable

attractor associated with either standing or spinning wave. In this case, background noise perturbs the system continuously, allowing it to visit other points in the phase space, such as repelling or saddle point solutions. In this case, the joint PDF of amplitudes of two eigenmodes exhibits a unimodal distribution, roughly centered at the stable FP. This type of model was first studied by Noiray and Schuermans [100], who introduced background noise effects by including stochastic additive forcing into their model. They showed that how stochastic forcing manifests itself in a unimodal joint PDF of two standing mode amplitudes, which could be centered around standing or spinning wave-dominant behaviors, depending on the level of azimuthal non-uniformity. Second, the deterministic model could have multiple attractors. In the deterministic case, the system will remain on one attractor, based upon initial conditions. However, with sufficient noise levels, the system can travel between these multiple attractors. The joint PDF in this case exhibits multiple peaks in the distribution, associated with the different stable attractors [81, 9, 79]. For example, Faure-Beaulieu et al. [82] developed a background noise driven model with non-uniform flame describing function, and found that the system can switch between two stable CCW/CW spinning attractors with a sufficient level of turbulent noise intensity. Similarly, Ghirardo and Juniper [103] developed a deterministic model that incorporated sensitivity of heat release to transverse velocity oscillations, and showed that the standing and spinning waves could be bistable at a fixed operating point, and thus, the system could intermittently switch between them due to background noise. Thirdly, parametric noise can qualitatively change system dynamics, stabilizing or destabilizing attractors for sufficient parametric noise. For instance, Bothein et al. [102] noted that the preference of standing or spinning wave is very sensitive to azimuthal flame temperature non-uniformity. Thus, the parametric noise would be expected to lead to intermittency between standing and spinning waves at a fixed operating condition. In any of these cases, it is clear that the inherent background noise that is present in combustion systems plays an important role in the system's dynamics.

Another interesting point about azimuthal modes is the behavior of the nodal line during

the limit cycle. As noted earlier, in a system with azimuthal symmetry, there is no reason for the nodal line to remain fixed during azimuthal mode oscillations, in contrast to axial/radial mode oscillations. For example, LESs have shown that the nodal line of the standing wave slowly rotates at a mean swirl velocity [72, 132]. Similarly, the experimental study by Vignat et al. [141] reported the nodal line moving in a seemingly random fashion. However, the system's non-uniformities can fix the nodal line at a certain azimuthal location as shown in the experiments [89] as well as reduced order models [82, 104].

In addition, the deterministic motion of the nodal line has been observed. Experimental studies from Worth et al. [81] showed that the nodal line periodically oscillates around a fixed azimuthal location with a slow time scale (referred to as quasi-periodic standing wave hereafter). In other words, the nodal line's average location appeared to be fixed, but it did oscillate about this point in an approximately sinusoidal, coherent fashion; i.e., not randomly. These oscillations lead to modulations in pressure amplitude measured at a fixed azimuthal position. To the best of the author's knowledge, none of the low order models captures these observations. We show in this chapter that this behavior is the manifestation of quasi-periodic oscillations, associated with two closely spaced frequencies, and is a strong function of linear growth/damping rate and azimuthal non-uniformities.

We note in closing an additional point around modeling nonlinear systems with two closely spaced frequencies, which introduce an additional slow time scale, $1/(\omega_1 - \omega_2)$, and, therefore additional terms when applying the method of averaging techniques for nonlinear oscillator dynamics. These additional terms have not been applied in most studies of nonlinear azimuthal modal dynamics [97, 96, 100], but as noted by Acharya et al. [142], they can incorporate additional sensitivities to frequency spacing, as well as influence limit cycle amplitudes and their stability. In extending this work to noise driven systems, John et al. [143] similarly noted how these additional slow time scale terms led to drift in phase-space trajectories.

To summarize the findings of reduced order models, azimuthal modes exhibit a purely

spinning wave during the limit cycle if the system is axisymmetric. The spinning direction depends on initial conditions, but non-degeneracy causes the system to prefer one direction over the other. In systems with azimuthal non-uniformity, the system may show a mixed or standing wave, and the orientation of the nodal line relies on the shape of the non-uniformity. Lastly, background noise may responsible for switching between standing and spinning waves.

While previous models capture some of the aforementioned effects, the main contribution of this chapter is to present a comprehensive framework that includes all of the effects, as well as the additional slow time scale interactions associated with two closely spaced frequencies.

7.2 Mathematical Formulation

This section derives the governing equations that describe the azimuthal modal dynamics. This approach closely follows the procedure used in prior studies – namely, assuming linear acoustics with nonlinear source terms, using a Galerkin expansion to decompose the nonlinear partial differential equation into a system of nonlinear, coupled ordinary differential equations [97, 96, 100]. The resulting equations are then temporally averaged over the fast acoustic time scale, following the Krylov-Bogoliubov method [144], leaving nonlinear coupled equations for the slow time scale evolution of the disturbance amplitude and phase difference. The key contribution of this section is incorporating all the effects noted into Introduction in a rigorous, unified fashion.

7.2.1 Governing equations

This subsection briefly summarizes the development of the stochastic, nonlinear wave equation, presented below, closely following prior studies, [97, 145].

$$\frac{\partial^2 p}{\partial t^2} - \frac{c^2}{R^2}\frac{\partial^2 p}{\partial \theta^2} = h_1\left(p, \frac{dp}{dt}\right) + \xi_1(t) + h_2\left(p, \frac{dp}{dt}\right)\xi_2(t) \tag{7.2}$$

Here, p is the acoustic pressure, c the sound speed, R the chamber radius, ξ_1 an additive background noise term, ξ_2 a parametric noise term, and $h_{1,2}$ represent all other source/sink and wave propagation terms due to unsteady heat release, temperature non-uniformity, bulk flow effects, and nonlinearities [145]. Notice that the wave equation has been spatially integrated into the axial and radial directions, and that mean flow, density gradient, and losses at boundaries are encapsulated in these general functions, $h_{1,2}(p, dp/dt)$.

Note that the solutions of the homogeneous wave equation, given by:

$$p(\theta, t) = \sum_{n=1}^{\infty} [\eta_{1,n} \cos(n\theta) + \eta_{2,n} \sin(n\theta)] \tag{7.3}$$

constitute a complete, orthogonal set of basis functions. As such, the essence of the Galerkin method is to use these basis functions for writing the solution of the more general, nonlinear Equation 7.2. There is no approximation when the infinite summation is retained, but truncation necessarily introduces approximations. We will truncate this summation as a single mode that nonlinearly interacts with itself. Nonlinear interactions between multiple modes are essential to include for cases where gas dynamical nonlinearities are important, but these types of nonlinearities are negligible in the "low" acoustic amplitudes typically observed in lean premixed systems (e.g., Figure 6.9 (a) shows $(F + G)/\bar{p}$ levels of maximum 8%) [145, 146]. Furthermore, the heat release nonlinearities, which generally dominate nonlinear effects in lean premixed systems, lead to strong self-interactions of a mode with itself [147, 148, 149]. Thus, we shall approximate the acoustic pressure associated with a given n^{th} eigenmode as [97]

$$p(\theta, t) \approx \eta_1 \cos(m\theta) + \eta_2 \sin(m\theta)] \tag{7.4}$$

where η_1 and η_2 are the amplitudes of two orthogonal standing modes of azimuthal wavenumber, m. The subscript, m, in η has been omitted here.

Next, we can treat the function $h_1(p, dp/dt)$ in Equation 7.2 quite generally by expand-

ing it as a Taylor series [150] truncated at fourth order:

$$\begin{aligned} h_1\left(p, \frac{dp}{dt}\right) =& B_{00}(\theta) + B_{10}(\theta)p + B_{01}(\theta)\dot{p} + B_{20}(\theta)p^2 + B_{11}(\theta)p\dot{p} + B_{02}(\theta)\dot{p}^2 \\ &+ B_{30}(\theta)p^3 + B_{21}(\theta)p^2\dot{p} + B_{12}(\theta)p\dot{p}^2 + B_{03}(\theta)\dot{p}^3 + B_{40}(\theta)p^4 \\ &+ B_{31}(\theta)p^3\dot{p} + B_{22}(\theta)p^2\dot{p}^2 + B_{13}(\theta)p\dot{p}^3 + B_{04}(\theta)\dot{p}^4 \end{aligned} \tag{7.5}$$

where $\dot{p}$ is the time derivative of p, and B_{ij}'s are coefficients of $p^i\dot{p}^j$. Note that in previous studies, $h_1(p, \dot{p})$ was often considered as the time derivative of heat release fluctuation, $d\dot{Q}/dt$, where $\dot{Q}(p)$ is a function of pressure only [97, 96]. This approach, however, cannot capture some of the terms in Equation 7.5 (e.g., $B_{10}p$ and $B_{12}p\dot{p}^2$) that will be shown to introduce important qualitative features in the modal dynamics. The coefficients B_{ij} are non-time varying but can vary azimuthally; physically this would occur because of discrete nozzle locations, azimuthally non-uniform temperature distribution, azimuthally non-uniform thermo-acoustic coupling strength, etc. In order to account for this in a general fashion, we write them as the following series:

$$\begin{aligned} B_{01}(\theta) &= -\alpha + \underbrace{\beta\left(1 + \sum_{n=1}^{\infty} C_{n,01}\cos(n\theta) + \sum_{n=1}^{\infty} S_{n,01}\sin(n\theta)\right)}_{=\beta_0(\theta)} \\ B_{ij}(\theta) &= b_{ij}\left(1 + \sum_{n=1}^{\infty} C_{n,ij}\cos(n\theta) + \sum_{n=1}^{\infty} S_{n,ij}\sin(n\theta)\right) \text{ for } i \neq 0, j \neq 0 \end{aligned} \tag{7.6}$$

Although not necessary, it is convenient to decompose the linear growth/damping term, B_{01}, into a linear damping term, α, which is not dependent on θ, and the linear growth term, $\beta_0(\theta)$, which is a function of θ [97].

We next follow the standard steps in the Galerkin expansion approach - substitute Equation 7.4, Equation 7.5, and Equation 7.6 into Equation 7.2, multiply both sides by $\cos(m\theta)$

or $\sin(m\theta)$, and integrate these equations from 0 to 2π with respect to θ, producing two sets of second order differential equations,

$$\begin{aligned}\ddot{\eta}_1 + \left[\alpha - \beta\left(1 + \frac{C_{2m,01}}{2}\right)\right]\dot{\eta}_1 + \omega_1^2\eta_1 &= f_1(\eta_1, \eta_2, \dot{\eta}_1, \dot{\eta}_2) \\ \ddot{\eta}_2 + \left[\alpha - \beta\left(1 - \frac{C_{2m,01}}{2}\right)\right]\dot{\eta}_2 + \omega_2^2\eta_2 &= f_2(\eta_1, \eta_2, \dot{\eta}_1, \dot{\eta}_2)\end{aligned} \tag{7.7}$$

where

$$\begin{aligned}f_1(\eta_1, \eta_2, \dot{\eta}_1, \dot{\eta}_2) =& \frac{\beta}{2}S_{2m,01}\dot{\eta}_2 + \frac{b_{10}}{2}S_{2m,10}\eta_2 + \\ & \frac{b_{30}}{8}\begin{bmatrix}(6 + 4C_{2m,30} + C_{4m,30})\eta_1^3 + 3(2 - C_{4m,30})\eta_1\eta_2^2 + \\ 3(2S_{2m,30} + S_{4m,30})\eta_1^2\eta_2 + (2S_{2m,30} - S_{4m,30})\eta_2^3]\end{bmatrix} + \\ & \frac{b_{21}}{8}\begin{bmatrix}(6 + 4C_{2m,21} + C_{4m,21})\eta_1^2\dot{\eta}_1 + (2 - C_{4m,21})(\eta_2^2\dot{\eta}_1 + 2\eta_1\eta_2\dot{\eta}_2) + \\ (2S_{2m,21} - S_{4m,21})\eta_2^2\dot{\eta}_2 + (2S_{2m,21} + S_{4m,21})(\eta_1^2\dot{\eta}_2 + 2\eta_1\eta_2\dot{\eta}_1)\end{bmatrix} + \\ & \frac{b_{12}}{8}\begin{bmatrix}(6 + 4C_{2m,12} + C_{4m,12})\eta_1\dot{\eta}_1^2 + (2 - C_{4m,12})(\eta_1\dot{\eta}_2^2 + 2\eta_2\dot{\eta}_1\dot{\eta}_2) + \\ (2S_{2m,12} - S_{4m,12})\eta_2\dot{\eta}_2^2 + (2S_{2m,12} + S_{4m,12})(\eta_2\dot{\eta}_1^2 + 2\eta_1\dot{\eta}_1\dot{\eta}_2)\end{bmatrix} + \\ & \frac{b_{03}}{8}\begin{bmatrix}(6 + 4C_{2m,03} + C_{4m,03})\dot{\eta}_1^3 + 3(2 - C_{4m,03})\dot{\eta}_1\dot{\eta}_2^2 + \\ 3(2S_{2m,03} + S_{4m,03})\dot{\eta}_1^2\dot{\eta}_2 + (2S_{2m,03} - S_{4m,03})\dot{\eta}_2^3\end{bmatrix} + \\ & + \zeta + \int_0^{2\pi} h_2(\eta_1, \eta_2, \dot{\eta}_1, \dot{\eta}_2)\sin(n\theta)\xi_2 d\theta,\end{aligned} \tag{7.8}$$

$$
\begin{aligned}
f_2(\eta_1,\eta_2,\dot{\eta}_1,\dot{\eta}_2) =& \frac{\beta}{2}S_{2m,01}\dot{\eta}_1 + \frac{b_{10}}{2}S_{2m,10}\eta_1 + \\
& \frac{b_{30}}{8}\begin{bmatrix}(6-4C_{2m,30}+C_{4m,30})\eta_2^3+3(2-C_{4m,30})\eta_2\eta_1^2+\\ 3(2S_{2m,30}-S_{4m,30})\eta_2^2\eta_1+(2S_{2m,30}+S_{4m,30})\eta_1^3]\end{bmatrix} + \\
& \frac{b_{21}}{8}\begin{bmatrix}(6-4C_{2m,21}+C_{4m,21})\eta_2^2\dot{\eta}_2+(2-C_{4m,21})(\eta_1^2\dot{\eta}_2+2\eta_1\eta_2\dot{\eta}_1)+\\ (2S_{2m,21}+S_{4m,21})\eta_1^2\dot{\eta}_1+(2S_{2m,21}-S_{4m,21})(\eta_2^2\dot{\eta}_1+2\eta_1\eta_2\dot{\eta}_2)\end{bmatrix} + \\
& \frac{b_{12}}{8}\begin{bmatrix}(6-4C_{2m,12}+C_{4m,12})\eta_2\dot{\eta}_2^2+(2-C_{4m,12})(\eta_2\dot{\eta}_1^2+2\eta_1\dot{\eta}_1\dot{\eta}_2)+\\ (2S_{2m,12}+S_{4m,12})\eta_1\dot{\eta}_1^2+(2S_{2m,12}-S_{4m,12})(\eta_1\dot{\eta}_2^2+2\eta_2\dot{\eta}_1\dot{\eta}_2)\end{bmatrix} + \\
& \frac{b_{03}}{8}\begin{bmatrix}(6-4C_{2m,03}+C_{4m,03})\dot{\eta}_2^3+3(2-C_{4m,03})\dot{\eta}_2\dot{\eta}_1^2+\\ 3(2S_{2m,03}-S_{4m,03})\dot{\eta}_2^2\dot{\eta}_1+(2S_{2m,03}+S_{4m,03})\dot{\eta}_1^3\end{bmatrix} + \\
& + \zeta + \int_0^{2\pi} h_2(\eta_1,\eta_2,\dot{\eta}_1,\dot{\eta}_2)\cos(n\theta)\xi_2 d\theta.
\end{aligned}
\tag{7.9}
$$

Here,

$$
\omega = mc/R,\ \ \omega_1^2 = \omega^2 - b_{10}(1+C_{2m,10}/2),\ \ \omega_2^2 = \omega^2 - b_{10}(1-C_{2m,10}/2) \tag{7.10}
$$

and $\zeta(t)$ is a spatially averaged additive noise source. Equation 7.7 describes the second order harmonic oscillators of two orthogonal standing eigenmodes coupled through the source terms. Note that even order nonlinearities (e.g., terms multiplied by b_{20}, b_{11}, and b_{40}, etc) are eliminated during the spatial averaging , i.e., only the odd order terms survive [96]. Similarly, azimuthal non-uniformity terms higher than $4m$ order are averaged out, and only $2m$ and $4m$ terms have an impact on the dynamics [97]. For the first azimuthal mode ($n = 1$), for example, only terms multiplied by C_2, S_2, C_4, and S_4 remain. Moreover, the C_8 and S_8 terms, which would be nonzero for the eight outer nozzle configuration used in this experimental facility, average out. This is due to the truncation at fourth order in

Equation 7.5, e.g., if truncated at sixth order, Equation 7.8 and Equation 7.9 would contain the non-uniformity terms up to $6n$.

Consider the effects of non-uniformity on two oscillators. By comparing Equation 7.7 with Equation 7.1, one can see that the term, $\alpha - \beta(1 \pm C_{2m,01}/2)$, determines the linear stability of each oscillator. Specifically, when $C_{2m,01} = 0$, two oscillators have identical linear growth/damping rates. i.e., they are both linearly stable or unstable. However, when $C_{2m,01} \neq 0$, their linear growth/damping rate would be different. For instance, one oscillator could be linearly unstable while the other is stable. In addition, Equation 7.10 shows that $C_{2m,10}$ influences the natural frequencies of the two oscillators and, consequently, controls whether the natural frequencies of the two eigenmodes are identical or different. For example, when $C_{2m,10} > 0$ and $b_{10} < 0$, the natural frequency of η_1 is greater than that of η_2.

7.2.2 Averaged equations

Given the fact that $\eta(t)$ is oscillating harmonically with a temporally varying amplitude and phase, it is convenient to utilize a Van der Pol decomposition to rewrite the temporal dynamics, $\eta(t)$ [151].

$$\begin{aligned} \eta_1(t) &= A(t)\cos(\omega_1 t + \phi_A(t)) = A(t)\cos(\bar{\omega}t + \varphi_A(t)) \\ \eta_2(t) &= B(t)\cos(\omega_2 t + \phi_B(t)) = B(t)\cos(\bar{\omega}t + \varphi_B(t)) \end{aligned} \tag{7.11}$$

where

$$\begin{aligned} \bar{\omega} = \frac{1}{2}(\omega_1 + \omega_2), \quad \Delta\omega = \omega_2 - \omega_1 \\ \varphi_A(t) = \phi_A(t) - \frac{1}{2}\Delta\omega t, \quad \varphi_B(t) = \phi_B(t) + \frac{1}{2}\Delta\omega t \end{aligned} \tag{7.12}$$

We assume that the characteristic time scales over which the amplitudes and phase (A, B and ϕ, respectively) vary are much slower than the acoustic time scale, i.e., $\tau_{A,B,\varphi} >> 1/\omega$. Assuming ζ in Equation 7.8 and Equation 7.9 is Gaussian white noise, one can perform

deterministic and stochastic averaging [144, 152, 153, 154] to produce the following first order differential equations for the slowly varying amplitudes and phase:

$$\frac{dA}{d\tilde{t}} = \frac{1}{4}\big[\tilde{\beta}(2 + C_{2,01} - 2\tilde{\alpha})\big]A - \left[\frac{\tilde{b}_{10}S_{2,10}\sin\varphi}{2(\Delta-2)} + \frac{\tilde{b}_{01}}{4}S_{2,01}\cos\varphi\left(\frac{\Delta+2}{\Delta-2}\right)\right]B$$
$$+ \left[\frac{\tilde{b}_{21}}{64}(6 + 4C_{2,21} + C_{4,21}) + \frac{3\tilde{b}_{03}}{256}(\Delta-2)^2(6 + 4C_{2,03} + C_{4,03})\right]A^3$$
$$- \left[\begin{array}{c} \frac{3\tilde{b}_{30}\sin\varphi}{32(\Delta-2)}(2S_{2,30} + S_{4,30}) - \frac{\tilde{b}_{21}}{64}\cos\varphi\big(\frac{\Delta-6}{\Delta-2}\big)(2S_{2,21} + S_{4,21}) + \\ \frac{\tilde{b}_{12}}{128}\sin\varphi(5\Delta-2)(2S_{2,12} + S_{4,12}) + \frac{9\tilde{b}_{03}}{256}\cos\varphi(\Delta^2-4)(2S_{2,03} + S_{4,03}) \end{array}\right]A^2B$$
$$- \left[\begin{array}{c} \frac{3\tilde{b}_{30}\sin 2\varphi}{32(\Delta-2)}(2 - C_{4,30}) - \frac{\tilde{b}_{21}}{64}\big(2 - \big(\frac{3\Delta+2}{\Delta-2}\big)\cos 2\varphi\big)(2 - C_{4,21}) - \\ \frac{\tilde{b}_{12}}{128}\sin 2\varphi(\Delta+2)\big(\frac{3\Delta-2}{\Delta-2}\big)(2 - C_{4,12}) - \frac{3\tilde{b}_{03}}{256}(2 + \cos 2\varphi)(\Delta+2)^2(2 - C_{4,03}) \end{array}\right]AB^2$$
$$- \left[\begin{array}{c} \frac{3\tilde{b}_{30}\sin\varphi}{32(\Delta-2)}(2S_{2,30} - S_{4,30}) + \frac{\tilde{b}_{21}}{64}\cos\varphi\big(\frac{\Delta+2}{\Delta-2}\big)(2S_{2,21} - S_{4,21}) + \\ \frac{\tilde{b}_{12}}{128}\sin\varphi\big(\frac{(\Delta+2)^2}{\Delta-2}\big)(2S_{2,12} - S_{4,12}) + \frac{3\tilde{b}_{03}}{256}\cos\varphi\big(\frac{(\Delta+2)^3}{\Delta-2}\big)(2S_{2,03} - S_{4,03}) \end{array}\right]B^3$$
$$+ \frac{\Gamma}{4\bar{\omega}^3 A} + \frac{\zeta_A}{\bar{\omega}}$$

$$\frac{dB}{d\tilde{t}} = \frac{1}{4}\big[\tilde{\beta}(2 - C_{2,01} - 2\tilde{\alpha})\big]B - \left[\frac{\tilde{b}_{10}S_{2,10}\sin\varphi}{2(\Delta+2)} + \frac{\tilde{b}_{01}}{4}S_{2,01}\cos\varphi\left(\frac{\Delta+-2}{\Delta+2}\right)\right]A$$
$$+ \left[\frac{\tilde{b}_{21}}{64}(6 - 4C_{2,21} + C_{4,21}) + \frac{3\tilde{b}_{03}}{256}(\Delta+2)^2(6 - 4C_{2,03} + C_{4,03})\right]B^3$$
$$- \left[\begin{array}{c} \frac{3\tilde{b}_{30}\sin\varphi}{32(\Delta+2)}(2S_{2,30} - S_{4,30}) - \frac{\tilde{b}_{21}}{64}\cos\varphi\big(\frac{\Delta+6}{\Delta+2}\big)(2S_{2,21} - S_{4,21}) + \\ \frac{\tilde{b}_{12}}{128}\sin\varphi(5\Delta+2)(2S_{2,12} - S_{4,12}) + \frac{9\tilde{b}_{03}}{256}\cos\varphi(\Delta^2-4)(2S_{2,03} - S_{4,03}) \end{array}\right]B^2A$$
$$- \left[\begin{array}{c} \frac{3\tilde{b}_{30}\sin 2\varphi}{32(\Delta+2)}(2 - C_{4,30}) - \frac{\tilde{b}_{21}}{64}\big(2 - \big(\frac{3\Delta-2}{\Delta+2}\big)\cos 2\varphi\big)(2 - C_{4,21}) - \\ \frac{\tilde{b}_{12}}{128}\sin 2\varphi(\Delta-2)\big(\frac{3\Delta+2}{\Delta+2}\big)(2 - C_{4,12}) - \frac{3\tilde{b}_{03}}{256}(2 + \cos 2\varphi)(\Delta-2)^2(2 - C_{4,03}) \end{array}\right]BA^2$$
$$- \left[\begin{array}{c} \frac{3\tilde{b}_{30}\sin\varphi}{32(\Delta+2)}(2S_{2,30} + S_{4,30}) + \frac{\tilde{b}_{21}}{64}\cos\varphi\big(\frac{\Delta-2}{\Delta+2}\big)(2S_{2,21} + S_{4,21}) + \\ \frac{\tilde{b}_{12}}{128}\sin\varphi\big(\frac{(\Delta-2)^2}{\Delta+2}\big)(2S_{2,12} + S_{4,12}) + \frac{3\tilde{b}_{03}}{256}\cos\varphi\big(\frac{(\Delta-2)^3}{\Delta+2}\big)(2S_{2,03} + S_{4,03}) \end{array}\right]A^3$$
$$+ \frac{\Gamma}{4\bar{\omega}^3 B} + \frac{\zeta_B}{\bar{\omega}}$$

(continued on next page)

$$
\begin{aligned}
\frac{d\varphi}{d\tilde{t}} &= \Delta - \frac{3\tilde{b}_{30}}{32(\Delta^2-4)}\begin{bmatrix}\big((10+4C_{2,30}-C_{4,30})\Delta+(4+8C_{2,30}+6C_{4,30})\big)A^2\\ +\big((10-4C_{2,30}-C_{4,30})\Delta-(4-8C_{2,30}+6C_{4,30})\big)B^2\end{bmatrix}\\
&\frac{\tilde{b}_{12}}{128}\begin{bmatrix}\big((10+4C_{2,12}-C_{4,12})\Delta+(4+8C_{2,12}+6C_{4,12})\big)\big(\frac{\Delta-2}{\Delta+2}\big)A^2\\ -\big((10-4C_{2,12}-C_{4,12})\Delta-(4-8C_{2,12}+6C_{4,12})\big)\big(\frac{\Delta+2}{\Delta-2}\big)B^2\end{bmatrix}-\\
&\begin{bmatrix}\frac{\tilde{b}_{10}S_{2,10}}{2}\big(\frac{A/B}{\Delta+2}+\frac{B/A}{\Delta-2}\big)+\frac{3\tilde{b}_{30}}{32}\Big(\big(\frac{2S_{2,30}+S_{4,30}}{\Delta+2}\big)\frac{A^3}{B}+\frac{2S_{2,30}-S_{4,30}}{\Delta-2}\big)\frac{B^3}{A}\Big)\\ +\frac{9\tilde{b}_{30}(S_{2,30}\Delta+S_{4,30})}{8(\Delta+2)(\Delta-2)}\frac{A}{B}-\frac{\tilde{b}_{12}}{32}(S_{2,12}\Delta+3S_{4,12})AB\\ +\frac{\tilde{b}_{12}}{128}\Big((2S_{2,12}+S_{4,12})\frac{(\Delta-2)^2}{\Delta+2}\frac{A^3}{B}+(2S_{2,12}-S_{4,12})\frac{(\Delta+2)^2}{\Delta-2}\frac{B^3}{A}\Big)\end{bmatrix}\cos\varphi-\\
&\begin{bmatrix}\frac{\tilde{b}_{01}S_{2,01}}{4}\big(\frac{\Delta-2}{\Delta+2}\frac{A}{B}+\frac{\Delta+2}{\Delta-2}\frac{B}{A}\big)+\frac{3\tilde{b}_{03}S_{2,03}}{256}(\Delta^2-4)AB-\frac{\tilde{b}_{21}}{64}\frac{5S_{2,21}\Delta^2+6S_{4,12}\Delta+4S_{2,21}}{\Delta^2-4}AB\\ +\frac{3\tilde{b}_{03}}{256}\big((S_{2,03}+S_{4,03})\frac{(\Delta-2)^3}{\Delta+2}\frac{A^3}{B}+(S_{2,03}-S_{4,03})\frac{(\Delta+2)^3}{\Delta-2}\frac{B^3}{A}\big)\\ +\frac{\tilde{b}_{21}}{64}\big((2S_{2,21}+S_{4,21})\frac{\Delta-2}{\Delta+2}\frac{A^3}{B}+(2S_{2,21}-S_{4,21})\frac{\Delta+2}{\Delta-2}\frac{B^3}{A}\big)\end{bmatrix}\sin\varphi\\
&-\begin{bmatrix}\frac{3\tilde{b}_{30}}{32}(2-C_{4,30})\Big(\frac{A^2}{\Delta+2}+\frac{B^2}{\Delta-2}\Big)+\\ \frac{\tilde{b}_{12}}{128}(2-C_{4,12})\Big(\frac{(2-\Delta)(3\Delta+2)}{\Delta+2}A^2-\frac{(2+\Delta)(3\Delta-2)}{\Delta-2}B^2\Big)\end{bmatrix}\cos 2\varphi\\
&-\begin{bmatrix}\frac{3\tilde{b}_{03}}{256}(2-C_{4,03})\big((\Delta-2)^2A^2+(\Delta+2)^2B^2\big)-\\ \frac{\tilde{b}_{21}}{128}(2-C_{4,21})\Big(\big(\frac{3\Delta-2}{\Delta+2}\big)A^2+\big(\frac{3\Delta+2}{\Delta-2}\big)B^2\Big)\end{bmatrix}\sin 2\varphi+\left(\frac{1}{A}+\frac{1}{B}\right)\frac{\zeta_\varphi}{\bar{\omega}}
\end{aligned}
\tag{7.13}
$$

where $\varphi=\varphi_B-\varphi_A$, $\Delta=\Delta\omega/\bar{\omega}$, $\tilde{\alpha}=\bar{\omega}\alpha$, $\tilde{\beta}=\bar{\omega}\beta$, $\tilde{b}_{ij}=\bar{\omega}^{2-j}b_{ij}$, $\tilde{t}=\bar{\omega}t$, and ζ_A,ζ_B, and ζ_φ are uncorrelated white noises of intensity $\Gamma/2\bar{\omega}^2$. Here, the m in the subscript of C_{ij} and S_{ij} has been dropped. Also notice that the parametric noise term has been neglected for simplicity, i.e., $\xi_2(t)=0$. The effect of this term will be numerically considered later. Equation 7.13 describes the amplitudes and phase difference dynamics of the second order coupled oscillators in Equation 7.7. These equations are a quite general representation of the modal dynamics, and serve as a useful point of departure for a range of different types of analyses. For example, referring back to the discussion in section 7.1, azimuthal non-uniformity effects are parameterized by C_{ij} and S_{ij}, nondegeneracy by C_{ij}, S_{ij}, and Δ, nonlinearities by $\tilde{b}_{ij}$, and background noise by ζ. In subsequent sections, we will consider

the deterministic FP solutions of a simplified version of these equations, the stability of those FPs, and the bifurcation point.

7.3 Illustrative Results

While the equations developed earlier are quite general, they also exhibit a very broad range of behaviors, and the formulation has 2 independent linear and 24 independent nonlinear coefficients. Notice that in reality, some of these parameters may be interconnected to each other, preventing us from isolating them separately in experiments. The model problems considered in this section allow us to isolate each parameter, and thus, help us understand their individual effects. This section works from simple cases that are amenable to analytical results and insights to a more involved problem that captures the observed dynamics. In particular, we start by analytically considering problems with frequency spacing, Δ, and one of the non-uniform parameters, $S_{2,10}$, set to zero in subsection 7.3.2. Next, we consider the effects of Δ and $S_{2,10}$ in subsection 7.3.3, and effect of additive noise, Γ, in refeffect of additive noise, showing how these introduce quasi-periodic oscillations as well as the system's preference in CW/CCW direction. Finally, we consider parametric noise, $\xi_2(t)$, in subsection 7.3.5, and show how it is needed to capture the simultaneous presence of standing and spinning attractors. We will consider the first azimuthal mode ($m = 1$) since that was the mode appeared in the experiments.

7.3.1 Simplified equations

In order to reduce the number of independent parameters, we consider the model equations in Equation 7.14 below. First, without loss of generality, we define the azimuthal origin such that $S_{2,01} = 0$ [97]. Second, we consider a subset of the larger independent parameter space by (1) setting $C_{4,ij} = S_{4,ij} = 0$; this is equivalent to assuming that $4m$ nonuniformity is negligible relative to $2m$, and (2) setting the nonlinear coefficients, b_{30}, b_{12}, and b_{03} to zero. In the zero frequency spacing case that is analytically considered in the next

section, these assumptions eliminate the coupling between amplitude and phase dynamics, enabling us to solve for all FP's and their stability. It will be shown later that the simulation with these assumptions still can capture the experimental observations quite well. The governing equations then simplify to:

$$\begin{aligned}
\dot{A} &= [\beta(2+C_{2,01})-2\alpha]\frac{A}{4} - k_{A1}\sin\varphi B + k_{A2}A^3 + (k_3 + k_{A3}\cos 2\varphi)AB^2 + \frac{\Gamma}{4\bar{\omega}^3 A} + \frac{\zeta_A}{\bar{\omega}},\\
\dot{B} &= [\beta(2-C_{2,01})-2\alpha]\frac{B}{4} - k_{B1}\sin\varphi A + k_{B2}B^3 + (k_3 + k_{B3}\cos 2\varphi)BA^2 + \frac{\Gamma}{4\bar{\omega}^3 B} + \frac{\zeta_B}{\bar{\omega}},\\
\dot{\varphi} &= \Delta - \frac{b_{10}S_{2,10}}{2}\left(\frac{A/B}{\Delta+2} - \frac{B/A}{\Delta-2}\right)\cos\varphi + (k_{\varphi_A}A^2 + k_{\varphi_B}B^2)\sin 2\varphi + \left(\frac{1}{A}+\frac{1}{B}\right)\frac{\zeta_\varphi}{\bar{\omega}}
\end{aligned} \tag{7.14}$$

where

$$\begin{gathered}
k_{A1} = \frac{b_{10}S_{2,10}}{2(\Delta-2)},\ k_{B1} = \frac{b_{10}S_{2,10}}{2(\Delta+2)},\ k_{A2} = \frac{b_{21}}{32}(3+2C_{2,21}),\ k_{B2} = \frac{b_{21}}{32}(3-2C_{2,21}),\\
k_3 = \frac{b_{21}}{16},\ k_{A3} = -\frac{b_{21}}{32}\left(\frac{3\Delta+2}{\Delta-2}\right),\ k_{B3} = -\frac{b_{21}}{32}\left(\frac{3\Delta-2}{\Delta+2}\right),\\
k_{\varphi_A} = \frac{b_{21}}{64}\left(\frac{3\Delta-2}{\Delta+2}\right)\ k_{\varphi_B} = \frac{b_{21}}{64}\left(\frac{3\Delta+2}{\Delta-2}\right)
\end{gathered} \tag{7.15}$$

The tildes on α, β and b_{ij} have been omitted. Recall that $C_{2,01}, S_{2,10}$ and $C_{2,21}$ are parameters that describe the non-uniformities in the source term response, such as dQ/dt, to $\dot{p}, p$ and $p^2\dot{p}$, respectively. Note that these parameters and Δ cause the coefficients in the $\dot{A}$ and $\dot{B}$ equations to differ; stated differently, if $\Delta = C_{2,01} = S_{2,10} = C_{2,21} = 0$, the equations for $\dot{A}$ and $\dot{B}$ are symmetric. Equation 7.14 will be used to simulate the dynamics of A, B, and φ later.

7.3.2 Fixed points analysis with $\Delta = S_{2,10} = 0$

This section considers the deterministic limit cycle solutions (i.e., the FPs of A, B, and φ) and their stability with the absence of pressure coupled azimuthal non-uniformity

parameter, $S_{2,10} = 0$, and no frequency shift, $\Delta = 0$. The effects of nonzero values of these parameters will be numerically investigated in the subsequent subsections. For the deterministic FP analysis, the time derivative of each variable as well as the noise terms are set to zero, leading to the following equations.

$$\begin{aligned} 0 &= \frac{1}{4}[\beta(2 + C_{2,01}) - 2\alpha]A + k_{A1}A^3 + (k_2 + k_{A2}\cos 2\varphi)AB^2 \\ 0 &= \frac{1}{4}[\beta(2 - C_{2,01}) - 2\alpha]B + k_{B1}B^3 + (k_2 + k_{B2}\cos 2\varphi)BA^2 \\ 0 &= (k_{\varphi_A}A^2 + k_{\varphi_B}B^2)\sin 2\varphi \end{aligned} \tag{7.16}$$

The FPs are given by:

$$\begin{aligned} &\text{FP\#1: } A^{*2} = B^{*2} = 0 \\ &\text{FP\#2: } A^{*2} = \frac{16\alpha - (16 + 8C_{2,01})}{b_{21}(3 + 2C_{2,21})}, B^{*2} = 0 \\ &\text{FP\#3: } B^{*2} = \frac{16\alpha - (16 - 8C_{2,01})}{b_{21}(3 - 2C_{2,21})}, A^{*2} = 0 \\ &\text{FP\#4: } A^{*2} = \frac{8\alpha(1 - C_{2,21}) - 4\beta\big(C_{2,01}(2 - C_{2,21}) + 2(1 - C_{2,21})\big)}{b_{21}(2 - C_{2,21}^2)} \\ &\qquad B^{*2} = \frac{8\alpha(1 + C_{2,21}) + 4\beta\big(C_{2,01}(2 + C_{2,21}) - 2(1 + C_{2,21})\big)}{b_{21}(2 - C_{2,21}^2)} \\ &\qquad \varphi^* = \pm\frac{\pi}{2}, \pm\frac{3\pi}{2}, \pm\frac{5\pi}{2}, \dots \end{aligned} \tag{7.17}$$

where * is the value at each FP. Note that there are 4 possible solutions to this equation. Here, FP#1 is a zero amplitude mode, FPs #2 and #3 are purely standing waves orthogonal to each other, and FP#4 is a mixed wave. Although not written here, if FP#4 solution is recast as two counter rotating eigenmodes using Equation E.5 in Appendix E, it can be shown that the dominance between CW and CCW waves for FP#4 is determined by φ^*, i.e., if $\varphi^* = \pi/2$ $(-\pi/2)$, CW (CCW) dominates over CCW (CW). When $C_{2,01} = C_{2,21} = 0$, FP#4 becomes a purely spinning wave whose direction is determined by its initial condition.

The physical realization of the above FPs depends on the stability of each FP. The stability analysis can be done by perturbing the steady-state solutions:

$$\begin{aligned} \dot{A} &= A^* + A' \ \text{ where } \ A' \ll A^* \\ \dot{B} &= B^* + B' \ \text{ where } \ B' \ll B^* \\ \dot{\varphi} &= \varphi^* + \varphi' \ \text{ where } \ \varphi' \ll \varphi^* \end{aligned} \tag{7.18}$$

The details of the stability analysis are provided in Appendix F, showing that each FP is stable when:

$$\begin{aligned} &\text{FP\#1: } \gamma \leq \gamma_{Hopf,1} \\ &\text{FP\#2, 3: } \gamma_{Hopf,1} < \gamma \leq \gamma_{Hopf,2} \\ &\text{FP\#4: } \gamma > \gamma_{Hopf,2} \end{aligned} \tag{7.19}$$

where

$$\gamma = \beta/\alpha$$

$$\gamma_{Hopf,1} = \begin{cases} \frac{2}{2+C_{2,01}} & \text{if } \ 0 \leq C_{2,01} < 1 \ \text{ (FP\#2)} \\ \frac{2}{2-C_{2,01}} & \text{if } \ -1 < C_{2,01} < 0 \ \text{ (FP\#3)} \end{cases}$$

$$\gamma_{Hopf,2} = \begin{cases} \frac{2(1+C_{2,21})}{2(1-C_{2,01})+C_{2,21}(2-C_{2},01)} & \text{if } \ 0 \leq C_{2,01} < 1 \ \text{ and } \ C_{2,01} < \frac{2(C_{2,21}+1)}{2+C_{2,21}} \ \text{ (FP\#2)} \\ \frac{2(1-C_{2,21})}{2(1+C_{2,01})-C_{2,21}(2+C_{2},01)} & \text{if } \ -1 \leq C_{2,01} < 0 \ \text{ and } \ C_{2,01} < \frac{2(C_{2,21}-1)}{2-C_{2,21}} \ \text{ (FP\#3)} \end{cases} \tag{7.20}$$

It has been assumed that the non-uniformity parameters, $C_{2,01}$ and $C_{2,21}$, are bounded between ± 1. This physically implies that the non-uniform parameters are less than mean value in Equation 7.6. Here, $\gamma_{Hopf,1}$ corresponds to the bifurcation from FP#1 (zero amplitude) to FP#2 or #3 (standing wave), and $\gamma_{Hopf,2}$ is the bifurcation from FP#2 or #3 (standing wave) to FP#4 (mixed wave). Figure 7.1 summarizes the stability of each FP in

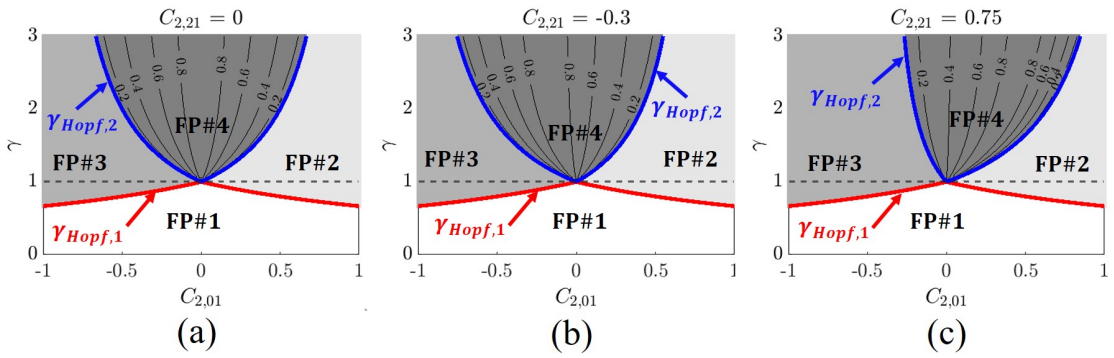

Figure 7.1: Stability map in $(C_{2,01}, \gamma)$ space with difference $C_{2,21}$ values. Red and blue lines denote the first and second bifurcation boundaries. The horizontal dash line denotes $\gamma = 1$. Contour lines indicate $|SR|$.

$(C_{2,01}, \gamma)$ space with different $C_{2,21}$ values. Here, the horizontal dash line indicates $\gamma = 1$, and the contour lines denote $|SR|$. Consider a case where γ is increasing with fixed values of $C_{2,01}$ and $C_{2,21}$. This is equivalent to moving in a vertical direction in the plot. As γ increases, a system transitions from FP#1 (zero amplitude) to FP#2 or #3 (standing wave), and then FP#4 (mixed wave). However, when $C_{2,01}$ is zero, the system transitions directly from FP#1 to FP#4. Specifically, when the system is azimuthally uniform, $C_{2,01} = C_{2,21} = 0$, the mode exists either as a zero amplitude or a purely spinning wave, depending upon γ. Also note from $\gamma_{Hopf,1}$ that the more $C_{2,01}$ deviates from zero, the lower γ the system becomes unstable at, i.e., the non-uniformity promotes the onset of the instability. When being unstable, the system transitions towards the standing wave with $C_{2,01}$ deviating from zero. Lastly, nonzero $C_{2,21}$ causes $\gamma_{Hopf,2}$ to be asymmetric about $C_{2,01} = 0$ line.

To summarize, this figure clearly shows that under unstable conditions, the system can be dominated by standing, spinning, or mixed waves, and shows how the relative dominance of these waves is controlled by linear damping/amplification effects, $(\gamma = \beta/\alpha)$, and azimuthal non-uniformities, $(C_{2,01}, C_{2,21})$.

Further insight into these FP's and their stability can be obtained from transient computations, showing the systems relaxation to these FP's from arbitrary initial conditions,

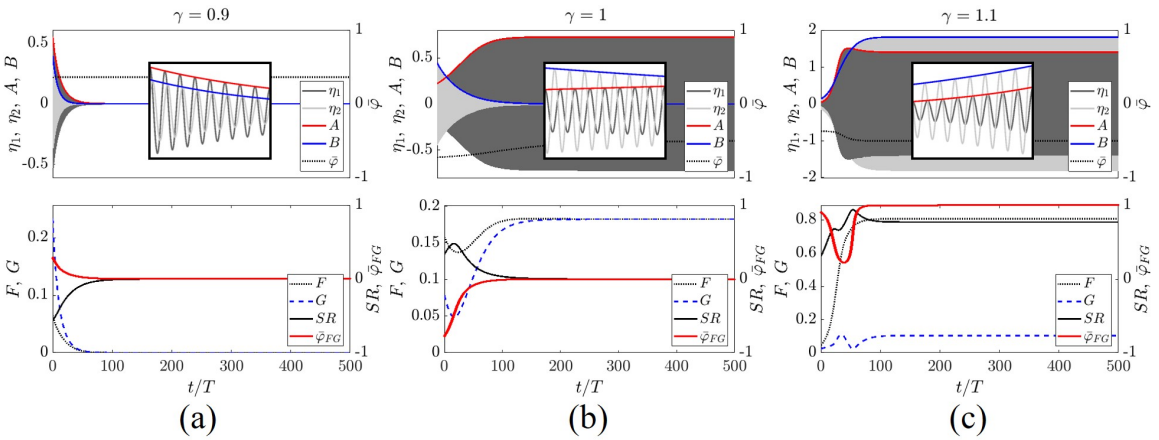

Figure 7.2: Top: simulations of η_1, η_2, A, B, and $\bar{\varphi}$. Subfigures describe the dynamics of the first eight cycles. Bottom: simulations of F, G, SR and φ_{FG}. γ values are (a) 0.9, (b) 1, and (c) 1.1. The other parameters are $b_{21} = -0.05, C_{2,01} = 0.05, S_{2,10} = 0, C_{2,21} = 0.75, \bar{\omega} = 1, \Delta = 0, \Gamma = 0$. The Hopf bifurcation points calculated from Equation 7.20 are $\gamma_{Hopf,1} = 0.9757, \gamma_{Hopf,2} = 1.041$.

see Figure 7.2. The first row illustrates simulations of η_1, η_2, A, B, and $\bar{\varphi}$ with different γ values. Here, $\bar{\varphi} \equiv \varphi/\pi$. η_1 and η_2 are numerically obtained from Equation 7.7, and A, B, and φ are from Equation 7.14. Subfigures in each plot demonstrate that the method of averaging technique closely captures the magnitudes of the second order oscillators. After each simulation, A, B, and φ are mapped into F, G, and φ_{FG} using Equation E.5. Lastly, SR is calculated by Equation 5.2.

Figure 7.2 (a) represents the zero amplitude mode (FP#1) where $\gamma < \gamma_{Hopf,1}$, and thus, both amplitudes, A and B, decay to zero, i.e., the system is linearly stable. In this case, $\bar{\varphi}, SR$, and φ_{FG} do not have any physical meaning.

Figure 7.2 (b) is the case where $\gamma_{Hopf,1} < \gamma < \gamma_{Hopf,2}$, and the system is linearly unstable. As expected from Equation 7.20, FP#2 is stable, and only A converges to a finite value since $C_{2,01} > 0$. The bottom plot shows that F and G converge to the same value, resulting in zero SR or a purely standing wave. Also note that $\bar{\varphi}_{FG}$ converges to zero, implying from Equation 4.6 that the anti-nodal line ($\theta_a = -\varphi_{FG}/2$) is located horizontally. This is physically reasonable because the flames that strongly couple with acoustics are oriented in the horizontal direction for positive $C_{2,01}$.

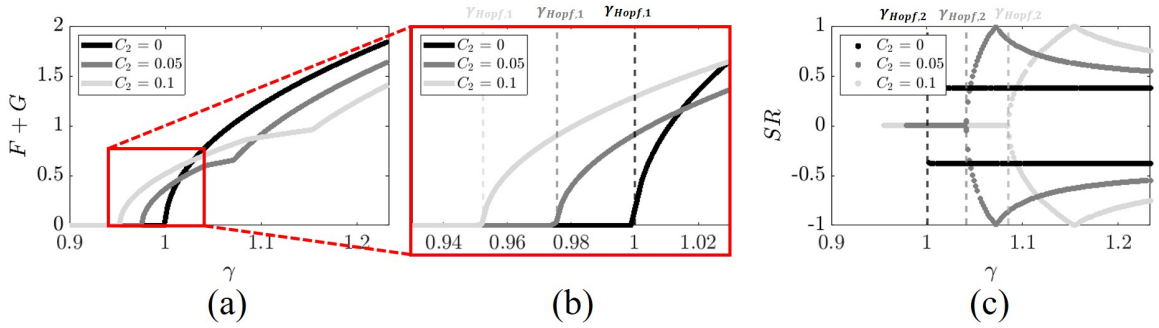

Figure 7.3: (a) Pressure anti-node magnitude as a function of γ with different $C_{2,01}$ values. (b) Zoom in version of (a). (c) SR as a function of γ with different $C_{2,01}$ values. The other parameters are $b_{21} = -0.05, S_{2,10} = 0, C_{2,21} = 0.75, \bar{\omega} = 1, \delta = 0, \Gamma = 0$. The grayscale vertical lines in (b) and (c) denote the first and second bifurcation points, respectively.

Further increase in $\gamma > \gamma_{Hopf,2}$ leads to a mixed wave as shown in Figure 7.2 (c) where both A and B converge to finite values. This state corresponds to FP#4 in Equation 7.17. In the bottom plot, F is greater than G at steady state, and thus, $SR > 0$. Notice that $\bar{\varphi}_{FG}$ converges to 1, indicating that the anti-nodal line of the mixed wave is in the vertical direction. Finally, note that, near the FP values, both A and B relax towards their equilibrium values as damped exponentials for all cases; i.e., they do not exhibit decaying oscillations as they asymptote to their FPs. As discussed in the next section, this is not true in general and, even in cases where the FPs are stable, damped oscillations about the FPs are possible. In this case, these systems exhibit significantly different behavior in the presence of background noise.

Figure 7.3 (a) describes the effect of linear damping/growth rate, γ, on the steady state pressure anti-node magnitude with different $C_{2,01}$ values, determined from computational solutions. Here, the simulation was run out to sufficient time to reach a steady state, and was repeated at different initial conditions to explore their effects. For reference, Figure 7.3 (b) shows a detail of Figure 7.3 (a) with the dashed vertical lines indicating the theoretical predictions for the bifurcation points, $\gamma_{Hopf,1}$. Note the excellent agreement between these computed results and Equation 7.20. As expected from Equation 7.20, the first Hopf bifurcation point, $\gamma_{Hopf,1}$, decreases with increasing $C_{2,01}$. In other words, the larger the

azimuthal non-uniformity, the earlier the system becomes unstable. The figure also shows that the higher the non-uniformity, the slower the instability amplitude grows with γ.

Figure 7.3 (c) plots SR as a function of γ with different $C_{2,01}$ values, showing the presence of purely standing and spinning waves, as well as mixed waves. When $C_{2,01} = 0$, the azimuthal mode has a constant $SR = \pm 0.38$, or a mixed wave. For $C_{2,01} > 0$, SR starts from zero at $\gamma = \gamma_{Hopf,1}$ and maintains this value until $\gamma = \gamma_{Hopf,2}$. After $\gamma_{Hopf,2}$, SR first rapidly approaches a pure spinning wave value of ± 1 and then decays to a mixed wave. Comparing between different $C_{2,01}$ cases, $\gamma_{Hopf,2}$ increases with increasing $C_{2,01}$, i.e., the non-uniformity delays the transition from a standing to a mixed wave. Note that there are two branches, positive and negative SR. Which branches the system is stabilized at depends on the initial conditions. These simulated results are consistent with the analytical results plotted in Figure 7.1 (c).

Figure 7.3 (c) demonstrates that the system does not exhibit a standing wave limit cycle when $C_{2,01} = 0$. However, the experimental data in Figure 6.5 (a) shows the standing wave even in the nominally "uniform" fuel staging case, implying that the value of $C_{2,10}$ in our facility is actually nonzero. This is probably due to inevitable manufacturing differences, leakage flows, and so forth. As such, these results show that relatively small manufacturing variations can introduce significant impacts on the dominance of spinning/standing waves, and so forth (e.g., see Figure 7.1, and also suggest that these behaviors can vary between engines.

7.3.3 Effect of frequency shift, Δ, and pressure coupled azimuthal non-uniformity, $S_{2,10}$

Having considered the basic FPs and their stability, this section considers the important generalization of more general azimuthal non-uniformities (i.e., nonzero $S_{2,10}$) and the difference in frequencies between the two eigenmodes, Δ. Although analytical solutions are not possible for these cases, some insights into their behavior (which are confirmed from the computations shown later) can be obtained from consideration of the equation structure

for small perturbations about the FPs derived in the prior section, denoted by A^* and B^*. The equation for φ can be written in a potential form as:

$$\dot{\varphi} = -\frac{dU}{d\varphi} \tag{7.21}$$

where the potential, U, is given by:

$$U = -\varphi\Delta + \frac{b_{10}S_{2,10}}{2}\left(\frac{A^*/B^*}{2+\Delta} - \frac{B^*/A^*}{2-\Delta}\right)\sin\varphi + \frac{1}{2}(k_{\varphi_A}A^{*2} + k_{\varphi_B}B^{*2})\cos 2\varphi \tag{7.22}$$

and, consistent with the approximation of considering very small departures of the system from the Section subsection 7.3.2 analysis, it has been assumed that the amplitudes, A and B, are constant at their FP values, A^* and B^* [82] in this equation. The potential in Equation 7.22 consists of three terms: the first term, proportional to Δ, causes φ to drift in one direction linearly with time. The second term, proportional to $S_{2,10}$, provides one-well potential at either CW or CCW spinning wave, which is determined by the sign of the second term. The third term, proportional to k_{φ_A} and k_{φ_B}, provides two-well potential at both CW/CWW spinning waves. Figure 7.4 shows each term as a function of φ and their contribution to the potential shape for two different cases. The figure clearly shows that $S_{2,10}$ term causes a preference to either CW or CCW spinning wave. When this term is sufficiently larger than the other terms, it will suppress one of the spinning waves, and foster the other spinning wave (Figure 7.4 (a)). In contrast, when Δ term dominates over the other terms, φ can continuously drift in one direction (Figure 7.4 (b)) without a local minimum, which serves as a local attractor. As can be seen in Equation E.5, this drift causes not only the out-of-phase oscillations between CW/CCW amplitudes, resulting in the oscillation of SR, but also the oscillation in φ_{FG}, both of which were observed experimentally.

We next present computations, starting first with the case where $S_{2,10} = 0$, but $\Delta \ll 1$. Notice that in a linear regime, a nonzero Δ imposes two different frequencies on the system.

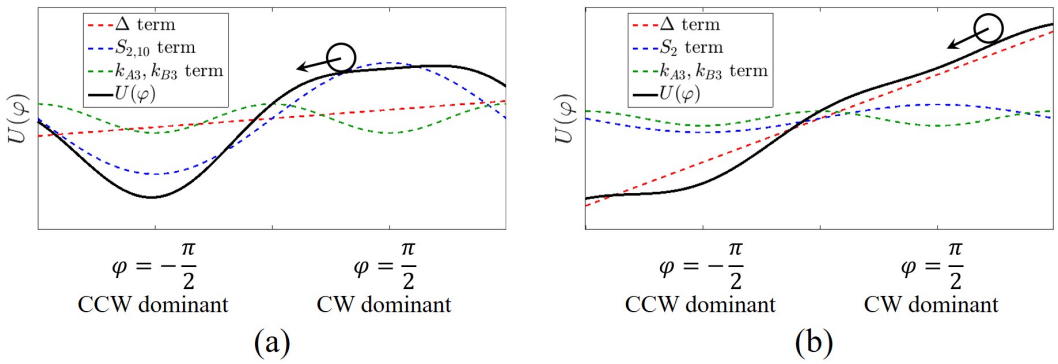

Figure 7.4: Potential and contributions of each term to its shape for two example cases (a) $S_{2,10}$ term dominant system, leading to a local minimum in U, (b) Δ term dominant system, which has no local minimum in U.

Depending upon the value of Δ, the ratio of the two frequencies may be irrational (i.e., quasi-periodic) or rational (leading to period-N oscillations, with the value of N being a function of Δ). Even if it is rational, if $\Delta \ll 1$, then N becomes so large that the system appears as quasi-periodic in real applications. Thus, we will use the word "quasi-periodic" in the rest of this chapter.

While a nonzero Δ implies a system with two distinct frequencies in the linear case, it does not necessarily do so in the nonlinear case at steady state conditions. Nonlinearities do this in two ways - first, through amplitude dependent frequency shifts which can synchronize the two distinct frequencies and, second, by "quenching", where two linearly unstable oscillators compete with each other and one oscillator's amplitude is driven to zero. Both behaviors are illustrated in Figure 7.5. The first row of Figure 7.5 (a) shows the simulations of A, B, and $\bar{\varphi}$ with a finite frequency spacing, showing how the system relaxes to "steady state" from a prescribed initial condition. In contrast to Figure 7.2 (a), note from the second row of Figure 7.5 (a) how F and G decay in an oscillatory manner towards the FP at the frequency of Δ, evidence of a damped quasi-periodic solution. However, the quasi-periodicity disappears at a steady state because one of the oscillators (B in this case) decays to zero, resulting in a single frequency oscillation. In other words, nonlinear competition between the two standing eigenmodes leads to quenching of oscillator B, even

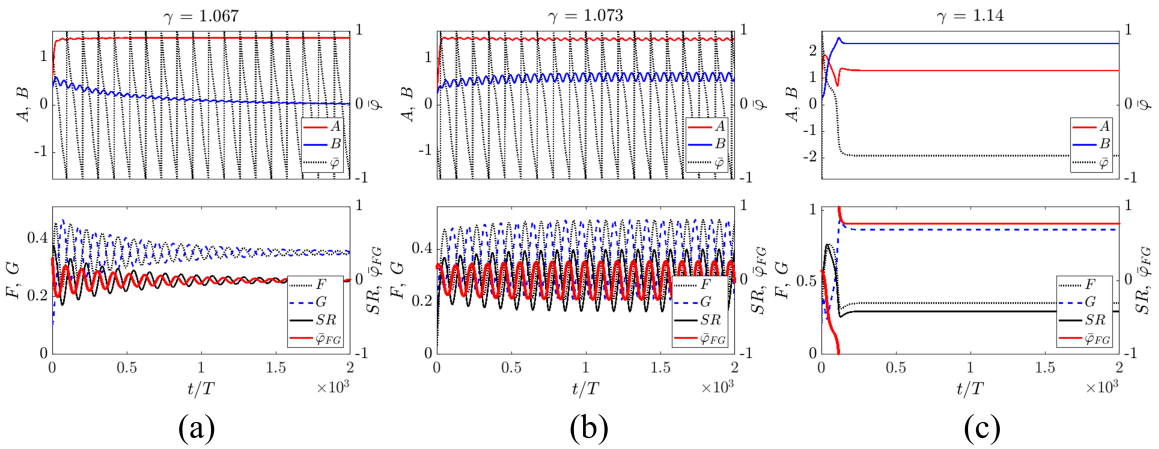

Figure 7.5: Top: simulations of A, B, and $\bar{\varphi}$. Bottom: simulations of F, G, SR and $\bar{\varphi}_{FG}$. γ values are (a) 1.067, (b) 1.073, and (c) 1.14. The other parameters are $b_{21} = -0.05, C_{2,01} = 0.05, S_{2,10} = 0, C_{2,21} = 0.75, \bar{\omega} = 1, \Delta = -0.01, \Gamma = 0$.

though both oscillators are linearly unstable.

Increase in γ causes a self-sustained quasi-periodic oscillation as shown in Figure 7.5 (b). Note from the first row that the two oscillators coexist, and their phase difference drifts in one direction, demonstrating a presence of two different frequencies in the system. This state corresponds to Figure 7.4 (b) where the drift term The second row in Figure 7.5 (b) shows that SR oscillates around zero, and the phase lag between $\bar{\varphi}_{FG}$ and SR is about 90°. This is in good agreement with the quasi-periodic standing wave observed in the experiments, e.g., Figure 6.5 (a), Figure 6.7 (a) and (d).

Further increase in γ alters the system to a mixed wave as shown in Figure 7.5 (c). The first row shows that the two oscillators coexist, but their phase difference is constant at a steady state, indicating that their oscillation frequencies are synchronized. Thus, the quasi-periodicity vanishes as shown in the second row of Figure 7.5 (c).

Figure 7.6 is a similar plot with Figure 7.3, but with a nonzero Δ. Here, the first and second bifurcation points, $\gamma_{Hopf,1}$ and $\gamma_{Hopf,2}$, for $\Delta = 0$ are indicated for comparison. Comparison between Figure 7.6 (a), (b) and Figure 7.3 (a), (b) shows that Δ has little impact on the pressure anti-node magnitude nor the first bifurcation point. In contrast, Figure 7.6 (c) demonstrates that nonzero Δ shifts the second bifurcation point from the

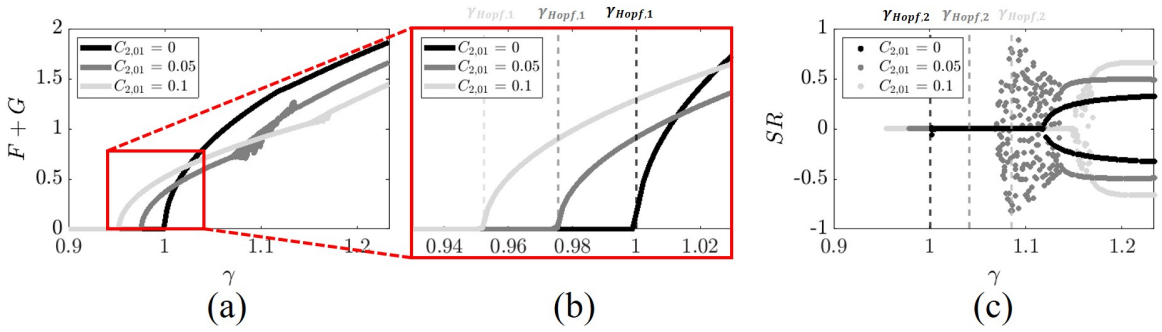

Figure 7.6: (a) Pressure anti-node magnitude as a function of γ with different $C_{2,01}$ values. (b) Zoom in version of (a). (c) SR as a function of γ with different $C_{2,01}$ values. The other parameters are $b_{21} = -0.05, S_{2,10} = 0, C_{2,21} = 0.75, \bar{\omega} = 1, \Delta = -0.01, \Gamma = 0$. The grayscale vertical lines in (b) and (c) denote the first and second bifurcation points, respectively, when $\Delta = 0$.

$\gamma_{Hopf,2}$ values analytically calculated in Equation 7.20. However, the largest qualitative change is the quasi-periodic regimes. When the system exhibits quasi-periodicity, it never converges to the steady state, but rather continuously oscillate around the FP, as shown in Figure 7.5 (b). This causes the oscillation in SR, which is shown in Figure 7.6 (c) for nonzero $C_{2,01}$ cases. The quasi-periodic behavior only appears at a certain range of γ, which depends on $C_{2,01}$.

We close this subsection by introducing a bifurcation plot in $(C_{2,01}, \gamma)$ space for the noise free system, which is similar to Figure 7.1, but with a finite frequency spacing. Figure 7.7 shows regions where the system is linearly stable (zero amplitude), exhibits single frequency standing waves (i.e., nonlinear effects lead to quenching of one of the standing eigenmodes), exhibits self-sustained quasi-periodic standing waves, and exhibits single frequency mixed waves (i.e., not purely standing or spinning). This plot shows a region where the quasi-periodic behavior can occur with a noise free system. The region becomes wider with increasing frequency split. Note that even if the system's parameters are not inside the region, but close to it, the system exhibits damped oscillation as shown in Figure 7.5 (a). However, when the system moves far away from the region, the oscillatory behavior disappears even with the noise contribution.

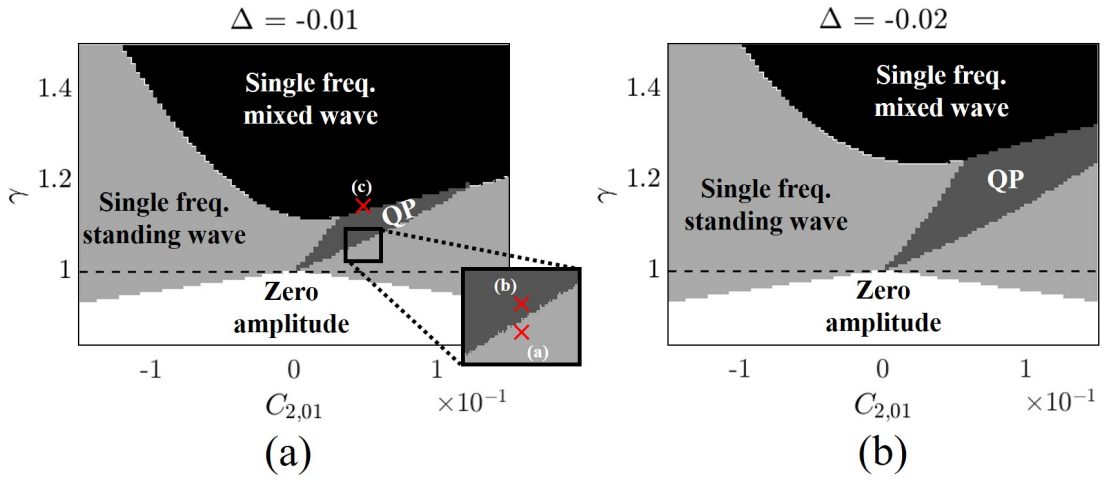

Figure 7.7: Bifurcation plot in $(C_{2,01}, \gamma)$ space showing quasi-periodic behavior with two different frequency spacing values (a) $\Delta = -0.01$ and (b) $\Delta = -0.02$. Here, QP = quasi-periodic standing wave region. The horizontal dash line denotes $\gamma = 1$. The red crosses in (a) indicate $(C_{2,01}, \gamma)$ in Figure 7.5 (a)-(c). The other parameters are $b_{21} = -0.05, S_{2,10} = 0, C_{2,21} = 0.75, \bar{\omega} = 1, \Gamma = 0$.

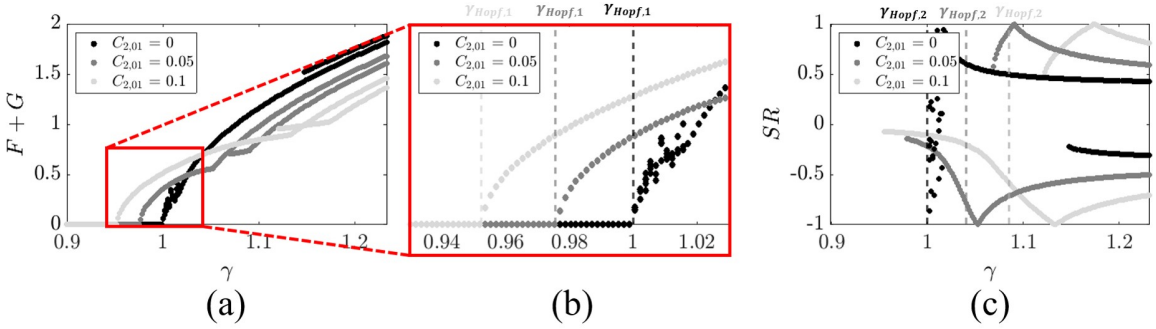

Figure 7.8: (a) Pressure anti-node magnitude as a function of γ with different $C_{2,01}$ values. (b) Zoom in version of (a). (c) SR as a function of γ with different $C_{2,01}$ values. The other parameters are $b_{21} = -0.05, S_{2,10} = 0.02, C_{2,21} = 0.75, \bar{\omega} = 1, \Delta = 0, \Gamma = 0$. The grayscale vertical lines in (b) and (c) denote the first and second bifurcation points, respectively, when $\Delta = 0$.

We next consider the effect of pressure coupled azimuthal non-uniformity, $S_{2,10}$. Recall from Figure 7.4 that $S_{2,10}$ has an impact on the preference in CW/CCW direction. Figure 7.8 represents the similar plot with Figure 7.3, but with non zero $S_{2,10} = 0.02 \ll 1$. Figure 7.8 (a) and (b) shows that $S_{2,10}$ does not dramatically alter the trends of pressure anti-node magnitude as well as the first bifurcation point. However, Figure 7.8 (a) demonstrates that after the second bifurcation point, the magnitude between positive/negative SR splits, and they have slightly different magnitudes. The effect of $S_{2,10}$ is well illustrated in Figure 7.8 (c). The figure clearly shows that $S_{2,10}$ imposes a preferential spinning direction. For $C_{2,01} = 0$, a system has a preference in a positive SR, or CCW direction, but CW direction also appears above $\gamma = 1.15$. In contrast, the system with $C_{2,01} = 0.05$ or 0.1 has a preference in a negative SR, or CW direction. The change in preferential direction is due to the sign change of the second term in Equation 7.22f. To summarize, introducing the non-uniformity, $S_{2,10}$, causes a mixed/spinning wave to be biased towards either CW or CCW direction. This provides a possible explanation for why the experimental data shown in Figure 6.5 (c) show a bias towards positive SR values.

7.3.4 Effect of additive noise, Γ

Figure 7.5 (a) shows that when $\Delta \ll 1$, quasi-periodic behavior only appears during the initial transient. However, in the presence of background noise, the damped oscillator B will be continuously excited and the phase averaged system will be quasi-periodic. To illustrate, Figure 7.9 plots representative time traces, and corresponding spectra, of SR and $\bar{\varphi}_{FG}$ for computed cases with background noise of two different noise intensities. The white noise terms in Equation 7.14 have been simulated using the Euler-Maruyama scheme [155]. The top is the raw signal, and the bottom is the low pass filtered signal whose bandwidth is shown as the shaded region in the spectra. Notice that introducing the background noise prevents the SR and $\bar{\varphi}_{FG}$ from decaying to zero, causing them to continuously oscillate around zero, i.e., as a quasi-periodic standing wave. In addition, noise intensity increases

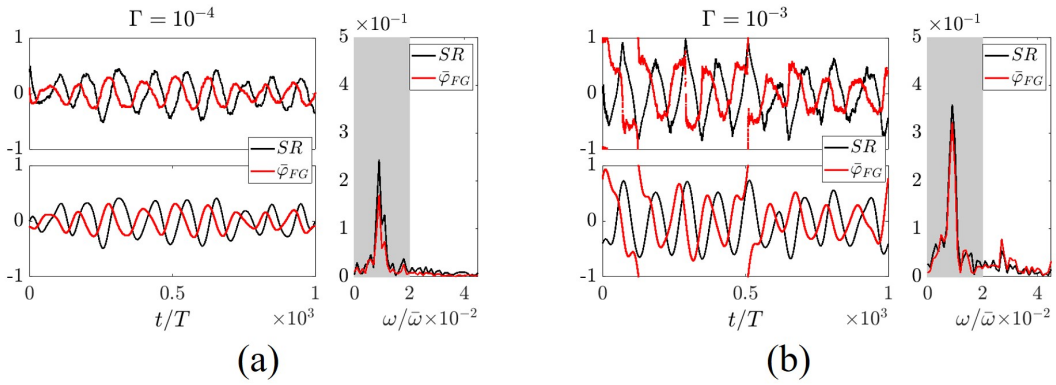

Figure 7.9: Simulation of SR and $\bar{\varphi}_{FG}$ with background noise (a) $\Gamma = 10^{-4}$ and (b) $\Gamma = 10^{-3}$. Top plot: raw signal, bottom plot: filtered signal, right plot: Fourier transform. The shaded region in the Fourier transform denotes the low pass filter width. The other parameters are $\gamma = 1.067, b_{21} = -0.05, C_{2,01} = 0.05, S_{2,10} = 0, C_{2,21} = 0.75, \bar{\omega} = 1, \Delta = -0.01$.

the oscillation amplitude. In particular, Figure 7.9 (b) shows that sufficiently high noise intensity may cause $\bar{\varphi}_{FG}$ to jump from ± 1 to ∓ 1 e.g., at $t/T = 500$, which was also seen experimentally in Figure 6.7 (d). Recalling that $\bar{\varphi}_{FG}$ is directly related to the anti-nodal line by Equation 4.6, this demonstrates the rotation of the anti-nodal line in CW/CCW direction.

To further explore the effect of noise on system's dynamics, Figure 7.10 (a) represents the pressure magnitude as a function of γ at different $C_{2,01}$ values with noise intensity, $\Gamma = 10^{-4}$. Notice that the frequency shift, Δ, and pressure coupled non-uniformity, $S_{2,10}$, are also present. It is shown that there is no quantitative difference between Figure 7.10 (a) and Figure 7.3 (a), especially in terms of the bifurcation points and relative magnitude between different $C_{2,01}$ values. Figure 7.10 (b) plots SR as a function of γ at different $C_{2,01}$ values The quasi-periodic regimes are denoted in the figure as well. Comparison between Figure 7.6 (c) and Figure 7.10 (a) shows that when exposed to the noise, the quasi-periodic behavior appears from the onset of instability to right before the mixed wave solutions. This makes it difficult to differentiate between noise driven and self-sustained quasi-periodic behavior from the time trace data (Figure 7.9) or the bifurcation plot (Figure 7.10 (b)). They can be differentiated, however, from the averaged phase portrait, such as shown in

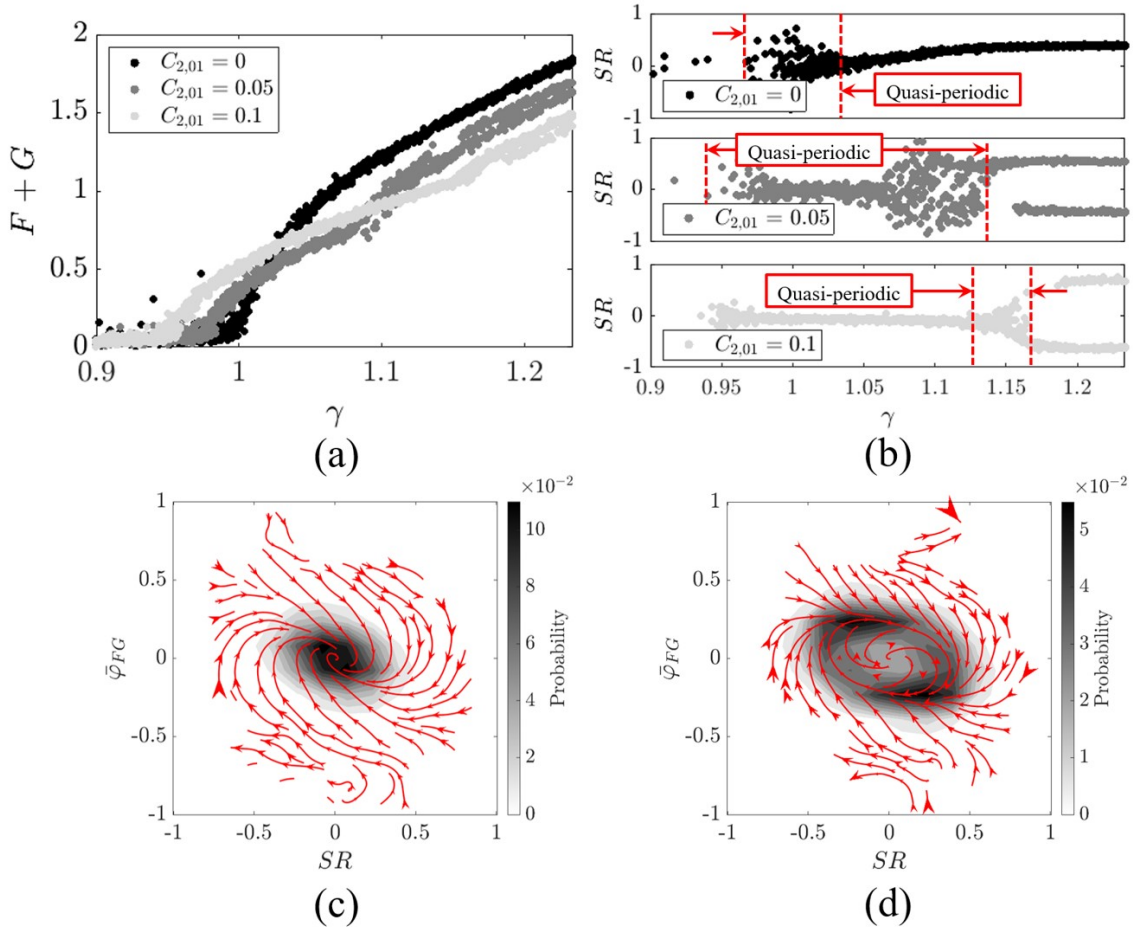

Figure 7.10: (a) Pressure anti-node magnitude as a function of γ with different $C_{2,01}$ values. (b) SR as a function of γ with different $C_{2,01}$ values with noise intensity, $\Gamma = 10^{-4}$. The data points with anti-node magnitude less than 0.1 are omitted because of their large fluctuations. The red vertical lines denote the quasi-periodic standing wave regions. Averaged phase portrait in SR and $\bar{\varphi}_{FG}$ space for (c) $\gamma = 1.067$ and (d) $\gamma = 1.073$. The other parameters are $b_{21} = -0.05, S_{2,10} = 0.02, C_{2,21} = 0.75, \bar{\omega} = 1, \Delta = -0.01$.

Figure 7.10 (c) and (d). The phase portrait was obtained by repeating the simulations at distributed initial conditions over the phase space. Figure 7.10 (c) and (d) are the phase portraits with the same condition as Figure 7.9 (b) and Figure 7.5 (b), respectively, with noise contribution. It can be seen that the center point is an attractor for the noise driven quasi-periodic case, whereas it is a repeller for the self-sustained quasi-periodic case. Also, note that the trajectory and the joint PDF form a ring structure around the center. Considering the experimental data, this suggests that the FP in Figure 6.6 (a) corresponds to a noise driven quasi-periodic standing wave, and the center FP in Figure D.1 (b) is a self-sustained quasi-periodic standing wave.

It is also interesting to note that the trajectories are CW spiraling into/around the FP in Figure 7.10 (c) and (d). As mentioned before, this is due to the 90° phase lag between SR and $\bar{\varphi}_{FG}$ oscillations. If SR and $\bar{\varphi}_{FG}$ exponentially decay to their FPs without oscillations such as a mixed wave solution in Figure 7.5 (c), the trajectories in the phase portrait would directly converge to the FP without the spiraling. This behavior can be seen experimentally in Figure 6.5 (c).

7.3.5 Effect of parametric noise, $\xi_2(t)$

This subsection considers parametric noise effects which, as noted in prior studies, introduces qualitatively new phenomenon [156, 157, 158, 159]. As noted in the prior sections, certain features of the data can be understood from purely deterministic considerations, some require additive noise, and as, discussed here, some also require introducing parametric noise. In particular, within the modeling assumptions described in subsection 7.3.1, parametric noise is required to capture the intermittency between the standing and mixed waves observed experimentally because these solutions are not simultaneously stable, as shown in Equation 7.20. Specifically, given the fact that the behavior of SR abruptly changes with γ, or equivalently β, for $C_{2,01} > 0$ as illustrated in Figure 7.10 (b), parametric noise in β will lead to the intermittency. To illustrate, we consider parametric

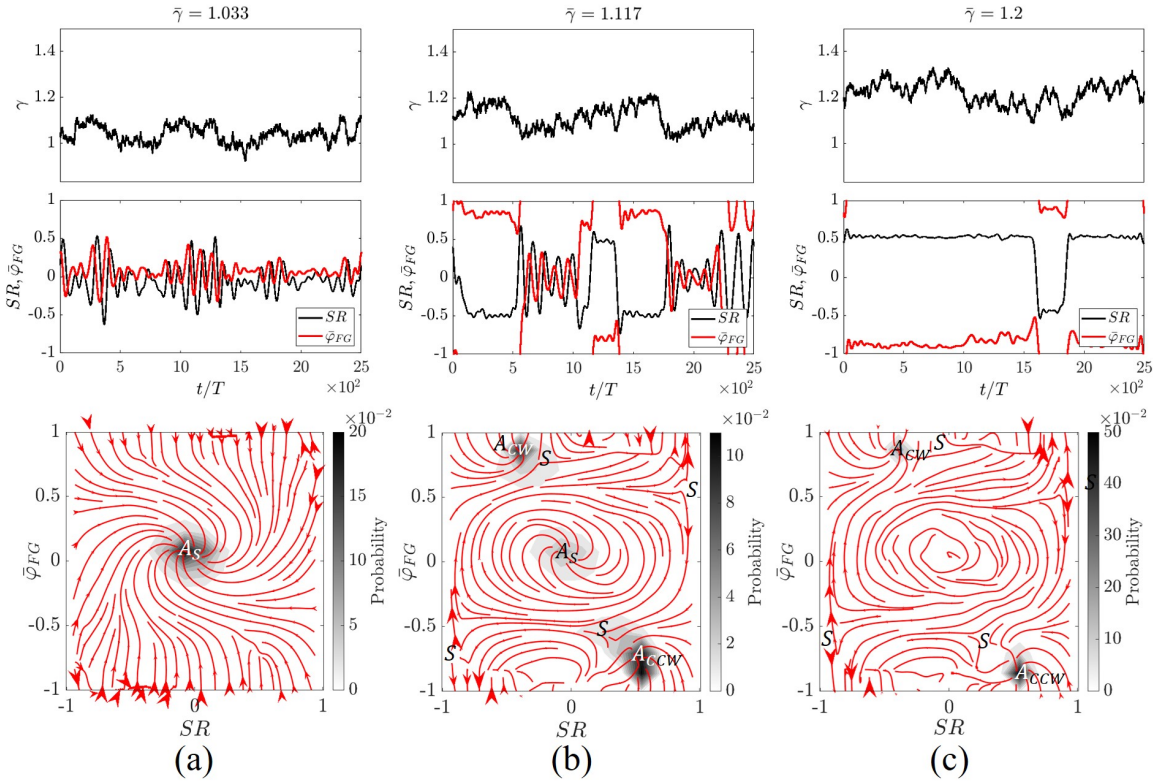

Figure 7.11: Top: time series simulation of $\gamma(t)$ for (a) $\bar{\gamma} = 1.033$, (b) $\bar{\gamma} = 1.117$, (c) $\bar{\gamma} = 1.2$. Middle: dynamics of SR and $\bar{\varphi}_{FG}$ for each $\bar{\gamma}$. Bottom: simulated phase portrait for for each $\bar{\gamma}$. The other parameters are $b_{21} = -0.05, C_{2,01} = 0.05, S_{2,10} = 0.02, C_{2,21} = 0.75, \bar{\omega} = 1, \Delta = -0.01, \Gamma = 10^{-4}$.

fluctuations in the parameter β, i.e., $h_2(p, p') = \beta\dot{p}$ and assume that the noise term, $\xi_2(t)$, follows the Ornstein–Uhlenbeck (OU) process [160], which drifts toward its mean value over time, numerically simulated with the Euler-Maruyama scheme [155]. This process is more appropriate than the Brownian motion, where the variance grows with time (i.e., in an unbounded fashion); in contrast, the variance for the OU process reaches a constant value.

Figure 7.11 illustrates three representative cases with $C_{2,01} = 0.05$ where the asymptotic means of $\gamma(t)$ are $\bar{\gamma} = 1.033, 1.117$, and 1.2. Figure 7.11 (a) - (c) describes the time trace of $\gamma(t)$ (top) as well as SR and $\bar{\varphi}_{FG}$ (middle), and the last row of Figure 7.11 represents the average phase portrait for each case.

For $\bar{\gamma} = 1.033$ (Figure 7.11 (a)), both SR and $\bar{\varphi}_{FG}$ fluctuate around zero. Note that the modulation amplitude is not steady as opposed to Figure 7.9 because of time varying

$\gamma(t)$. The dynamics of SR and $\bar{\varphi}_{FG}$ resemble the experiments in Figure 6.5 (a) except that $\bar{\varphi}_{FG}$ oscillates around 0.4. Given the fact that φ_{FG} is related to the anti-nodal line (Equation 4.6), the value of which depends on the azimuthal origin, the discrepancy can be eliminated by rotating the origin. The phase portrait in Figure 7.11 (a) shows a stable attractor at the center (A_S), and the trajectories are spiraling into the attractor. These results resemble the experimental observations in Figure 6.6 (a).

When $\bar{\gamma} = 1.117$, SR and $\bar{\varphi}_{FG}$ start to show intermittency. In particular, transition of SR and $\bar{\varphi}_{FG}$ from one state to the other occurs simultaneously, which was evident from the experiments in Figure 6.5 (b). In the simulation, they are hopping between three different states, i.e., quasi-periodic standing wave, and CCW/CW mixed waves. The phase portrait in Figure 7.11 (b) reveals three attractors, $A_S, A_{CW/CCW}$, as well as multiple saddle points. Notice that the joint PDF around A_{CCW} is denser than that around A_{CW}, manifesting the system's preference in a CCW mixed wave. The portrait reasonably coincides with Figure 6.6 (b).

Lastly, for $\bar{\gamma} = 1.2$ (Figure 7.11 (c)), SR stays either ± 0.5, and $\bar{\varphi}_{FG}$ remains around ± 1. The transition between two states may occur when $\gamma(t)$ drops below a certain value. The corresponding phase portrait in Figure 7.11 (c) manifests two stable attractors, $A_{CW/CCW}$, and multiple saddle points. Here, A_S is no longer a stable attractor, which explains the reason for no realization at the center in Figure 6.6 (c). Similar to Figure 7.11 (b), the joint PDF demonstrates the preference in CCW spinning wave. Comparing with Figure 6.6 (c), notice the similarities.

7.4 Discussion

It is worth relating the simulation results to the experimental observations. In particular, the different linear and nonlinear coefficients in the formulation are certainly coupled through various combustor and flame physics. This section briefly reflects on these points and how they manifest themselves in the data.

First, the modeling results clearly illustrate the very important role of azimuthal non-uniformities; because there are eight outer nozzles in the experimental facility, this implies that C_8 and S_8 are nonzero; as these higher order terms average out in the analysis, they have no impact on the first azimuthal mode, see Equation 7.7. In addition, lower order azimuthal non-uniformities, i.e., C_2, and S_2, are nonzero for non-uniform fuel staging cases. However, comparison of the modeling results and experimental data implies that C_2 and S_2 are nonzero even in the "uniform" fuel staging case, due to inevitable manufacturing differences, leakage flows, and so forth. As such, these results show that relatively small manufacturing variations can introduce significant impacts on spin direction, the dominance of spinning/standing waves, and so forth (e.g., see Figure 7.1), and also suggests that these behaviors can vary between engines.

Second, Equation 7.10 shows that Δ and $C_{2,10}$ (not $C_{2,01}$) are correlated, i.e., if $|C_{2,10}|$ gets larger, $|\Delta|$ as well. This explains the reason for higher modulation frequency with higher OR at a fixed instability amplitude in Figure 6.10 (a). However, the sign of the correlation depends on the sign of b_{10}. A natural question is whether it is positive or negative. This can be answered from a physical point of view. Given the azimuthal origin at 3 o'clock position, ω_1 and ω_2 are the undamped natural frequencies of two orthogonal standing waves oscillating in horizontal and vertical directions, respectively. $C_{2,10}$ is the coefficient of $\cos(2\theta)$ of the non-uniformity. If $C_{2,10} > 0$, then the temperature (or speed of sound) distribution in the horizontal direction would be higher than that in the vertical direction, giving rise to $\omega_1 > \omega_2$. Therefore, it is reasonable to assume $\Delta\omega = \omega_2 - \omega_1 < 0$ when $C_{2,10} > 0$, and vice versa, or equivalently, $b_{10} < 0$ from Equation 7.10. As shown in Figure 7.11, the simulation with this assumption provides CW spiraling trajectories around A_S in the phase portrait, which is in agreement with the experiments.

Third, it is shown that the non-uniformity, or the frequency spacing between two orthogonal standing eigenmodes, causes the oscillation in φ_{FG} for the quasi-periodic standing wave. Since φ_{FG} is the phase difference between CCW/CW waves, the time derivative of

φ_{FG}, or $d\varphi_{FG}/dt$, is the frequency difference between CCW/CW waves, which also oscillates in time. This explains why the spectra of both CCW/CW waves exhibit double peaks in Figure 6.4 (a), i.e., the frequency difference between CCW/CW waves is not constant, but rather oscillating. Furthermore, since φ_{FG} is directly related to the anti-nodal line, θ_a, by Equation 4.6, oscillation in φ_{FG} is equivalent to oscillation in anti-nodal line. Thus, one can interpret that the frequency difference between CCW/CW waves depends on the behavior of theanti-nodal line. For example, when the anti-nodal line is fixed, the frequency difference is zero. When the anti-nodal line is oscillatory, so is the frequency difference. When the anti-nodal line is rotating at a constant angular velocity, the frequency difference is constant. This rotation in the anti-nodal line may result from the azimuthal mean flow [98] but not necessarily because of the non-uniformity. For example, even if the azimuthal mean flow is present, the anti-nodal line can be stuck between the burners, and oscillate, leading to oscillation in frequency difference between CCW/CW waves as shown in this study.

Fourth, Figure 6.9 (a) and Figure 7.10 (a) are in good agreement in terms of instability amplitude. Specifically, the behavior of the first Hopf point in the experiment is in agreement with that in the simulation up to $OR \leq 0.55$. For $OR > 0.55$, however, the Hopf point is retarded as opposed to the model. The reason for this disagreement is most probably twofold. First, the direct comparison between Figure 6.9 (a) and Figure 7.10 (a) assumes that the mass flow rate is proportional to the ratio between linear coefficients, γ , which is not guaranteed. Furthermore, in reality, changing the mass flow rate may affect not only the linear coefficient, but also the other parameters such as non-uniformity and the damping rate, which in turn, affect the first Hopf point. Second, the governing equations in this paper assumed weakly nonlinear, which may not valid for strong non-uniform fuel staging. Specifically, the pressure expansion in Equation 7.4 is not valid for large spatial temperature variations.

7.5 Conclusion

This chapter presented low order modeling work to better understand wave structures and temporal dynamics of azimuthal modes in combustors. The chapter analyzed a weakly nonlinear model, derived from the wave equation and a generalized source term. The source term was modeled with a Taylor expansion up to fourth order with the additive and parametric noise terms. Each coefficient in the expansion was allowed to vary azimuthally. This model clearly showed that these parameters influence the azimuthal mode stability as follows.

- Linear damping/growth coefficients, α and β, determine the linear stability of two standing eigenmodes.
- The parameter, $C_{2m,01}$, describing the azimuthal non-uniform coupling between the source and $\dot{p}$, influences both linear (stability boundary) and nonlinear process (dependence of limit cycle amplitude, such as upon β). It also affects relative preference between standing and spinning/mixed waves.
- The parameter, $C_{2m,21}$, describing the azimuthal non-uniform coupling between the source and $p^2\dot{p}$, affects relative preference between standing and spinning/mixed waves.
- The parameter, $S_{2m,10}$, describing the azimuthal non-uniform coupling between the source and p, introduces a preference in CW/CCW spinning direction on the system.
- The parameter, $C_{2m,10}$, describing the azimuthal non-uniform coupling between the source and p, causes a frequency spacing between the two orthogonal standing eigenmodes, Δ, which introduces quasi-periodic oscillations. The system can decay or self-excited in an oscillatory manner depending upon β.
- Additive noise, Γ, with nonzero Δ leads to quasi-periodic oscillations, even in cases

where the limit cycle FP is stable, as it excites oscillatory, but decaying, disturbances around the limit cycle FP at a specific frequency, Δ.

- Parametric noise, $\xi_2(t)$, is responsible for the intermittency between standing and spinning/mixed waves.

The effects of each parameter are summarized in Figure 7.12. The low order modeling was clearly useful in understanding the experimental observations. First, the instability magnitude increases with linear growth rate (or mass flow rates), but the rate of increase is reduced with increasing the non-uniformity (or OR). Second, as the magnitude increases, the azimuthal mode starts from a standing wave, passes the intermittency between standing and mixed waves, and then becomes a mixed wave. Third, a quasi-periodic oscillation appears during the standing wave. Last, the mode prefers CCW to CW spinning direction during the mixed wave. Finally, the model clearly emphasized that important real world effects, such as azimuthal asymmetry, introduce qualitatively important phenomena, such as quasi-periodicity.

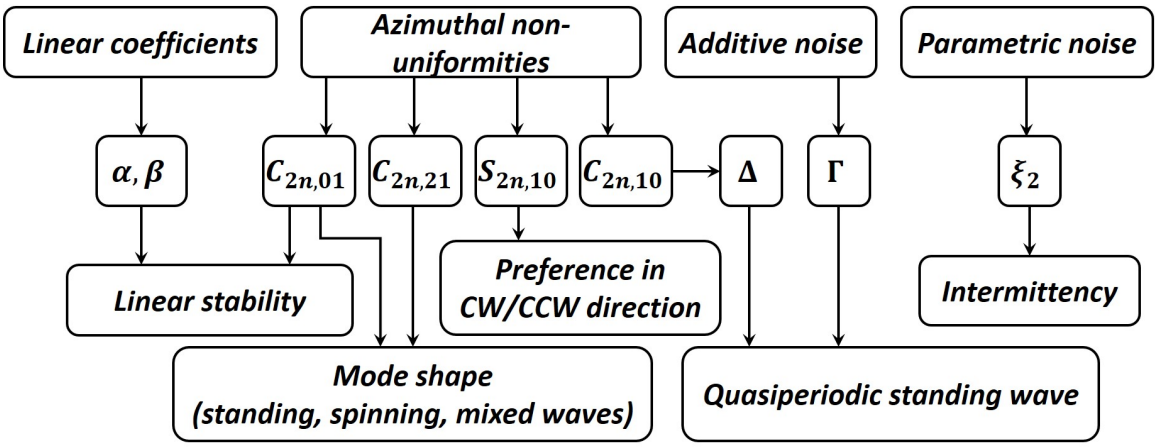

Figure 7.12: Effects of each parameter on azimuthal modal dynamics.

CHAPTER 8
CONCLUSION AND FUTURE WORK

This chapter summarizes the key contributions of this thesis. It recapitulates the results and key findings of each chapter. Additionally, this chapter proposes future works and new topics that originated from the current works.

8.1 Summary of Contributions

The first major contribution of this paper is that it introduces the optimal sensor locations for detecting the azimuthal thermoacoustic instabilities. In many research studies [87, 85, 82], multiple sensors were placed equidistantly to measure the pressure oscillations along the circumference. As shown in chapter 4, however, this sensor configuration may result in an infinite error for a certain azimuthal mode number, and thus, uniform sensor distribution must be avoided in real applications. In addition, for large scale, expensive facilities or testing campaigns, such as engine testing, equidistant configuration may not be possible because of the limited space. This leads to a question of where to place those multiple sensors. Chapter 4 directly tackled this problem. Given the azimuthal mode number and the number of sensors, the optimal sensor locations are determined in such a way that they minimize the variance of the estimates, which in this case is the complex amplitudes of CW/CCW rotating waves. For a single azimuthal mode, simultaneous nonlinear equations, the solutions of which correspond to the optimal sensor locations, are analytically derived. The nonlinear equations can be solved numerically, but the physical interpretation of the equations allows us to solve them intuitively without computational efforts. This method is verified by comparing the sensor locations obtained from the computation. For multiple azimuthal modes considered, the chapter proposes two different methods for determining the optimal sensor locations; mini-max and mini-sum approaches. The mini-max

approach numerically finds the sensor locations that minimize the worst cases, whereas the mini-sum approach minimizes the sum of the variances from each azimuthal mode number. Table A.1 summarizes the optimal sensor locations with different combinations of a number of sensors and azimuthal mode numbers. This will help manufacturers determine the sensor locations depending on their interests.

The second major contribution is the identification of high frequency azimuthal acoustic modal dynamics. One of the problems of the high frequency instabilities is that the frequencies of potential modes are too close to each other, preventing us from differentiating between them. For a can combustor, for example, the natural frequencies of longitudinal and azimuthal modes as well as mixed modes between them are so densely distributed that they may occur simultaneously as shown in this study. This high frequency characteristic makes it difficult to differentiate between complex modes solely based on the frequency contents. Chapter 5 solved this problem by measuring pressure signals at multiple axial and azimuthal locations and implementing axial and azimuthal wave equations that are coupled through the dispersion relation. The pressure distributions obtained from this method are compared with those obtained from the FEM, showing excellent agreements between them. Moreover, this method is particularly important in combustors experiencing the thermoacoustic instabilities in terms of mitigation strategy. For example, the effectiveness of an acoustic damper, which has been used to suppress the instabilities, strongly depends on its location relative to pressure anti-node. Since this method enables us to estimate the location of the pressure anti-node, it will help us determine the optimal location for the acoustic damper.

Chapter 6 further analyzed the modal dynamics of azimuthal instabilities. Given the fact that the azimuthal mode can take the form of either a standing, spinning, or mixed wave, it is quite important to identify how the modal structure varies with different operating conditions. The results showed that the instability magnitude and the modal nature are very sensitive to the operating conditions, such as the mass flow rates (or thermal power) and

azimuthal fuel staging (or outer ratio). Similar works have been conducted in past studies, but the major difference between the facility used in this study and the facilities used in prior research institutes is its thermal power comparable to the industrial scale combustor. The facility is capable of delivering the thermal power of 2.5 MW with a high Reynolds number. In addition, the facility contains multiple nozzles with different swirl directions, making flow fields and flame structure very complicated (i.e., it is not simply a single bunsen flame), but they are more comparable to the industrial scale combustors. These imply that the experimental results from this study can be applied to real applications.

The last contribution of this thesis is the development of the low order modeling that captures the important experimental observations. These observations can be summarized as follows: azimuthal non-uniformities, background noise, oscillations of nodal line and spinning direction, and frequency spacing from the spectrum. While previous models capture some of these effects, a key contribution of chapter 7 is to present a comprehensive framework that includes all these effects. This chapter used a traditional approach used in many previous studies, but we are able to accomplish this goal by introducing a generalized source term in the wave equation, which differentiates this from the past studies. It is interesting to note that although the experimental facility is significantly complicated in terms of flow fields and flame structure, the low order model successfully captures the important features observed in the experiments.

The contributions from each chapter are essential to monitoring the azimuthal thermoacoustic instability, providing mitigation strategy, and developing the stability margin in real time. The author believes that the works presented here will be greatly beneficial to combustion systems experiencing thermoacoustic issues.

8.2 Future Work

This section recommends several future works that have not been answered from this thesis or that can support the hypotheses suggested from the thesis. These future works

will enhance the understanding of the physics governing the azimuthal thermoacoustic instabilities.

The first recommended future work is experimental. The experimental study in chapter 6 shows that the instability magnitude as well as the modal natures are strongly dependent on the azimuthal non-uniformity. This azimuthal non-uniformity is quantified by the outer ratio, which is the fuel split between two separate fuel lines going through the outer nozzles. However, this does not represent the actual flame non-uniformity. To better quantify the non-uniformity, the flame structure needs to be measured. For example, chemiluminescence or planar laser induced fluorescence (PLIF) can be used to measure the flame structure. Note that we have used the chemiluminescence measurement where the camera is pointing the flame from the side window. To estimate the azimuthal non-uniformity, however, the measurements must be taken from the downstream, pointing to the upstream flame direction. This experimental setup may be challenging because of the hot product flowing towards the camera, but an air cooled mirror can be used to avoid this situation [9, 80]. The azimuthal non-uniformity obtained from the flame structure can be directly related to the azimuthal non-uniformity parameters, C_n and S_n, in the low order model.

In addition, Figure 6.19 shows the dependence of azimuthal spinning direction on pilot ratio. We hypothesize that this might be related to the bulk flow motion [98], i.e., for high pilot ratio, the pilot nozzle, the swirl direction of which is CW, is more dominant than the outer nozzles with CCW swirlers, resulting in a CW mixed wave. Furthermore, Figure 6.20 shows the effect of preheat temperature on the modal nature. This suggests that increasing preheat temperature may change the bulk azimuthal flow direction, which, in turn, affects the azimuthal spinning direction. To support these hypotheses, azimuthal flow field must be measured, for example, using a particle image velocimetry (PIV). With this measurement, we can understand how the dominant azimuthal bulk flow changes with the operating conditions such as pilot ratio and preheat temperature.

The second recommendation for the future work is system identification. We learn from the low order model that the azimuthal instability is a strong function of γ, or the ratio between linear amplification/damping coefficients. The distance between γ and unity provides the linear stability of the system. For example, if γ is much lower than unity, the system is linearly stable and far away from the stability boundary. If γ is less than unity, but close to it, the system is still linearly stable, but close to the stability boundary. In order to make this information useful in practical systems, we need to be able to extract this parameter from the measurements, i.e., system identification. The system identification for thermoacoustic instability has been developed by other researchers [161, 162, 163, 164, 165, 166]. Typically, the method uses pressure magnitude measured from one sensor, and then extracts the linear damping/growth coefficients using a Fokker-Planck equation. However, the method is applicable for only a longitudinal mode where the pressure magnitude is relatively steady, but not for the azimuthal mode because the pressure magnitude measured at a single point is typically not constant. Rather, it oscillates periodically because of the oscillation in the anti-nodal line, see Figure 6.4 (a). Therefore, a new system identification approach needs to be developed for the azimuthal mode. One potential method could be using pressure magnitude at the anti-node instead of pressure magnitude at a single sensor. As can be seen in Equation 4.6), the anti-node pressure magnitude is not a function of anti-node location, and thus, it is only perturbed by the additive noise. Therefore, the traditional method, the Fokker-Planck equation, may be applicable for extracting the linear coefficient, which needs to be proven in the future.

Appendices

APPENDIX A

SUMMARY OF OPTIMAL SENSOR LOCATIONS

Table A.1 summarizes the optimal sensor locations for different combinations of sensor number, n, and azimuthal mode numbers, m. Here, S1 is fixed at 0°, and the values in the table indicate the other sensor's locations. For $n = 3$ and $m = \{1, 2\}$, for example, the optimal locations for S2 and S3 are either $(60°, 120°)$ or $(120°, 240°)$. Δ in $n = 4$ case means the angle between each pair. For example, $\Delta = \{45°, 135°\}$ indicates that the sensors are optimally located as long as the angle between two sensors of each pair is either 45° or 135°. The relative angle between two pairs does not matter. Similarly, $\Delta = \{90°\}$ indicates that two sensors of each pair must be placed 90° apart.

Table A.1: Optimal sensor locations for different combinations of n and m.

m	n		
	2	3	4
{1}	90°	60°, 120° 120°, 240°	Δ={90°}
{2}	45° 135°	30°, 60° 30°, 150° 60°, 120° 60°, 210° 120°, 240°	Δ={45°, 135°}
{3}	30° 90° 150°	20°, 40° 20°, 100° 20°, 160° 40°, 80° 40°, 140° 40°, 200° 80°, 160° 80°, 220° 100°, 200°	Δ={30°, 90°, 150°}
{1, 2}	52° 128°	60°, 120° 120°, 240°	45°, 90°, 135° 90°, 135°, 225°
{1, 3}	90°	79.5°, 100.5° 79.5°, 159° 100.5°, 201°	Δ={90°}
{2, 3}	34.5° 145.5°	38°, 76° 38°, 142° 76°, 218°	15°, 45°, 150° 15°, 45°, 330° 15°, 150°, 225° 30°, 75°, 220° 30°, 135°, 165° 45°, 90°, 135° 45°, 135°, 270° 45°, 150°, 195°
{1, 2, 3}	37° 143°	41.5°, 83° 41.5°, 138.5° 83°, 221.5°	45°, 90°, 135° 90°, 135°, 225°

APPENDIX B

ESTIMATION OF SPIN RATIO BIAS

As can be seen in Figure 6.5, SRis an intrinsically noisy or oscillatory quantity and, the fact that it cannot exceed unity means that there is a potential for bias errors in its estimate. For example, if the average SRis 0.9, and it oscillates about its value with an amplitude of 0.2, its maximum value still cannot exceed 1.0, while its minimum is 0.7. As such, the estimate of it will be biased towards SR$= 0$ when exposed to noise. Understanding the magnitude of this bias error is important relative to understanding the nature of the attractors. For example, an estimated SRof 0.7 can be interpreted in different ways, such as a mixed wave of SR$= 0.8$ with small noise intensity, or a spinning wave of SR$= 1$ with large noise intensity. In order to estimate this bias error, we used Monte Carlo simulations to find a combination of true SRand noise variance such that the peak and skewness of the simulated SR PDF coincide with those of the experimental SR PDF.

To illustrate this point, CCW/CW waves were modeled as a sum of complex oscillatory signal and noise following the complex normal distribution with a variance of σ^2.

$$\begin{gathered} \hat{f}(t) = Fe^{i\omega t} + \xi_F(t) \ \text{ and } \ \hat{g}(t) = Ge^{i\omega t} + \xi_G(t) \\ \text{where } \ \xi_{F,G} \sim CN(0, \sigma^2) \end{gathered} \tag{B.1}$$

Here, F and G are the constant CCW/CW magnitudes. The true SR(SR_t) and simulated SR(SR_s) are then given by:

$$SR_t = \frac{F-G}{F+G}, \ \ SR_s(t) = \frac{|\hat{f}(t)| - |\hat{g}(t)|}{|\hat{f}(t)| + |\hat{g}(t)|} \tag{B.2}$$

The PDF of SR_s at different combinations of SR_t and σ was numerically obtained to extract the peak and the skewness. Next, a combination of SR_t and σ that yields the peak

and the skewness similar to those from the experiments was found. The bias error was then evaluated as the difference between SR_t and the average of SR_s.

APPENDIX C

SOUND SPEED ESTIMATION

In order to utilize Equation 5.6, we must determine the axial wavenumber in advance, which depends on the sound speed. The axial wavenumber and the sound speed are related by the dispersion relation. For homogeneous sound speed with no mean flow in a cylindrical duct, the dispersion relation is given by Equation 2.23 or

$$f = \frac{c}{2\pi}\sqrt{k_r^2 + k_z^2} = \frac{c}{2\pi}\sqrt{\left(\frac{\alpha_{ml}}{R}\right)^2 + k_z^2} \tag{C.1}$$

where R is the chamber radius, c sound speed, and α_{ml} the root of $\frac{d}{dr}J_m(\alpha_{ml}) = 0$. The set of α_{ml} for the different radial and azimuthal mode number is tabulated in Table C.1 . Given the frequency, f, from the spectrum Figure 5.3 and the dispersion relation, Equation C.1, we can obtain the axial wavenumber, k_z, as a function of sound speed. Given k_z, we can utilize Equation 5.6 and the associated error, which depends on speed of sound.

Without any noise, R_z^2 given by Equation 5.7 would be unity. However, the noise is inevitable in a turbulent combustion environment, resulting in R_z^2 less than unity. Therefore, R_z^2 is evaluated for a range of values of sound speed, and the optimal sound speed is

Table C.1: Roots of $\frac{d}{dr}J_m(\alpha_{ml}) = 0$

$\alpha_{ml}/2\pi$	$m=0$	$m=1$	$m=2$	$m=3$
$l=0$	0	0.2930	0.4861	0.6686
$l=1$	0.6098	0.8485	1.0673	1.2757
$l=2$	1.1166	1.3586	1.5867	1.8058

determined as the value that maximizes R_z^2 [111].

$$c_{\mathrm{opt}} = \underset{c\in[c_l,c_u]}{\operatorname{argmax}} \mathrm{R}_z^2 \tag{C.2}$$

where $c_{l/u}$ are the lower and the upper bounds for the sound speed values, which are estimated from the measured temperature at the exhaust (1200 K) and the adiabatic flame temperature (1800 K), respectively. R_z^2 was evaluated at the range of sound speed given each peak, f_{p1} and f_{p2}, yielding two plots of R_z^2 with respect to sound speed values as shown in Figure C.1 (a). Here, $\mathrm{R}_{z,1}^2$ and $\mathrm{R}_{z,2}^2$ denote the R_z^2 value of f_{p1} and f_{p2}, respectively. The optimal sound speed is supposed to maximize both R_z^2 simultaneously, but the trends of each R_z^2 are quite different. Therefore, the optimal value is selected in such a way that it maximizes the product of each R_z^2, i.e., $\mathrm{R}_{z,1}^2 \cdot \mathrm{R}_{z,2}^2$. In Figure C.1 (a), the two red dots represent the first and the second local maxima of $\mathrm{R}_{z,1}^2 \cdot \mathrm{R}_{z,2}^2$. As shown in the result section, the sound speed of the first maxima, which is 794 m/s, provides a good agreement between the experiments and the FEM, validating the method of sound speed estimation. For reference, this sound speed value corresponds to a temperature of 1570 K. However, considering the uncertainty of the least squares fit, the value at the other local maxima, which is 763 m/s, is also investigated here.

Figure C.1 (b) illustrates the eigenfrequencies of each mode obtained from the FEM depending on the sound speed at the combustion region. Note that the eigenfrequencies of 1A-a and 1A-b modes saturate at high sound speed because of the frequencies being lower than the cutoff frequency. Given the sound speed of 763 m/s, f_{p1} and f_{p2} from the experiments are close to 1A1L-a and 1A1L-b modes from the FEM, respectively. Therefore, the pressure distribution along the axial direction for these modes are compared in Figure C.2.

Figure C.2 illustrates the pressure magnitude and phase distribution from the experiments and the FEM in the axial direction for 1A1L-a and 1A1L-b modes. Notice that for 1A1L-a mode, a discrepancy between the experiments and the FEM appears, i.e., the nodal line location is not consistent, and the phase relationship between the sensors does

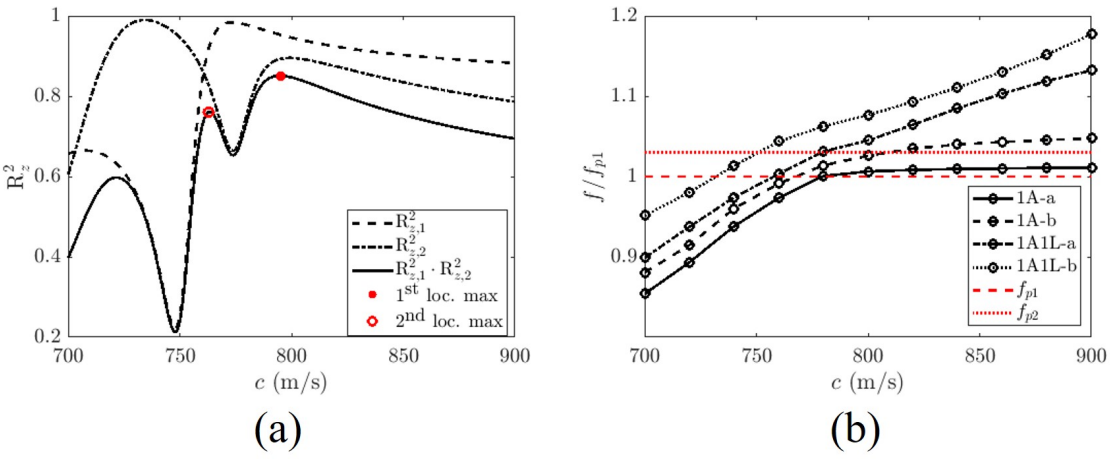

Figure C.1: (a) R_z^2 with respect to sound speed for each peak. (b) sound speed versus eigenfrequencies of each mode obtained from FEM.

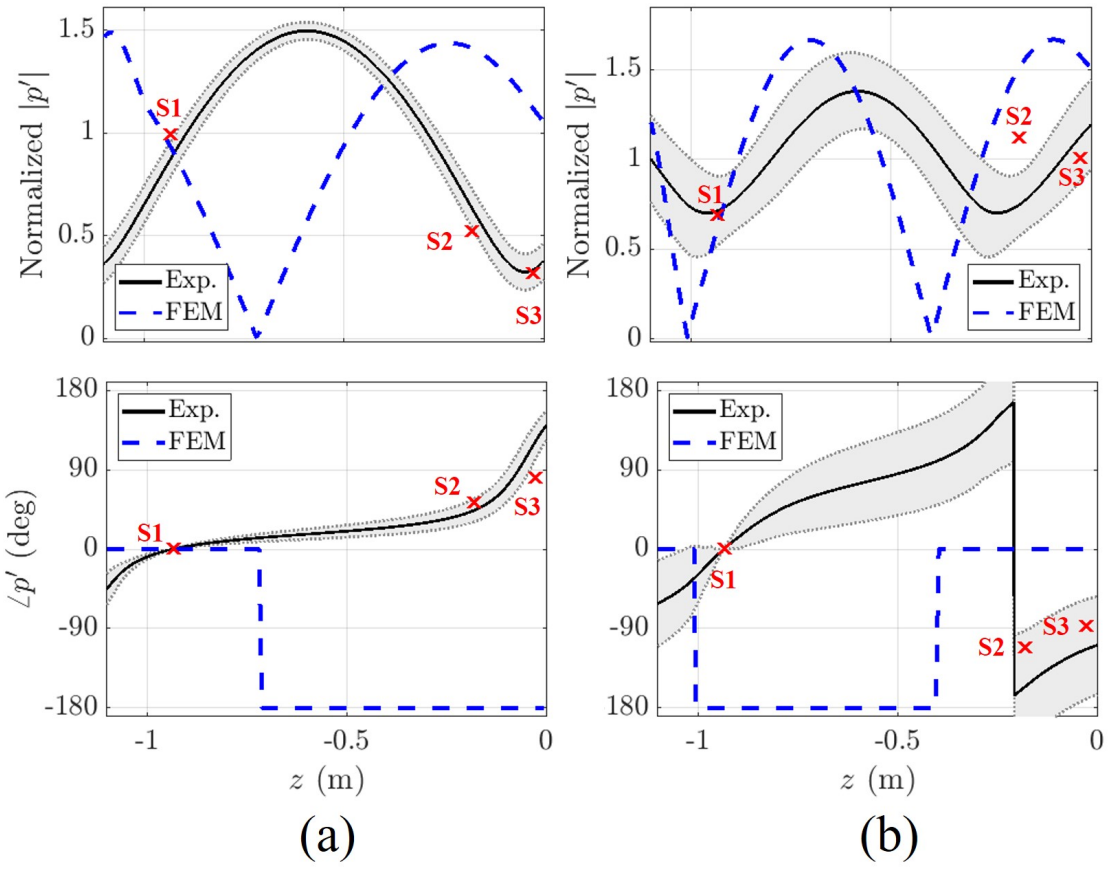

Figure C.2: Pressure magnitude and phase distributions along the axial direction for $c =$ 763 m/s. (a): 1A1L-a mode. (b): 1A1L-b mode.

not match. Specifically, sensor 1 is nearly in phase with sensors 2 and 3 in the experiments, which is not in the FEM. 1A1L-b mode from the FEM is relatively close to that from the experiment, but the optimal sound speed is supposed to provide a good agreement for both modes simultaneously. Therefore, one can conclude that not only is 794 m/s the optimal sound speed, but also estimating the sound speed by minimizing a least squares error is acceptable. Once the sound speed is determined, the associated temperature can be estimated from the ideal gas assumption, i.e., $c = \sqrt{\gamma \mathcal{R} T}$ where γ and $\mathcal{R}$ are specific heat ratio and the gas constant for air, respectively, under lean condition.

APPENDIX D

PHASE AVERAGED PORTRAIT AT DIFFERENT OPERATING CONDITIONS

Figure D.1 shows two phase portraits at two different operating conditions. The sampling length was 30 seconds, or approximately 50,000 cycles of oscillations. The portraits demonstrate the system's preference in CCW (Figure D.1 (a)) and CW (Figure D.1 (b)) mixed wave depending on the operating conditions, which are summarized in Table D.1.

Table D.1: Operating conditions for Figure D.1

Case	Preheat temp. (K)	Equiv. ratio (-)	PR	OR	Air mass flow (kg/s)
Figure D.1 (a)	625	0.57	0.087	0.5	1.41
Figure D.1 (b)		0.55	0.09		1.34

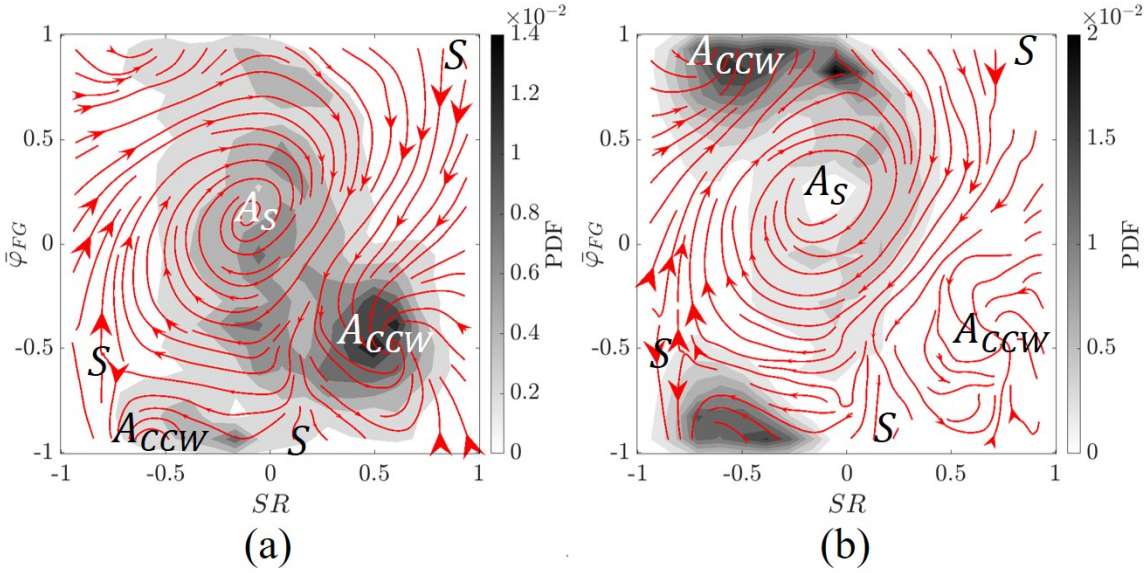

Figure D.1: Representative data obtained under conditions detailed in Figure D.1 that exhibit (a) CCW and (b) CW preferred wave dynamics.

APPENDIX E

RELATIONSHIP BETWEEN TWO DECOMPOSITION METHODS

There are two methods to decompose the azimuthal pressure. One decomposes the pressure into two purely standing eigenmodes orthogonal to each other. The governing equations, Equation 7.13 are derived based on this method. When one of the modes has a zero amplitude or the phase difference between two modes is 0 or $\pm\pi$, the final mode is a purely standing wave. When they have equal amplitudes with a phase difference of $\pm\pi/2$, the final mode is a purely spinning wave. As shown, this decomposition method requires amplitudes and phase difference information to determine the final mode. However, their values strongly depend on the orientation of acoustic structure relative to the azimuthal origin. This will be problematic for a case where the structure is fluctuating as shown in Figure 6.5 (a).

Alternatively, two counter-rotating decomposition method has been used widely, especially in experimental studies. This method decomposes the pressure into CW and CCW eigenmodes. When one of the modes is suppressed, the final mode is a purely spinning wave, and when they have equal amplitude, then the final mode is a purely standing wave. The key advantage of this decomposition method is that first, the final mode is determined based on only CCW/CW amplitudes. The phase difference only affects the orientation of the wave structure. Second, the CCW/CW amplitudes do not depend on the azimuthal origin. For these reasons, numerous experimental studies including this work adopted this decomposition method, and presented their results. In this work, we simulated the governing equation describing the dynamics of two orthogonal standing modes, and transformed them into the two counter-rotating modes to present the results. This appendix introduces the relationship between the two decomposition methods.

Equation 6.2 represents the complex acoustic pressure in azimuthal direction written as

the superposition of CW and CCW waves. To convert the pressure into a real quantity, we add a complex conjugate ($c.c.$) to Equation 6.2

$$p(\theta,t) = Fe^{i(m\theta+\varphi_F-\bar{\omega}_{FG}t)} + Ge^{-i(m\theta-\varphi_G-\bar{\omega}_{FG}t)} + c.c. \tag{E.1}$$

After some manipulations, the acoustic pressure can be rewritten as follows.

$$\begin{aligned} p(\theta,t) =& [2F\cos(\bar{\omega}_{FG}t-\varphi_F) + 2G\cos(\bar{\omega}_{FG}t) - \varphi_G]\cos(m\theta) \\ &+ [2F\sin(\bar{\omega}_{FG}t-\varphi_F) - 2G\sin(\bar{\omega}_{FG}t-\varphi_G)]\sin(m\theta) \end{aligned} \tag{E.2}$$

Comparing Equation E.2 with Equation 7.4 and Equation 7.11 yields the following relations.

$$\begin{aligned} 2F\cos(\bar{\omega}_{FG}t-\varphi_F) + 2G\cos(\bar{\omega}_{FG}t-\varphi_G) &= A\cos(\bar{\omega}t+\varphi_A) \\ 2F\sin(\bar{\omega}_{FG}t-\varphi_F) - 2G\sin(\bar{\omega}_{FG}t-\varphi_G) &= B\sin(\bar{\omega}t+\varphi_B) \end{aligned} \tag{E.3}$$

Using the trigonometric identities, one can deduce the following relations.

$$\begin{aligned} \bar{\omega}_{FG} &= \bar{\omega} \\ A^2 &= 4(F^2+G^2+2FG\cos\varphi_{FG}) \\ B^2 &= 4(F^2+G^2-2FG\cos\varphi_{FG}) \\ \varphi &= \arctan\left(\frac{2FG\sin\varphi_{FG}}{G^2-F^2}\right) - \frac{\pi}{2} \end{aligned} \tag{E.4}$$

Equation E.4 enables us to transform the variables, F, G, and φ_{FG} into A, B, and φ. The opposite transformation can be achieved by the following relations.

$$\begin{aligned} F^2 &= \frac{1}{16}(A^2+B^2-2AB\sin\varphi) \\ G^2 &= \frac{1}{16}(A^2+B^2+2AB\sin\varphi) \\ \varphi_{FG} &= \arctan\left(\frac{2AB\cos\varphi_{FG}}{A^2-B^2}\right) \end{aligned} \tag{E.5}$$

Table E.1 summarizes which conditions of A, B, and φ give the standing or spinning wave.

For simplicity,Table E.1 considers only purely standing and spinning waves. The other cases that are not described in Table E.1 correspond to a mixed wave.

Table E.1: Azimuthal mode dependence on A, B, φ, F, G, and φ_{FG}

Decomposition method	Standing wave	CCW spinning wave	CW spinning wave
Two standing eigenmodes	$AB = 0$ or $\varphi = 0, \pm\pi$	$A = B \neq 0$ and $\varphi = -\frac{\pi}{2}$	$A = B \neq 0$ and $\varphi = -\frac{\pi}{2}$
Two spinning eigenmodes	$F = G \neq 0$	$F \neq 0$ and $G = 0$	$G \neq 0$ and $F = 0$

APPENDIX F

FIXED POINT STABILITY ANALYSIS

Substituting Equation 7.18 into Equation 7.14 with $\Delta = S_{2,10} = \Gamma = \zeta = 0$ yields the following linear system:

$$\begin{bmatrix} \dot{A}' \\ \dot{B}' \\ \dot{\varphi}' \end{bmatrix} = \boldsymbol{J} \begin{bmatrix} A' \\ B' \\ \varphi' \end{bmatrix} \tag{F.1}$$

where the elements of the 3×3 Jacobian matrix $\boldsymbol{J}$ are given by:

$$\begin{aligned}
\boldsymbol{J}_{11} &= \left(\frac{1}{2} + \frac{C_{2,01}}{4}\right)\beta - \frac{\alpha}{2} + \frac{3b_{31}}{32}[9A^2 + (2+\cos 2\varphi)B^2] \\
\boldsymbol{J}_{12} &= \frac{3b_{31}}{16}AB(2+\cos 2\varphi) \\
\boldsymbol{J}_{13} &= -\frac{3b_{31}}{16}AB^2 \sin 2\varphi \\
\boldsymbol{J}_{21} &= \frac{3b_{32}}{16}AB(2+\cos 2\varphi) \\
\boldsymbol{J}_{22} &= \left(\frac{1}{2} - \frac{C_{2,01}}{4}\right)\beta - \frac{\alpha}{2} + \frac{3b_{32}}{32}[9B^2 + (2+\cos 2\varphi)A^2] \\
\boldsymbol{J}_{23} &= -\frac{3b_{32}}{16}BA^2 \sin 2\varphi \\
\boldsymbol{J}_{31} &= -\frac{3b_{32}}{16}A \sin 2\varphi \\
\boldsymbol{J}_{32} &= -\frac{3b_{31}}{16}B \sin 2\varphi \\
\boldsymbol{J}_{33} &= -\frac{3}{16}(b_{32}A^2 + b_{31}B^2)\cos 2\varphi
\end{aligned} \tag{F.2}$$

In order to determine the stability of each FP, we first need to find the eigenvalues that satisfies the following characteristic equation:

$$\det(\boldsymbol{J}|_{A=A^*,B=B^*,\varphi=\varphi^*} - \lambda \boldsymbol{I}) = 0 \tag{F.3}$$

Here, λ is the eigenvalue and $\boldsymbol{I}$ is a 3×3 identity matrix. Since the system is three dimensional, the characteristic equation can be expressed as the polynomial up to cubic order in terms of λ:

$$\lambda^3 + a_2\lambda^2 + a_1\lambda + a_0 = 0 \tag{F.4}$$

where a_0, a_1, and a_2 are the coefficients of the characteristic equation. For any given FP to be stable, all solutions of Equation F.4 must be real and negative, which requires solving the cubic equation. Alternatively, the stability of each FP can be assessed by using the Routh Hurwitz (RH) criterion without solving the equation [167, 168, 169, 170]. The RH criterion states that the necessary and sufficient conditions for a FP to be stable are:

$$\textbf{i}.\ a_i > 0 \ \text{ for } \ i = 0, 1, 2 \quad \text{and} \quad \textbf{ii}.\ a_2 \cdot a_1 > a_0 \tag{F.5}$$

The RH criterion gives four inequalities, which are greater than the number of eigenvalue solutions. However, a key advantage of the RH criterion is that we do not have to solve Equation F.4 to assess the stability.

REFERENCES

[1] T. C. Lieuwen and V. Yang, *Combustion instabilities in gas turbine engines: operational experience, fundamental mechanisms, and modeling*. Reston, VA: American Institute of Aeronautics and Astronautics, 2005, vol. 210, ISBN: 1600866808.

[2] C. J. Goy, S. R. James, and S. Rea, "Monitoring combustion instabilities: E. on uk's experience," *Progress in Astronautics and Aeronautics*, vol. 210, p. 163, 2005.

[3] H. Mongia, T. Held, G. Hsiao, and R. Pandalai, "Incorporation of combustion instability issues into design process: Ge aeroderivative and aero engines experience," Combustion instabilities in gas turbine engines, 2005.

[4] J. Cohen, G. Hagen, A. Banaszuk, S. Becz, and P. Mehta, "Attenuation of gas turbine combustor pressure oscillations using symmetry breaking," in *49th AIAA Aerospace Sciences Meeting including the New Horizons Forum and Aerospace Exposition*, 2011, p. 60.

[5] K. O. Smith and J. Blust, "Combustion instabilities in industrial gas turbines: Solar turbines' experience," *Combustion Instabilities in Gas Turbine Engines: Operational Experience, Fundamental Mechanisms, and Modeling*, pp. 29–42, 2005.

[6] J. M. Cohen, W. Proscia, J. DeLaat, T. Lieuwen, and V. Yang, "Characterization and control of aeroengine combustion instability: Pratt & whitney and nasa experience," *Combustion Instabilities in Gas Turbine Engines: Operational Experience, Fundamental Mechanisms, and Modeling*, pp. 113–145, 2005.

[7] W. Krebs, S. Bethke, J. Lepers, P. Flohr, B. Prade, C. Johnson, and S. Sattinger, "Thermoacoustic design tools and passive control: Siemens power generation approaches," *Combustion Instabilities in Gas Turbine Engines Operational Experience, Fundamental Mechanisms and Modeling*, 2005.

[8] M. Zellhuber, C. Meraner, R. Kulkarni, W. Polifke, and B. Schuermans, "Large eddy simulation of flame response to transverse acoustic excitation in a model reheat combustor," *Journal of Engineering for Gas Turbines and Power*, vol. 135, no. 9, p. 091 508, 2013.

[9] J. R. Dawson and N. A. Worth, "Flame dynamics and unsteady heat release rate of self-excited azimuthal modes in an annular combustor," *Combustion and Flame*, vol. 161, no. 10, pp. 2565–2578, 2014.

[10] J. B. Sewell and P. A. Sobieski, "Monitoring of combustion instabilities: Calpine's experience," *Combustion Instabilities in Gas Turbine Engines: Operational Experience, Fundamental Mechanisms, and Modeling*, vol. 210, pp. 147–162, 2005.

[11] H. Ebrahimi, "Overview of gas turbine augmentor design, operation, and combustion oscillation," in *42nd AIAA/ASME/SAE/ASEE Joint Propulsion Conference Exhibit*, p. 4916.

[12] D. E. Rogers, "A mechanism for high-frequency oscillation in ramjet combustors and afterburners," *Journal of Jet Propulsion*, vol. 26, no. 6, pp. 456–462, 1956.

[13] I. Elias, "Acoustical resonances produced by combustion of a fuel-air mixture in a rectangular duct," *The Journal of the Acoustical Society of America*, vol. 31, no. 3, pp. 296–304, 1959.

[14] W. Kaskan and A. Noreen, "High-frequency oscillations of a flame held by a bluff body," *ASME Transactions*, vol. 77, no. 6, pp. 855–891, 1955.

[15] C. R. King, "Experimental investigation of effects of combustion-chamber length and inlet total temperature, total pressure, and velocity on afterburner performance," 1957.

[16] L. L. Staff, *A summary of preliminary investigations into the characteristics of combustion screech in ducted burners*, 1958.

[17] T. C. Lieuwen, *Unsteady combustor physics*. Cambridge, U.K.: Cambridge University Press, 2012, ISBN: 1107015995.

[18] P. L. Rijke, "Lxxi. notice of a new method of causing a vibration of the air contained in a tube open at both ends," *The London, Edinburgh, and Dublin Philosophical Magazine and Journal of Science*, vol. 17, no. 116, pp. 419–422, 1859.

[19] J. W. S. B. Rayleigh, *The theory of sound*. Macmillan, 1896, vol. 2.

[20] R. Balachandran, B. Ayoola, C. Kaminski, A. Dowling, and E. Mastorakos, "Experimental investigation of the nonlinear response of turbulent premixed flames to imposed inlet velocity oscillations," *Combustion and Flame*, vol. 143, no. 1-2, pp. 37–55, 2005.

[21] D. McKinney and D. Dunn-Rankin, "Acoustically driven extinction in a droplet stream flame," *Combustion science and technology*, vol. 161, no. 1, pp. 27–48, 2000.

[22] T. Kim, M. Ahn, J. Hwang, S. Kim, and Y. Yoon, "The experimental investigation on the response of the burke–schumann flame to acoustic excitation," *Proceedings of the Combustion Institute*, vol. 36, no. 1, pp. 1629–1636, 2017.

[23] Y. Sun, M. Sun, J. Zhu, Y. Xie, H. Wang, M. Wan, and Y. Chen, "The local extinction and the nonlinear behaviors of a premixed methane/air flame under low-

frequency acoustic excitation," *Modern Physics Letters B*, vol. 34, no. 13, p. 2 050 138, 2020.

[24] S. Ducruix, T. Schuller, D. Durox, and S. Candel, "Combustion dynamics and instabilities: Elementary coupling and driving mechanisms," *Journal of propulsion and power*, vol. 19, no. 5, pp. 722–734, 2003.

[25] K. Venkataraman, L. Preston, D. Simons, B. Lee, J. Lee, and D. Santavicca, "Mechanism of combustion instability in a lean premixed dump combustor," *Journal of Propulsion and Power*, vol. 15, no. 6, pp. 909–918, 1999.

[26] T. J. Poinsot, A. C. Trouve, D. P. Veynante, S. M. Candel, and E. J. Esposito, "Vortex-driven acoustically coupled combustion instabilities," *Journal of fluid mechanics*, vol. 177, pp. 265–292, 1987.

[27] K. Schadow, E. Gutmark, T. Parr, D. Parr, K. Wilson, and J. Crump, "Large-scale coherent structures as drivers of combustion instability," *Combustion science and technology*, vol. 64, no. 4-6, pp. 167–186, 1989.

[28] S. K. Thumuluru and T. Lieuwen, "Characterization of acoustically forced swirl flame dynamics," *Proceedings of the Combustion Institute*, vol. 32, no. 2, pp. 2893–2900, 2009.

[29] P. Palies, D. Durox, T. Schuller, and S. Candel, "The combined dynamics of swirler and turbulent premixed swirling flames," *Combustion and Flame*, vol. 157, no. 9, pp. 1698–1717, 2010.

[30] Preetham, H. Santosh, and T. Lieuwen, "Dynamics of laminar premixed flames forced by harmonic velocity disturbances," *Journal of Propulsion and Power*, vol. 24, no. 6, pp. 1390–1402, 2008.

[31] C. O. Paschereit, E. Gutmark, and W. Weisenstein, "Coherent structures in swirling flows and their role in acoustic combustion control," *Physics of Fluids*, vol. 11, no. 9, pp. 2667–2678, 1999.

[32] Y. Huang and V. Yang, "Effect of swirl on combustion dynamics in a lean-premixed swirl-stabilized combustor," *Proceedings of the Combustion Institute*, vol. 30, no. 2, pp. 1775–1782, 2005.

[33] I. Hughes and A. Dowling, "The absorption of sound by perforated linings," *Journal of Fluid Mechanics*, vol. 218, pp. 299–335, 1990.

[34] T. Hofmeister, T. Hummel, B. Schuermans, and T. Sattelmayer, "Quantification of energy transformation processes between acoustic and hydrodynamic modes in non-compact thermoacoustic systems via a helmholtz-hodge decomposition ap-

proach," in *ASME Turbo Expo 2019: Turbomachinery Technical Conference and Exposition*, American Society of Mechanical Engineers Digital Collection, 2019.

[35] T. Hofmeister, T. Hummel, B. Schuermans, and T. Sattelmayer, "Modeling and quantification of acoustic damping induced by vortex shedding in noncompact thermoacoustic systems," *Journal of Engineering for Gas Turbines and Power*, vol. 142, no. 3, 2020.

[36] Shreekrishna, S. Hemchandra, and T. Lieuwen, "Premixed flame response to equivalence ratio perturbations," *Combustion Theory and Modelling*, vol. 14, no. 5, pp. 681–714, 2010.

[37] T. Lieuwen and B. T. Zinn, "The role of equivalence ratio oscillations in driving combustion instabilities in low nox gas turbines," in *Symposium (International) on combustion*, Elsevier, vol. 27, 1998, pp. 1809–1816.

[38] D. L. Straub and G. A. Richards, "Effect of fuel nozzle configuration on premix combustion dynamics," in *ASME 1998 International Gas Turbine and Aeroengine Congress and Exhibition*, American Society of Mechanical Engineers Digital Collection, 1998.

[39] T. Lieuwen, H. Torres, C. Johnson, and B. T. Zinn, "A mechanism of combustion instability in lean premixed gas turbine combustors," *J. Eng. Gas Turbines Power*, vol. 123, no. 1, pp. 182–189, 2000.

[40] G. Richards and M. Janus, "Characterization of oscillations during premix gas turbine combustion," 1998.

[41] D. W. Kendrick, T. J. Anderson, W. A. Sowa, and T. S. Snyder, "Acoustic sensitivities of lean-premixed fuel injectors in a single nozzle rig," in *ASME 1998 International Gas Turbine and Aeroengine Congress and Exhibition*, American Society of Mechanical Engineers Digital Collection, 1998.

[42] J. H. Cho and T. Lieuwen, "Laminar premixed flame response to equivalence ratio oscillations," *Combustion and flame*, vol. 140, no. 1-2, pp. 116–129, 2005.

[43] J. Stufflebeam, D. Kendrick, W. Sowa, and T. Snyder, "Quantifying fuel/air unmixedness in premixing nozzles using an acetone fluorescence technique," *J. Eng. Gas Turbines Power*, vol. 124, no. 1, pp. 39–45, 2002.

[44] A. Sandrowitz, J. Cooke, and N. Glumac, "Flame emission spectroscopy for equivalence ratio monitoring," *Applied spectroscopy*, vol. 52, no. 5, pp. 658–662, 1998.

[45] T. Sattelmayer, "Influence of the combustor aerodynamics on combustion instabilities from equivalence ratio fluctuations," *J. Eng. Gas Turbines Power*, vol. 125, no. 1, pp. 11–19, 2003.

[46] J. G. Lee, K. Kim, and D. Santavicca, "Measurement of equivalence ratio fluctuation and its effect on heat release during unstable combustion," *Proceedings of the Combustion Institute*, vol. 28, no. 1, pp. 415–421, 2000.

[47] A.-L. Birbaud, S. Ducruix, D. Durox, and S. Candel, "The nonlinear response of inverted "v" flames to equivalence ratio nonuniformities," *Combustion and flame*, vol. 154, no. 3, pp. 356–367, 2008.

[48] H. M. Altay, R. L. Speth, D. E. Hudgins, and A. F. Ghoniem, "The impact of equivalence ratio oscillations on combustion dynamics in a backward-facing step combustor," *Combustion and Flame*, vol. 156, no. 11, pp. 2106–2116, 2009.

[49] G. Ledder and A. Kapha, "The response of premixed flames to pressure perturbations," *Combustion science and technology*, vol. 76, no. 1-3, pp. 21–44, 1991.

[50] D. Keller and N. Peters, "Transient pressure effects in the evolution equation for premixed flame fronts," *Theoretical and Computational Fluid Dynamics*, vol. 6, no. 2, pp. 141–159, 1994.

[51] P. Clavin, P. Pelcé, and L. He, "One-dimensional vibratory instability of planar flames propagating in tubes," *Journal of Fluid Mechanics*, vol. 216, pp. 299–322, 1990.

[52] A. Wangher, G. Searby, and J. Quinard, "Experimental investigation of the unsteady response of premixed flame fronts to acoustic pressure waves," *Combustion and flame*, vol. 154, no. 1-2, pp. 310–318, 2008.

[53] H. Schmidt and C. JIMenez, "Numerical study of the direct pressure effect of acoustic waves in planar premixed flames," *Combustion and flame*, vol. 157, no. 8, pp. 1610–1619, 2010.

[54] A. McIntosh, "The interaction of high frequency low amplitude acoustic waves with premixed flames," in *Nonlinear Waves in Active Media*, Springer, 1989, pp. 218–231.

[55] A. McIntosh, "The linearised response of the mass burning rate of a premixed flame to rapid pressure changes," *Combustion Science and Technology*, vol. 91, no. 4-6, pp. 329–346, 1993.

[56] A. McIntosh, "Pressure disturbances of different length scales interacting with conventional flames," *Combustion Science and Technology*, vol. 75, no. 4-6, pp. 287–309, 1991.

[57] A. Van Harten, A. Kapila, and B. Matkowsky, "Acoustic coupling of flames," *SIAM Journal on Applied Mathematics*, vol. 44, no. 5, pp. 982–995, 1984.

[58] F. M. Berger, T. Hummel, B. Schuermans, and T. Sattelmayer, "Pulsation-amplitude-dependent flame dynamics of high-frequency thermoacoustic oscillations in lean-premixed gas turbine combustors," *Journal of Engineering for Gas Turbines and Power*, vol. 140, no. 4, p. 041 507, 2018.

[59] J. O'Connor and T. Lieuwen, "Disturbance field characteristics of a transversely excited burner," *Combustion Science and Technology*, vol. 183, no. 5, pp. 427–443, 2011.

[60] J. O'Connor and T. Lieuwen, "Influence of transverse acoustic modal structure on the forced response of a swirling nozzle flow," in *Turbo Expo: Power for Land, Sea, and Air*, American Society of Mechanical Engineers, vol. 44687, 2012, pp. 1491–1503.

[61] J. O'Connor, V. Acharya, and T. Lieuwen, "Transverse combustion instabilities: Acoustic, fluid mechanic, and flame processes," *Progress in Energy and Combustion Science*, vol. 49, pp. 1–39, 2015.

[62] J. O'Connor and T. Lieuwen, "Recirculation zone dynamics of a transversely excited swirl flow and flame," *Physics of fluids*, vol. 24, no. 7, pp. 2893–2900, 2012.

[63] J. J. Hutt and M. Rocker, "High-frequency injection-coupled combustion instability," *Progress in Astronautics and Aeronautics*, vol. 169, pp. 345–356, 1995.

[64] J. Hulka and J. J. Hutt, "Instability phenomena in liquid oxygen/hydrogen propellant rocket engines," *Progress in Astronautics and Aeronautics*, vol. 169, pp. 39–72, 1995.

[65] G. Staffelbach, L. Gicquel, G. Boudier, and T. Poinsot, "Large eddy simulation of self excited azimuthal modes in annular combustors," *Proceedings of the Combustion Institute*, vol. 32, no. 2, pp. 2909–2916, 2009.

[66] J. Blimbaum, M. Zanchetta, T. Akin, V. Acharya, J. O'Connor, D. Noble, and T. Lieuwen, "Transverse to longitudinal acoustic coupling processes in annular combustion chambers," *International journal of spray and combustion dynamics*, vol. 4, no. 4, pp. 275–297, 2012.

[67] J. O'Connor and V. Acharya, "Development of a flame transfer function description for transversely forced flames.," Sandia National Laboratories, Tech. Rep., 2012.

[68] L. Selle, L. Benoit, T. Poinsot, F. Nicoud, and W. Krebs, "Joint use of compressible large-eddy simulation and helmholtz solvers for the analysis of rotating modes in an industrial swirled burner," *Combustion and Flame*, vol. 145, no. 1-2, pp. 194–205, 2006.

[69] P. Wolf, G. Staffelbach, A. Roux, L. Gicquel, T. Poinsot, and V. Moureau, "Massively parallel les of azimuthal thermo-acoustic instabilities in annular gas turbines," *Comptes Rendus Mecanique*, vol. 337, no. 6-7, pp. 385–394, 2009.

[70] C. Sensiau, F. Nicoud, and T. Poinsot, "A tool to study azimuthal standing and spinning modes in annular combustors," *International Journal of Aeroacoustics*, vol. 8, no. 1, pp. 57–67, 2009.

[71] P. Wolf, G. Staffelbach, R. Balakrishnan, A. Roux, and T. Poinsot, "Azimuthal instabilities in annular combustion chambers," in *Proceedings of the Summer Program*, Citeseer, 2010, pp. 259–269.

[72] P. Wolf, G. Staffelbach, L. Y. Gicquel, J.-D. Müller, and T. Poinsot, "Acoustic and large eddy simulation studies of azimuthal modes in annular combustion chambers," *Combustion and Flame*, vol. 159, no. 11, pp. 3398–3413, 2012.

[73] A. Ghani, T. Poinsot, L. Gicquel, and J.-D. Müller, "Les study of transverse acoustic instabilities in a swirled kerosene/air combustion chamber," *Flow, Turbulence and Combustion*, vol. 96, no. 1, pp. 207–226, 2016.

[74] T. Schmitt, G. Staffelbach, S. Ducruix, S. Gröning, J. Hardi, and M. Oschwald, "Large-eddy simulations of a sub-scale liquid rocket combustor: Influence of fuel injection temperature on thermo-acoustic stability," in *Proceedings of the 7th European Conference for Aeronautics and Aerospace Science (EUCASS), Milan, Italy*, 2017, pp. 3–6.

[75] W. Krebs, G. Walz, P. Flohr, and S. Hoffmann, "Modal analysis of annular combustors: Effect of burner impedance," in *ASME Turbo Expo 2001: Power for Land, Sea, and Air*, American Society of Mechanical Engineers, V002T02A009–V002T02A009.

[76] W. Krebs, P. Flohr, B. Prade, and S. Hoffmann, "Thermoacoustic stability chart for high-intensity gas turbine combustion systems," *Combustion science and technology*, vol. 174, no. 7, pp. 99–128, 2002.

[77] J. P. Moeck, M. Paul, and C. O. Paschereit, "Thermoacoustic instabilities in an annular rijke tube," in *Turbo Expo: Power for Land, Sea, and Air*, vol. 43970, 2010, pp. 1219–1232.

[78] N. A. Worth and J. R. Dawson, "Self-excited circumferential instabilities in a model annular gas turbine combustor: Global flame dynamics," *Proceedings of the Combustion Institute*, vol. 34, no. 2, pp. 3127–3134, 2013.

[79] N. A. Worth and J. R. Dawson, "Modal dynamics of self-excited azimuthal instabilities in an annular combustion chamber," *Combustion and Flame*, vol. 160, no. 11, pp. 2476–2489, 2013.

[80] J. R. Dawson and N. A. Worth, "The effect of baffles on self-excited azimuthal modes in an annular combustor," *Proceedings of the Combustion Institute*, vol. 35, no. 3, pp. 3283–3290, 2015.

[81] N. A. Worth and J. R. Dawson, "Effect of equivalence ratio on the modal dynamics of azimuthal combustion instabilities," *Proceedings of the Combustion Institute*, vol. 36, no. 3, pp. 3743–3751, 2017.

[82] A. Faure-Beaulieu, T. Indlekofer, J. R. Dawson, and N. Noiray, "Experiments and low-order modelling of intermittent transitions between clockwise and anticlockwise spinning thermoacoustic modes in annular combustors," *Proceedings of the Combustion Institute*, 2020.

[83] J.-F. Bourgouin, D. Durox, J. P. Moeck, T. Schuller, and S. Candel, *Self-sustained instabilities in an annular combustor coupled by azimuthal and longitudinal acoustic modes*, ser. ASME Turbo Expo 2013: Turbine Technical Conference and Exposition, American Society of Mechanical Engineers. American Society of Mechanical Engineers, 2013, V01BT04A007–V01BT04A007.

[84] D. Durox, J.-F. Bourgouin, J. P. Moeck, M. Philip, T. Schuller, and S. Candel, "Nonlinear interactions in combustion instabilities coupled by azimuthal acoustic modes," in *n3l-Int'l Summer School and Workshop on Non-Normal and Nonlinear Effects In Aero-and Thermoacoustics*, 2013, p. 14.

[85] J.-F. Bourgouin, D. Durox, J. Moeck, T. Schuller, and S. Candel, "A new pattern of instability observed in an annular combustor: The slanted mode," *Proceedings of the Combustion Institute*, vol. 35, no. 3, pp. 3237–3244, 2015.

[86] J.-F. Bourgouin, D. Durox, J. P. Moeck, T. Schuller, and S. Candel, "Characterization and modeling of a spinning thermoacoustic instability in an annular combustor equipped with multiple matrix injectors," *Journal of Engineering for Gas Turbines and Power*, vol. 137, no. 2, 2015.

[87] D. Laera, T. Schuller, K. Prieur, D. Durox, S. M. Camporeale, and S. Candel, "Flame describing function analysis of spinning and standing modes in an annular combustor and comparison with experiments," *Combustion and Flame*, vol. 184, pp. 136–152, 2017.

[88] K. Prieur, D. Durox, T. Schuller, and S. Candel, "A hysteresis phenomenon leading to spinning or standing azimuthal instabilities in an annular combustor," *Combustion and flame*, vol. 175, pp. 283–291, 2017.

[89] K. Prieur, D. Durox, T. Schuller, and S. Candel, "Strong azimuthal combustion instabilities in a spray annular chamber with intermittent partial blow-off," *Journal of Engineering for Gas Turbines and Power*, vol. 140, no. 3, 2018.

[90] M. Mazur, H. T. Nygård, J. R. Dawson, and N. A. Worth, "Characteristics of self-excited spinning azimuthal modes in an annular combustor with turbulent premixed bluff-body flames," *Proceedings of the Combustion Institute*, vol. 37, no. 4, pp. 5129–5136, 2019.

[91] J. Schwing, T. Sattelmayer, and N. Noiray, "Interaction of vortex shedding and transverse high-frequency pressure oscillations in a tubular combustion chamber," in *Turbo Expo: Power for Land, Sea, and Air*, vol. 54624, 2011, pp. 259–268.

[92] T. Hummel, K. Hammer, P. Romero, B. Schuermans, and T. Sattelmayer, "Low-order modeling of nonlinear high-frequency transversal thermoacoustic oscillations in gas turbine combustors," *J. Eng. Gas Turbines Power*, vol. 139, no. 7, p. 071 503, 2017.

[93] F. M. Berger, T. Hummel, M. Hertweck, J. Kaufmann, B. Schuermans, and T. Sattelmayer, "High-frequency thermoacoustic modulation mechanisms in swirl-stabilized gas turbine combustors—part i: Experimental investigation of local flame response," *Journal of Engineering for Gas Turbines and Power*, vol. 139, no. 7, 2017.

[94] B. Schuermans, C. Paschereit, and P. Monkewitz, "Non-linear combustion instabilities in annular gas-turbine combustors," in *44th AIAA aerospace sciences meeting and exhibit*, 2006, p. 549.

[95] S. R. Stow and A. P. Dowling, "A time-domain network model for nonlinear thermoacoustic oscillations," *Journal of engineering for gas turbines and power*, vol. 131, no. 3, 2009.

[96] T. Hummel, F. Berger, B. Schuermans, and T. Sattelmayer, "Theory and modeling of non-degenerate transversal thermoacoustic limit cycle oscillations," Thermoacoustic Instabilities in Gas Turbines and Rocket Engines: Industry Meets Academia, 2016.

[97] N. Noiray, M. Bothien, and B. Schuermans, "Investigation of azimuthal staging concepts in annular gas turbines," *Combustion Theory and Modelling*, vol. 15, no. 5, pp. 585–606, 2011.

[98] M. Bauerheim, M. Cazalens, and T. Poinsot, "A theoretical study of mean azimuthal flow and asymmetry effects on thermo-acoustic modes in annular combustors," *Proceedings of the Combustion Institute*, vol. 35, no. 3, pp. 3219–3227, 2015.

[99] G. Ghirardo, M. Juniper, and J. P. Moeck, "Weakly nonlinear analysis of thermoacoustic instabilities in annular combustors," 2016.

[100] N. Noiray and B. Schuermans, "On the dynamic nature of azimuthal thermoacoustic modes in annular gas turbine combustion chambers," *Proceedings of the Royal Society A: Mathematical, Physical and Engineering Sciences*, vol. 469, no. 2151, 2013.

[101] G. Ghirardo and F. Gant, "Background noise pushes azimuthal instabilities away from spinning states," *arXiv preprint arXiv:1904.00213*, 2019.

[102] M. R. Bothien, N. Noiray, and B. Schuermans, "Analysis of azimuthal thermoacoustic modes in annular gas turbine combustion chambers," *Journal of Engineering for Gas Turbines and Power*, vol. 137, no. 6, p. 061 505, 2015.

[103] G. Ghirardo and M. P. Juniper, "Azimuthal instabilities in annular combustors: Standing and spinning modes," *Proceedings of the Royal Society A: Mathematical, Physical and Engineering Sciences*, vol. 469, no. 2157, p. 20 130 232, 2013.

[104] G. Ghirardo, H. T. Nygård, A. Cuquel, and N. A. Worth, "Symmetry breaking modelling for azimuthal combustion dynamics," *Proceedings of the Combustion Institute*, 2020.

[105] M. Reader-Harris and J. Sattary, "The orifice plate discharge coefficient equation—the equation for iso 5167-1," in *Proceedings of the 14th North Sea Flow Measurement Workshop, Peebles, UK*, 1996, pp. 25–28.

[106] D. T. Harrje, *Liquid propellant rocket combustion instability*. Scientific, Technical Information Office, National Aeronautics, and Space Administration, 1972, vol. 194.

[107] D. W. Vincent, *Experimental Investigation of Acoustic Liners to Suppress Screech in Storable Propellant Rocket Motors*. National Aeronautics and Space Administration, 1968.

[108] G. Garrison, "The role of acoustic absorbers in preventing combustion instability," in *7th Propulsion Joint Specialist Conference*, 1971, p. 699.

[109] J. G. Lee and D. A. Santavicca, "Experimental diagnostics of combustion instabilities," *Progress in astronautics and aeronautics*, vol. 210, p. 481, 2005.

[110] A. A. Hale, W. D. Cothran, and K. M. Sabo, "Analysis technique to determine the underlying wave structure of combustion instabilities from surface mounted high response static pressure sensors," in *ASME Turbo Expo 2018: Turbomachinery Technical Conference and Exposition*, American Society of Mechanical Engineers Digital Collection.

[111] G. Singla, N. Noiray, and B. Schuermans, "Combustion dynamics validation of an annular reheat combustor," in *ASME Turbo Expo 2012: Turbine Technical Conference and Exposition*, American Society of Mechanical Engineers Digital Collection, pp. 447–455.

[112] P. Shah and F. Udwadia, "Optimal sensor location for identification of building structures using response to earthquake ground motions," in *Sixth World Conference in Earthquake Engineering, New Delhi*, 1976.

[113] P. Shah and F. Udwadia, "A methodology for optimal sensor locations for identification of dynamic systems," *Journal of Applied Mechanics.*, vol. 45, pp. 188–196, 1978.

[114] D. C. Kammer, "Sensor placement for on-orbit modal identification and correlation of large space structures," *Journal of Guidance, Control, and Dynamics*, vol. 14, no. 2, pp. 251–259, 1991.

[115] L. Yao, W. A. Sethares, and D. C. Kammer, "Sensor placement for on-orbit modal identification of large space structure via a genetic algorithm," in *[Proceedings 1992] IEEE International Conference on Systems Engineering*, IEEE, 1992, pp. 332–335.

[116] I. Laory, N. B. Hadj Ali, T. N. Trinh, and I. F. Smith, "Measurement system configuration for damage identification of continuously monitored structures," *Journal of Bridge Engineering*, vol. 17, no. 6, pp. 857–866, 2012.

[117] K. Worden and A. Burrows, "Optimal sensor placement for fault detection," *Engineering structures*, vol. 23, no. 8, pp. 885–901, 2001.

[118] D. Li, H. Li, and C. Fritzen, "The connection between effective independence and modal kinetic energy methods for sensor placement," *Journal of sound and vibration*, vol. 305, no. 4-5, pp. 945–955, 2007.

[119] B. Li, J. Ou, X. Zhao, and D. Li, "Optimal sensor placement in health monitoring system of xinghai bay bridge," in *Int. Workshop on Advanced Smart Materials and Smart Structures Technology*, DEStech Publications Lancaster, PA, 2011.

[120] F. M. Hemez and C. Farhat, "An energy based optimum sensor placement criterion and its application to structural damage detection," in *Proceedings-SPIE the In-*

ternational Society for Optical Engineering, SPIE INTERNATIONAL SOCIETY FOR OPTICAL, 1994, pp. 1568–1568.

[121] G. Heo, M. Wang, and D. Satpathi, "Optimal transducer placement for health monitoring of long span bridge," *Soil dynamics and earthquake engineering*, vol. 16, no. 7-8, pp. 495–502, 1997.

[122] B. Schuermans, "Modeling and control of thermoacoustic instabilities," EPFL, Tech. Rep., 2003.

[123] J. A. Holdener, "Math bite: Sums of sines and cosines," *Mathematics Magazine*, vol. 82, no. 2, pp. 126–126, 2009.

[124] J. L. Harp, W. W. Velie, and L. Bryant, *Investigation of Combustion Screech and a Method of its Control*. National Advisory Committee for Aeronautics, 1954.

[125] E. Laudien, R. Pongratz, R. Pierro, and D. Preclik, "Experimental procedures aiding the design of acoustic cavities," *Liquid Rocket Engine Combustion Instability*, vol. 169, pp. 377–399, 1995.

[126] N. Hannum, L. Russell, and J. Wanhainen, "Evaluation of speech suppression concepts in a 20,000 pound thrust hydrogen oxygen rocket," 1967.

[127] S. R. Stow and A. P. Dowling, "Modelling of circumferential modal coupling due to helmholtz resonators," in *ASME Turbo Expo 2003, collocated with the 2003 International Joint Power Generation Conference*, American Society of Mechanical Engineers Digital Collection, pp. 129–137.

[128] S. Camporeale, A. Forte, B. Fortunato, M. Mastrovito, and A. Ferrante, "Numerical simulation of the acoustic pressure field in an annular combustion chamber with helmholtz resonators," in *ASME Turbo Expo 2004: Power for Land, Sea, and Air*, American Society of Mechanical Engineers Digital Collection, pp. 713–724.

[129] M. Zahn, M. Schulze, C. Hirsch, and T. Sattelmayer, "Impact of quarter wave tube arrangement on damping of azimuthal modes," in *ASME Turbo Expo 2016: Turbomachinery Technical Conference and Exposition*, American Society of Mechanical Engineers Digital Collection.

[130] M. Betz, M. Wagner, M. Zahn, N. V. Stadlmair, M. Schulze, C. Hirsch, and T. Sattelmayer, "Impact of damper parameters on the stability margin of an annular combustor test rig," in *ASME Turbo Expo 2017: Turbomachinery Technical Conference and Exposition*, American Society of Mechanical Engineers Digital Collection.

[131] M. Mazur, H. T. Nygård, J. Dawson, and N. Worth, "Experimental study of damper position on instabilities in an annular combustor," in *ASME Turbo Expo 2018: Tur-*

bomachinery Technical Conference and Exposition, American Society of Mechanical Engineers Digital Collection.

[132] T. Poinsot, P. Wolf, G. Staffelbach, L. Gicquel, and J. Muller, "Identification of azimuthal modes in annular combustion chambers," *Center for Turbulence Research Annual Research Briefs*, vol. 2011, pp. 249–258, 2011.

[133] F. Nicoud, L. Benoit, C. Sensiau, and T. Poinsot, "Acoustic modes in combustors with complex impedances and multidimensional active flames," *AIAA journal*, vol. 45, no. 2, pp. 426–441, 2007.

[134] M. Schulze, T. Hummel, N. Klarmann, F. Berger, B. Schuermans, and T. Sattelmayer, "Linearized euler equations for the prediction of linear high-frequency stability in gas turbine combustors," *Journal of Engineering for Gas Turbines and Power*, vol. 139, no. 3, p. 031 510, 2017.

[135] G. A. Richards, D. L. Straub, and E. H. Robey, "Passive control of combustion instabilities in stationary gas turbines," *Combustion Instabilities in Gas Turbine Engines*, vol. 210, 2005.

[136] C. O. Paschereit, P. Flohr, W. Geng, C. Steinbach, P. Stuber, K. Bengtsson, and E. Gutmark, "Combustion control by extended ev burner fuel lance," in *ASME Turbo Expo 2002: Power for Land, Sea, and Air*, American Society of Mechanical Engineers Digital Collection, pp. 721–730.

[137] H. Hermsmeyer, B. Prade, U. Gruschka, U. Schmitz, S. Hoffmann, and W. Krebs, "V64. 3a gas turbine natural gas burner development," in *ASME Turbo Expo 2002: Power for Land, Sea, and Air*, American Society of Mechanical Engineers Digital Collection, pp. 689–695.

[138] C. Pankiewitz and T. Sattelmayer, "Time domain simulation of combustion instabilities in annular combustors," *J. Eng. Gas Turbines Power*, vol. 125, no. 3, pp. 677–685, 2003.

[139] A. H. Nayfeh, D. T. Mook, and P. Holmes, "Nonlinear oscillations," 1980.

[140] T. Hummel, F. Berger, M. Hertweck, B. Schuermans, and T. Sattelmayer, "High-frequency thermoacoustic modulation mechanisms in swirl-stabilized gas turbine combustors—part ii: Modeling and analysis," *Journal of Engineering for Gas Turbines and Power*, vol. 139, no. 7, 2017.

[141] G. Vignat, D. Durox, A. Renaud, and S. Candel, "High amplitude combustion instabilities in an annular combustor inducing pressure field deformation and flame blow off," *Journal of Engineering for Gas Turbines and Power*, vol. 142, no. 1, 2020.

[142] V. Acharya, M. Bothien, and T. Lieuwen, "Modal dynamics of thermoacoustic systems with closely-spaced eigenfrequencies," in *Proceedings of the International Symposium "Thermoacoustic Instabilities in Gas Turbines and Rocket Engines: Industry meets Academia", Munich, Germany*, vol. 30, 2016, pp. 1–11.

[143] T. John, G. Giulio, V. Acharya, M. Bothien, and T. Lieuwen, "Nonlinear dynamics of closely spaced thermoacoustic modes in the presence of noise," 2019.

[144] N. Kryloff and N. Bogoliuboff, "Introduction to nonlinear mechanics, princeton univ," *Press, Princeton, NJ*, 1947.

[145] F. Culick, "Nonlinear behavior of acoustic waves in combustion chambers—ii," *Acta Astronautica*, vol. 3, no. 9-10, pp. 735–757, 1976.

[146] F. Culick, V. Burnley, and G. Swenson, "Pulsed instabilities in solid-propellant rockets," *Journal of Propulsion and Power*, vol. 11, no. 4, pp. 657–665, 1995.

[147] T. C. Lieuwen, "Experimental investigation of limit-cycle oscillations in an unstable gas turbine combustor," *Journal of Propulsion and Power*, vol. 18, no. 1, pp. 61–67, 2002.

[148] A. Peracchio and W. Proscia, "Nonlinear heat-release/acoustic model for thermoacoustic instability in lean premixed combustors," in *Turbo Expo: Power for Land, Sea, and Air*, American Society of Mechanical Engineers, vol. 78644, 1998, V003T06A022.

[149] A. P. Dowling, "Nonlinear self-excited oscillations of a ducted flame," *Journal of fluid mechanics*, vol. 346, pp. 271–290, 1997.

[150] T. C. Lieuwen, "Statistical characteristics of pressure oscillations in a premixed combustor," *Journal of Sound and Vibration*, vol. 260, no. 1, pp. 3–17, 2003.

[151] A. H. Nayfeh and P. F. Pai, *Linear and nonlinear structural mechanics*. John Wiley & Sons, 2008.

[152] R. L. Stratonovich, *Topics in the theory of random noise*. CRC Press, 1967, vol. 2.

[153] P. D. Spanos, "Stochastic analysis of oscillators with non-linear damping," *International Journal of Non-Linear Mechanics*, vol. 13, no. 4, pp. 249–260, 1978.

[154] J. Roberts and P. Spanos, "Stochastic averaging: An approximate method of solving random vibration problems," *International Journal of Non-Linear Mechanics*, vol. 21, no. 2, pp. 111–134, 1986.

[155] P. E. Kloeden and E. Platen, "Stochastic differential equations," in *Numerical Solution of Stochastic Differential Equations*, Springer, 1992, pp. 103–160.

[156] P. Clavin, J. Kim, and F. Williams, "Turbulence-induced noise effects on high-frequency combustion instabilities," *Combustion Science and Technology*, vol. 96, no. 1-3, pp. 61–84, 1994.

[157] V. Burnley and F. Culick, "Influence of random excitations on acoustic instabilities in combustion chambers," *AIAA journal*, vol. 38, no. 8, pp. 1403–1410, 2000.

[158] T. Lieuwen and A. Banaszuk, "Background noise effects on combustor stability," *Journal of Propulsion and Power*, vol. 21, no. 1, pp. 25–31, 2005.

[159] G. Bonciolini, A. Faure-Beaulieu, C. Bourquard, and N. Noiray, "Low order modelling of thermoacoustic instabilities and intermittency: Flame response delay and nonlinearity," *Combustion and Flame*, vol. 226, pp. 396–411, 2021.

[160] G. E. Uhlenbeck and L. S. Ornstein, "On the theory of the brownian motion," *Physical review*, vol. 36, no. 5, p. 823, 1930.

[161] T. Lieuwen, "Online combustor stability margin assessment using dynamic pressure data," *J. Eng. Gas Turbines Power*, vol. 127, no. 3, pp. 478–482, 2005.

[162] M. Lee, Y. Zhu, L. K. Li, and V. Gupta, "System identification of a low-density jet via its noise-induced dynamics," *Journal of Fluid Mechanics*, vol. 862, pp. 200–215, 2019.

[163] E. Boujo and N. Noiray, "Robust identification of harmonic oscillator parameters using the adjoint fokker–planck equation," *Proceedings of the Royal Society A: Mathematical, Physical and Engineering Sciences*, vol. 473, no. 2200, p. 20 160 894, 2017.

[164] M. Lee, K. T. Kim, V. Gupta, and L. K. Li, "System identification and early warning detection of thermoacoustic oscillations in a turbulent combustor using its noise-induced dynamics," *Proceedings of the Combustion Institute*, vol. 38, no. 4, pp. 6025–6033, 2021.

[165] N. Noiray, "Linear growth rate estimation from dynamics and statistics of acoustic signal envelope in turbulent combustors," *Journal of Engineering for Gas Turbines and Power*, vol. 139, no. 4, p. 041 503, 2017.

[166] N. Noiray and A. Denisov, "A method to identify thermoacoustic growth rates in combustion chambers from dynamic pressure time series," *Proceedings of the Combustion Institute*, vol. 36, no. 3, pp. 3843–3850, 2017.

[167] J. G. Truxal, "Automatic feedback control system synthesis," 1955.

[168] V. Del Toro and S. R. Parker, *Principles of control systems engineering*. McGraw-Hill, 1960.

[169] J. E. Gibson, "Nonlinear automatic control," 1963.

[170] W. E. Vander Velde, *Multiple-input describing functions and nonlinear system design*. McGraw-Hill, New York, 1968.